Coarse-grained molecular modelling of amphiphilic polymers at a water/air interface

PRASITNOK, KHONGVIT

Coarse-grained molecular modelling of amphiphilic polymers at a water/air interface

Khongvit Prasitnok

A thesis submitted in partial fulfilment of the requirements for the degree of Doctor of Philosophy

Department of Chemistry
Durham University
England
September 2012

Coarse-grained molecular modelling of amphiphilic polymers at a water/air interface

by Khongvit Prasitnok

PhD Thesis, September 2012

Abstract

Previous atomic-level simulations have been shown to provide invaluable insight into the adsorption behaviour of amphiphilic polymers at a water-air interface. Neutron reflectivity profiles generated from these simulations showed good agreement with experiment, particularly at low surface concentrations. Unfortunately, previous detailed atomistic simulations have failed to produce adequate results at high surface concentrations due to crowded configurations, which could not relax within the simulation times available. To tackle this problem, a coarse-graining (CG) technique, where the structure of the simulated molecule is simplified to a chain of beads, has been employed in this study. This provides for the simulation of larger time and length scales allowing for a more detailed study of the capture of polymer chains by a surface and the structure of surface layers.

The work presented in this thesis involves development of coarse-grained models for water and for poly(ethylene oxide) (PEO)/water systems, with the aim of reproducing the properties of key importance for the bulk and liquid/vapour interfacial states. These models are then used in the coarse-grained simulation studies of di- and trifluoro dendritic end-capped PEO at an air-water interface; the amphiphilic polymers that have been studied recently by neutron reflectivity experiments.

It is shown in this study that simulation of very large polymer chains comparable to that used in real experiments, is achievable using coarse-grained molecular dynamics. Neutron reflectivity profiles generated from simulations of di- and trifluoro dendritic end-capped PEO materials at low polymer concentrations are in good agreement with experiment data. Simulations at high polymer concentrations showed no evidence of a stretched brush structure, in accordance with experimental findings. It is shown from these simulations that there are polymers adsorbed to

the interface by a combination of fluorocarbon ends and ethylene oxide segments, resulting in a rather flat layer structure. At high surface concentrations of polymers, it proved possible to see the formation of polymer micelles in bulk water. The process of micelle capture by the surface and incorporation of the micelle contents into the surface, were also observed.

Declaration

The material contained within this thesis has not previously been submitted for a degree at Durham university or any other university. The research within this thesis has been conducted by the author unless indicated otherwise.

Statement of Copyright

Acknowledgements

First and foremost I would like to express my sincerest gratitude to Prof. Mark Wilson for giving me the opportunity to join his research group. I am grateful for his support, time and guidance throughout my studies, and this thesis would not have been possible without his excellent supervision. I am also grateful for the financial support from the Royal Thai Government Scholarship during my PhD research in Durham.

I would like to thank Dr. Richard Thompson and Dr. Simon Bartram for providing data, help and advice with respect to the neutron reflectivity work included in this thesis. I would also like to thank all of the members of Mark's research groups and everyone in CG200, both past and present, for their friendship and for making my four years in Durham full of interesting memories. Special thanks also go to all Thai students in Durham who have been very helpful and have made my days so enjoyable.

Finally, I am deeply indebted to my parents, grandma and my sister for their unconditional love and support. Without them I could never have accomplished this far. My special gratitude also goes to Orrasa, who is always by my side. I am grateful for her support, her friendship and her love. This thesis is dedicated to all the people mentioned here, and to all family members, friends and teachers who have supported me all the way through.

Contents

List of Figures

List of Tables

Chapter 1

Introduction

1.1 Polymers

Polymers are very large molecules (macromolecules), made up of smaller units called monomers (or repeating units), covalently bonded together. Because of the extremly wide range of properties of polymeric materials [1], they play a very important role in all aspects of life today [2]. This role ranges from familiar synthetic plastics and rubbers to natural biopolymers such as nucleic acids and proteins that are essential for life.

Often it is desirable to combine the properties of two or more polymers together, and this leads to several different types of polymer molecule, including random copolymers, block copolymers, graft copolymers and dendritic polymers (dendrimers), as shown in figure 1.1. A typical random copolymer would have the monomer units distributed throughout the molecule in purely random fashion. Block copolymers are rather more ordered, being made up of alternating segments of single monomer type. Graft copolymers are more interesting materials, and are in the simplest cases, composed of two monomer types. One of the monomers generally forms a long chain known as the *backbone*, and the other monomer forms secondary chains (*side-chains*) which radiate out from this backbone, at branching points. Dendritic polymers or dendrimers are a highly branched (hyperbranched) polymers, and their properties can vary dramatically from the properties of the equivalent conventional linear polymers. Dendrimers are highly organized structures, typically consisting of

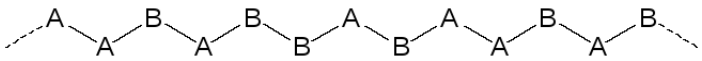

(a) Random copolymer

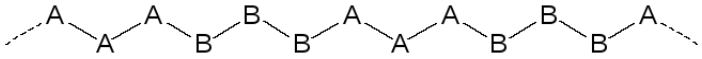

(b) Block copolymer

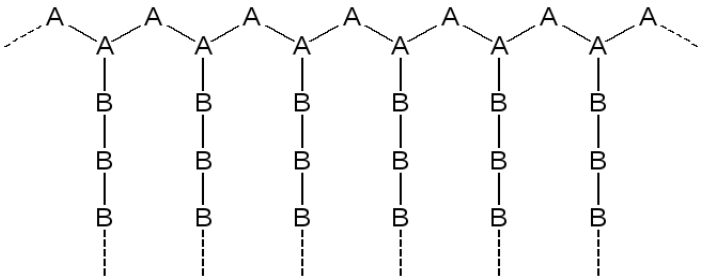

(c) Graft copolymer

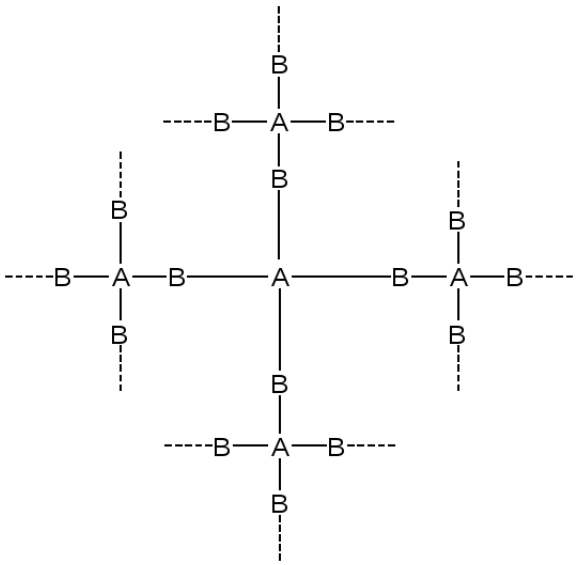

(d) Dendritic polymer (dendrimer)

Figure 1.1: Four common types of polymer. Open bonds represent a continuation of the repeat patterns. A and B are chemically different repeat units.

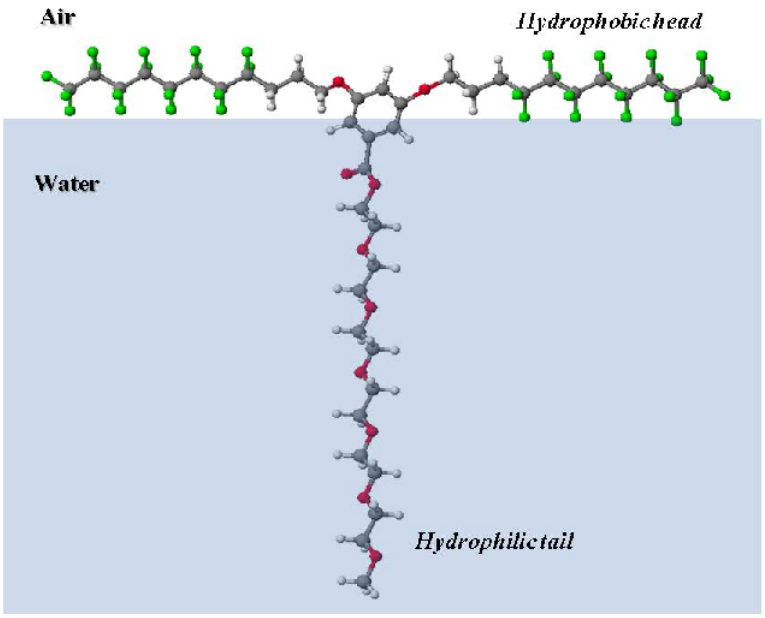

Figure 1.2: An amphiphilic fluorocarbon end-capped poly(ethylene oxide) at an air-water interface.

molecular chains that are branched out from a common center.

1.2 Amphiphilic polymers

The term "amphiphilic" (amphiphile) describe a molecule possessing both "hydrophilic" (water-loving, polar) and "hydrophobic" (water-fearing, non-polar) properties. Such amphiphilic behaviour can be found in any kind of copolymer providing that the structure is made up from both hydrophobic and hydrophilic monomers. An example of an amphiphilic polymer is poly(ethylene oxide) (PEO) end-capped with a fluorocarbon group. In this case, because of its hydrophilic nature, the PEO tail will attempt to immerse itself into water to maximise the favourable monomer-solvent interactions. The fluorocarbon head group, which is hydrophobic, will minimise its energy by avoiding the water. This leads to a system where the head group remains at the surface, while the tail chain penetrates into the aqueous subphase, as shown in figure 1.2.

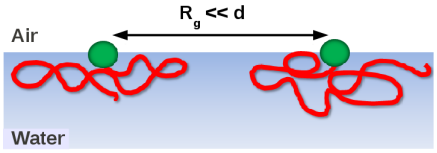

(a) "pancake" conformation

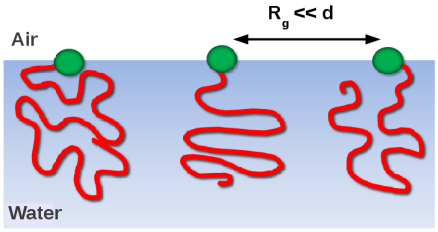

(b) "mushroom" conformation

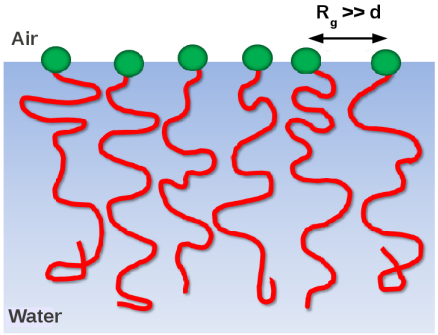

(c) "brush" conformation

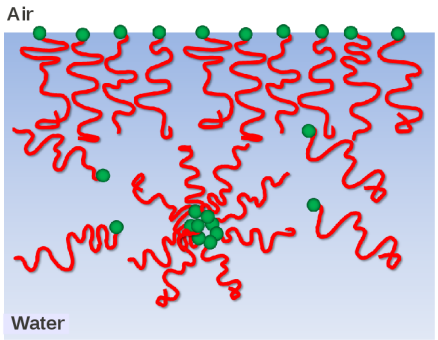

(d) "micelle" formation

Figure 1.3: The three major morphologies of a tethered polymer and micelle formation of polymer chains.

1.3 Polymers at interfaces and tethered polymers

Polymers at interfaces have been a rich field of study due to the wide variety of applications that they can provide. Processes involved in lubrication [3–5] and adhesion [6, 7] are often enhanced using polymer-mediated surface contacts. The role of tethering polymers in stabilizing colloidal dispersions has been appreciated for a considerable time [8]. Studies are also underway to use this type of molecule for specific targeting in drugs using a biodegradable polymer shell to deliver and release the drug at a specific place in the body and over a set amount of time [9–11].

An interface is defined as a boundary between two different types of matter or space and can be simplified down to boundaries between solid, liquid, and gas (or vacuum). The majority of work done with amphiphilic polymers involve studies at a liquid-gas interface and the simplest interface of this type is an air-water interface, as this can be easily created experimentally and is an ideal model for more complex biological systems.

Placing amphiphilic polymers at the water-air interface promptly leads to a segregation of the hydrophobic head group away from the bulk water and an aggregation of the hydrophilic tail group into the bulk water, resulting in tethering of the molecule at the interface. Polymer chains in bulk solution are known to exhibit a random walk behaviour, in which the chain is free to adopt a wide variety of conformations simply by rotation about the single bonds in the backbone of the molecule. A chain that is adsorbed to a surface, however, does not have much freedom to follow a random walk due to the restriction of the interface at which it is tethered. Noteworthy, it turns out that this adsorption can promote some interesting and novel conformations which lead to a profound change of the surface properties.

Depending upon the packing density at the interface, tethered polymers can form a number of different conformations, some of the common ones are discussed here. The first conformation (figure 1.3 (a)) arises when the space between graft points (or tethered ends) is much greater than the radius of gyration of the isolated chains. This conformation is known as a “pancake” and typically adopted by polymers at low grafting density in a poor solvent, such as a hydrophobic polymer in water. Since polymer-solvent interactions are unfavourable, the chains thus minimizes its

energy by lying at the surface and has very little or no interaction with surrounding chains.

The second conformation known as a "mushroom" (figure 1.3 (b)), which is also observed when the space between tethered ends (or graft points) is much greater than the radius of gyration for the polymer. However, in this case the polymer-solvent interactions are more favourable than the polymer-surface interactions. As a result, the chains extend down into the solvent to minimise their energy. This conformation is typical of a tethered hydrophilic polymer in water.

The third conformation (figure 1.3 (c)) occurs when the mean distance between tethered ends is less than the radius of gyration which typically occurs for amphiphilic polymer systems with a reasonably high graft density. Excluded volume interactions between neighbouring chains cause the tethered polymer to stretched normal to the interface, hence minimising monomer-monomer contact whilst maximising the enthalpically favourable monomer-solvent interactions. The lowering of free energy resulting from the reduction of the excluded volume interactions is counterbalanced by the loss of entropy (unfavourable contribution to the free energy) from the stretching of the chains from their initial random walk configurations. It is the balance between these two forces that controls the extent of stretching of polymer chains, which are commonly referred to as polymer "brushes".

Upon increasing the the polymer concentration above the conditions required for brush formation, one reaches a point where there is no space available to add more chains to the interface. This is known as the "critical micelle concentration" (CMC) and above this point one sees the formation of micelles beneath the surface excess layer, as shown in figure 1.3 (d) (noting that micelles can also be formed by some molecules without the necessity of a surface excess layer). In this case the tethered head groups (e.g. highly hydrophobic head groups in a water solvent) will attempt to lower the highly unfavourable head group–solvent interactions by migrating together to form a pocket where there is very little solvent present. As a result the polymer tails will extend out from the core of the micelle and spread into the solvent to minimize their energy.

There are usually two methods used in experiments to prepare amphiphilic poly-

mer at an air-water interface. The first method is to spread an insoluble polymer onto a water surface. This is achieved by first dissolving the polymer in an appropriate volatile solvent that is a good solvent for the polymer but insoluble in the water substrate. After spreading polymer onto the water surface, the volatile solvent is evaporated out, leaving the polymer film on the water surface. The second method involves dissolving an amphiphilic polymer in the liquid water. Diffusion of the polymer will lead to self assembly of a surface excess layer due to the amphiphilic nature of the polymer. Above the surface saturation concentration, one can also sees micelle formation from this method.

1.3.1 Neutron reflectometry

Neutron reflectometry is a well-established technique for investigating the structural properties of polymer materials at surfaces and interfaces [12, 13]. This approach is attractive due to its ability to provide the most direct access to such aspects as layer composition and thickness of a "buried" interface. Apart from its applications in a study of polymer organization at fluid interfaces [14–18], this technique has also been used to study liquid-metal interfaces [19], surfaces of liquid-liquid mixtures [20] and the magnetic/structural properties of metallic thin films [21, 22].

The neutron reflectometry process involves firing a beam of neutrons at a surface, and measuring the reflectivity of the interface by analysing the specularly reflected beam's properties relative to those of the incident beam. By monitoring the changes in reflectivity as a function of probe depth, the molecular organisation normal to the interface can be profiled.

When a beam of neutrons is incident on such a surface four different processes occur including specular reflection, transmission, bulk scattering and non-specular reflection, as outlined in figure 1.4.

Specular reflection (1) from a surface occurs when the angle of incidence equals that of reflection. This is used to study structure of samples perpendicular to the surface and can probe thicknesses of a few angstroms up to a few microns. Non-specular reflection (4) occurs when the surface under study has been roughened by, for example, thermal fluctuations, but the intensity of reflection from these processes

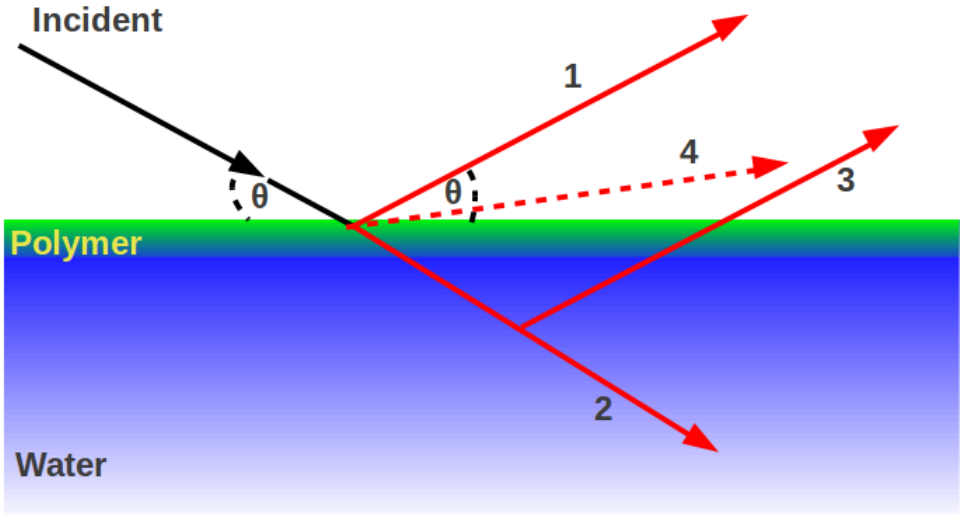

Figure 1.4: Schematic of processes that occur when an incident beam of neutrons hits an interface/surface: (1) specular reflection; (2) transmission; (3) bulk scattering; (4) non-specular reflection.

is normally less than the background signal. Specular reflection also occurs from the bulk subphase (3) (if a scattering species is present), which contributes to the background signal. If the beam is not reflected to any extent then it is completely transmitted into the subphase (2).

The processes involved in neutron reflectometry are analogous to those in optical reflectivity experiments (light or X-rays), since the beam is reflected to an extent depending on the refractive index of the sample. The significant difference between the two techniques is the interaction that occurs between the probing radiation and interface, since X-rays are scattered by electrons and neutrons are scattered by nuclei. When discussing the reflection of neutron, the conventional optical terms of scattering angle and reflective index are replaced by the terms *wavevector*, Q, and *scattering length density*, ρ, respectively.

The wavevector is defined as the magnitude of the vector between the specularly reflected beam and the transmitted beam at the interface. This quantity can be related to the wavelength of the incident beam, as well as the angle of incidence by equation 1.1,

$$Q = \frac{4\pi}{\lambda} \sin\theta, \tag{1.1}$$

where λ is the wavelength of the incident neutron beam, and θ is the angle of incidence.

When considering a macroscopically smooth surface and ignoring any absorption effects (which are generally negligible for neutron reflectivity), the neutron refractive index, n, can be expressed as

$$n = 1 - \frac{\lambda^2}{2\pi}\rho \tag{1.2}$$

where ρ is the scattering length density, which depends on the number density, n_i, and scattering length, b of species i, present at the surface.

$$\rho = \sum_i n_i b_i. \tag{1.3}$$

By combining equation 1.2 and 1.3, it is evident that the surface refractive index is dependent on the scattering length density and consequently the atomic composition normal to the surface.

Values for the scattering length and scattering length densities for nuclei and components relevant to our study are given in table 1.1. The most important factor in a neutron scattering measurement is the big difference between the scattering length of hydrogen and deuterium. Whilst the negative scattering of the former results in a poorly reflected beam (which can be easily merged with the background), the positive scattering length of the latter can be used to amplify the reflected beam. By preparing various contrasts through isotropic substitution, the reflectivity can be analysed as a function of composition allowing the observer to deduce further information on the system's structure without perturbing the structure itself.

The opposing signs of light (H_2O) and heavy (D_2O) water allow the preparation of a subphase with a scattering length density of zero, simply by mixing the components in an appropriate ratio. This mixture is referred to as *null reflecting water* (NRW), and can be used to eliminate all coherent scattering due to the water subphase.

Nucleus	b / 10^{-4} Å
^{1}H	-0.37
^{2}H	0.68
C	0.67
O	0.58
F	0.57

Species	$\sum b$ / 10^{-4} Å	ρ / 10^{-6} Å^{-2}
H_2O	-1.68	-0.56
D_2O	1.92	6.35
Air	0	0
Ethylene oxide (H)	0.41	0.56
Ethylene oxide (D)	4.58	6.33
Difluoro dendritic end-cap $(C_8F_{17}C_3H_6O)_2$-C_6H_3-CO-OCH_2-	35.14	-
Trifluoro dendritic end-cap $(C_8F_{17}C_3H_6O)_3$-C_6H_2-CO-OCH_2-	50.40	-

Table 1.1: Scattering lengths, b, and scattering length densities, ρ, of units present in the amphiphilic/interface system of interest [23, 24]. (H) is hydrogenous and (D) is deuterated.

1.3.2 The Langmuir Trough

The Langmuir trough is a laboratory instrument that is used to set up polymer films of varying surface concentrations. The trough is filled with a liquid (typically pure water), and has a movable barrier to allow easy variation of the surface area of the liquid within. Studies of amphiphilic polymers at a water surface are often undertaken using a Langmuir trough, in which surface concentration can be altered by moving this barrier. A molecular monolayer of polymer is typically prepared by gradually dripping a solution of amphiphile onto the water surface. A volatile solvent that is immiscible with water (such as diethyl ether or chloroform) is used for this, to ensure that the only species present are the water and the amphiphile upon evaporation of the solvent. The amphiphilic molecules then remain at the water interface where their surface concentration can be freely altered using the barrier. Neutron reflectivity studies are often performed on materials in a Langmuir trough.

1.3.3 Surface pressure isotherms

Surface pressure is defined as the difference between the surface tension of the pure subphase material A (e.g. water) and that of the material's surface in the presence of material B (e.g. amphiphile). The variation of surface pressure with surface concentration of amphiphilic molecule can be measured by means of Langmuir trough equipment.

Surface pressure can be measured using a *Wilhelmy plate* (a simple piece of high quality filter paper connecting to a displacement transducer that can accurately measure forces acting on the plate due to the surface tension of the liquid phase). Since the surface tension of water is reduced by the introduction of an amphiphilic molecules to the surface, the force acting on the Wilhelmy plate will vary with the composition of the surface being studied. By monitoring changes in the surface pressure as a function of surface concentration a qualitative insight into the molecular organisation of the film at the interface can be obtained.

An example of an ideal isotherm for low molecular weight materials at a surface, for example stearic acid, is given in figure 1.5. This diagram highlights the three individual orientation states that simple molecules exhibit: the gaseous (G); liquid expanded (LE) and the liquid condensed (LC) state.

The gaseous state occurs when the surface concentration of molecules is low, hence the area per molecule is large and the surface pressure is low. The individual components have freedom to move independently over the surface in this state. By compression of the barriers, the gaseous state can undergo a phase transition to the liquid expanded state where the molecules still have freedom to move on the surface but they begin to overlap and interact with each other. Upon further compression, the high surface concentration regime is reached via another phase transition in which the molecules are forced to packed closely and orient steeply towards the surface. This is known as the liquid-condensed state and a steep rise in the surface pressure can be observed.

In general, polymer films do not undergo distinct changes in state, hence their surface pressure isotherms are relatively featureless [25]. When a polymer film is compressed the surface pressure tends to increase in a uniform manner and the

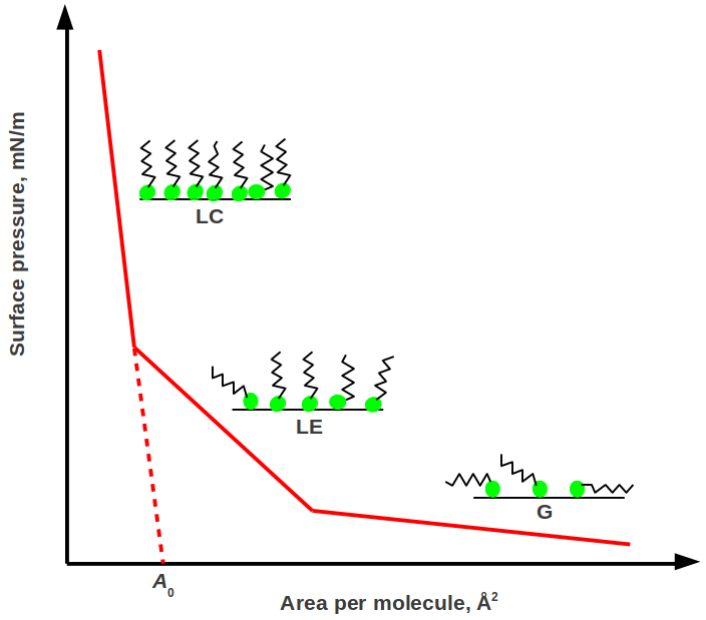

Figure 1.5: A typical surface pressure isotherm for low molecular weight material representing the three different monolayer states: gaseous (G), liquid expanded (LE) and liquid condensed (LC). A_0 represents the minimum area per molecule.

molecules gradually move from a liquid expanded state into a liquid condensed phase. If the region of sharpest increase in the isotherm is extrapolated to zero surface pressure (dotted line in figure 1.5), the minimum area per molecule (A_0) can easily be calculated. One should be careful however when interpreting this value for polymeric material as the chain segment may be coiled or desorbed at the surface thus rendering it difficult to discuss the actual organisation of the polymer monolayer. However, by analysing the shape of each isotherm a qualitative picture of molecular orientation as a function of surface concentration can be drawn.

1.4 Poly(ethylene oxide)

Poly(ethylene oxide)(PEO), also known as poly(ethylene glycol)(PEG) is one of the most researched water-soluble synthetic polymers. The presence of an oxygen atom in the PEO's basic constituent unit, -(CH_2-CH_2-O)-, changes entirely the nature of the chain interactions compared to a hydrocarbon system and therefore the thermodynamics of PEO when dissolved in various solvents. This polymer is of great scientific and technological interest for a wide variety of applications, many of which

depend upon the properties of the polymer in aqueous solution. The great deal of research interest in PEO/water systems also originates from PEO's ability to adsorb on surfaces and at interfaces. Its use is found in lubricants [26,27], control of particle aggregation in solution [28,29], environmental cleanup agents [30], etc. PEO is also of great importance in industry, since it is used, for example, as a plasticiser [31], a component in block copolymers [32,33] and a head group in nonionic surfactants [34]. The similarity of its specific interactions (hydrogen-bonding and hydrophobic interactions) to those found in proteins and other biological materials makes PEO/water a useful simple model system to study biomolecular interactions [35,36]. This also has potential for biomedical use in future [37–39]. Given a variety of applications, therefore, it is very desirable to understand behavior of PEO in aqueous solutions.

1.4.1 Poly(ethylene oxide) in aqueous solution

1.4.1.1 Theory

In typical hydrocarbon systems, the temperature-concentration (T-c) phase diagram exhibits an *upper critical solution temperature* (UCST) above which the polymer and solvent are in a single phase. In contrast, many water-soluble polymer systems exhibit an inverted coexistence curve, known as, a *lower critical solution temperature* (LCST) above which there is coexistence between two phases [40, 41]. Nonionic, water-soluble polymer systems can exhibit properties not seen in typical hydrocarbon systems. Examples are a negative entropy of mixing and polymer aggregation under good-solvent conditions and unusual phase behaviour. PEO is a polymer which exhibits all of the above-mentioned behaviour. At temperatures below 100°C PEO is completely water soluble at all proportions and molecular weights [42]. However, at higher temperature a phase separation into a PEO rich phase and an almost pure water phase occurs. Many of the properties of PEO/water solutions responsible for their wide range of applications are related to their LCST behaviour [43–46].

Several mechanisms have been proposed to explain the phase separation, such as the structure of the surrounding water [47], the conformation of the PEO chains [48], and hydrogen bonding between the ether oxygens of the polymer chain and wa-

ter [49]. Kjellander and Florin [47] suggested that PEO is easily accommodated into the liquid water network, resulting in favorable enthalpic interactions between the ether and water. However, the hydrophobic hydration of the methyl units results in increased water structure that is entropically unfavorable. This low-entropy structure of water is responsible for the phase separation at elevated temperatures. As the temperature is increased even more, entropy of mixing results in miscibility. Karlstrom [48] and Goldstein [49] emphasize differences in interactions between hydrophilic and hydrophobic regions of the polymer chain with water. They suggested that the intermolecular potential between the two types of molecules forming a solubility gap (water and PEO) has small regions which are strongly attractive and large regions which are repulsive. At low temperatures the molecules are primarily in the attractive domain, but at elevated temperatures the importance of the repulsive regions increases, resulting in an enthalpically driven phase separation. At an even higher temperature, the mixing entropy will dominate again, resulting in a miscible system. The physical nature of the difference between attractive and repulsive domains is not clear. Goldstein suggested that this difference is due to the capability of different domains to make greater or fewer hydrogen bonds with surrounded water. Karlstrom assumed that the origin of this classification arises from differences in polar interactions of various PEO conformers with water.

Several theoretical models have been proposed for the closed-loop phase behaviour of PEO solutions [40, 50, 51]. These models describe the LCST behaviour either in terms of the composition and temperature dependence of the population of hydrophilic conformers or PEO-water hydrogen bonding. A mean field-like approach by Dormidontova [52], which also takes into account the effect of hydrogen bonding between water-water, achieved very good quantitative agreement with most of the experimental data reported [41, 53, 54], in particular reproducing the closed loop regions of phase coexistence.

1.4.1.2 Experiment studies

The aqueous solution properties of poly(ethylene oxide) have been studied extensively both experimentally and theoretically in the last decade. Many of these involve

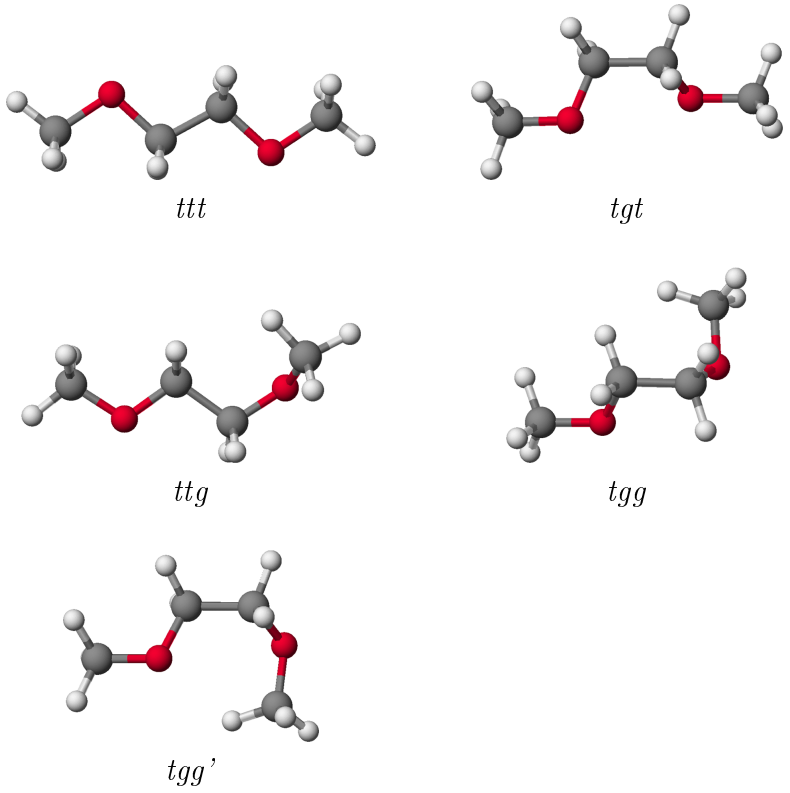

Figure 1.6: Low-energy conformers of 1,2-dimethoxyethane (DME).

investigations of aqueous solution of a small model system for PEO, named 1,2-dimethoxyethane (DME). The molecular formula for DME is $CH_3OCH_2CH_2OCH_3$, contains all dihedral types present in the PEO molecule. The possible conformations of DME are listed in figure 1.6.

Using light scattering techniques, Devanand and Selser [55] found that the second virial coefficient, the radius of gyration, and the hydrodynamic radius for PEO in water are much larger than those typically found for linear flexible polymers in good solvents, indicating that water is an extremely good solvent for PEO.

Conformation of PEO in aqueous solution have been examined by a number of experimental methods. Among those studies, Raman spectroscopy has been frequently used to provide information of relative conformational populations. This technique is usually combined with infrared spectroscopy to gain a further insight into the structural aspect of the polymer. A series of the Raman and infrared spectroscopy experiments for the DME/water and low molecular weight PEO/water systems have been made by Matsuura and co-workers [56–59]. These measurements revealed that

the *tgt* conformer of DME becomes the most favorable in aqueous solution, which is supported by measurement of PEO solution from Hsu et al. [60]. The populations of the less hydrophilic (*ttt* and *tgg'*) conformers of DME decrease on increasing concentration of water, while the populations of the more hydrophilic conformers (*tgt* and *tgg*) conformers increase [59]. At high temperature, the *tgt* and *tgg* conformers are replaced by the *ttt* and *tgg'* ones, suggesting that the inverse temperature solubility of PEO in water originates from conformational changes of the polymer chain, as has been proposed by Karlstrom [48]. For more details in this study [59], the *tgg'* conformer, which is the highest entropy one (in aqueous solution), is found to be the most rapidly populated conformer on increasing temperature. They concluded that the appearance of the -CH_2O-CH_2-CH_2-OCH_2- segment in the *tgg'* conformation within the PEO chain is a basic mechanism of the phase separation observed in aqueous solutions. There are indirect evidences supporting this hypothesis. It has been demonstrated that on increasing temperature the PEO chain becomes less hydrated and collapses [61,62]. The same trend was observed on subjecting aqueous solutions of PEO to a high pressure [63, 64]. Both processes-the dehydration and the collapse of the polymer chains-were suggested to be greatly facilitated by the appearance of the *tgg'* conformational segments within the chain, leading eventually to a phase separation.

1.4.1.3 Simulation studies

Beside experimental investigations, molecular modeling techniques have been used to gain a more physical picture, e.g. the influence of temperature and composition on hydrogen bonding or conformer populations of PEO/water systems.

Using a force field based upon *ab initio* quantum chemistry, calculations of DME/water interactions by Smith and co-workers [65] showed a strong dependence of DME conformation on temperature and solution composition. Conformer populations are quite different in aqueous solutions from those found in the gas phase or neat liquid. The binding energy of water to DME in the *tgt* conformation (-7.7 kcal/mol) was found to be greater than that for the other low energy DME conformers (-6.1 kcal/ mol for *ttt* and -6.4 kcal/mol for tg^+g' respectively) [66]. This

was suggested to be due to the strong interaction of the water hydrogen atoms with both ether oxygen atoms in the *tgt* conformer. Analysis of the calculated conformer populations as a function of composition confirmed a strong preference for the *tgt* conformer in aqueous solution, and analysis of the pair distribution functions appeared to be consistent with suggestions that this is due to the compatibility of the DME *tgt* geometry with the structure of liquid water.

An optimized potentials for liquid simulations-all-atom (OPLS-AA) force field was modified by Anderson and Wilson and used in simulations of PEO solutions [67]. Conformational results from this PEO model are in agreement with the simulation results by Smith et al. and Raman spectroscopy measurements [59, 60] which indicated that the PEO solution is dominated by the *tgt* conformation. It was also showed from this simulation that as polymer concentration decreases, the *tgt* and *tgg* conformations increase in population while the *ttt* and *tgg'* conformations become less populated.

A series of simulations have been performed on the PEO/water system by Smith and co-workers. Study of the local structure of water around different DME conformers [65] revealed that water tends to form clusters of 4-5 molecules on a nearest-neighbour length scale rather than randomly distribute in the system. The entropic penalty associated with this "water structure" increased with increasing DME concentration and temperature, thereby increasing the free energy of hydrophilic conformers relative to hydrophobic ones.

A complex dependence of PEO-water and water-water hydrogen bonding on both composition and temperature was noted in reference [68]. Strong water clustering was seen in concentrated solutions. PEO-water hydrogen bonding increased rapidly with dilution until $w_{PEO} \approx 0.5$, at which point EO-water hydrogen bonding is nearly saturated. Upon increasing temperature, a dramatic decrease in PEO-water hydrogen bonding, consistent with the experimentally observed closed-loop phase behavior [40, 41] were observed. They suggested from this study that the water clustering and PEO-water hydrogen bond saturation, have to be incorporated into any model attempting to describe phase behaviour in PEO/water solutions.

Detailed study of the temperature and composition dependence of the excess

thermodynamic properties, e.g. $\Delta G^{\mathrm{EX}} = G(\mathrm{solution}) - [G(\mathrm{solvent}) + G(\mathrm{solute})]$, has been made by Smith et al. [69]. They found that, at room temperature, the excess enthalpy ΔH^{EX} of the DME in water is favourable, and dominates the unfavourable excess entropy ΔS^{EX}, resulting in a favourable ΔG^{EX} (i.e. miscibility of PEO/water solutions). The favourable excess enthalpy and unfavourable excess entropy have been known to be a results of formation of ether-water hydrogen bonds and the structuring of the water comprising the first hydration shell of the ether [70]. From their calculations [69], the $T\Delta S^{\mathrm{EX}}$ term became more favourable with increasing temperature for both dilute and concentrated solutions of PEO, indicating that unfavourable entropic effects are not responsible for phase-separation of PEO/water solutions at higher temperatures. The enthalpy of solvation of DME, especially in dilute solution, became dramatically less favourable with increasing temperature, consistent with a dramatic decrease in ether-water hydrogen bonding [68]. These thermodynamic properties are in agreement with predictions from the theoretical models of Karlstrom [48] and Dormidontova [52], leading to the conclusion that the LCST in PEO/water solutions is enthalpy-driven.

1.4.2 Poly(ethylene oxide) at a water-air interface

1.4.2.1 Experimental studies

PEO has a surface tension of 42.5 mN/m (24 °C) [71], much lower than that of pure water, which is 72.8 mN/m [72]. As a result, although PEO is water soluble, it has also been shown that PEO can form stable spread films at the water-air interface under certain circumstances [73–75]. The -CH_2 -O-CH_2 - component is sufficiently hydrophobic to escape from the water subphase and to form an adsorbed layer at a surface. This structure is energetically preferable and this disturbs the hydrogen bonded network of water at the surface and as a result, the surface tension of the system drops in the presence of this surfactant [75–78].

The PEO layer is found to be rather flat and can be classified as a pancake organization rather than a brush-like layer [74, 75]. The surface excess for PEO is found to be around 0.5-0.7 mg m^{-2}. At a concentration above this point, the mono-

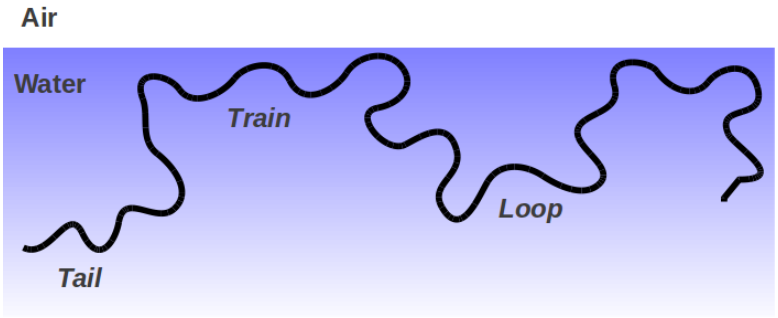

Figure 1.7: Illustration of the tail, loop and train conformation of an absorbed polymer.

layer collapsed with PEO chains starting to penetrate through the liquid substrate probably as loop and tail conformations (figure 1.7) [74, 79].

Modification of PEO by attaching a hydrophobic group to one or both ends dramatically changes the adsorption behavior of the polymer and, therefore, surface properties of solutions. The highest surface activity at the critical micelle concentration (at 25 °C) has been measured for PEO incorporating either fluorinated (19 mN/m) [80] or silioxane (20 mN/m) [81] terminal groups. Since functional groups incorporating fluorocarbons are among the most effective surface active agents, the perfluorocarbon group has always been chosen as the terminal substituent.

Based on analysis of the surface tension and the infrared reflectance features, PEO with perfluoroalkyl [82] and perfluorodecanoyl [83] end groups were found to be highly surface active and adsorbed more strongly to the interface than unfunctionalized equivalent PEO. It was also shown that the functionalised polymers are able to form a brush-like structure at the air-water interface, especially at high surface coverage [82, 83].

Indication for any change of the interfacial structure, e.g. from pancake to brush, has previously been deduced from the interfacial pressure developed in tethered polymer layers. However, a key parameter to prove the presence of such structures is the thickness of the layer (or brush height) and its dependence on surface coverage [18]. To gain direct access to layer composition and thickness of amphiphilic polymers at a water/air interface, the neutron reflectometry technique has been introduced [14–16, 84].

Neutron reflectometry measurements on fluorocarbon end-capped PEO by Richards

et al. [18] revealed that, for a PEO molecular weight of 2000 g mol^{-1}, the layer thickness is more than twice the radius of gyration of the polymer, confirming the existence of a brush configuration, which is adsorbed to the interface by the fluorocarbon end group. The brush conformation is, however, not supportable for the two higher molecular weight polymers (Mw_{PEO} = 5000 g mol^{-1} and 10 000 g mol^{-1}), where the layer thickness is of the same order as its R_g. The rather flat layers, in the cases of higher molecular weight polymers, also suggest that as well as fluorocarbon ends being adsorbed, some of the ethylene oxide units are also adsorbed at the air-water interface. Although the surface excess for these two polymers is considerably less than that of the 2000 g mol^{-1} polymer, there is still considerably more polymer adsorbed than for unmodified PEO. At high concentrations of polymer in solution, the surface excess region has a two-layer organization, the lower layer consisting of micelles at the underside of an upper layer at the air-water interface. As investigated further by small-angle neutron scattering, the micelles of the higher molecular weight polymers appear to have a more diffuse organization than those formed by the lowest molecular weight polymer.

With the aim of increasing the surface tethering strength, new amphiphilic polymers wherein the PEO chain is functionalized by two (F2) and three (F3) fluorocarbon head groups (the structures are showed in figure 1.8 (b) and (c)) have been synthesized and studied by Bartram [85]. Although only ∼50 % of PEO was successfully functionalized (∼50 % left as unmodified PEO), the solution of these mixed components gave surface tensions as low as polymers with 100% of the PEO chains functionalized by one fluorinated (F1) group [18] (figure 1.8 (a)). A more detailed study of the surface organization using neutron reflectivity [85] showed that the tethering strength of F3 materials is significantly higher than that of F1 and F2 materials. The F1 and F2 materials do not appear to tether sufficiently to the water surface to reach high packing densities, reflecting the fact that the surface tethering strength is primarily induced by the hydrophobicity of the fluorine contained in the head groups of the molecules. The multiple fluorocarbon head group allows the tethering of a much higher molecular weight of PEO materials. For example, while F1 head group has been shown to be effective in strongly tethering PEO chains up

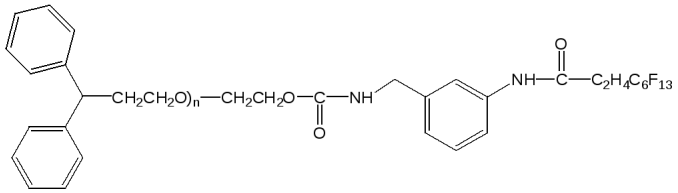

(a) F1 structure used in ref. [18]

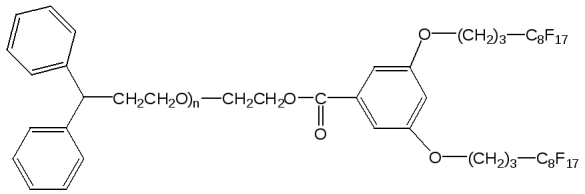

(b) F2 structure used in ref. [85]

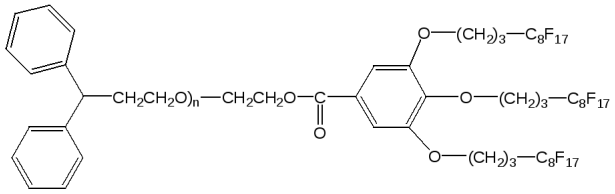

(c) F3 structure used in ref. [85]

Figure 1.8: Structures of fluorocarbon end-capped PEO used in previous studies.

to 2000 g mol^{-1} [18], the F3 materials are shown to be effective up to a molecular weight of 10 000 g mol^{-1}.

1.4.2.2 Simulation studies

Molecular simulation is becoming a useful tool for the study of polymeric materials at interfaces [86]. Phase transitions in amphiphilic monolayer have been investigated using molecular dynamics simulations [87]. Monte Carlo simulation has been used to calculate configurational free energies for systems involving amphiphile-oil–water systems [88]. Coarse-grained simulations have also proved to be a very efficient means of studying lipid bilayers [89, 90].

There are several simulation studies relevant to the work in this thesis. A system consisting of a polynorbornene backbone grafted with poly(ethylene oxide) have been simulated using Monte Carlo simulation [91]. Here, amphiphilic molecules were placed at an idealized interface between hydrophobic and hydrophilic regions, which were represented by external potentials. Transition from pancake to brush confor-

mation was observed when the surface concentration was increased. The calculated neutron reflectivity profiles at low surface concentrations were found to be in good agreement with experimental results [15, 16]. At high surface concentrations, however, simulation failed to describe the behaviour of the hydrophilic chains due to the use of an over-simplified confinement potential that exaggerated the extension of the PEO chains into the aqueous subphase.

The promising results obtaining from the simple model mentioned above prompted the authors to use a more 'realistic interface' provided by an explicit water model [67]. Fully atomistic simulations were performed on the same molecular system and it was clearly shown that PEO chains undergo a transition from the pancake regime to a brush structure when surface concentration was increased. Neutron reflectivity profiles generated from the simulations showed excellent agreement with experiment, particularly at low surface concentrations. Agreement at higher concentrations is significantly better than in a previous model which neglected water. However, simulations at the highest surface concentrations ($\sim$3.0 mg m^{-2}) failed to produce adequate results due to "too crowded" starting configurations, which were not able to relax over time scales available for simulation [92].

Several coarse-grained surfactant models have been developed to deal with complex phenomena occurring in a wide range of length- and time-scales. This class of models is efficient enough to permit the study of surfactant systems at concentrations high enough to see, for example, budding and fission of micelles from surfactant monolayers at an air-water interface [86].

For example, surfactant model containing PEO segments has been developed by Klein and co-workers [93–95]. The CG surfactants yielded spontaneous self-assembly in bulk solution as well as at air-water and oil-water interfaces. Experimental results, e.g. surface/interfacial tension, density and lipid layer thickness, are well reproduced by the CG simulations. The faster relaxation of the CG model enables observation of complex phenomena occurring on the mesoscale level, including budding and fission of micelles from surfactant monolayers at an air/water interface and a repartitioning of surfactants at an oil/water interface.

The molecular mechanism for the collapse of a lipid monolayer at the air-water

interface, that is crucial for maintaining low surface tension at the gas-exchange interface in the lungs during breathing, has successfully been investigated using coarse-grained models [96]. The structures of lipid aggregates formed upon collapse can be characterized experimentally, but the mechanism leading to these structures is not fully understood. By applying lateral compression, the CG simulation showed that the collapse begins with buckling of the monolayer, followed by folding of the buckle into a bilayer in the water phase. After collapse, the bilayer folds have a semi-elliptical shape, in accord with theoretical predictions. Furthermore, the folds can transform into flat circular bilayers or vesicles and disconnect from the monolayer.

In the list of the simulation studies described above, it has been shown that molecular modeling techniques can provide very useful insight into exactly what the amphiphilic molecules are doing and how they are behaving at a water/air interface. Previous experiments have only been able to infer molecular changes, e.g. neutron reflectivity, where the layer composition and thickness are obtained from fitting of structural models to reflectivity data. Furthermore, some phenomena that are difficult to detect experimentally, e.g. budding and fission of micelles from surfactant monolayers, are also shown to be observable by using state-of-the-art simulation techniques.

In order to simulate systems comparable to those used in experiments, e.g. in neutron reflectometry measurements, it is necessary to model a very long PEO chain with a realistic molecular weight. To accommodate many large chains at the interface, huge numbers of solvent (water) molecules would also be required. It is impractical and far too computationally expensive to simulate sufficient atoms to model very large polymer systems (i.e. many 1000s of monomers). In addition, fully atomistic simulations at high surface concentrations fail to produce adequate results due to crowded configurations, which cannot relax within the simulation times available [67, 92]. For these reasons a "coarse-grained" simulation technique, which has successfully been applied to various polymeric and biological systems, will be used to circumvent these problems.

1.5 Scope of this thesis

The aim of this project involves simulations of poly(ethylene oxide) (PEO)/water system at a fully atomistic level. These simulations will be used to develop a new coarse-grained (CG) description of PEO in water, which can be used to study the complex behaviour of this molecule at a water-air interface. The models will further be used to help explain and predict the behaviour of dendritic fluorocarbon capped PEO molecules, which have been studied recently by neutron reflectivity techniques.

Chapter 2 gives a brief introduction to computer simulation, including the molecular dynamics, ideas behind force fields and the computational methods relevant to this work. An overview of coarse-grained molecular simulation is also presented, along with some descriptive details of this technique that are implemented in our work.

The first set of results are reported in chapter 3 for the development of coarse-grained model of water. CG potentials are derived under the requirements of reproducing true behaviour of water both in bulk and at a water-air interface. Several models are developed, and comparisons of obtained results to those from experiments and previous proposed models in the literature are made.

In chapter 4, a coarse-grained model for the PEO/water system is presented. The resulting model is validated through a series of simulations of single PEO chains with different molecular weight in aqueous solutions. Transferability of the model to a water-air interface system is also explored, followed by measuring the speed-up of the CG model compared to the atomistic one.

Coarse-grained models for di-and trifluoro dendritic end-capped PEO are presented in chapter 5. Simulations using these models are then performed in chapter 6, spanning a range of polymer concentrations at a water-air interface. The simulated neutron reflectivity profiles and adsorption behaviour obtained from these simulations are then used to compare and discuss with the experimental results of the corresponding systems.

Finally, the thesis work is concluded with a summary and outlook in chapter 6.

Chapter 2

Computational methods

A wide variety of simulation techniques and models have been developed for studying molecular systems at different levels of detail. The most detailed *ab initio* methods deal explicitly with the electrons in a system, therefore, the calculations are computationally very expensive. This method usually limits calculations to tens or hundreds (on large computers) of atoms with only short time scales accessible (picoseconds). Their main use has been found in modeling catalytic and enzymatic reactions in chemical and biological systems, and in structural studies in material chemistry.

Molecular mechanics studies ignore electronic motions and calculate the energy of a system as a function of nuclear positions only. This technique is thus always used to perform calculations on systems containing significant numbers of atoms. Many simulations today are atomistic ("*all atom*"), meaning that each atom in the simulated system corresponds to a single atom in the real system. For some computationally expensive calculations, however, the "*united atom*" approximation, where hydrogens are fused with heavier atoms into single particles, is used. This dramatically reduces computational cost, since in many organic systems the hydrogen atom is the most common. Hence, the term "*atom*" in simulation is often used to denote united atoms (say, a -CH_2 - group represented by a single particle) as well as traditional atomistic particles.

This simplification can be taken further with the so-called "*coarse-graining*" (CG) methodology. A typical example of a coarse-grained simulation could involve the

structure of the simulated molecule being simplified to a chain of beads or hard spheres. Coarse-grained models have increasingly been used in simulations of polymeric systems to help overcome the problem of slow relaxations and extend the time and length scales accessible.

This chapter outlines the essential components of the computer simulations that are used in this thesis work. The molecular dynamics and relevant computational methods are presented in section 2.1. The coarse-graining techniques, which are applied throughout this work, are introduced in section 2.2. Implementation details and points for consideration in coarse-graining are included in the same section. Finally, section 2.3 describes the relevant equations that are used to calculate properties reported in this thesis.

2.1 Molecular dynamics

The molecular dynamics (MD) method is used to calculate the trajectories of all particles in a simulated system, by evaluating the force acting upon each atom in the system due to all other atoms, and then adjusting the acceleration, velocity and position of the particle according to *Newton's laws of motion*. Newton's 2nd law for a simple system is given by equation 2.1, where $\boldsymbol{F}_i$ is the force acting on atom i, m_i is the mass of i, t is time, E is the potential energy and $\boldsymbol{r}_i$ represents the atomic coordinates of i. Integration of a set of particles, modelled by equation 2.1 allows one to find the trajectory that describes positions, velocities, and accelerations of particles as a function of time. Knowing the positions and velocities allows one to predict the state of the system at any time.

$$m_i \frac{\partial^2 \boldsymbol{r}_i}{\partial t^2} = \boldsymbol{F}_i,$$

where

$$\boldsymbol{F}_i = -\frac{\partial E}{\partial \boldsymbol{r}_i}. \tag{2.1}$$

There are several different integration algorithms in use, but the most commonly used ones are the Leapfrog and Velocity Verlet algorithms.

2.1.1 Leap-frog algorithm

The leap-frog algorithm [97] uses positions $\boldsymbol{r}$ at time t and velocities $\boldsymbol{v}$ at time $t - \frac{1}{2}\Delta t$; it updates positions and velocities using the forces $\boldsymbol{F}(t)$ determined by the positions at time t:

$$\boldsymbol{v}\left(t + \frac{1}{2}\Delta t\right) = \boldsymbol{v}\left(t - \frac{1}{2}\Delta t\right) + \frac{\Delta t}{m}\boldsymbol{F}\left(t\right) \tag{2.2}$$

$$\boldsymbol{r}\left(t + \Delta t\right) = \boldsymbol{r}\left(t\right) + \Delta t \boldsymbol{v}\left(t + \frac{1}{2}\Delta t\right) \tag{2.3}$$

The leap-frog algorithm's staggering of velocity and position results in a slight inconvenience when trying to calculate both the potential (position-based) and kinetic (velocity-based) energies for the same point in time.

2.1.2 Velocity Verlet algorithm

The velocity Verlet algorithm [98] allows the calculation of positions and velocities at the same time; velocities at the previous half step are not required. Thus it tends to be more accurate in terms of the trajectory generated than the leap-frog algorithm.

$$\boldsymbol{v}\left(t + \frac{1}{2}\Delta t\right) = \boldsymbol{v}\left(t\right) + \frac{\Delta t}{2m}\boldsymbol{F}\left(t\right) \tag{2.4}$$

$$\boldsymbol{r}\left(t + \Delta t\right) = \boldsymbol{r}\left(t\right) + \Delta t \boldsymbol{v}\left(t + \frac{1}{2}\Delta t\right) \tag{2.5}$$

$$\boldsymbol{v}\left(t + \Delta t\right) = \boldsymbol{v}\left(t + \frac{1}{2}\Delta t\right) + \frac{\Delta t}{2m}\boldsymbol{F}\left(t + \Delta t\right) \tag{2.6}$$

or equivalently:

$$\boldsymbol{r}\left(t + \Delta t\right) = \boldsymbol{r}\left(t\right) + \Delta t \boldsymbol{v} + \frac{\Delta t^2}{2m}\boldsymbol{F}\left(t\right) \tag{2.7}$$

$$\boldsymbol{v}\left(t + \Delta t\right) = \boldsymbol{v}\left(t\right) + \frac{\Delta t}{2m}\left[\boldsymbol{F}\left(t\right) + \boldsymbol{F}\left(t + \Delta t\right)\right] \tag{2.8}$$

Given a single starting file with the *same* starting point $x(0)$ and $v(0)$, leapfrog and velocity Verlet will not give identical trajectories, as leapfrog will interpret the velocities as corresponding to $t = -\frac{1}{2}\Delta t$, while velocity Verlet will interpret them as corresponding to the timepoint $t = 0$.

2.1.3 Force fields

Before any simulation can be carried out, a good representation of the interatomic interactions must be selected. Such a model is known as a "*force field*". A force field is an energy function that describes the potential energy of a particular set of interacting particles. The ability of computer simulations to describe the behaviour of a material depends critically upon the accuracy of inter and intramolecular potential energy functions. A good force field should be able to describe the concentration and temperature dependency of the conformations as well as macroscopic thermodynamic equilibrium properties.

In molecular simulations, the force field is typically written as

$$E_{\text{tot}} = E_{\text{bonded}} + E_{\text{nonbonded}}, \tag{2.9}$$

where E_{bonded} describes chemical bonds and angles, and $E_{\text{nonbonded}}$ describe the nonbonded interactions that contibuted from electrostatic and van der Waals contributions.

The bonded term is written as a sum of contributions from bond length and angle vibration and dihedral potentials, for example, as follows:

$$\begin{aligned} E_{\text{bonded}} = &\sum_{\text{bonds}} \frac{1}{2} k_{ij}^{b} \left(r_{ij} - r_{ij}^{0}\right)^2 + \sum_{\text{angles}} \frac{1}{2} k_{ijk}^{\theta} \left(\theta_{ijk} - \theta_{ijk}^{0}\right)^2 \\ &+ \sum_{\text{dihedrals}} k_{ijkl}^{\phi} \cos\left(n_{ijkl}\phi_{ijkl} - \phi_{ijkl}^{0}\right) \\ &+ \sum_{\text{impropers}} \frac{1}{2} k_{ijkl}^{\xi} \left(\xi_{ijkl} - \xi_{ijkl}^{0}\right)^2 . \end{aligned} \tag{2.10}$$

The first and second terms use harmonic potentials with force constants k_{ij}^{b} and

k^{θ}_{ijk} to keep bond lengths and angles around their reference values r^0_{ij} and θ^0_{ijk}. The sums run over all pairs ij or triplets ijk of particles connected by bonds. The third term describes rotation about bonds with k^{ϕ}_{ijkl} determining the stiffness, n_{ijkl} the multiplicity, and ϕ^0_{ijkl} the reference angle. Different functional forms can be used for more complex cases with multiple minima of unequal depth [99, 100]. The last term describes so-called improper dihedrals that are used to force planarity of certain groups of particles, as well as preventing changes in the chirality of molecules. The functional forms in equation 2.10 are not the only possibilities, some force fields use different functions to achieve more efficient computation of the forces [100] or additional terms for more accurate description [101].

The non-bonded electrostatic term is the standard Coulombic interaction

$$E_{\text{es}} = \sum_{i,j} \frac{q_i q_j}{4\pi\varepsilon_0 r_{ij}}, \tag{2.11}$$

where q_i, q_j are the partial charges on the atoms separated by distance r_{ij}.

For the van der Waals term, the Lennard- Jones (LJ) interaction is typically used:

$$E_{\text{vdW}} = \sum_{i,j} 4\epsilon_{ij} \left[\left(\frac{\sigma_{ij}}{r_{ij}} \right)^{12} - \left(\frac{\sigma_{ij}}{r_{ij}} \right)^{6} \right]. \tag{2.12}$$

The second term includes dipole–dipole, dipole–induced dipole, and induced dipole– induced dipole interactions. All these are attractive on average and have a common r^{-6} dependence [102]. The first term is a computationally efficient implementation of repulsion at short interatomic distances, resulting from electronic overlap. The parameters ϵ_{ij} and σ_{ij} determine the depth of the attractive minimum and the distance at which the potential crosses zero, respectively.

2.1.3.1 MD in different ensembles

Statistical mechanics provide a link between individual molecular properties and those of the bulk. When setting up the MD calculation one must decide on an ensemble to use. The natural ensemble for MD is the micro-canonical, *NVE*, in which the number of particles N, volume V and the total energy E are conserved

[103]. If different ensembles are desired, for example the NVT (canonical) or NPT (isobaric/isothermal), a thermostat or thermo- and barostat respectively, needs to be applied to keep the temperature T, and the pressure P, constant. Popular choices for thermostats include the Berendsen [104] and Nosè-Hoover thermostats [105,106]. The Berendsen algorithm mimics weak coupling of the system to an external heat bath with given temperature T_0. Deviation of the system temperature from T_0 is corrected according to:

$$\frac{dT}{dt} = \frac{T_0 - T}{\tau} \tag{2.13}$$

where T is the current temperature and τ is a time constant that gives the strength of the coupling. The Berendsen thermostat is very efficient in reaching the desired temperature, but it does not produce a well-defined ensemble, as it suppresses fluctuations in the kinetic energy.

Perhaps the most popular approach for obtaining the full canonical ensemble is to use the Nosè-Hoover thermostat [105, 106], where a thermal reservoir and a friction term are introduced into the equation of motion:

$$\frac{d^2\boldsymbol{r}_i}{dt^2} = \frac{\boldsymbol{F}_i}{m_i} - \frac{p\xi}{Q}\frac{d\boldsymbol{r}_i}{dt}. \tag{2.14}$$

The friction force is proportional to the product of each particle's velocity and a friction parameter, ξ. This friction parameter (or "heat bath" variable) is a fully dynamic quantity with its own momentum ($p\xi$) and equation of motion with the time derivative calculated from the difference between the current kinetic energy and the reference temperature:

$$\frac{dp\xi}{dt} = (T - T_0)\,. \tag{2.15}$$

The reference temperature is denoted T_0, while T is the current instantaneous temperature of the system. The strength of the coupling is determined by the constant Q (usually called the "mass parameter" of the reservoir) in combination with the reference temperature.

Volume and pressure form a set of variables similar to energy and temperature,

and in many situations, a constant pressure simulation would be more appropriate than a constant volume one. This can be achieved with barostats, which are formulated in a similar way to thermostats, but control the pressure tensor P instead of the temperature. Again, a simple box rescaling scheme, the Berendsen barostat [104], is often used for its simplicity, but it does not produce the correct fluctuations seen in, for example, the constant-NPT ensemble. An extended ensemble method, similar to Nosè-Hoover, is called the Parrinello-Rahman barostat [107], and is often used when the volume fluctuations are important.

2.1.4 Stochastic dynamics

Stochastic or velocity Langevin dynamics [108, 109] adds a friction and a random force to Newton's equations of motion:

$$m_i \frac{d^2 \boldsymbol{r}_i}{dt^2} = \boldsymbol{F}_i(\boldsymbol{r}) - m_i \xi_i \frac{d\boldsymbol{r}_i}{dt} + \boldsymbol{F}_i^r(t) \tag{2.16}$$

where ξ_i is the friction constant (1/ps) and $\boldsymbol{F}_i^r(t)$ is a random force that has the properties

$$\langle \boldsymbol{F}_i^r(t) \rangle = 0, \tag{2.17}$$

$$\left\langle \boldsymbol{F}_i^r(t)\, \boldsymbol{F}_j^r\left(t'\right) \right\rangle = 2 m_i \xi_i k_B T \delta_{ij} \delta\left(t - t'\right). \tag{2.18}$$

A frictional force added to the conservative force is proportional to the velocity, and it adjusts the kinetic energy of the particle so that the temperature matches the set temperature. The random force is randomly determined from a Gaussian distribution to add kinetic energy to the particle, and its variance is the function of set temperature and time step. Therefore, the random force is balanced with the frictional force and maintains the system temperature at the set value. When $1/\xi_i$ is large compared to the time scales present in the system, one could see stochastic dynamics as molecular dynamics with stochastic temperature-coupling. The advantage compared to MD with Berendsen temperature coupling, is that in case of SD

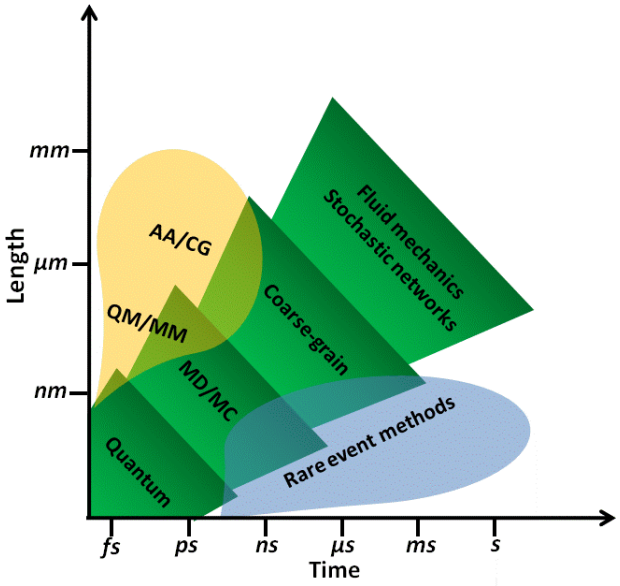

Figure 2.1: Schematic outline of time and length scales accessible to current simulation methods (reproduced from ref. [125]), ranging from highly accurate but computational very demanding *ab initio* calculations (quantum) to highly efficient but very low-detail continuum models and stochastic network methods. In between, we find atomistic molecular dynamics and Monte Carlo simulations followed by coarse-grained molecular modelling. Hybrid multiscale modelling, where two levels of resolution are combined, can also be used to move off-diagonal in the direction of large length scales. Advanced sampling methods, so-called rare event techniques, allow for sampling of slow processes on long time scales.

the generated ensemble is known. For simulating a system in vacuum there is the additional advantage that there is no accumulation of errors for the overall translational and rotational degrees of freedom. When $1/\xi_i$ is small compared to the time scales present in the system, the dynamics will be completely different from MD, but the sampling of configurational space is still correct.

2.2 Coarse-graining

The quick growth of computer power as predicted by Moore's law [110], combined with a highly efficient parallel programs [111–114] allow one to keep expanding the size of the detailed all-atom or united-atom systems that one wish to simulate. The largest simulation recorded is molecular dynamics simulations of a trillion (10^{12}) Lennard-Jones (LJ) particles in a simple cubic lattice with the edge length of the simulated crystal of 2.55 micrometers [115]. Such massive calculations however are

only successful by using very high performance computers, and still require a couple of days to reach 10 ps of simulation time. In general, the accessible time scale of MD simulations on million-atom systems is typically less than 100 ns [116]. Perhaps the best is yet to come, it is very promising that the adoption of new architectures, such as graphical processor units (GPU) [117, 118], in combination with the innovation of the underlying techniques, i.e. a massively fast parallel algorithms, will enable one to model realistic materials with all their inherent complexities in the foreseeable future.

In many soft matter systems such as synthetic or biological materials, it is well known that their physical phenomena and properties are governed by interactions and processes on a wide range of length- and time-scales [119–121]. Brute-force simulations alone will not be sufficient to deal with these issues. In order to access the mesoscopic time- and length-scales relevant to material properties, methods that bridge from the atomistic (microscopic) to a coarser (mesoscopic) level have been developed. Figure 2.1 illustrates the length and time scales accessible to current simulation methods. Many polymeric materials show a large degree of universality in their static [122] as well as dynamic [123] behaviours, and these universal scaling properties as a function of chain length, temperature and composition can be most efficiently studied via, so-called "coarse grained (CG)" molecular models [124]. Current coarse-graining approaches have striven to improve computational efficiency in simulations and has attracted a significant amount of attention in recent years [116, 125, 126].

2.2.1 What is coarse-grained model

The term "Coarse-grained" is generally used to refer to a simplified representation of a more detailed system. It is constructed by systematically reducing the number of degrees of freedom of the target system and keeping only the important ones so that the properties of interest still hold. For example, it could used for turning an all-atom to an united-atom model or an explicit solvent model to an implicit one, etc. In these cases, "a more detailed system" refers to the all-atom model. A typical example of a coarse-grained model is shown in figure 2.2, where the structure of the

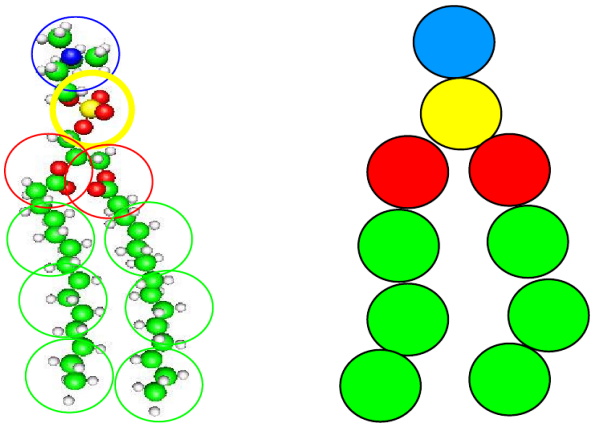

All-atom model 118 atoms Coarse-grained model 10 sites

Figure 2.2: (a) All-atom and (b) Coarse-grained models.

molecules is simplified to a chain of beads. Usually, CG models provide much more speed-up in CPU time compared to AA models for similar systems. This speed-up arises from three factors, which result from the reduction in the number of degrees of freedom: (i) reducing the overall computational cost due to reducing the number of interaction sites (ii) increase in the simulation time step due to less steep interaction potentials and (iii) quicker movement of the system through configurational space due to smaller energy barriers and/or a smoother energy landscape. This makes the CG models promising choices for tackling the problems of time and length scales accessible in molecular simulations.

2.2.2 Coarse-graining methods

A wide varieties of coarse-graining methods have been reported in the literature. In general, they all share a common procedure which starts from a detailed atomistic model or experimental data; then defines a coarse-grain model by replacing groups of atoms/molecules with CG sites (mapping) and finally constructs an effective potential to describe the statistical mechanics of these CG sites (usually based on simple pairwise additive potentials). To derive the interaction potentials, three sorts of properties are frequently used as targets: (i) thermodynamics (ii) structure and (iii) force. Of course, one has to know which key properties play the decisive role in the system of interest, then, choose the right ones to be reproduced.

2.2.2.1 Thermodynamic-based coarse-graining

In thermodynamic-based coarse-graining, the target properties are mainly selected from experimental measurements, e.g. critical points [127, 128], interfacial tension [129], hydration free energy [94], etc. This is classified as a "top-down" bridging approach since microscopic CG representations are derived from a macroscopic properties [130]. The success of this approach is illustrated in the popular MARTINI model [89,90] where partitioning free energies between polar and apolar phases were used to optimize coarse-grain interaction parameters. This approach has proven to be particularly useful for studying processes such as lipid membrane association. Since it targeted at reproducing energies, this method does not guarantee the reproduction of the structure of the system.

2.2.2.2 Structural-based coarse-graining

Structural-based coarse-graining, which is solely used in this thesis, aims at finding CG interactions that reproduce predefined target structures such as RDFs obtained from more detailed simulations, are classified as "bottom-up" coarse-graining approach. With this approach, it is possible to insert atomistic coordinates back into a CG structure (backmapping) [120, 131, 132]. Backmapping has been found to be very useful in some areas of application, for example, in NMR studies, one can perform CG simulations over long time and large length scale to obtain well-equilibrated structures, atomistic details then put back into the CG structures and trajectories, which can be used to compare directly with experimental data [133, 134]. On the other hand, structural-based coarse-graining itself does not guarantee reproduction of thermodynamic properties of the system, unless one applies a post-corrections for these property of interest [135–138]. There are two methods which are frequently used to derive structural-based CG potentials: (i) inverse Monte Carlo method (IMC) [139] and (ii) iterative Boltzmann inversion (IBI) method [135].

According to the Henderson theorem [140], the solution to the problem of finding an isotropic pair potential that exactly reproduces a given pair structure is unique. The effective potentials generated from both methods, thus, in principle are the same (within statistical error). Some comparisons between IMC and IBI techniques

have been made in the work by Rühle and co-workers [141]. IMC usually provides faster convergence since the potential update is rigorously derived using statistical mechanics. Another advantage of the IMC is that, in the case of multicomponent mixtures, it takes into account cross-correlations between different particle types for every potential update. These updates are independent in the IBI method, which often leads to convergence problems for multicomponent systems. As cross-correlations have been evaluated, the IMC method, however, requires much longer sampling to get statistics that are good enough to calculate the potential update to a similar accuracy as IBI. Another issue of the IMC method is the stability of the scheme. This can be influenced by several factors, such as the box size. As reported in reference [141], a box of size three times the RDF cutoff was not enough to achieve a converged potential for IMC, while it worked well with system sizes of the order of 2x RDF cutoff using IBI method.

In this thesis, the IBI method is used throughout coarse-graining studies of water, PEO/water and amphiphilic/water systems. The basic ideas and implementation for this technique are described in detail in the section 2.2.3.

2.2.2.3 Force matching method

Another approach to evaluate coarse-grained potentials is the force matching (FM) method [142,143], which has been successful in developing CG models for many systems, in particular biomolecular systems [144–146]. In contrast to structural-based CG methods which try to reproduce distributions functions, its aim is to minimise the difference between the instantaneous forces defined by the CG force field and the original atomistic force field. It is known that, for this method, forces applying to CG sites are inherited from the many-body multidimensional potential of mean force of the underlying atomistic system [147]. Thus, it does not necessarily guarantee that the local structural properties such as pair distributions, will be perfectly reproduced. To improve the reproduction of the underlying atomistic qualities, it was suggested that the FM method requires the inclusion of explicit higher-order interactions [141, 148].

2.2.3 Systematic coarse-graining by iterative Boltzmann inversion

The iterative Boltzmann inversion (IBI) procedure has been pioneered by Reith et al. [135]. This is perhaps the most popular approach. It is conceptually straightforward, allows any type and number of distribution function as input, and converges relatively fast. This technique has successfully been applied to polymer melts [133,149,150], liquid crystals [151], solutions [137,152] as well as to low molecular weight species [138,153,154].

The IBI method essentially consists of three steps: (a) performing an atomistic simulation to create the particle trajectories from which target function(s) can be extracted afterward; (b) choosing how to group together atoms from the detailed level onto the CG level (mapping) and extraction of the coarse-grained topologies and target functions; (c) performing the actual iteration by repeatedly simulating the system in its mesoscale representation and evaluating the functions of interest.

After each iteration loop, the potential(s) 1,..., n are corrected according to the formula

$$U_{i+1}(x) = U_i(x) + \alpha k_B T \ln\left[\frac{P_i(x)}{P_{\text{target}}(x)}\right], \; i = 0, 1, 2 \ldots, \tag{2.19}$$

where i denotes the iteration step number, k_B is Boltzmann's constant, T is the temperature, x is the independent variable, and $P(x)$ represents a probability distribution function such as a RDF, bond length or bond angle probability distributions. The algorithm involves updating trial effective potentials, $U_i(x)$, by successively adding correction terms that account for the deviation between the trial probability distribution function in the CG simulations and the corresponding target distribution function from the atomistic simulations. The α parameter is an arbitrary number that is chosen to appropriately scale the magnitude of the correction term so that fast convergence of the effective potentials is attained. An effective CG potential that reproduces the same structural features from the corresponding atomistic simulations is obtained when the trial and target distribution functions are equal or nearly equal within some prescribed tolerance value.

To generate the initial guesses ($i = 0$) for the effective CG potentials, the target RDF, bond length probability distribution, $P(l)$, bond angle probability distribution, $P(\theta)$, and dihedral angle probability distribution, $P(\Phi)$, obtained from the atomistic simulations, are Boltzmann inverted via the following equations, respectively:

$$U_0(r) = -k_B T \ln\left[RDF_{\text{target}}(r)\right], \tag{2.20}$$

$$U_0(l) = -k_B T \ln\left[P_{\text{target}}(l)\right], \tag{2.21}$$

$$U_0(\theta) = -k_B T \ln\left[\frac{P_{\text{target}}(\theta)}{\sin\theta}\right], \tag{2.22}$$

$$U_0(\Phi) = -k_B T \ln\left[P_{\text{target}}(\Phi)\right]. \tag{2.23}$$

It should be noted that $U_0(x)$ given above is a potential of mean force (PME), not a potential energy. However, it is usually sufficient as an initial guess for an iterative procedure. In the case that the PME does not work well, one might start the iteration with some simple type of potentials such as Lennard-Jones for nonbonded interactions and harmonic bond and angle potentials for bonded interactions.

2.2.3.1 Including thermodynamic properties as targets

According to the Henderson theorem [140], under fairly general conditions, an isotropic potential derived to reproduce the pair structure of a fluid is unique up to a constant. However, there usually exist a whole family of potentials that give RDFs with differences from the target within a line thickness. Notably, the possibility of changing the potential without disrupting the local structure can be used to fit other thermodynamic properties of interest, such as average energy and/or pressure [135–138]. It should be noted for coarse-grained models that removing degrees of freedom will also removes their friction contribution. Thus, leaving out friction will speed up the dynamics and, in most cases, produce extremely high pressure

for the system. Therefore, pressure correction is usually preformed alongside the structural fit.

The correction to the pressure, for example, can be done by introducing a linear tail function to the previously optimized potential [135]. The correction to the potential is

$$\Delta U(r) = A_0 \left(1 - \frac{r}{r_{\text{cutoff}}}\right). \tag{2.24}$$

The correction fulfills the following essential conditions: $\Delta U(r = 0) = A_0$ and $\Delta U(r_{cutoff}) = 0$. Depending on whether the pressure in the current iteration is above or below the target value, A_0 value can be adjusted to decrease or increase in the next iteration. The corrected potentials is then taken as an initial guesses of a re-optimisation of the potentials against the structure using the IBI method. After that, the pressure is re-evaluated and the procedure continued until convergence has occurred.

2.2.4 Notes for coarse-graining

2.2.4.1 State-point dependence and transferability of potentials

Coarse-grained potentials, particularly ones generated by structural or force based approaches, are averaged out from many atomistic degrees of freedom, whose effect is different depending on the given conditions. For this reason, the coarse-grained models are highly specific to the thermodynamic state at which the optimisation is performed and cannot be assumed to be transferable to a different set of conditions, i.e. temperature or composition. As an examples, Ghosh and Faller [153] studied the glass transition behaviour of a small organic molecule, ortho-terphenyl, using a CG model derived by the IBI method. They found that using potentials generated at 300 K does not produce any glass transition at 250 K or above, in contrast to the atomistic model which gave a glass transition at 260 K. Villa *et al.* [155] showed that the CG model obtained by reproducing the structural properties of pure liquid benzene is not well-suited to represent benzene in dilute aqueous solution. The model does not favor benzene aggregation as observed in detailed atomistic simulations.

Another example, the coarse-grained poly(acrylic acid) model [156] predicts the wrong temperature dependence of the hydrodynamic radius. It was shown that, with increasing temperature, the polymer contracts instead of expands.

Whilst the reasons for transferability problems are clearly demonstrated [157, 158], on the other hands, some degree of transferability still exists [159, 160]. There are many reports on successfully using iterative Boltzmann inversion derived force fields at specific thermodynamic states to describe a broader range of them. Using a low level of coarse-graining (2 CH_2 groups : 1 CG bead), Vettorel and Mayer [161] showed that the phase transition to an ordered state of short polyethylene chains is qualitatively described by using the same potential. Full transferability, over the thermodynamic range of interest, for the CG model of polyamide-6,6 has been reported by Carbone *et al.* [150]. It was also shown in this study that the polymer chain length does not affect the transferability of the force field. In the same year, the same research group [162] has reported CG potentials for polystyrene and ethylbenzene (basic monomer of polystyrene), that are capable of reproducing true structure and density over a desired range of temperatures, compositions and chain lengths. For a case study more closely related to the work in this thesis, implicit-solvent CG potentials for poly(oxyethylene) oligomers have been constructed using the IBI technique [137]. Comparing CG structures (radius of gyrations and end-to-end distances) with atomistic simulations and experiments shows that state-specific potentials are transferable both to a wide concentration range and to much larger molecules (up to 150-fold larger PEO chains than in the 10-mer used in the fit). The experimental scaling law for R_g was reproduced almost quantitatively by the potentials with explicitly including of dihedral interactions. Having shown possibilities of using state-specific CG potentials to describe other conditions, the problem of transferability, nevertheless, has to be tested with very great care. For some systems that have exhibited behaviours highly dependent on thermodynamics conditions, a whole optimisation process might be necessary for studying in a new environments.

2.2.4.2 Mapping schemes

The way of representing a detailed chemical structures by coarse-graining, the so-called "mapping" procedure, is so far a free choice. There is no general procedure to determine how many atoms can be lumped together into one coarse grained particle, or where the CG bead should be placed (i.e. centre-of-mass-based or centre-of-geometry). Several studies suggest that using rather small degrees of coarse-graining leads to better potential transferability to different temperatures [150, 153, 161, 163] or chain lengths [149, 156, 164]. Nevertheless, it is the responsibility of the developer to decide this, which very much relies on the best compromise between capturing the details of the system of interest and computational convenience.

For example, in coarse-graining of water, the most used scheme is the 4-to-1 mapping [89, 165–167]. One reason for this is because each water molecule has approximately 3.5 hydrogen bonds [168]. Hence, it seems reasonable to group 4 molecules into a single CG unit. In the case of polarizable model, the choice of 4 water molecules per 1 CG bead seems to be convenient since the average dipole moment of these clusters are similar for bulk water, the air/water interface, and salt solutions [166]. In addition, Hadley and McCabe [165] have showed that a 4-to-1 mapping model provides the optimal balance between computational efficiency and accurate solvation and structural properties when compared to water models ranging from one to nine waters per bead.

The choice of positioning a coarse-grained centre sometimes plays a crucial role. In the study of polystyrene melts by Müller-Plathe and co-workers, they observed that, with 1 CG bead representing 1 polystyrene monomer and the CG beads centred on methylene carbons [150], the model was transferable only over a narrow range of temperatures, i.e. it fails to reproduce the bulk density when temperature is 80 K lower than the optimisation temperature. With a different mapping scheme, where the centres of the beads are on the real centre of mass of polystyrene monomer [162], they successfully obtained CG potentials that are capable of reproducing true structure and density over a board range of temperature and chain length.

2.3 Analysis of simulation data

2.3.1 Radial distribution function

The radial distribution function (RDF) or pair correlation function $g_{AB}(r)$ between particles of type A and B is defined in the following way:

$$g_{AB}(r) = \frac{\langle \rho_B(r) \rangle}{\langle \rho_B \rangle_{local}}$$
$$= \frac{1}{\langle \rho_B \rangle} \frac{1}{N_A} \sum_{i \in A}^{N_A} \sum_{j \in B}^{N_B} \frac{\delta(r_{ij} - r)}{4\pi r^2} \tag{2.25}$$

with $\langle \rho_B(r) \rangle$ the particle density of type B at a distance r around particles A, and $\langle \rho_B \rangle_{local}$ the particle density of type B averaged over all spheres around particles A.

2.3.2 Radius of gyration

The radius of gyration (R_g) indicates roughly the compactness of a structure. It is calculated as

$$R_g = \left(\frac{\sum_i (\mathbf{r}_i)^2 m_i}{\sum_i m_i} \right)^{\frac{1}{2}}, \tag{2.26}$$

where m_i is the mass of atom i and $\mathbf{r}_i$ the position of atom i with respect to the centre of mass of the molecule.

2.3.3 Mean square displacement

The self diffusion coefficient (D_A) of particles A can be determined from the mean square displacement (MSD), using the Einstein relation [169]:

$$\text{MSD} = lim_{t \to \infty} \left\langle \frac{1}{N} \sum_{i=0}^{N} (r_i(t) - r_i(0))^2 \right\rangle = 6 D_A t \tag{2.27}$$

where N is the number of particles, t corresponds to time, and $r_i(t) - r_i(0)$ is the vector distance traveled by a given particle over the time interval.

2.3.4 Interfacial tension

For a planar interface perpendicular to the z axis, the liquid-vapour interfacial tension (γ) was computed from the ensemble average normal P_{zz} and lateral P_{xx}/P_{yy} pressure components [170] according to

$$\gamma = \frac{1}{2} L_z \left(\left\langle P_{zz} - \frac{P_{xx} + P_{yy}}{2} \right\rangle \right) \tag{2.28}$$

The factor $\frac{1}{2}$ accounts for the two interfaces present in the chosen box. L_z is the box length in the z direction. For a planar interface, the normal component P_{zz} does not depend on z and is equal to the vapour pressure (p) [171].

2.3.5 Summary

The computational methods described here are employed throughout the following chapters in this thesis. The IBI technique is used to derived a CG models for water, PEO/water and amphiphilic polymers/water systems in chapter 3, 4 and 5, respectively. Simulations of water in the next chapter are performed using stochastic dynamics, and the study of PEO and amphiphilic polymers in chapter 4-6 is carried out employing molecular dynamics simulations. Calculation of the radial distribution function is conducted in almost every chapter, as it is very important for the coarse-graining process. The radius of gyration is worked out in chapter 4 for structural studying of PEO in aqueous solution. Since we focus our study on a water/air interface behaviour, surface tension for the simulated system is always reported alongside.

Chapter 3

Coarse-grained model for water

3.1 Introduction

Due to its role in chemical and biological processes, water is one of the most studied liquids in both all-atom representations [172–178] and coarse-grained models [89,138,143,165–167,179–184]. For all-atom representation, many different models have been proposed with varying computational cost and agreement with the real behaviour of water. In 2004, Dr Philip Anderson [92], a previous member of the Durham simulation group, carried out extensive simulations and assessments on these water models as the aim of selecting the most appropriate model to be used in the simulations of amphiphilic molecules at a water/air interfaces. From his conclusions it was the TIP4P model [173] that gives the best compromise in terms of a true representation of water behaviours and computational cost.

Since then TIP4P has been found to provide a qualitatively correct description of the phase diagram of water. The choice of TIP4P geometry was later used to develop further models of water such as TIP4P/Ew [177], TIP4P/2005 [178] and TIP4P/Ice [178]. These new generation models have been specifically designed to be used with the Ewald sums technique [185] that includes a proper treatment of the long-range electrostatic interactions. TIP4P/Ice has been found to reproduce the experimental melting temperature of water. However, this model significantly overestimates the value of the critical temperature [186,187] and, thus, overestimates the surface tension [171]. The TIP4P/Ew model has been found to yield a much

better prediction of the vapour-liquid behaviour than other widely used models such as SPC, TIP3P, and TIP5P [171, 186]. Among the three recent TIP4P models, the TIP4P/2005 model seems to provide the best description of the true water, from consideration of phase diagrams, vapour-liquid equilibria and critical properties [171, 186].

This chapter focuses on developing coarse-grained models of water that can be used to study behaviours of amphiphilic molecules at the water/air interface. Section 3.2 reviews some of the CG water models that relate to our work. In section 3.3 we describe how we develop our own water models. Results and discussion are given in section 3.4. The choice of the model to be used in the next work is discussed in section 3.5. Finally, the research work in this chapter is concluded in section 3.6.

3.2 Coarse-grained water models

Several coarse-grained models of water have been developed over the past two decades to deal with phenomena covering a wide range of length- and time-scales. Models were proposed using different mapping schemes, ranging from one water molecule per bead [138, 143, 158, 165, 182] to two [143, 165], three [179, 180], four [89, 165–167] or even five [184]. Most of these models involve a liquid particles with one pairwise interaction site per bead. The van der Waals and electrostatic interactions are incorporated into an effective pairwise potential energy, which is represented by either analytical or numerical functions. As models were developed for different purposes, the represented properties are often different. High resolution coarse graining, e.g. 1-to-1 mapping, can easily reproduce the essential structural features, such as radial distribution functions, as observed in all-atom simulations. Coarser-grained models such as 3- or 4-to-1 mapping are usually developed using thermodynamics properties as a targets. This higher degree of coarse-graining also provides much more speed-up in simulations, but with the cost of losing some structural details. Therefore, for a particular application, one might also need to find the best compromise between accuracy and efficiency. Some interesting CG models of water that could potentially be used to study amphiphilic polymers at the water/air

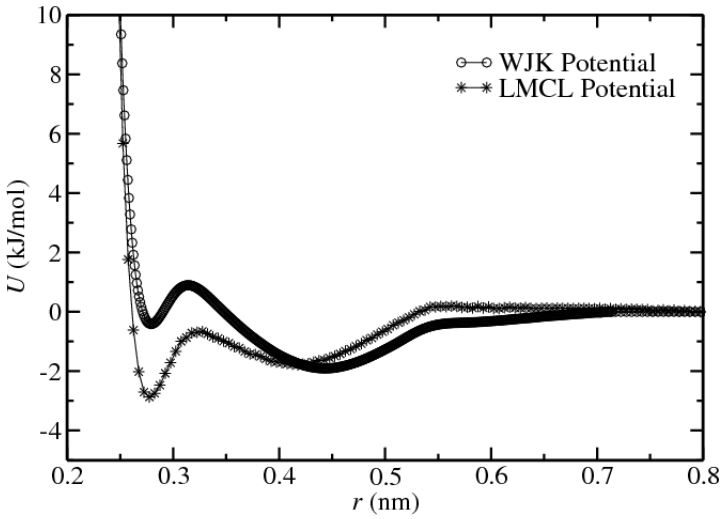

Figure 3.1: Effective coarse-grained water potentials potentials generated from iterative Boltzmann inversion (WJK model) and reverse Monte Carlo (LMCL model) methods.

interface are discussed below.

3.2.1 The WJK model

This model has been presented by Wang *et al.* [138]. WJK refers to the acronym of the last names of the people who developed this model. Here, one water molecule is represented by one CG site (1-to-1 mapping). The CG potentials were derived based on structural coarse-graining, using the iterative Boltzmann inversion (IBI) technique. Their aims are to build the CG water that can preserve the structural properties of water as well as to match some thermodynamics properties to all-atom models. The procedure includes constructing of an effective potential that reproduces the centre of mass (oxygen-oxygen) radial distribution function (RDF) of atomistic models of the bulk liquid state. The process after obtaining a correct RDF involves a pressure correction step, which has already described in section 2.2.3.1 of chapter 2.

The pressure-corrected coarse-grained potentials are plotted in figure 3.1. As discussed in reference [192], the first potential well at the distance of 2.8 Å could presumably be due to H-bonding between waters, while the second minimum could be interpreted as an effective dipole-dipole attraction. These characteristic features can only be represented by the effective potential of the 1-to-1 mapping scheme.

Table 3.1: Thermodynamic properties of atomistic TIP4P-Ew and 1-to-1 mapping coarse-grained water models. Simulations were performed at 298 K using an integration time step of 1 fs and 4 fs for atomistic and CG models, respectively. The experimental data were taken from references [72, 188–191]. *The properties presented in the table are from left to right: bulk density ρ (g/cm^3), bulk pressure P (bar), isothermal compressibility κ_T (10^{-10} m^2/N), self diffusion coefficient D (10^{-9} m^2/s), liquid-vapour pressure p (bar) and liquid-vapour interfacial tension γ (mN/m).

Water Model	ρ	P	κ_T	D	p	γ
TIP4P-Ew	0.995	1.0	4.8	2.4	0.07	65.5
CG WJK cutoff 0.7 nm	0.998	0.5	29.7	15.6	-	-
CG LMCL cutoff 1.0 nm	0.990	53.0	25.1	10.2	-	-
CG cutoff 1.2 nm	1.081	-344.5	19.9	5.4	16.39	53.0
CG cutoff 1.4 nm	1.087	-378.1	19.6	5.5	15.26	62.1
CG cutoff 1.6 nm	1.091	-558.3	19.1	5.1	14.87	94.6
CG WJK-like cutoff 1.4 nm	1.018	-72.8	28.5	6.2	40.19	59.4
CG LMCL-like cutoff 1.4 nm	1.043	-161.8	26.3	6.0	40.40	42.5
Experiment (298 K)	0.998	-	4.6	2.3	0.03	73.0

*The density and isothermal compressibility were calculated from 20 ns NPT simulations with the pressure setting at 1 bar. The pressure and self diffusion coefficient were calculated from 20 ns NVT simulations with the box density of 1.000 g/cm^3. The liquid-vapour pressure and liquid-vapour interfacial tension were calculated from 50 ns NVT simulations. The simulated vapour pressure reported in the table is actually the normal component of the pressure (P_{zz}). We assume that, for a planar interface, (P_{zz}) does not depend on z and is equal to the vapor pressure, p [171].

Table 3.1 lists the calculated thermodynamics properties of the WJK and the other 1-to-1 mapping coarse-grained models that will be mentioned later in this chapter. The data for atomistic TIP4P-Ew model and experiment were also listed for comparison.

Several properties of water, for example, the pressure and the isothermal compressibility, could not be reproduced correctly by these models at the same time. This seems to be example of "*representability problems*" as reported in the works by Louis *et al.* [157, 158]. They have clearly demonstrated that, at a given state point (i.e., density and temperature), the pair potential that reproduce the RDF is unique (the Henderson uniqueness theorem [140]), hence, it is not possible to simultaneously represent the pair structure and all equilibrium thermodynamic properties of water using state point dependent isotropic pair potentials. So, users of effective potentials need to decide the key properties to focus on. Nevertheless, as the internal degrees of freedom have been removed, four times larger time scale (4 fs vs. 1 fs) can be applied in the CG simulation. And with no electrostatic interaction calculation, altogether, the 1-to-1 mapping model leads to a speed-up of the order of 50 in computer time.

3.2.2 The LMCL model

This 1-to-1 mapping model has been proposed by Lyubarsev *et al.* [182], using a reverse Monte Carlo coarse-graining scheme [139]. The CG model was derived from an atomistic RDF of the liquid/gas phase-separated system (low density), where the total pressure is relatively low. Thus, apart from correction of water structure, a realistic pressure is also achieved without further correction for the potential.

The effective potential obtained from this technique is also plotted in figure 3.1. This potential generated from an atomistic target at the density of 0.25 g/cm^3, which provides practically correct density and pressure as reported in table 3.1. By comparing with the WJK model in figure 3.1, despite providing identical liquid structure, the two potentials are different in characteristic. The shape of the potential is likely to depend on the state from which it was derived. As the LMCL model was originated from a low density state (separation of liquid and gas phases), it could be the surface tension of the liquid phase that dominates a higher attractive

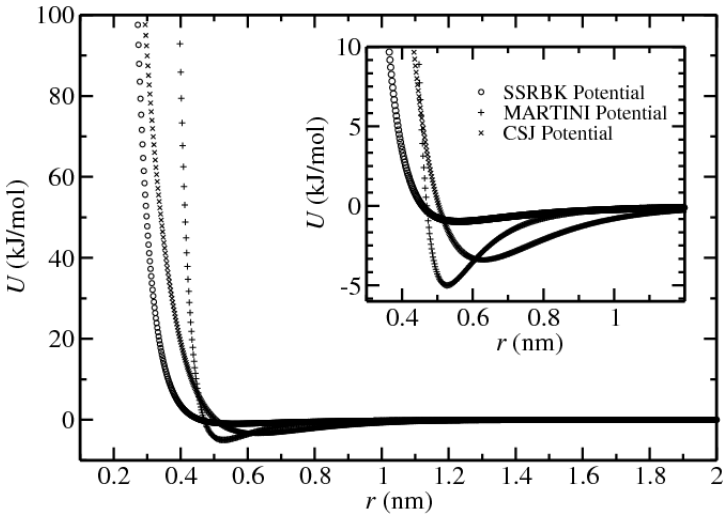

Figure 3.2: Coarse-grained potentials for the SSRBK [179], MARTINI [89, 90] and CSJ [183] water models.

first well of the potential. The WJK potential, which was derived from the bulk liquid state, shows more repulsion at short distance, but has a wider attractive well at large distances. We believe that it is a compensation between attractive and repulsive forces within each model that makes them provide a similar liquid structure and the same pressure level.

3.2.3 The SSRBK model

The SSRBK model has been developed by the Klein research group [93, 179] to help studying phospholipid and self-assembly processes of amphiphilic copolymer systems. The model with one spherical site representing a group of three water molecules (3-to-1 mapping) was developed under the requirements of reproducing the correct thermodynamics of water (e.g. hydrodynamics and density) and at the same time, be able to maintain a liquid-vapour interface over the desired temperature range.

The Lennard-Jones 6-4 potential in equation 3.1 was used to describe the interactions between the CG sites.

$$U\left(r_{ij}\right) = \frac{15}{4}\epsilon_{ij}\left\{\left(\frac{\sigma_{ij}}{r_{ij}}\right)^{6} - \left(\frac{\sigma_{ij}}{r_{ij}}\right)^{4}\right\} \tag{3.1}$$

Here, r_{ij} is the distance between sites i and j, ϵ_{ij} is the well depth at the minimum

Table 3.2: Thermodynamic properties of the SSRBK, MARTINI and CSJ water models. The simulated results were taken form the work by Chiu and coworkers [183], which performed at 298 K using an integration time step of 10 fs. The experimental data were taken from references [72, 188, 189, 191]. The properties presented in the table are from left to right: bulk density ρ (g/cm^3), isothermal compressibility κ_T (10^{-10} m^2/N), self diffusion coefficient D (10^{-9} m^2/s), free energy of solvation ΔG_S (kJ/mol), heat of vaporization ΔH_{vap} (kJ/mol) and liquid-vapour interfacial tension γ (mN/m).

Water model	ρ	κ_T	D	ΔG_S	ΔH_{vap}	γ
SSRBK cutoff 1.88 nm	0.993	15	6.6	-19	32.6	71
MARTINI cutoff 1.2 nm	1.005	9	1.6	-18	30.2	32
CSJ cutoff 1.6 nm	0.998	17	4.3	-28	38.4	71
Experiment (298 K)	0.998	4.6	2.3	-26.5	44.0	73

and σ_{ij} is the distance at which the potentials is zero. This potential is shown in figure 3.2.

To prevent freezing of particles within the normal liquid range, the epsilon was fixed at 212.1 K (1.76 kJ/mol) to allow the melting point to occur around this temperature (212.1 K). The sigma was set at 4.58 Å to reproduce the water density at 303.15 K. With a relatively wide potential minimum, liquid-vapour coexistence could be maintained for a wide range of temperature (0-100 °C). Some key properties for the SSRBK water together with the potential cutoff used are listed in table 3.2.

3.2.4 The MARTINI model

The popular MARTINI force field was first developed by Marrink and co-workers for studying biomolecular systems [89]. For the MARTINI water model, four water molecules are grouped in to one CG site and interactions between these CG beads are described by the standard Lennard-Jones 12-6 potential. The accuracy of the model is maximized by matching the key thermodynamic properties of water such as density, compressibility and self diffusion coefficient (see table 3.2). This results in the effective minimum distance of approach between two particles, σ_{ij} at 4.7 Å

and the depth of the potentials well, ϵ_{ij} is 5.0 kJ/mol. The potential for this model is also plotted in figure 3.2.

As can be seen in the figure 3.2, the MARTINI potential is essentially highly attractive. This might be the reason why the model can maintain liquid-vapour coexistence phase at room temperature, despite using a shorter potential cutoff comparing to the SSRBK model. An undesirable consequences of a very attractive potential is that it freezes above the experimental freezing point of water [90]. This problem has been solved by adding some amount of antifreeze particles [90]; basically the same kind of water but with a bigger spherical size (σ_{ij} = 5.4 Å), in order to disturb the formation of nucleation sites. Another deficiency of this model is that it has too low a surface tension compared to experiment due to the potential being truncated at rather short distances, and is therefore missing long-range dispersion interactions.

3.2.5 The CSJ model

The CSJ water has recently proposed by Chui *et al.* [183]. The main purpose for this work is to obtain a model that can properly represent the phase changes and coexistence of water. The model is a single bead representing a group of four water molecules similar to the MARTINI model. However, the CG interactions were represented with a flexible Morse-like potential, rather than using a potential of the Lennard-Jones form. The Morse potential has the form

$$U\left(r_{ij}\right) = \varepsilon \left[e^{\alpha\left(1-\frac{r_{ij}}{R_0}\right)} - 2e^{1/2\alpha\left(1-\frac{r_{ij}}{R_0}\right)} \right] \tag{3.2}$$

where R_0 is the distance of the minimum energy ε and α is a parameter that determines the softness of the potential. This potential form allows a flexibility of tuning the parameters to fit a variety of experimental data. Here, the adjustable parameters ε and R_0 are parametrized to fit the experimental density and heat of vaporization. The selection of the value of α is based on the agreement of the simulated vapour-liquid interfacial tension with the experimental data.

As shown in figure 3.2, the CSJ potential is softer than the MARTINI model in

a short-range region. This permits using of a large integration time step, e.g. 40 fs, without producing energy sinks that cause a freezing effect. As summarized in table 3.2, both the CSJ and SSRBK water models have calculated surface tension of 71 mN/m at 298 K, in good agreement with the experimental value of 73 mN/m. However, the CSJ model works with a shorter potential cutoff, thus, promotes faster calculation than the SSRBK model. Moreover, the heat of vaporization is better reproduced by the CSJ water compared to the SSRBK model which considerably underestimates the experimental value. This also reflects a rather high vapour pressure found in the simulations of the SSRBK model at room temperature [179]. As summarized in table 3.2, water properties are reproduced reasonably well by the CSJ water model. This make the model a good candidate for simulation studies of processes involving water, especially, ones that occur at the water/air interface system.

3.3 Deriving a coarse-grained model for water

Due to the important role of H-bonds between water-water and PEO-water on the solution properties of PEO/water system [47, 50, 52], one aim of this research is to obtain the coarse-grained model of water that could represent this. Equally important, the model should behave correctly in the liquid/vapour coexistence region over the desired temperature range.

As we have mentioned in the previous section, the 1-to-1 mapping model could carry H-bond features in its effective potential. The WJK and LMCL models worked well in term of reproducing structure and some thermodynamics of water. Unfortunately, since they were developed for liquid bulk water, they are unable to imitate liquid/vapour equilibrium as tested by us. Figure 3.3 shows a failure of both models to maintain the separate phases at room temperature. Instead, most of water particles diffused (evaporated) to the air and formed a mixing of liquid drops and gas particles throughout the simulation box.

We hypothesize that the fundamental problem might come from the use of a rather short potential cutoff, which could not cover the missing long-range attrac-

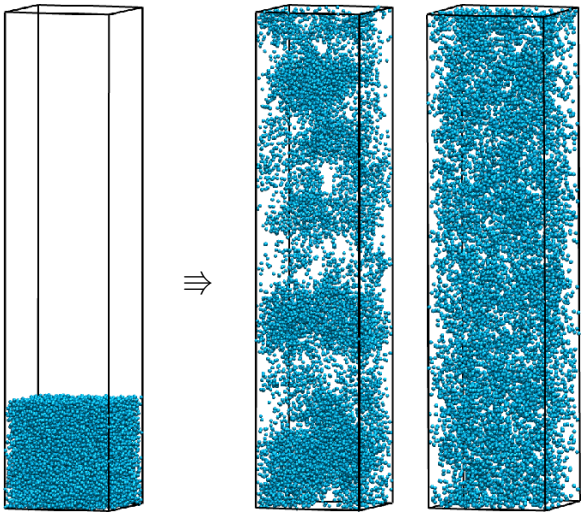

Figure 3.3: Starting and final snapshots from 50 ns simulations of the WJK and LMCL models in an attempt to simulate the water/air interface.

tions between particles. The result is that particles could not be held within the water slab and, eventually, evaporated. The success of the SSRBK and the CSK models in maintaining a liquid/vapor interface comes from the fact that they have a wider attractive range to the potential and larger cutoff. Therefore, in order to gain correction for both structural and liquid/vapour properties, the iterative Boltzmann inversion method together with a long-range potential cutoff is used below to derive a new 1-to-1 CG model of water for this work.

In addition, the surface tension can cause stronger interactions between water molecules at the surface region compared to those in the bulk. This can be one reason that explains why the potential derived from the RDF of the bulk state did not work for the water/air interface system. This is symptomatic of a general feature of isotropic CG potential known as "*transferability problems*" (discussed in section 2.2.4.1 of chapter 2), concerning the fact that the CG potential derived in one state point does not perform well in different conditions. Given these reasons, the RDF of a water/air interface system will be used directly as a target property in our coarse-graining method.

3.3.1 Computational details

3.3.1.1 Atomistic simulations

Molecular dynamics simulations are performed using GROMACS version 4.0.7 (single precision) [109]. The equations of motion were integrated using the leap-frog algorithm [97] with a time step of 1 fs. The temperature was kept constant by using a Nose-Hoover [105, 106] thermostat with a relaxation time of 2.5 ps. A Rahman-Parrinello barostat [107] with relaxation time of 5.0 ps were employed in the cases of constant pressure simulations. Electrostatics were treated by employing the smooth particle mesh Ewald method [185] with a real space cutoff of 1.2 nm. A Fourier mesh spacing of 0.1 nm, and fourth-order interpolation were adopted. Lennard-Jones interactions were truncated at 1.2 nm with tail corrections applied for both energy and pressure. Here, periodic boundary conditions have been applied for all simulations. We used a Verlet-type neighbor list updated every 10 steps with a list cutoff radius of 1.2 nm. Bond constraints were solved using the Linear Constraint Solver (LINCS) algorithm [193] with a linc-order of 4 (number of matrices in the matrix inversion).

3.3.1.2 Reference simulation of TIP4P-Ew water at a water/air interface

In this work, the TIP4P-Ewald water [177] was used as an atomistic reference simulation. This model was re-parameterized from the standard TIP4P water model [173] to deal with long-range Coulombic interactions using the Ewald sum technique [185]. The overall properties of the model have been shown to be improved relative to its predecessor [186]. More importantly, it has been shown that the modified TraPPE-UA force field for PEO [194] in combination with TIP4P-Ew water provides excellent conformational and thermodynamics properties for aqueous PEO solutions. The TIP4P-Ew model has three charge sites per water molecule that are placed on the two hydrogen centres and an additional site (M-site) along the H-O-H bisector. The geometry and interaction parameters of this water model are given in figure 3.4.

To set up a water/air interface, 10000 water molecules were first placed in the

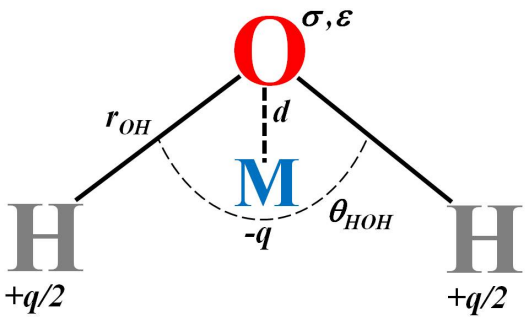

σ	=	3.16435 Å
ε	=	0.680446 kJ mol^{-1}
q	=	1.04844 e^{-}
d	=	0.1250 Å
r_{OH}	=	0.9572 Å
Θ_{HOH}	=	104.52°

Figure 3.4: Depiction of a TIP4P-Ew water molecule. Below are numeric values of the force field parameters.

cubic box of size $x = y = z = 8.0$ nm. This initial system was subjected to a short NPT equilibration to allow any high energy gaps or overlaps between water atoms to relax into more energetically favourable positions and to allow the density of the system to reach equilibrium. This resulted in the system box size decreasing to 6.74 nm for all dimensions. The final configuration from the bulk simulation was then used as the starting structure for this task. Here, the z dimension of the box was increased from 6.74 nm to 26.74 nm without changing the coordinations of water molecules. This setup is expected to stabilize two planar liquid-vapour interfaces perpendicular to the z axis of the simulation cell. The system was first allowed to equilibrate over a short NVT simulation, allowing two equilibrated water/vapor interfaces to form. Reported results were evaluated from production runs that lasted 20 ns using the NVT ensemble. Simulation details are summarized in table 3.3.

3.3.1.3 Coarse-grained simulations

Simulations of the coarse-grained systems were also performed using the GROMACS 4.0.7 program (single precision), using numerical potentials for interactions between CG beads. All simulations were performed in the NVT ensemble employing periodic boundary conditions. Temperature was kept constant at 298 K by a Langevin

Table 3.3: Simulation details of atomistic reference and corresponding coarse-grained system used in the iterative Boltzmann inversion procedure.

System	n_{water}	box (nm) $x \times y \times z$	T /K	simulated time
Atomistic reference	10000	6.74×6.74×26.74	298	20 ns
Coarse-grained fit	10000	6.74×6.74×26.74	298	10 ns per iteration step

thermostat [169] with a friction constant of 5 ps^{-1}. Equations of motions were integrated applying the leap-frog algorithm with a time step of 4 fs. No electrostatics were present for the coarse-grained simulations. Cutoff corrections were obsolete, since all tabulated potentials were designed to shift smoothly to zero at the cutoff distances.

In this work, each water molecule was replaced by one coarse-grained site that isotropically interacts with others via a coarse-grained potential. The iterative Boltzmann inversion technique was then used to construct an effective potential that reproduces the oxygen-oxygen radial distribution function of the reference TIP4P-Ew water. We applied three sets of the potential cutoffs, 1.2 nm, 1.4 nm and 1.6 nm, in the IBI fitting process to test which range provided the best results. Simulation details of the coarse-grained systems are given in table 3.3.

For this work, a long-range attractive interaction was implemented for the CG potentials by the process described below.

At a distance from 8.0 Å to the cutoff, where there is no structure appearing in the target RDF, the potential energy was fixed, using the form

$$U\left(r_{ij}\right) = \frac{E}{r_{ij}^3} - U_{\text{shift}} \tag{3.3}$$

where the constant E was set to be -4.5×10^{-2} kJ/mol. The term U_{shift} was added as to ensure that the potential vanished to zero at the cutoff

$$U_{\text{shift}} = \frac{E}{r_{\text{cutoff}}^3}. \tag{3.4}$$

We should mention that we have tried many attractive forms of potentials, ranging from r^{-2} to a common r^{-6} dependence. The energy function and parameter in equation 3.3 are the form and value that gave the best result in our experiments. This potential range, 8.0 Å $\rightarrow r_{\text{cutoff}}$, will be fixed during the IBI fitting process to maintain the long-range attractive force.

3.4 Results and discussion

Figure 3.5 compares the atomistic RDF to those obtained from the final IBI iteration of the different potential cutoffs. It can be seen from the figure that the derived CG models match the all-atom RDF extremely well. It took at least 20 iteration steps for the CG potentials to converge. We noted that it takes more iteration steps for fitting of the longer cutoff, e.g. 40 steps for the cutoff of 1.6 nm. The corresponding CG potentials are plotted in figure 3.6. From the picture, all three cutoffs provide a similar potential shape. The longer potential cutoff comes with a shallower well depth, as to balance the interaction so that the RDF is fitted.

As reported in the table 3.1 the calculated bulk density for all CG models is slightly higher than atomistic and real water, but is still in an acceptable range. The bulk pressure is the same order as an atomistic model but has a negative value. This can be a result of the effect of the surface tension passing from the atomistic to the CG models, which causes a higher pressure and thus higher density inside the water slab of water/air interface simulations. When the models were tested in the bulk phase, this effect manifests in lowering (negative value) pressure since the surface is no longer present. The calculated diffusion coefficient of CG particles is 2-3 times larger than normal water. In case it is needed, the dynamic can be tuned to match closely to real water by changing the friction term in a Langevin thermostat [192, 195].

Promisingly, with a potential cutoff of 1.4 nm the surface tension can be raised to 62.1 mN m^{-1}, which is very close to the parent atomistic simulation (65.5 mN m^{-1}). Increasing the potential cutoff to 1.6 nm led to a situation where the calculated surface tension was far too high. This implies that the surface tension is very

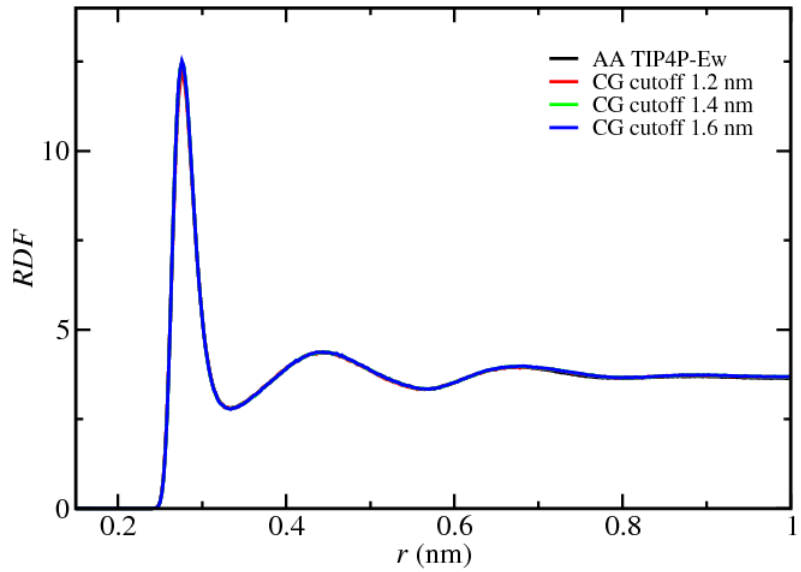

Figure 3.5: Comparison between the RDF of all-atom TIP4P-Ew water at a water/air interface and the final Boltzmann iteration fits, using three different cutoffs. All four curves are coincident.

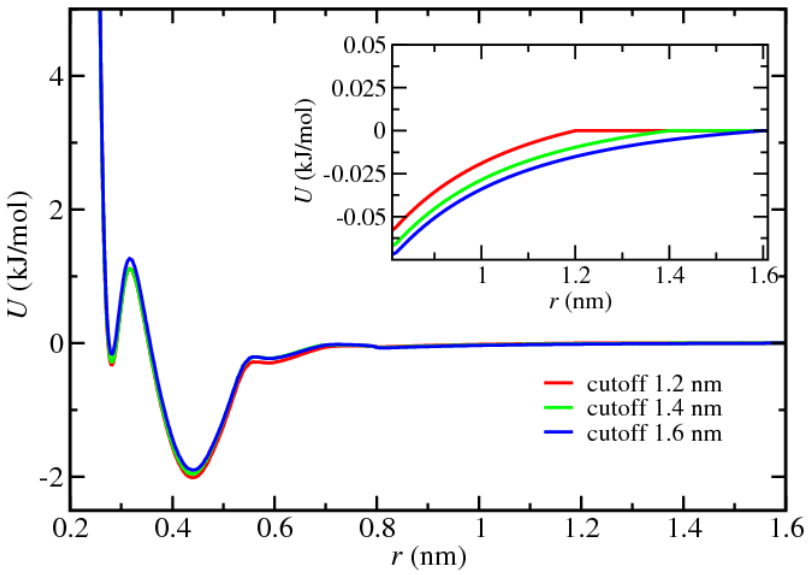

Figure 3.6: The final coarse-grained potentials generated from a water/air interface simulations, using the IBI method with the three different cutoffs.

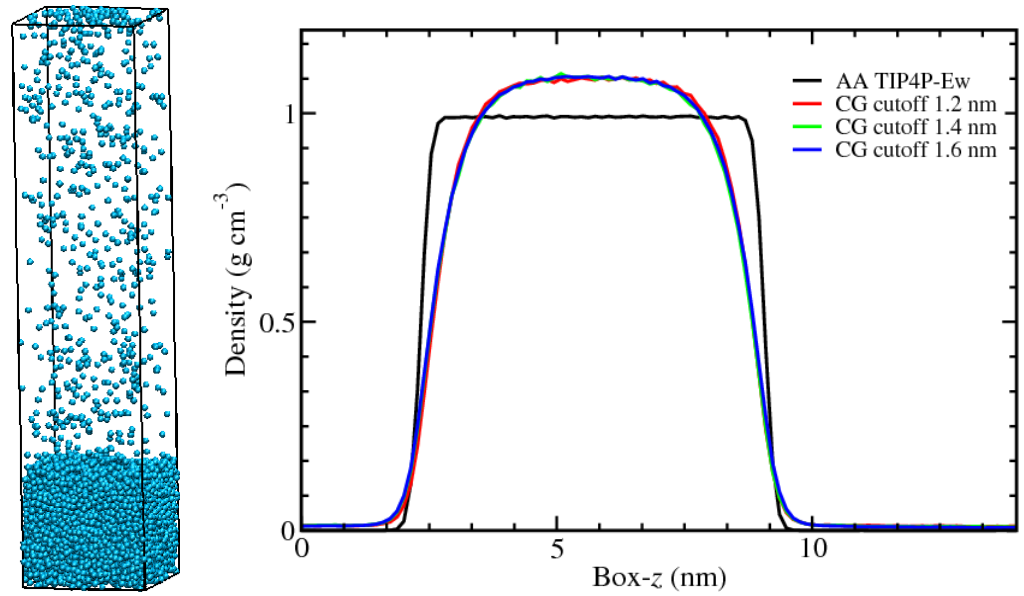

(a) (b)

Figure 3.7: (a) Typical picture of a CG simulation at a water/air interface using a cutoff of 1.4 nm, taken from the end of a 50 ns simulation. (b) The liquid-vapour density profiles along the z direction of TIP4P-Ew water and the CG models deriving from three different cutoffs.

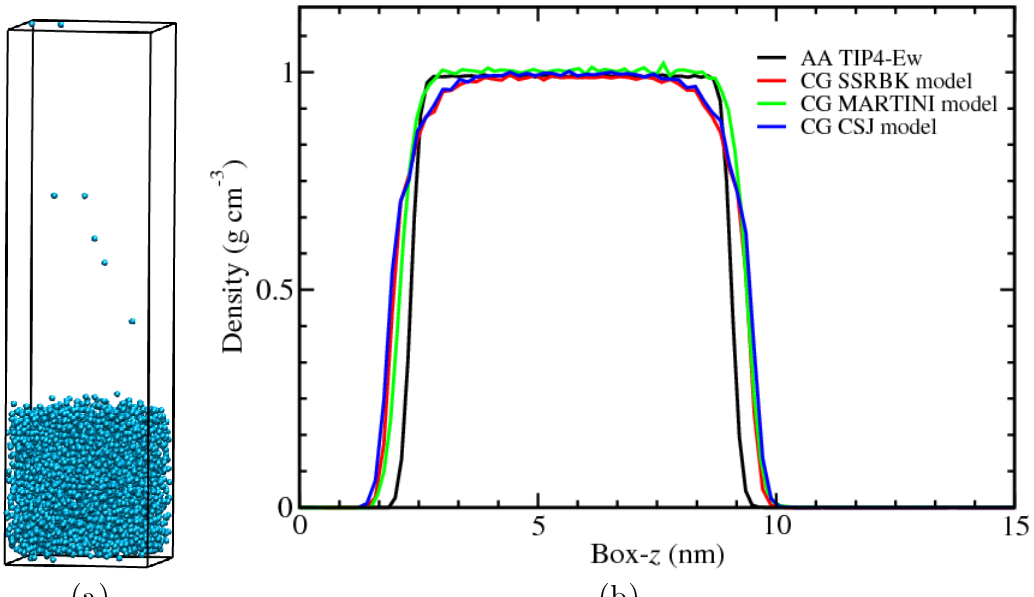

(a) (b)

Figure 3.8: (a) Typical picture of a CG simulation at a water/air interface for the CSJ model, taken from the end of a 50 ns simulation. (b) The liquid-vapour density profiles along the z direction of TIP4P-Ew, SSRBK, MARTINI and CSJ models.

sensitive to the long-range attraction that we applied in the model.

Figure 3.7 (a) shows the final snapshot from the CG simulation at a water/air interface with a cutoff of 1.4 nm. It can be seen that the liquid-vapour phase was maintained reasonably well with only a small numbers of particles (∼5 %) diffusing to the vapour phase (and exchanging with the liquid at equilibrium). These diffused particles contribute a rather high vapour pressure to the system as reported in table 3.1.

The liquid-vapour density profiles are compared with the atomistic model in figure 3.7 (b). It can be seen that, for all the derived models, density profiles are somewhat difference from that of the TIP4P-Ew model. The coarse grained density profiles show a higher density of particles in the region of the bulk phase (middle of the water slab), which results in a higher density compared to that of normal water. At the interface regions, diffusing of CG particles to the air leads to a lower density compared to the underlying atomistic model.

Figure 3.8 (b) compares the liquid-vapour density profiles for the TIP4P-Ew and the other three CG models (SSRBK, MARTINI and CSJ). As shown in the picture, all of these models provide almost equal distribution of water particles along the water slab. As the heat of vaporization for these models is comparable to real water, only few particles (less than 0.2 %) are found to be diffusing to the air, see figue 3.8 (a).

3.4.1 Some other attempts to improve the coarse-grained water properties

To improve the liquid-vapour density profiles and prevent diffusion of particles to the air, several attempts such as varying height/depth of the potentials, applying more attractive interactions at the long range distances or changing the state point where the potential was derived were made. Unfortunately, no success was achieved in our experiments. For example, applying wider attraction at long range distances helped hold particles together in the water slab. However, when a simulation was allowed to run longer at the room temperature, it started forming frozen domains of water particles due to the high attractive interactions that we applied. The water

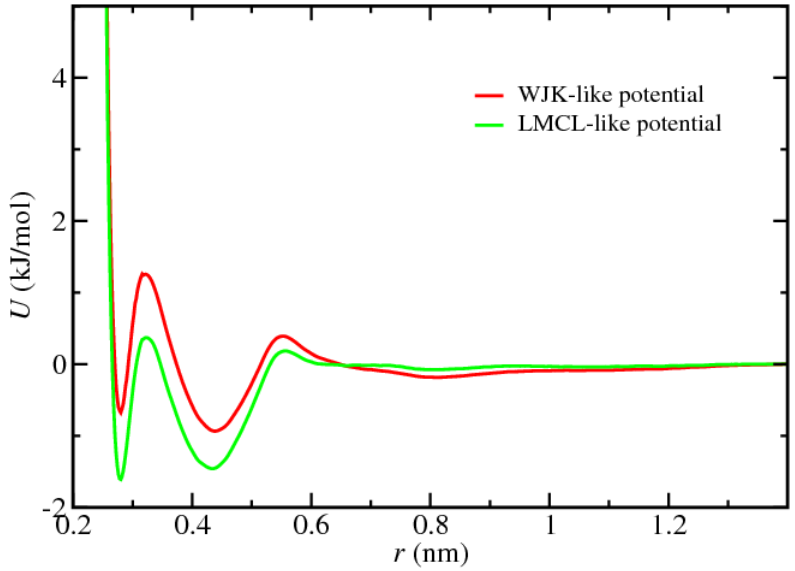

Figure 3.9: The coarse-grained potentials generated from a bulk liquid simulations, using the IBI method with the potential cutoff of 1.4 nm.

slab eventually turned to a crystalline form of water.

Some attempts were made to use a liquid bulk state as a target system. In these tasks, the CG potential was derived from an atomistic RDF of the bulk liquid simulation of 10000 water molecules. Since it provided the best results from previous study, the cutoff of 1.4 nm was chosen for the IBI fitting process. Figure 3.9 shows two examples of CG potentials generated from this study. The first one named as the "WJK-like potential" since its potential shape (depth/height) looks similar to the WJK model. By the same reason, the second one was called the "LMCL-like potential". These two potentials provide essentially identical RDFs that matched very well to the atomistic model (figure 3.10). As also listed in table 3.1, these models provide better bulk density and pressure than those of the previous models which derived from the water-air interface state. Nevertheless, the right density and pressure come with the cost of decreasing the surface tension of the model. This causes increases diffusion of the particles at the interface, and the problem with the unequally distributed density profile still remained, as shown in figure 3.11.

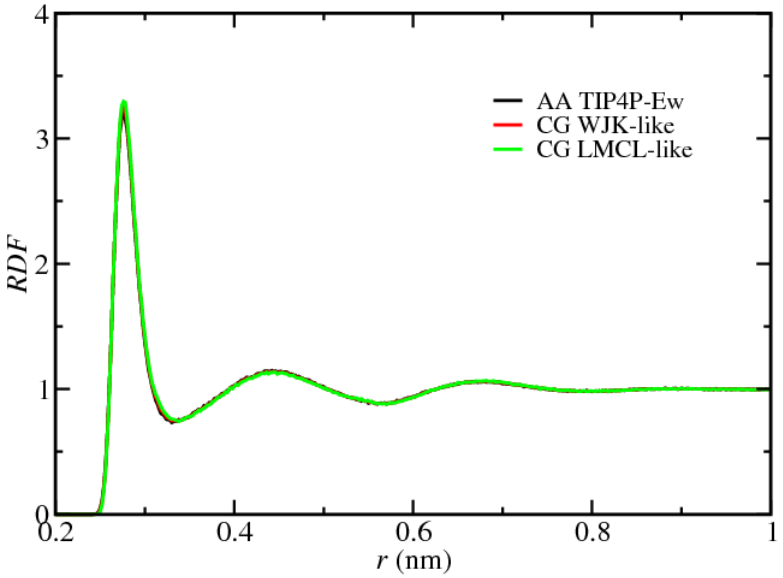

Figure 3.10: Comparison between the RDF of all-atom TIP4P-Ew water in a bulk liquid state and the final Boltzmann iteration fits using the potential cutoff of 1.4 nm.

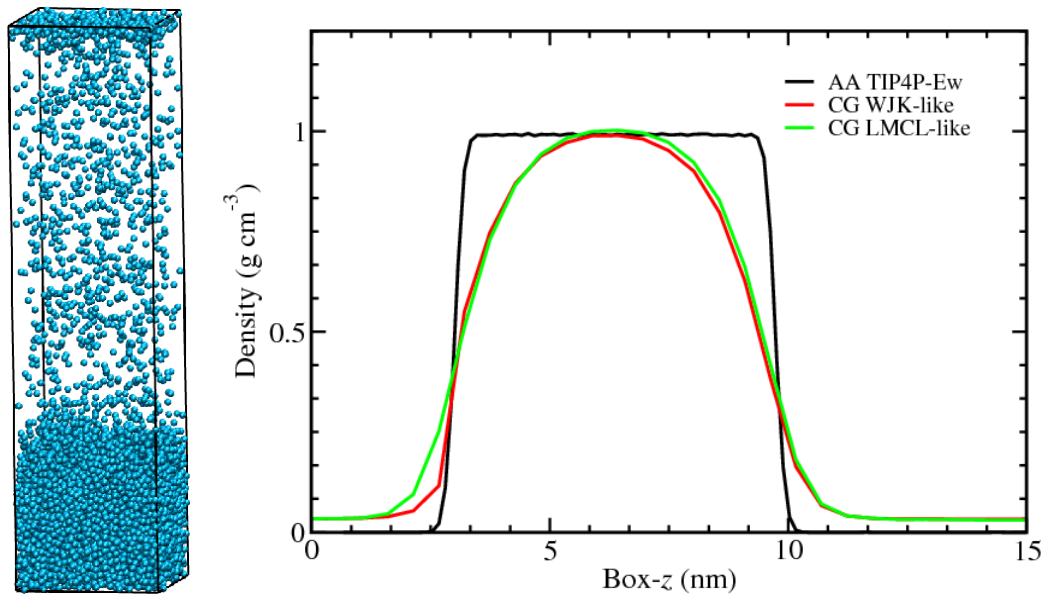

Figure 3.11: (a) Typical picture of a CG simulation at a water/air interface of the WJK-like model, taken from the end of a 50 ns simulation. (b) The liquid-vapour density profiles along the z direction of the TIP4P-Ew, CG WJK-like and CG LMCL-like models.

3.5 Choosing the coarse-grained water model

Whilst the bulk properties and the surface tension are faithfully reproduced, other surface properties, e.g. density profile and liquid-vapour pressure are not represented well by the CG models we developed. Again, we have learned that it is not possible to simultaneously reproduce all the underlying atomistic/experiment properties using a simple isotropic coarse-graining potential. As in this study, our model, with one CG bead representing one water molecule, could preserved the water structure (RDF) but failed at capturing some interface behaviours. On the other hand, the coarser models, e.g. 3 or 4-to-1 mapping, in which liquid structure has been removed, could reproduce very well the liquid-vapour properties. To this end, it is inevitable that properties of key importance have to be decided before choosing which model to use.

As surface properties are crucial to our study, we decided to abandon the coarse-grained models that we have developed above and look for the others that could support this. Searching through the literatures, there exists no report attempting to use the 1-to-1 mapping CG water to study system involving water/air interface. Therefore, the choice is confined to the coarser models that have already discussed in section 3.2.

We are aware also of polarizable coarse-grained models that have recently been developed [166, 167, 184]. These models explicitly treat the electrostatic interactions between clusters of water molecules by including dipolar representation (2 or 3 charge sites) on one CG bead. The main reason for including polarizability in the model is the expectation that processes involving interactions between charged and polar groups, such as the lipid membranes, are more realistically described.

To study structural organization of amphiphilic polymers or surfactants, however, a simple isotropic Lennard-Jones solvent particle seems to be sufficient and more efficient than a polarizable model (one should keep in mind that using polarizable water makes the simulations computationally more demanding due to charge sites added to the model). For example, Klein and co-workers [93, 94, 180] have been shown that the SSRBK model, which is a simple Lennard-Jones liquid, can be successfully used with copolymer and surfactant models to study spontaneous self-assembly behaviours in bulk aqueous solution as well as at the air/water and

oil/water interface systems. Furthermore, other properties, for instance, the polymer layer thickness and surface/interfacial tension agrees very well with the experimental findings.

According to data compared in table 3.2 and details discussed in section 3.2.5, the CSJ model by Chui and co-workers [183] is the most suitable one to be used as a solvent for our system, considering bulk and interfacial properties as well as computational efficiency. It should also noted that even the popular atomistic models themselves, for example, the SPC-E or TIP4P-Ew, all underestimate the experimental surface tension by about 10 mN/m (see table 3.1). This might also cause a side effect in simulations of amphiphilic polymer at high surface concentrations because a water sub-phase can be unstable when accommodating a polymer monolayer. For all the reasons discussed above, the CSJ model will be used as the coarse-grained water model for future chapters.

3.6 Conclusions

Coarse-grained models of water have been developed using the iterative Boltzmann inversion method to construct an effective potential that reproduces the oxygen-oxygen radial distribution function of the atomistic model. The resulting models with one bead representing one water molecule has been found to carry some H-bonding features in its effective potential, i.e. shallow well at short separations. These models could potentially support studying the PEO/water system in which H-bonds between water-water and PEO-water play an important role.

Beside the bulk liquid properties, the model is also required to reproduce the true behaviours of water at a liquid/vapour interface. By applying a long-range attraction to the potentials, the models have found to provide correct surface tension and liquid/vapour equilibrium was maintained reasonably well. However, there exists some properties that we could not get right by any kind of potential. The first deficiency is the unequal distribution of the liquid/vapour density profile, in which we found that it showed a higher density of particles in the bulk phase than at the surface region of the water slab. A second problem involved a significant amount of

water particles diffusing from the water surface at room temperature, resulting in a rather high vapour pressure compared to the atomistic model or the experimental value. We, therefore concluded from this study that it is not possible to simultaneously reproduce all the underlying atomistic/experiment properties using simple isotropic potentials.

The coarser models with 3-to-1 or 4-to-1 mappings ignore structural features of water, but provide practically correct thermodynamic properties both in bulk and at interface conditions. Considering both the best representation of physical properties and computational efficiency, we decide to leave the models that we have developed and use the CSJ model by Chui and co-workers [183] for studying the system of PEO/water and amphiphilic polymer at a water/air interface in next chapters of this thesis.

Chapter 4

A coarse-grained model for poly(ethylene oxide)/water system

4.1 Introduction

Poly(ethylene oxide) (PEO) is among one of the most studied polymers. This interest arises from the fascinating behaviour of this polymer in aqueous solutions, as well as from its adsorption behaviour at different kinds of surfaces, which leads to a wide variety of applications. Alongside experimental studies, it is desirable to obtain a molecular understanding of the solubility and adsorption of PEO using computational models. Reviews of previous experimental and computational studies for PEO in aqueous solutions and at a water-air interfaces have already been given in chapter 1.

The work in this chapter focuses on developing a coarse-grained model for the PEO/water system. The model is also designed to be used with fluorocarbon end-capped PEO model in the next chapter, to help study the adsorption behaviour of this amphiphilic polymer at a water-air interface.

This chapter is organised as follows. Section 4.2 briefly reviews atomistic and coarse-grained models of PEO relevant to this work. Section 4.3 provides computational details of the methods used in deriving and testing a coarse-grained model. The results and discussion consist of five subsections. Section 4.4.1 presents general results obtained from the coarse-graining process. Sections 4.4.2 compares molec-

ular weight dependence of chain dimensions from CG simulations of a single chain PEO in aqueous solutions. Section 4.4.2.1 considers the concentration dependence of radius of gyration for the CG model. The transferability of the model to a water-air interface system is also explored in section 4.4.3. Here, adsorption behaviour, density profile and surface energy are discussed. The approximate speed-up of the CG model compared to the atomistic one is investigated in section 4.4.4, using a water-air interface system as a benchmark. Finally, the work is summarised with conclusions in section 4.5.

4.2 Poly(ethylene oxide)/water models

4.2.1 Atomistic models

There are a vast number of atomistic force fields available for simulating PEO/water systems, each with its own strengths and weakness for particular applications. This section briefly reviews some of models that connect to our work.

Atomistic models for PEO have been introduced over the last two decades, using force fields modified from quantum mechanics calculations of 1,2-dimethoxyethane (DME), the basic constituent of PEO with the structure of H_3C-O-CH_2-CH_2-O-CH_3. In terms of quantity, we should refer to Smith and co-workers who have done a great deal of work in the field. In 1993, they performed *ab initio* calculations [196] on the DME conformations listed in figure 1.6 of chapter 1. The relative energies of these conformations were later used to developed a new atomistic force fields for DME and PEO [197]. Using their force field in molecular dynamics study of DME in gas phase [198] revealed that the *tgg'* and *ttt* conformations are more populated, and *tgt* is less populated than in the liquid phase, in agreement with the IR spectroscopic study [199]. In 1998, further *ab initio* calculations were performed in order to develop force field parameters especially for DME/PEO that interact with water [66]. Testing the model in simulations of aqueous DME [65] showed good agreement of conformational behaviour with Raman spectroscopic study [59] as the DME concentration was varied.

Smith's force fields, however, failed to accurately reproduce the conformational

Table 4.1: Summary of TraPPE-UA modified force field parameters for non-bonded, bonds and angle bending interactions. All parameters for harmonic bonds and angle bending interactions indicated are used as $U_{\text{bond}}(r) = \frac{1}{2}k^{\text{AB}}\left(r - r_0^{\text{AB}}\right)^2$ and $U_{\text{bend}}(\phi) = \frac{1}{2}k^{\text{ABC}}\left(\phi - \phi_0^{\text{ABC}}\right)^2$.

site	ϵ (kJ/mol)	σ (Å)	q (e)
$C(H_3)$	0.81482	3.75	+0.25
$C(H_2)$	0.38247	3.95	+0.25
O	0.45730	2.80	-0.50

bonds	r_0 (Å)	k_{ij} $\left[\text{kJ}/\left(\text{mol}\,\text{Å}^2\right)\right]$
C-C	1.54	2177
C-O	1.41	2679

bends	ϕ_0 (deg)	k_{ij} $\left[\text{kJ}/\left(\text{mol}\,\text{rad}^2\right)\right]$
C-C-O	112	418.2
C-O-C	112	519.6

populations of DME in the liquid-phase as compared to the experimental work of Goutev *et al.* [59], especially for the *tgt* and *tgg'* conformations which were found to be respectively over- and underpopulated in the simulations. Ten year later, as a powerful computers became more widely available, this problem was investigated again by Anderson and Wilson [200], using more accurate basis sets for structure optimisations and energy evaluations. Calculated conformational energy were used to fit new O-C-C-O and C-O-C-C torsional interaction parameters for the OPLS-AA force field [201]. The resulting DMEFF force field shows improvement in conformational populations compared to the optimized potentials for OPLS-AA and Smith force fields. In addition, artificially decreasing the energy of the underpopulated *tgt'* conformation ("engineered" force field) provided results with much better agreement between simulation and experiment in the liquid phase. Using their force fields for simulations of PEO in TIP4P water [67] provided conformational results in agreement with Raman spectroscopic observations [59] for almost all conformations of PEO /water solutions.

A new force field for PEO in aqueous solution has recently proposed by Sadowski and co-workers [194]. In order to improve the performance of former force fields, the dihedral potentials of the TraPPE-united atom force field by Siepmann *et al.* [202] were reparameterised to match *ab initio* data by Anderson and Wilson. The "engineered" force field by Anderson and Wilson showed best performance in describing the equilibrium conformations, but at the cost of extremely high in-

Table 4.2: Summary of TraPPE-UA modified force field parameters for torsions. All parameters are used according to $U_{\mathrm{dih}}\left(\phi^{\mathrm{ABCD}}\right) = \sum_{i=0}^{n} k_i \left[1 + \cos\left(n_i \phi^{\mathrm{ABCD}} - \phi_{0,i}^{\mathrm{ABCD}}\right)\right]$.

Dihedrals	n_i	k_i (kJ/mol)	$\phi_{0,i}$ (deg)
O-C-C-O	0	-7.75967	0
	1	7.58526	0
	2	6.70523	0
	3	8.40071	0
	4	0.63221	0
	5	0.11063	0
	6	0.35962	0
	7	0.01683	0
C-O-C-C	0	-0.25390	0
	1	-5.15997	0
	2	-0.67911	0
	3	5.35013	0
	4	0.80312	0
	5	0.28307	0
	6	0.09526	0
	7	-0.05797	0

terconformational barriers, which reduce its applicability in dynamical simulations. The TraPPE-UA by Siepmann *et al.*, was found to perform best in reproducing thermodynamic properties, but it showed some deficiency in describing the conformer equilibria. Modification of the TraPPE-UA force field was done by refitting dihedral interactions while all other parameters were kept unchange. The dihedral parameters obtained from the fit, together with stretching, bending and nonbonded parameters are given in table 4.1 and 4.2. Many thermodynamic as well as structural properties of aqueous solutions of PEO oligomers were reproduced very well using their modified TraPPE-UA force field together with TIP4P-Ew water [177]. Moreover, this force field also represents both concentration- and temperature-dependent conformer populations better than the original TraPPE-UA force field, the OPLS-DMEFF force field, and the Smith *et al.* force fields. The authors have concluded that this force field in combination with the TIP4P-Ew water model is very suitable for simulations of PEO oligomers in aqueous solution.

4.2.2 Coarse-grained models

Although recent development of computer power allows one to simulate many condensed systems with full atomistic details, it is still impractical to use this technique to study large and slowly relaxing systems, especially in the area of macromolecules such as long chain polymers or large proteins. To overcome limitations of accessible time and length scales, various coarse-grained models for PEO and copolymers with PEO as a component have recently been developed.

This work started in 2004 when Klein *et al.* [93] used a CG model of poly(ethylene oxide)-polyethylethylene (PEO-PEE) diblock copolymer to study self-assembly of this amphiphilic molecule in membrane bilayers. The model was developed by fitting structural properties, e.g. bond and angle distributions and radial distribution functions, to the targets taken from all-atom molecular dynamics simulations. Bulk density and surface tension were also required to match to experimental data. With an explicit solvent, the model was shown to be able to self-assemble into a bilayer, and spherical micelles were also observed when adding more of the hydrophobic PEE fraction. The hydrophobic thickness of the bilayer, which was not used in the parametrization process was found to be in good agreement with experimental findings.

A more elaborate surfactant model containing PEO segments was proposed in 2008 [94] by the same research group. Here the model is designed to reproduce several key properties, including interfacial tension, bulk density, hydration/transfer free energy as well as distribution functions obtained by atomistic simulations. The CG surfactants exhibit spontaneous self-assembly in bulk solution as well as at air–water and oil–water interfaces. The faster relaxation of the CG model enables them to observe complex phenomena occurring on the mesoscale level. For instance, budding and fission of micelles from surfactant monolayers at an air/water interface and a repartitioning of surfactants at an oil/water interface, which are difficult to detect even by experiment.

In 2006, Bedrov *et al.* [203] presented an implicit solvent model of poly(ethylene oxide)-poly(propylene oxide)-poly(ethylene oxide) (PEO-PPO-PEO) triblock copolymer for the purpose of investigating the formation of micelles in aqueous solution.

The model was parameterised using a structural-based coarse-graining approach.

An implicit solvent model for PEO solution has also been proposed by Fisher and co-workers in 2008 [137]. The intra- and intermolecular potentials were derived using an iterative Boltzmann inversion technique, where the target properties were taken from atomistic reference simulations. By comparing structural properties (radius of gyration and end-to-end distances) to atomistic simulations and experiment, the state-specific potential (with explicit dihedral interactions) was found to be transferable both to a wide concentration range and to a large array of chain lengths.

In 2009, Lee *et al.* published their work on developing of a CG PEO model in aqueous solutions [204]. The model was developed within the MARTINI force field (FF) frame work, incorporating the MARTINI single site waters as a solvent model. Interactions between polymer units were optimized on the basis of comparison of densities of low molecular weight PEO to experimental values, whilst interactions between PEO and water were tuned so that chain dimensions of a single PEO chain in water matched atomistic simulation results. Parameters for bonded interactions were obtained by comparing distributions from atomistic simulations. Evaluating the model through simulation of a series of single PEO chains with molecular weight varying from 400 to 7000 in water yields excellent agreement with experimental observations [55,205] and theoretical predictions [123] for the coefficient v in the scaling relation $R_g \propto M_W^v$. The hydrodynamic radia of low to medium M_W chains were also comparable to those measured by experiment [206]. Testing the model by grafting PEO to a hydrophobic surface shows a transition from a mushroom to brush conformation, which is in good agreement with theoretical predictions. This model was recently used to help study induction effects of PEGylated-lipids (PEG conjugated to lipid) on the phase behaviors of liposomes, bicelles, and micelles in aqueous solution [207], with a view towards development of drug carriers in pharmaceutical applications.

From the above reviews of coarse-grained PEO models and copolymers with PEO as a component, it is possible to study these molecules using a cheap implicit solvent models. To study these polymers at a water-air interface, nevertheless re-

quires an explicit solvent model [94]. Anderson and Wilson [67] have shown that using explicit solvent with amphiphilic molecule at water-air interface yields far better agreement between neutron reflectivity data from simulation and experiment compared to a model which neglected water [17]. The models developed by Klein research group [93, 94] performed well in terms imitating self-assembly. However, their CG parameters were optimised under the framework of copolymers or lipid molecules in water, in which the PEO part was not considered separately. The MARTINI CG force field for PEO with explicit solvent model [204] is the one that shows most relevance to our work. Unfortunately, this water model does not support well a water/air interface systems, due to its low surface tension (30 mN/m [90,183]) compared to the experiment value (73 mN/m [208]). As discussed in the previous chapter, the CSJ water [183] provides a better quality model for both bulk water and the water/vapour interface in comparison to the SSRBK [93,179] and MARTINI models [89, 90]. We, therefore, decided to develop a new PEO/water model using CSJ water as a solvent.

4.3 Computations

4.3.1 Atomistic simulations

4.3.1.1 Reference simulation for deriving a coarse-grained potentials

Molecular dynamics simulation of atomistic systems were performed using GROMACS 4.0.7 package [109]. The modified TraPPE-UA force field [194] and TIP4P-Ew water [177] were used with the same MD setting options as described in section 3.3.1.1 of chapter 3. The reference system used in the coarse-grainning process was constructed as follows. A chain, of structure CH_3-(O-CH_2-CH_2)$_9$ -O-CH_3 (PEO10) was constructed and subjected to stochastic dynamics simulation in order to allow an initially linear chain to collapse into a more realistic random coil arrangement. The aqueous simulation was set by placing 16 relaxed PEO10 chains into the 50.0 Å/side box of 1,600 water molecules. This initial system was subjected to a short *NPT* equilibration run to allow any high energy gaps or overlaps between water

and PEO atoms to relax into more energetically favourable positions and to allow the density of the system to reach equilibrium. This results in the system box size decreasing to 38.9 Å for all dimensions. Reported results were then evaluated from production runs that lasted 50 ns under the *NVT* ensemble.

4.3.1.2 Aqueous solutions of PEO10 to PEO77

A single PEO chain with a chain length of $n = 10$ to 77 (n represents the number of repeat units in the chain) was first simulated by stochastic dynamics simulation in order to obtain a chain with random coil arrangement. Then, systems with 10, 19, and 28-mers were solvated by 2,940 water molecules in a periodic box of size 44.8 Å/side; systems with 37 and 45-mers were solvated by 10,000 water molecules in a box of dimension 67.2 Å/side; and systems with 68 and 77-mers were solvated with 13,600 water molecules in a box of dimension 74.5 Å/side. Simulations were performed under *NVT* ensemble conditions for 30 ns, with the final 25 ns used for analysis.

4.3.2 Coarse-grained simulations

In this work, the repeat unit -CH_2-O-CH_2- was grouped into one coarse-grained site, an "EO" site, to preserve structural symmetry with a coarse-graining level compatible to the CSJ water model. As reported from previous works [137, 203, 204] this mapping scheme yields good results for both structural and dynamic properties of PEO in aqueous solution. Simulations of a coarse-grained system were also performed using the GROMACS 4.0.7 program, employing numerical potentials for all types of inter-and intramolecular interactions. Temperature was kept constant at 298 K using a Nose-Hoover thermostat with a relaxation time of 0.2 ps. Equations of motions are integrated applying the Leap-frog algorithm with a time step of 10 fs. The CSJ water developed by Chiu *et al.* [183] was used for all CG simulations in this study. A potential cutoff of 16.0 Å was used for nonbonded interactions. No electrostatics were present for CG simulations.

The CG system used in the iterative Boltzmann inversion process was chosen to mimick the atomistic reference, using 16 chains of PEO10 (10 EO sites per chain)

in a box of 38.9 Å/side and 400 water beads (equivalent to 1,600 water molecules). Simulations were run under const-NVT conditions for at least 10 ns for each IBI iteration.

4.3.2.1 Deriving coarse-grained potentials

The PEO chain was modelled via four types of interactions, including nonbonded, bonds, bends and dihedrals. Nonbonded interactions were also applied for CG beads separated by more than two bonds. It was suggested in previous works [137, 204] that an explicit dihedral interaction would need to be included in the potential set in order to reproduce *gauche*-like conformations observed in atomistic simulations.

The bonded potentials were derived on the basis of matching the distribution functions to those of the atomistic reference. Interactions between EO sites (the most crucial interaction), was derived from the RDF between the centre of mass of the C-O-C units from atomistic simulation using the iterative Boltzmann inversion technique. For EO-W interactions, since each W site in the CSJ model represents four water molecules, comparison between CG and atomistic RDFs cannot be simply made because the EO-W atomistic RDF cannot be represented within the 4:1 CG mapping. To remedy this situation, we chose to match the number integral of the RDF between CG and atomistic models in order to keep approximately the same amount of water in the hydration shell of the polymer units. This is a similar approach to that applied in the coarse-graining of a phospholipid bilayer model by Klein and co-workers [179].

A set of CG potentials was obtained by successively adjusting the different potential contributions in the order of their relative strengths: $U_{stretch} \rightarrow U_{bend} \rightarrow U_{nonbonded} \rightarrow U_{dihedral}$. Choosing this order seems to be the most efficient way of obtaining CG potentials with the IBI technique, since it has already been shown from the previous works that the intramolecular degree of freedoms can be treated almost independently from intermolecular ones [135].

4.3.2.2 Aqueous solutions of PEO10 to PEO159

A fully extended PEO chain with a chain length of n = 10 to 159 (n represents directly the number of EO sites in the chain) was first equilibrated using a Langevin thermostat simulation to obtain a chain with a random coil arrangement. For systems of n = 10 to 77, the number of water beads and the box size correspond to those used in atomistic simulations of section 4.3.1.2 (note that one CG water bead is equivalent to 4 atomistic water molecules). For systems of n = 91 to 159, the chain was placed into a box of dimension 125.4 Å/side and solvated by 16,400 water beads. CG simulations were performed under the NVT ensemble with 100 ns equilibration and a further 400 ns for data analysis.

4.3.2.3 Concentration dependence of radius of gyration

CG simulations of PEO at three different concentrations were established by placing 8, 40 and 72 chains of PEO77 into a box of 134.3, 136.8 and 139.2 Å/side, leading to the polymer concentration of 18.6, 88.0 and 150.4 mg cm^{-3}, respectively. The R_g of 15.0 Å was used as an initial configuration for PEO77. Each box was then solvated by ∼20,000 water beads. Simulations were conducted under the NVT ensemble with 200 ns equilibration period and a further 500 ns production run.

4.3.2.4 PEO77 at a water-air interface

Twelve surface concentrations in polymer were established by placing PEO77 chains in a box of dimension $x = y$ = 91.0 Å and z = 150.0 Å, followed by solvation with water beads. The number of PEO77 molecules, water beads and the equivalent surface concentration for each system are given in table 4.3. To set up the water/air interface, the z axis for each system was increased to 450.0 Å (z is the axis perpendicular to the surface plane). This creates two interfaces in the simulation box (due to periodic boundaries) with sufficient distance between them to prevent interactions between them. It should be noted here that PEO chains were placed into the box at a positions close to only one side of the water slab. This forced all PEO chains go to the same surface when they reached equilibrium and is convenient for comparisons of results among the systems. All systems were first subjected to a

Table 4.3: Number of PEO77 molecules, water beads and the equivalent surface concentration for the twelve CG simulations at a water-air interfaces.

PEO77 molecules	Water beads	*Surface concentration, Γ (mg m^{-2})
1	5,000	0.07
3	5,000	0.20
5	5,000	0.34
8	5,000	0.54
9	5,000	0.61
10	5,000	0.68
11	9,093	0.75
12	9,093	0.82
13	9,093	0.88
14	9,093	0.95
15	9,093	1.02
16	9,093	1.09

*It is important to note that the surface concentration is calculated on the assumption that all polymer stays at the interface. Experimental reports use the same assumption, though this is not true for a concentration higher than saturated monolayer.

short equilibration run to allow a equilibrated water/vapour interface to form. Once the water/air interface was set up, each system was then subjected to another equilibration run to make sure that it has reached an equilibrium state (chains remain steady at the water surface). Then, an additional 500 ns was carried out for data analysis. All calculations were performed under *NVT* ensemble at 298 K.

4.4 Results and discussion

4.4.1 Deriving a coarse-grained potentials

Figure 4.1 shows an excellent matches of the bond-, angle- and dihedral angle distributions, which took only a few steps of iteration to converge. For the nonbonded interactions, it was difficult to perfectly match both the RDF_{EO-EO} and the number integral of the RDF_{EO-W} to their targets at the same time. This is because the two nonbonded potentials can have an effect on the structure of each other. For example, changing the EO-W potential imposed dramatically changes in the RDF_{EO-EO}. The best solution for this task is to allow the RDF_{EO-EO} to deviate slightly from

the target in order to maintain the good fit for both of them.

Figure 4.2 compares the atomistic and the final coarse-grained RDFs for the EO-EO and EO-W sites. For the RDF_{EO-EO}, the match is very good with only a small discrepancy at the distance around 8 to 10 Å, which is not really important to the structure. For the EO-W case, the RDF was distorted from the atomistic one (EO-Oxygen(H_2O)) because the first peak cannot be matched to a four site model (as discussed in section 4.3.2.1). The first peak is shifted to distance about 4.3 Å, which exactly corresponds to the second hydration radius of EO in the atomistic model. The number integral for EO-W pairs in the atomistic and CG simulation are also plotted in figure 4.2. The plot clearly guarantees that we have obtained approximately the same level of hydration of the EO site in the CG and atomistic simulation.

We should mention that the structural optimisation discussed above has been run at constant volume and without long-range correction for the nonbonded interactions. This causes a large deviation between the pressure of the CG simulation ($p \approx 850$ bar) and the underlying atomistic system ($p \approx$ -180 bar). Fortunately, with the IBI method, one could correct the pressure of the CG system by introducing an attractive linear tail function to the previous optimized nonbonded potential (described in section 2.2.3.1 of chapter 2), and of course, without lowering the quality of the previous fitted RDFs. In this work, an attractive function was applied simultaneously for both the EO-EO and EO-W potentials in order to avoid perturbing the fit of one potential by dramatically altering the other potential. Using this technique, the CG pressure was successfully reduced to ≈ -170 bar. This represents well the state of the parent atomistic system and also implies transferability of the CG potentials to constant-pressure simulations. The nonbonded potentials obtained from the final correction are shown in figure 4.3.

4.4.2 Molecular weight dependence of chain dimension

Chain dimensions in terms of radius of gyration R_g and end-to-end distances $<h^2>^{1/2}$ are listed in table 4.4. Results from the MARTINI model and atomistic simulations are also included. The overall R_g and $<h^2>^{1/2}$ are in good agreement with the

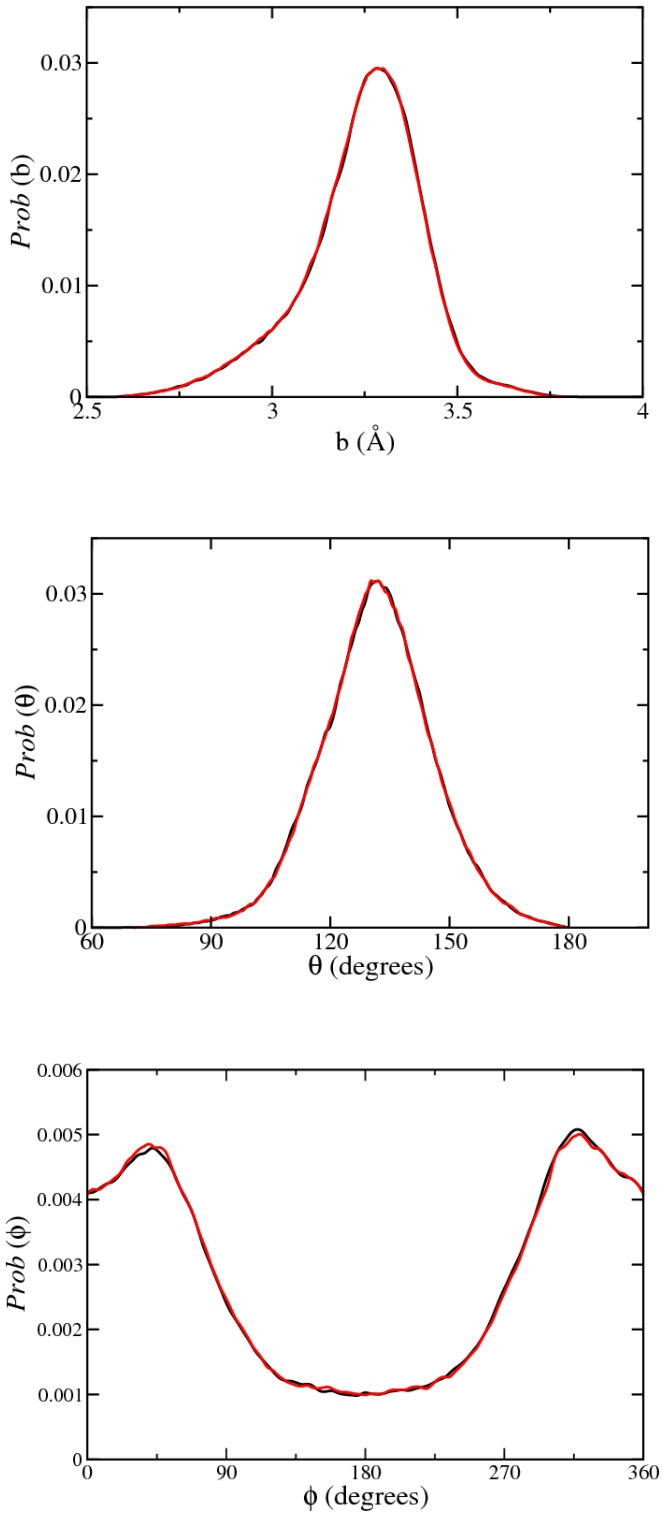

Figure 4.1: Probability distributions of bond lengths (top), bond angles (middle), and dihedral angles (bottom) of PEO10 from atomistic simulation (black) and coarse-grained simulation at the final Boltzmann iteration step (red).

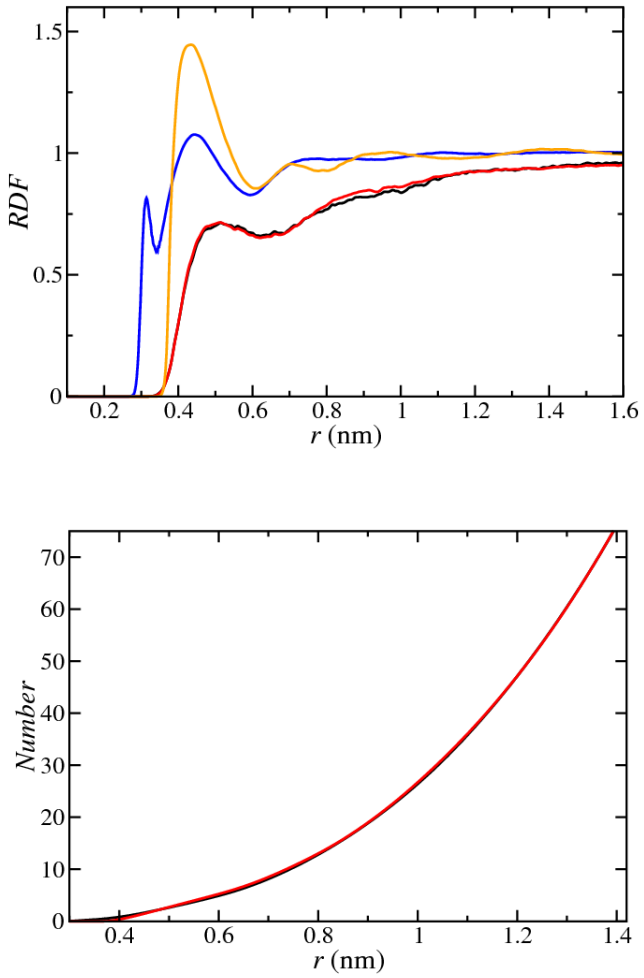

Figure 4.2: Top: radial distribution functions for the EO-EO sites, atomistic (black) and CG (red) and the EO-W sites, atomistic (blue) and CG (orange). Bottom: number integrals of RDF_{EO-W}, atomistic (black) and CG (red).

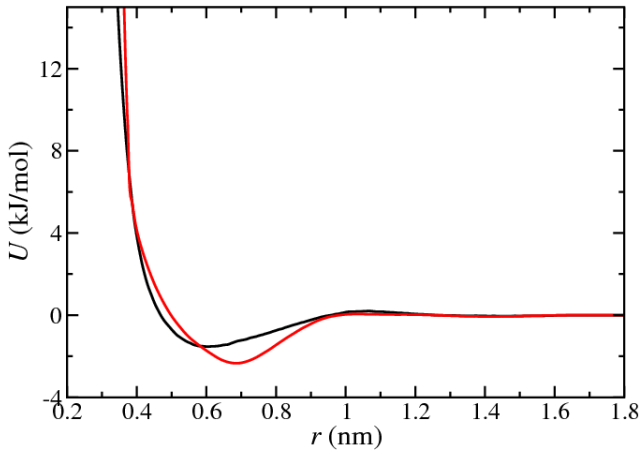

Figure 4.3: Nonbonded potentials between EO-EO sites (black) and EO-W sites (red) obtained from the final Boltzmann iteration with pressure correction.

MARTINI and atomistic model except for $M_W > 3438$ where our model yields slightly higher end-to-end distances than the MARTINI model. The calculated R_g for PEO77 is 19.3 Å, in excellent agreement with the value of 19.7 Å obtained from neutron scattering of poly(ethylene glycol) (PEG) of equivalent molecular weight at low concentration [209].

The molecular weight dependence of R_g according to a power law relation $R_g \propto M_W^v$ has been worked out. Least square fits from the plots of log R_g against log M_W in figure 4.4 give a slope, $v = 0.567$ for $1632 < M_W < 7007$. This result is in excellent agreement both with the theoretical prediction for a real chain of 0.588 [123] and a light scattering measurements of high molecular weight PEO by Devanand *et al.* ($v = 0.583 \pm 0.031$) [55] and Kawaguchi *et al.* ($v = 0.550$) [210]. In addition, the MARTINI model obtained $v = 0.57 \pm 0.02$ from the fit using the same range of molecular weight.

4.4.2.1 Concentration dependence of radius of gyration

Decreasing of R_g with increasing polymer concentration has been reported by small angle neutron scattering (SANS) measurements [209, 211]. SANS measurements on PEG77 (equivalent to PEO77) revealed a drastic decrease in the R_g from 19.7 Å at 30 mg cm^{-3} to 8.0 Å at 160 mg cm^{-3} [209]. Changes in the three-dimensional structure and repulsive intermolecular interactions (excluded volume effects) at high concentration are possible explanations for this. However, there is no evidence of a reduction of R_g at higher concentration as studied by atomistic [137, 204] and the CG simulations [204].

Figure 4.5 plots the average R_g as a function of simulation time for PEO77 at three concentrations. From the plots, there is no significant difference of time taken by these systems to relax the structures. For all systems, the R_g reached equilibrium values within 10 ns, which is very fast compared to the relaxation time of 70 ns for a single atomistic chain of PEO30 in aqueous solution [137]. The R_g as averaged over all chains for the concentration of 18.6, 88.0 and 150.4 mg cm^{-3} is 19.4 ± 0.2, 19.2 ± 0.1 and 19.1 ± 0.2 Å, respectively. Thus, this clearly indicates that R_g is not dependent on polymer concentration as studied using our model. It is still unclear

Table 4.4: Radius of gyration R_g and mean-squared end-to-end distance $<h^2>^{1/2}$ for coarse-grained PEO of length n. The results from the CG MARTINI model were taken from Ref [204].

n (M_W)	R_g (Å)			$<h^2>^{1/2}$ (Å)		
	CG	CG MARTINI	atomistic	CG	CG MARTINI	atomistic
10 (443)	6.0 ± 0.1	6.3 ± 0.1	6.3 ± 0.1	14.5 ± 0.5	15.7 ± 0.1	15.8 ± 0.6
19 (839)	8.8 ± 0.2	9.1 ± 0.1	9.4 ± 0.1	21.4 ± 0.7	22.6 ± 0.3	24.4 ± 0.7
28 (1236)	10.9 ± 0.2	11.1 ± 0.1	10.3 ± 0.2	26.8 ± 0.9	27.2 ± 0.6	24.6 ± 1.0
37 (1632)	12.8 ± 0.2	12.7 ± 0.2	12.3 ± 0.2	31.9 ± 1.1	30.9 ± 0.8	29.0 ± 1.1
45 (1984)	14.4 ± 0.3	14.5 ± 0.2	13.2 ± 0.2	36.0 ± 1.3	36.6 ± 0.8	32.9 ± 0.8
68 (2998)	18.2 ± 0.4	17.9 ± 1.6	17.9 ± 0.3	45.2 ± 1.6	43.6 ± 3.3	46.2 ± 1.7
77 (3438)	19.3 ± 0.4	19.1 ± 0.7	19.7 ± 0.2	47.5 ± 1.7	46.1 ± 1.5	48.0 ± 1.2
91 (4011)	21.5 ± 0.4	19.9 ± 0.4		53.7 ± 1.8	46.3 ± 1.5	
113 (4980)	24.0 ± 0.5	25.2 ± 0.5		59.2 ± 2.1	56.3 ± 1.1	
136 (5993)	26.5 ± 0.5	25.6 ± 0.7		65.4 ± 2.4	54.2 ± 2.4	
159 (7007)	29.7 ± 0.6	29.8 ± 0.5		72.5 ± 2.4	61.1 ± 4.5	

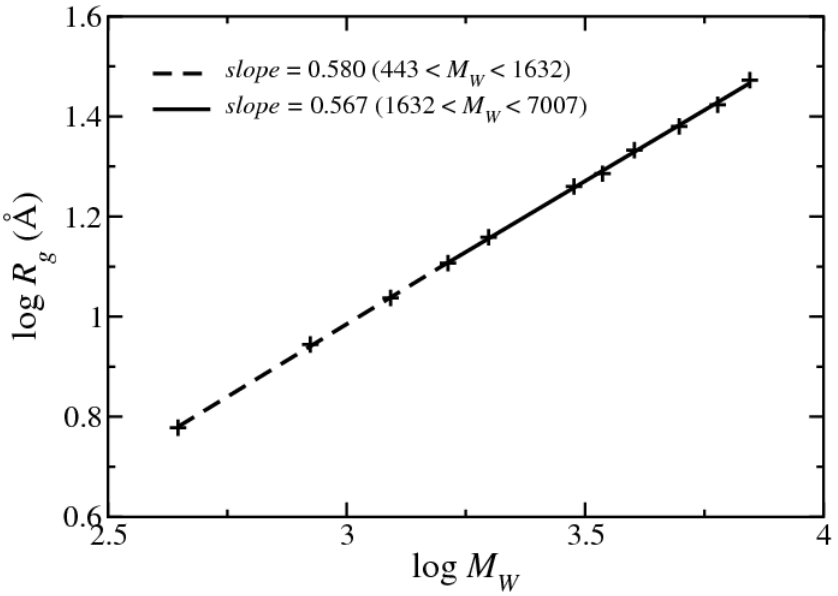

Figure 4.4: log R_g versus log M_W from simulations of PEO10 to PEO159.

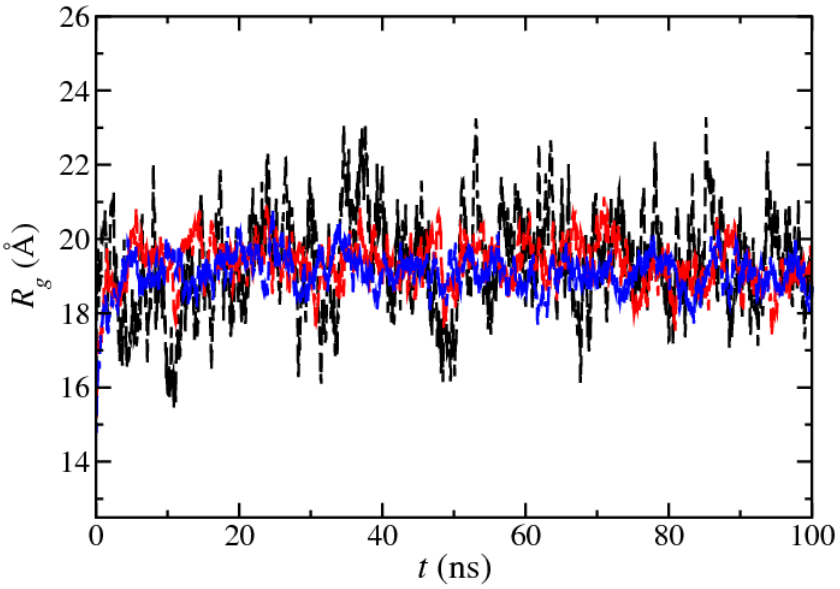

Figure 4.5: Time series of the radius of gyration R_g for PEO77 at concentration of 18.6 mg cm^{-3} (black), 88.0 mg cm^{-3} (red) and 150.4 mg cm^{-3} (blue).

whether there is a disagreement with results obtained from SANS and simulation studies. As noted by Lee *et al.* [204], decreasing of R_g at high concentration might arise from interchain scattering of an entangled polymer. The supporting reason for this is that SANS spectra are sensitive to an isolated coil, which can provide a reliable value of R_g only in a very dilute solutions [209, 212].

4.4.3 PEO77 at a water-air interfaces

4.4.3.1 General observations

As outlined in section 1.4.2 of chapter 1, one interesting behaviour of PEO is that it can form stable spread films at an air-water interface under certain circumstances [73–75]. A drop of surface tension when polymer concentration is increased was observed by many experiments [75–78, 213]. It was also found that at higher surface concentrations polymer segments extend into the water subphase as loops and tails. This extension increases as a surface concentration increases [74]. From the simulation point of view, it is worth examining transferability of our coarse-grained model in terms of capturing adsorption activities discussed above. To study this, CG simulations of PEO at a water-air interface have been carried out.

Figure 4.6 shows the final configuration from the simulation of 12 chains of

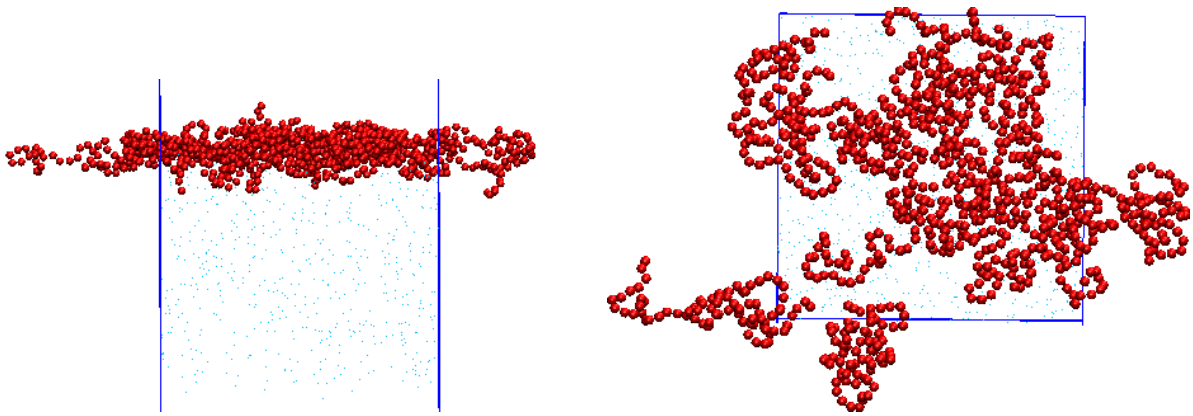

Figure 4.6: Side view and top view of the final stucture obtained from the simulation of 12 molecules of PEO77 at a water-air interface.

PEO77 (Γ = 0.82 mg m^{-2}) at the water-air interface. This concentration is close to the saturation of surface excess of high molecular weight PEO at water-air interface, as reported from previous works [73,213,214]. The surface excess at saturation concentration will be discussed more in the next section. Figure 4.6 clearly shows that PEO chains can form a layer at the water surface with some polymer segments penetrating into the water subphase by forming tail and loop conformations. Observing trajectory movies through the course of the simulation showed that polymer chains move from the bulk liquid phase to the interface region and started aligning themselves onto the surface plane. A polymer layer was then formed and persisted until the end of the simulation.

4.4.3.2 Density profiles

Figure 4.7 plots mass density profiles of PEO normal to the surface for twelve surface concentrations. On the basis of the density profiles in the plot, several characteristics can be distinguished as described below.

At low polymer concentrations (0.07-0.34 mg m^{-2}), almost all the polymer segments locate beneath the liquid surface with only a small fraction of the polymer penetrating into the vapour phase (see also figure 4.8 (a)). This finding is in agreement with recent atomistic simulation of PEO50 at a free water surface ($\Gamma \approx$ 0.4 mg m^{-2}) by Darvas *et al.* [215]. From their work, about 1% of the monomer units

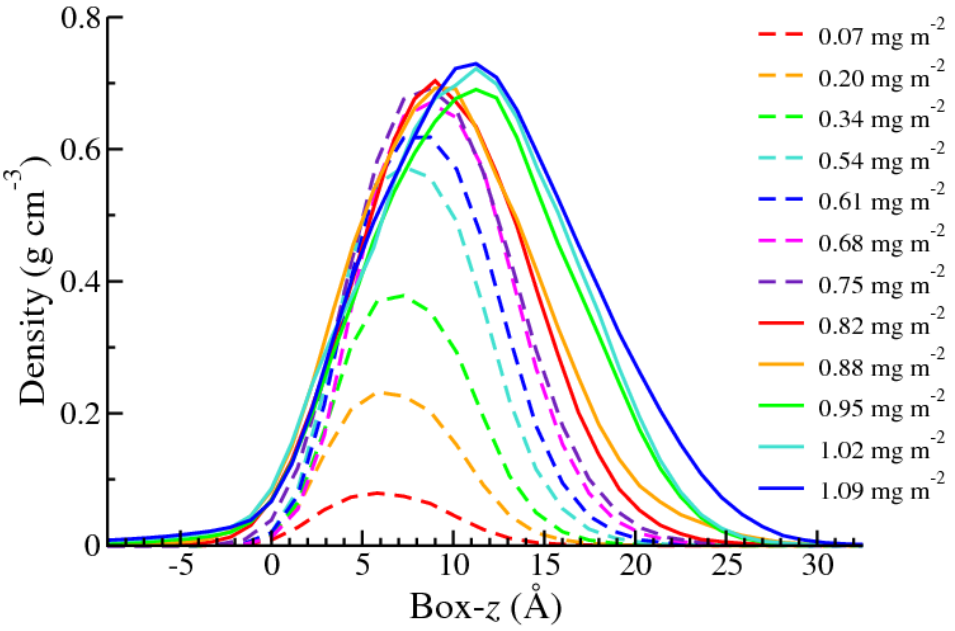

Figure 4.7: Density profiles of PEO from the simulations of twelve systems with the surface concentration ranging from 0.07 to 1.09 mg m^{-2}. Polymer layer is formed at the interface region and the left-hand side (-z) and right-hand side (+z) approximately represent air- and bulk water phase, respectively.

were found to be penetrated into the vapour phase.

The surface region gets more occupied by PEO segments as the concentration of polymer is increased. Forming of a PEO layer at the interface is energetically favorable, resulting in water being excluded from the interface and pushed down into the subphase region. Figure 4.8 (b) shows the final configuration obtained from simulation of the system of 10 PEO77 molecules ($\Gamma = 0.68$ mg m^{-2}). It shows lesser amount of water have penetrated into the polymer layer compared to the lower concentration system in figure 4.8 (a).

Adsorption of PEO at the surface continues to increases with increasing polymer concentration until a surface concentrations of 0.75 mg m^{-2}. Above 0.75 mg m^{-2}, the amplitudes of the density profiles at the surface are essentially unchanged, but do show an extension of PEO segments into the subphase. This is due to surface saturation at these high concentrations, where there is no more space for more molecules to pack themselves at the surface.

When polymer concentration is increased higher than 0.82 mg m^{-2}, the surface profile appears to collapse and extend more into the water subphase. This indicates

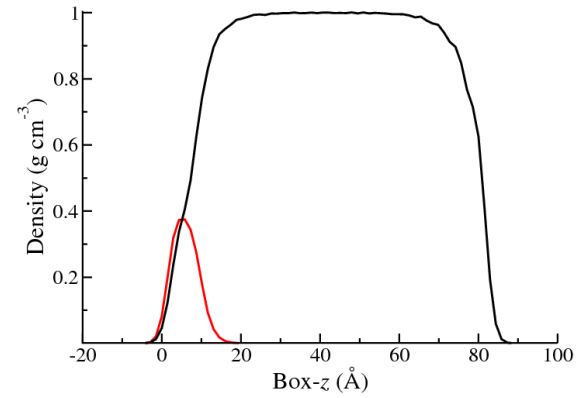

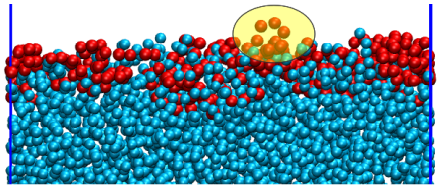

(a) 5 chains (0.34 mg m^{-2})

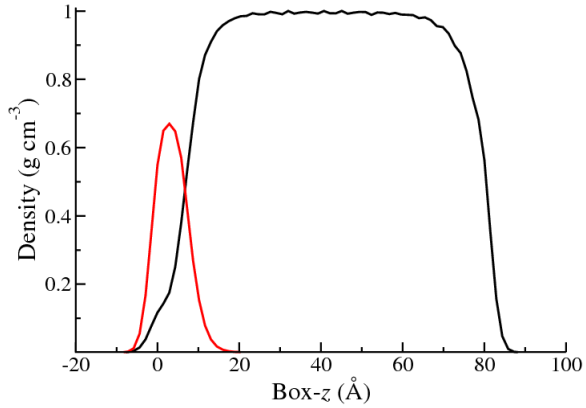

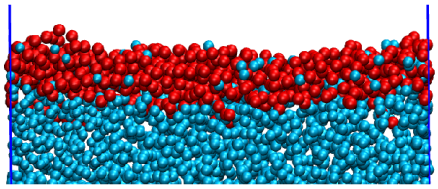

(b) 10 chains (0.68 mg m^{-2})

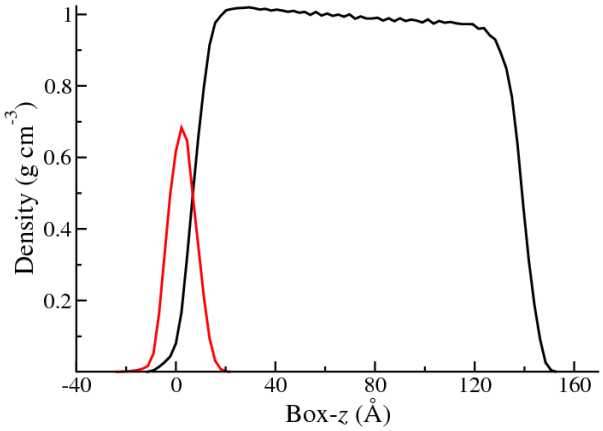

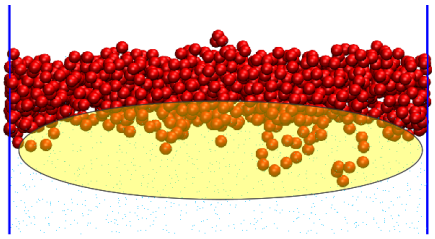

(c) 14 chains (0.95 mg m^{-2})

Figure 4.8: Density profiles and typical pictures obtained from simulations of (a) 5 chains (0.34 mg m^{-2}), (b) 10 chains (0.68 mg m^{-2}) and (c) 14 chains (0.95 mg m^{-2}) at a water-air interface. The highlight in (a) shows small PEO units penetrate into the vapour phase and in (c) shows extension of PEO segments in to the water subphase as loops and tails conformations.

that the aqueous subphase can no longer accommodate more PEO segments at the surface and the excess of PEO above the amount required to form a monolayer is extended into a water subphase. Increasing to further higher concentration results in even more extension of polymer into liquid subphase.

The "collapse" and "extension" of PEO monolayers has been previously proposed in experiments [74, 79, 214, 216, 217]. From neutron reflectometry of high molecular weight PEO by Henderson *et al.* [74], the saturation of the monolayer was attained at surface concentrations of approximately 0.5 mg m^{-2}. Increasing surface concentration above 0.5 mg m^{-2} did not change the number density of PEO segments in the topmost layer, but resulted in increasing extension of the lower polymer layer into the liquid subphase probably as loop and tail conformations. Kuzmenka and Granick [79, 214, 217] noted that at low surface concentration there was a loss of entropy due to confinement of the molecules to two dimensions. At higher surface coverages there was a gain in entropy as the monolayer "collapsed" to a three-dimensional structure (buckling and looping into the water substrate). Kawaguchig *et al.* [218], and Rennie *et al.* [73] have also mentioned the loops and tails conformations for a high surface concentration regime. Unfortunately, there are no direct experimental methods to prove occurring of these conformational structures. To investigate this with our model, final snapshot of the system of 14 molecules ($\Gamma = 0.95$ mg m^{-2}) in which the density profile has already shown to be collapsed from the saturation point, was taken and depicted in figure 4.8 (c). Satisfactorily, extension of PEO segments in to the water subphase as loops and tails conformations was captured in our simulations.

The layer thickness of the PEO monolayer is also interesting to consider and this has been previously reported by experiments. By analyzing neutron reflectivity data, Henderson *et al.* [74] reported the monolayer thickness of 16 $\pm$ 2 Å, 19 $\pm$ 2 Å and 22 $\pm$ 2 Å for the surface concentration of 0.5 mg m^{-2}, 0.6 mg m^{-2} and 0.8 mg m^{-2}, respectively, whilst a thickness of 23 $\pm$ 2 Å for the concentration of 0.6 $\pm$ 0.1 mg m^{-2} was reported by Lu *et al.* [75]. Both studies found nearly the same equilibrium surface excess (0.5 mg m^{-2} for Ref [74] and 0.53 $\pm$ 0.05 mg m^{-2} for Ref [75]). Based on the density profiles in figure 4.7, the layer thickness of the PEO

monolayer is estimated to be 18 Å , 19 Å and 24 Å respectively for the concentration of 0.54 mg m^{-2}, 0.61 mg m^{-2} and 0.82 mg m^{-2}. Therefore, the thicknesses observed in simulations are in agreement with results from neutron reflectometry for the same surface concentration range. It should be noted that the equilibrium surface excess has shown to be around 0.75 mg m^{-2} in the simulations, which is slightly higher than those observed in both experiments mentioned above. However, there are experimental studies that found the saturation of surface excess in the same range as obtained in our simulations. These experiments are related to the surface pressure isotherm measurement which will be discussed later in the next section.

4.4.3.3 Surface tension and surface pressure isotherm

As discussed in the previous section, the excess of PEO above the amount required to form a monolayer is extended into the water subphase. These excess molecules were supposed to not contribute (or ineffectively contribute) to the reduction in the surface tension of the system [76–78]. In other words, the surface pressure of the system should be constant after saturation of the monolayer. The concentration where the surface pressure approaches equilibrium is refered to as "the saturation of surface excess".

According to the density profiles in figure 4.7, the PEO monolayer is shown to be saturated at concentration of approximately 0.75 mg m^{-2}. Theoretically, the surface pressure should reach an equilibrium value at this concentration. To investigate this, the surface tension and surface pressure isotherm has been calculated from our simulations. The conventional surface pressure is defined as

$$\pi = \gamma_0 - \gamma, \tag{4.1}$$

where γ is the surface tension of the monolayer system and γ_0 is that of pure water; $\gamma_0 = 70.9$ mN m^{-1} is obtained in our simulation of the CSJ model at 298 K. Since we have put PEO only on one side of the water surface, the other side is assumed to has a surface tension equal to that of pure CSJ water. This factor has been taken into account in calculations of the surface pressure reported in this work.

Figure 4.9 plots surface tension together with surface pressure as a function

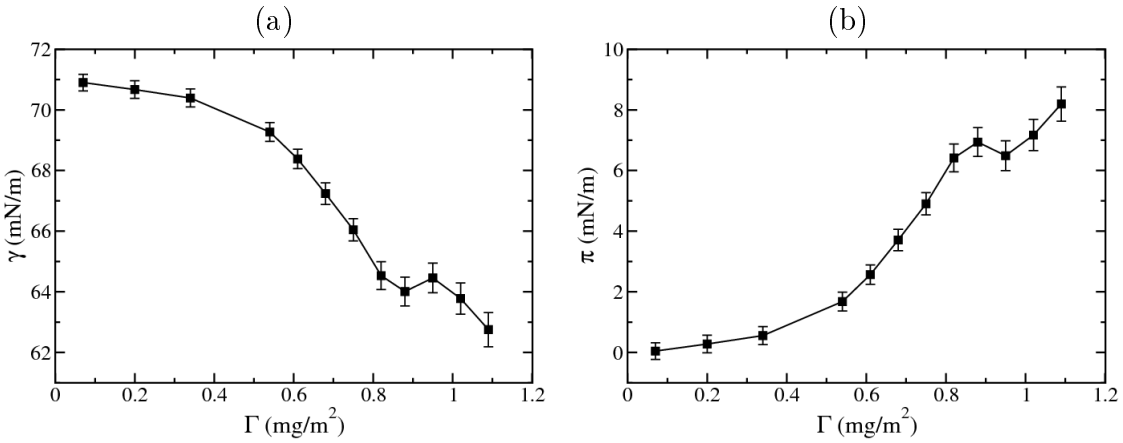

Figure 4.9: Surface tension (a) and surface pressure (b) against the surface concentration of PEO77. Error bars on points in the plots signify 95% confidence intervals.

of surface concentration. From the plot, in the low concentration regime (0.07-0.34 mg m^{-2}), the surface tension is slightly decreased with increasing polymer concentration, followed by a nearly linear decreasing of the surface tension in the concentration range 0.54 mg m^{-2} $< \Gamma <$ 0.82 mg m^{-2}. This is the same as surface activity of PEO that has been observed in experiments [75, 77, 78, 213, 219].

The interesting finding is in the high concentration regime, the surface pressure reaches a plateau at $\Gamma \approx 0.82$ mg m^{-2} with a value of approximately 6.5 mN/m. Then it seems to be steady (within standard error of calculation) for the next three concentration points. Thus, based on the surface tension calculations, saturation of the surface excess is observed at about 0.82 mg m^{-2}. This surface excess is close to that suggested by the density profile result. Therefore, we deduced from the simulations that the saturation of surface excess is attained between 0.75 and 0.82 mg m^{-2}.

In experimental studies, neutron reflection and surface tension measurements by Henderson *et al.* [74] and Lu *et al.* [75] revealed that the surface excess at saturation concentration was between 0.5 and 0.6 mg m^{-2}. The results of Sauer and Yu [220] and Rennie *et al.* [73] showed that at 298 K equilibrium surface pressure is reached when the surface excess is between 0.65 and 0.7 mg m^{-2}. The further higher surface excess, $\Gamma \approx 0.8$ mg m^{-2}, was reported by Kuzmenka and Granick [79,214] and Gilányi *et al.* [213]. The different results listed above are outside the experimental error, and could be attributed to the differences of molecular weight and polydispersity used

in their studies, which lead to the different of the surface excess at the interface (noted that all the experimental results mentioned here were measured at room temperature).

It can be noted from the plot in figure 4.9 that there is a further decrease of surface tension when $\Gamma > 1.02$ mg m^{-2} instead of remaining constant. Additional reduction of surface tension at a concentration above the saturation point has also been reported by Cao and Kim [76–78]. This reduction was found to strongly depend on PEO molecular weight and occurred at the concentration regime that are much higher than those observed in our simulations. The further reduction of surface tension observed here is likely due to a deficiency of the model that is not specifically optimised for the water/air interface and, of course, surface energy of the system.

4.4.4 Speed-up of the coarse-grained model

The speed-up of the CG model was tested by measuring the time required by the system to equilibrate polymer structure at a water surface. The starting configuration for the atomistic model was obtained by randomly placing 10 relaxed chains of PEO77 into a slab of 20,000 water molecules. The box of dimensions $x = y =$ 86.5 Å and $z = 286.5$ Å (z is the axis perpendicular to the surface plane) was used. The CG structure was extracted from the atomistic coordinates to ensure that the same starting configuration was used. However, the number of waters was reduced to 5,000 beads to make it correspond to the number of waters in the atomistic system. Simulations were performed on the same conditions, e.g. running parallel on 32 calculation nodes.

Figure 4.10 shows the starting and ending configurations for the atomistic and CG models. It took more than 50 ns for all atomistic PEO chains to move slowly from the liquid phase to the interface regions and form a stable layer there. This phenomenon happened very quickly for the CG system, where all the chains reach the surface within 5 ns.

Figure 4.11 compares the variation in z-component of the radius of gyrations ($R_{g,z}$) for atomistic and CG systems. At the start of the simulation, PEO chains in the liquid phase can freely move along the z-dimension toward the interfaces,

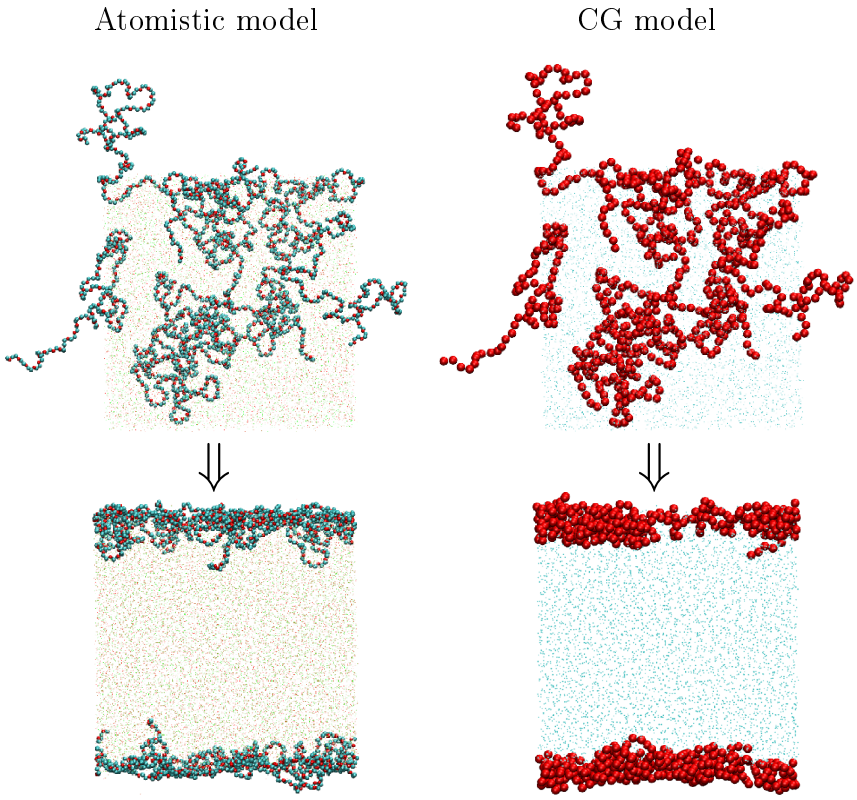

Figure 4.10: Side views for the starting (top) and ending (bottom) configurations from atomistic and CG simulations of 10 chains of PEO77 at a water-air interfaces.

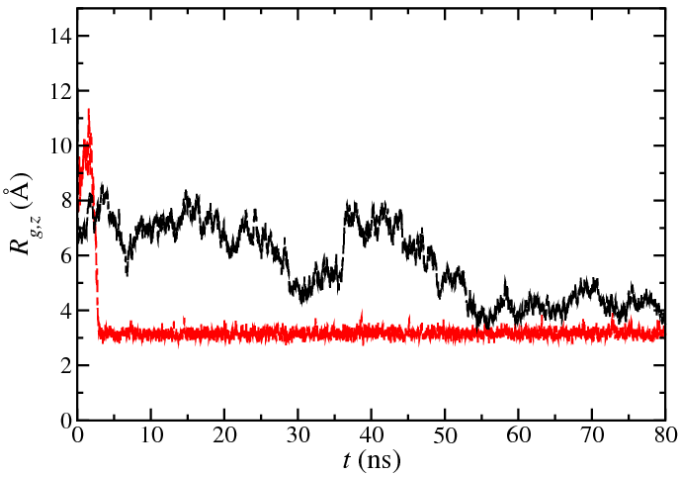

Figure 4.11: Time series of radius of gyration in z-direction ($R_{g,z}$) for PEO chains in atomistic (black) and CG (red) simulations at water-air interfaces.

resulting in a large fluctuation of $R_{g,z}$ at this point. After the system has reached equilibrium, the $R_{g,z}$ value should remain steady since molecules are confined in two dimensions (x-y) layer at the interfaces. Thus, following the variation in $R_{g,z}$ with time seems to be a suitable choice to detect the equilibration time taken by both systems. As shown in figure 4.11 the average $R_{g,z}$ has reached equilibrium at simulation times of $\approx$ 55 ns and $\approx$ 4 ns for atomistic and CG chains, respectively. Thus, the CG model can relax approximately 14 times faster than the atomistic model in terms of raw speed. However, it should also be pointed out that we spent 116.71 hour in real time to gain 55 ns in atomistic simulation, whilst it took only 0.122 hour to obtain 4 ns in CG simulation. Therefore, for the medium-size system in this study, the CG model provides roughly a 1,042x speed-up for equilibration.

It is very promising to use the current model to help study the behaviour of amphiphilic PEO molecules for high surface concentrations, where is not feasible to use atomistic models since they cannot relax a highly crowded configuration within the simulation time available [67]. Furthermore, one can combine CG simulations with the back-mapping technique (reinsertion of atomistic details into a CG structure) [120, 133] to obtain a well-equilibrated atomistic structures, which could be used as a starting point for further production runs.

4.5 Conclusions

A coarse-grained model for polyethylene oxide (PEO)/water system has been developed using a structural-based coarse-graining technique. Radial distribution functions and distributions of bond, angle, dihedrals are matched excellently to those from reference atomistic simulations. Simulations of PEO10 to PEO159 ($442 < M_W < 6998$) in aqueous solution showed successful reproduction of the theoretical and experimental scaling laws for the radius of gyration R_g. The simulated R_g for PEO77 (Mw $\approx$ 3400) is in excellent agreement with neutron scattering measurements for an equal sized PEG. Simulations of multiple PEO77 chains at a concentration ranging from low to high show no concentration dependence of R_g, in agreement with previous atomistic and coarse-grained simulations, but contradicts experimental ob-

servations where the measured R_g was found to decrease as concentration increases.

The transferability of the model to a water-air interface system has been explored through a series of simulations with surface concentration ranging from the low to high regime. PEO chains are found to form a layer at the water-air interface and the adsorption increases with increasing surface concentration. At higher surface concentrations polymer segments extend into the water subphase as loop and tail conformations and this extension increases as the surface concentration increases. This is in accordance with an experimental study, concluding that the excess of PEO above the amount required to form a monolayer is collapsed and extended into the water subphase. Other properties such as the saturation adsorption and the thickness of PEO layers obtained from CG simulations are in good agreement with experimental findings. Although the CG potential was not particularly optimized for interface systems and the surface energy itself, a drop of surface tension was shown to follow the same general trends as observed in experiments.

The present model is noted to provide a very efficient means of speeding up the path through phase space to equilibrium. We expect that it can be used to help study surface behaviour of systems composed of long PEO chains functionalized by strongly hydrophobic head groups, which will be discussed in the next chapter.

Chapter 5

A coarse-grained models for dendritic fluorocarbon end-capped poly(ethylene oxide) at a water/air interface

5.1 Introduction

After completing the development of a PEO/water model in the previous chapter, we turn our attention to coarse-graining of dendritic fluorocarbon end-capped poly(ethylene oxide) polymer. As mentioned in chapter 1, the main aim of this thesis is to develop a model of this polymer that can be used to help explain and predict adsorption behaviour at the water-air interface, which has been studied recently by neutron reflectivity techniques [85]. In this chapter, we focus on models of di- and trifluoro dendritic end-capped poly(ethylene oxide) at an air-water interface. The molecular structures of these molecules are depicted in figure 5.1 (a) (hereafter referred to as F2) and figure 5.1 (b) (hereafter referred to as F3). These polymers are directly analogous to those synthesized and analysed experimentally by Dr. Simon Bartram [85], a previous member of the soft matter research group in Durham.

The first part of this chapter describes simulation details used in this work. A brief summary of atomistic force-fields currently available for simulation of fluorocar-

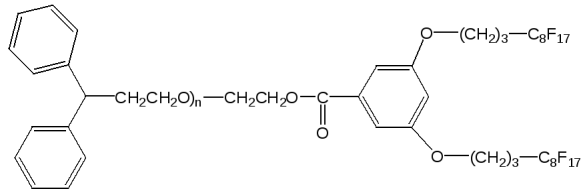

(a) Difluoro dendritic end-capped PEO (F2)

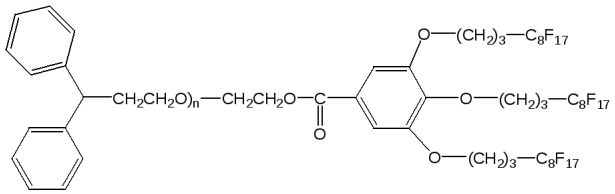

(b) Trifluoro dendritic end-capped PEO (F3)

Figure 5.1: Structures of dendritic fluorocarbon end-capped poly(ethylene oxide) used in previous neutron reflectometry studies [85].

bon systems are given in section 5.2.1, followed by details of the atomistic reference simulations used for deriving coarse-grained potentials in section 5.2.2. Afterwards, we describe in detail how the coarse-grained models were derived in section 5.2.3.

The second part of this chapter presents results obtained from the coarse-graining process along with discussion of these results. Comparisons of structural probability distributions and density profiles between the coarse-grained models and their atomistic counterparts are given in section 5.3.1-5.3.2 and in section 5.3.3, respectively. Finally, the work of this chapter is concluded in section 6.4.

5.2 Simulation details

5.2.1 Atomistic force-fields

Fluorocarbon systems have been less studied by simulation in comparison to their hydrocarbon counterparts. This is mainly because of a lack of accurate force fields in the past, which are capable of describing the complex conformational nature of these systems [221]. Like many other organic systems, the properties of fluorocarbons are vitally controlled by their chemical structure and intermolecular interactions [222].

For reliable simulations of these systems it is therefore necessary to have a force field that accurately describes intermolecular interactions as well as the detailed chemical structure of the molecule.

Currently, there are two reliable *ab inito*-based force fields that have been proposed for perfluorinated alkane polymers: the Optimized Parameter for Liquid Simulation-All Atom (OPLS- AA) force field of Jorgensen *et al.* [201, 223, 224] and the force field of Borodin *et al.* (an exp-6 force field) [225, 226].

A modified form of the OPLS-AA force field, which includes specific dihedral terms for H–F blocks [227] and corrections to the H–F nonbonded interaction [228], and a new version of the exp-6 force field [229] have been shown to provide good agreement with the available experimental liquid density and surface tension data for semifluorinated alkane diblock copolymers [229]. Both force fields were also found to be transferable over significant temperature ranges and for a variety of chain lengths and compositions.

Comparisons have been made on simulations of perfluorinated alkane systems at the liquid-vapour interface using OPLS-AA and exp-6 force fields [221]. Both force fields provided similar liquid densities, which are in excellent agreement with existing experimental data for short chains. The OPLS force field was found to offer better agreement with experimental data for surface tension at lower molecular weights than the exp-6 force field, which overpredicted this by as much as 9%. However, for longer chains (n $\geqslant$ 20, for a molecular formula C_nF_{2n+2}) the OPLS force field predicted higher surface tension than the exp-6 force field, which therefore predicts too high a melting temperature.

By considering the structures in figure 5.1, three sets of force field parameters, including force field parameters for the fluorocarbon head group, for the PEO tail and for water, are required to describe the systems. It is of crucial importance that these set of force fields have to be compatible and allow the same conventional use (i.e. using the same scaling factor for cross-interactions). Since the exp-6 force field of Borodin *et al.* [225, 226] has been specifically parameterised for fluorinated systems, the parameters between this head group and PEO (water) are not known. The standard OPLS-AA based force field, therefore, would be more suitable for our

work.

The OPLS-AA force field has been successfully used to study liquid-liquid interfaces of semifluorinated alkane diblock copolymers with SPC/E water [230]. For the OPLS force field of PEO, Anderson and Wilson showed that their modified OPLS-AA force field for PEO (OPLS-DMEFF) [67] in combination with TIP4P water can be used to study amphiphilic graft copolymer molecules at a water-air interface. In their work, neutron reflectivity profiles calculated from the simulation trajectories agree well with those acquired experimentally for low density films.

Since the models of perfluorocarbon and PEO mentioned above were modified based on the same OPLS-AA force field family, they can be used together via the OPLS-AA combination rule and scaling factor for 1-4 Coulomb- and Lennard-Jones potentials. The choice of water model to be used is open. The common water models such as SPC/E [174], TIP4P [173], TIP4P-Ew [177] are designed to exhibit properties that are solely controlled by their own interaction parameters. These models can be integrated easily with the OPLS-AA potential, and has been used in a number of previous liquid-vapour interface simulations. Since the TIP4P-Ew model seems to provide better prediction of the vapour-liquid behaviour than the former two models [231], it will be chosen as the water model for this simulation work.

5.2.2 Reference atomistic simulations for deriving coarse-grained potentials

In this work, we use the OPLS- AA force field of Watkins and Jorgensen [201, 223, 224] to model the perfluorocarbon head groups. Ab initio calculations by Padua [227] have extended this force field for simulation of semifluorinated alkanes by providing the required torsional potential parameters for rotation around the chemical bond between the hydrocarbon and fluorocarbon blocks and these results are used here. The modified form of OPLS-AA force field (OPLS-DMEFF) by Anderson and Wilson [200] was adopted for the poly(ethylene oxide) chains. Water was modelled using TIP4P-Ew force field and remaining parts of the structure were modelled using OPLS-AA based parameters. Molecular dynamics conditions and setting options

adopted here are the same as those described in section 3.3.1.1 of chapter 3.

Simulations of F2 and F3 reference systems were performed in a similar manner, and are described as follows. 16 chains of dendritic fluorocarbon end-capped PEO with 10 EO units (the structures shown in figure 5.2) were first placed in the box of dimension $x = y = z = 60.0$ Å, then solvated with 4,330 water molecules for the F2 system (4,112 water molecules for F3 system). To set up the water/air interface, the z axis was increased to 155.0 Å (z is the axis perpendicular to the surface plane). This will promote a sufficient distance between the water and air interface to prevent interactions occurring between them. It should be noted here that amphiphilic molecules were placed into the box at positions close to only one side of the water slab (each simulated box has two water/air interfaces due to the periodic boundary conditions). This will force all molecules go to the same surface when they reach equilibrium, and will be convenient for analysis and comparison of results. The system was then subjected to a short equilibration run to allow equilibrated water/vapour interface to form. Once the water/air interface was set up, the system was then subjected to another equilibration run to make sure that it had reached an equilibrium state (the density distribution normal to the water surface remained steady). Then, an additional 60 ns was carried out for data analysis. The calculations were performed within the NVT ensemble at 298 K.

5.2.3 Deriving coarse-grained potentials

The first step in the coarse-graining procedure is to define the CG level. Mapping of the all-atom dendritic fluorocarbon end-capped poly(ethylene oxide) to coarse-grain units is pictorially shown in figure 5.2. Since both F2 and F3 molecules are composed of the same basic constituents, they were coarse-grained in a similar fashion here. For the fluorocarbon moiety, we group three consecutive backbone atoms along with their fluorine and hydrogen atoms into a single CG site. All atoms that belong to the phenyl ring were lumped together into one CG bead. Next to the phenyl ring towards the PEO tail chain, three consecutive backbone atoms along with their oxygen and hydrogen atoms were grouped into another CG unit.

In this manner, for the head group we have five CG particle types; FX (-

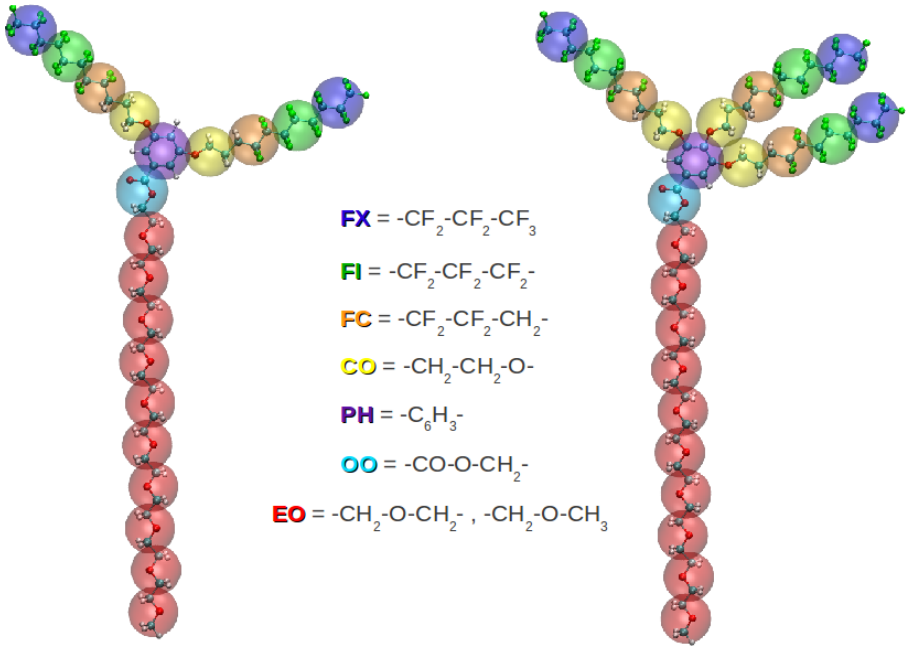

Figure 5.2: Schematic definition of coarse-grained particles for di- and trifluoro dendritic end-capped poly(ethylene oxide). Different colours represent different types of coarse-grained units.

$CF_2CF_2CF_3$), FI (-$CF_2CF_2CF_2$-), FC (-$CF_2CF_2CH_2$-), CO (-CH_2CH_2O-), PH (-C_6H_3-) and OO (-CO-OCH_2-). It should be noted that each CG site is placed on the centre of mass position of its underlying atomistic units. For the PEO segments and water, we apply the same mapping schemes as described in section 4.3.2 of chapter 4.

Apart from coarse-grained potentials of PEO/water, that have already been derived in chapter 4, the fluorocarbon head group was modelled via three types of interactions, including bond stretching, angle bending and nonbonded interaction. A dihedral potential was not included for this case due to a rather flat dihedral distributions found in atomistic reference systems. These three types of interactions have been shown to be sufficient to represent structural behaviour of perfluorocarbon systems [232]. Both intramolecular and intermolecular potentials were derived on the basis of matching structural probability distributions to those of the atomistic references. These processed in a similar way to that already described in section 4.3.2.1 of chapter 4 for the PEO/water coarse-graining case.

The composition of the CG systems used in the iterative Boltzmann inversion

process is equivalent to their atomistic references. 16 chains of F2 (F3) are included in a box of dimension $x = y = 60.0$ Å and $z = 155.0$ Å with 1,083 water beads (equivalent to 4,332 water molecules) for the F2 system and 1028 water beads (equivalent to 4,112 water molecules) for F3 system. Simulations were performed under NVT conditions for a short 5 ns run for each IBI iteration. When fittings of bond and angle distributions and radial distribution functions were satisfied, the resulting potentials were tested again with a longer run of 30 ns to make sure that structural distributions obtained from the final iteration were stable.

5.3 Results and Discussion

5.3.1 Bonded interactions and intramolecular distributions

We constructed two sets of potentials based on target functions from the F2 and F3 systems. Comparisons between intramolecular distributions from coarse-grained simulations and their underlying atomistic systems are shown in figure 5.3 (F2) and 5.4 (F3). It can be seen that the IBI procedure achieves a very good match for both bond and angle distributions. In the optimisation procedure, potential corrections for different types of bonds were done simultaneously at each IBI step until all of them were converged together. Due to bi- and trimodal probability distributions found in atomistic results, several IBI steps were required to satisfy this process (starting from initial guess potentials from Boltzmann inversion of atomistic distribution functions). It is important to note here that a simulation time step of 10 fs (as used before for the coarse-grained PEO/water model) is too large to use in matching the bond lengths observed in atomistic simulations of the F2 and F3 systems. To solve this problem the time step was reduced to 5 fs, where it provided almost perfectly matches to bond distributions as shown in the figures. Matchings of angle distributions were carried out in a similar way. However, since there are several types of angles in the F2 and F3 structures and they are all interdependent, it took many iterations to complete this task.

In overall results, both bond length and angle distributions are rather similar for the F2 and F3 systems. The only difference is due to the existence of the third

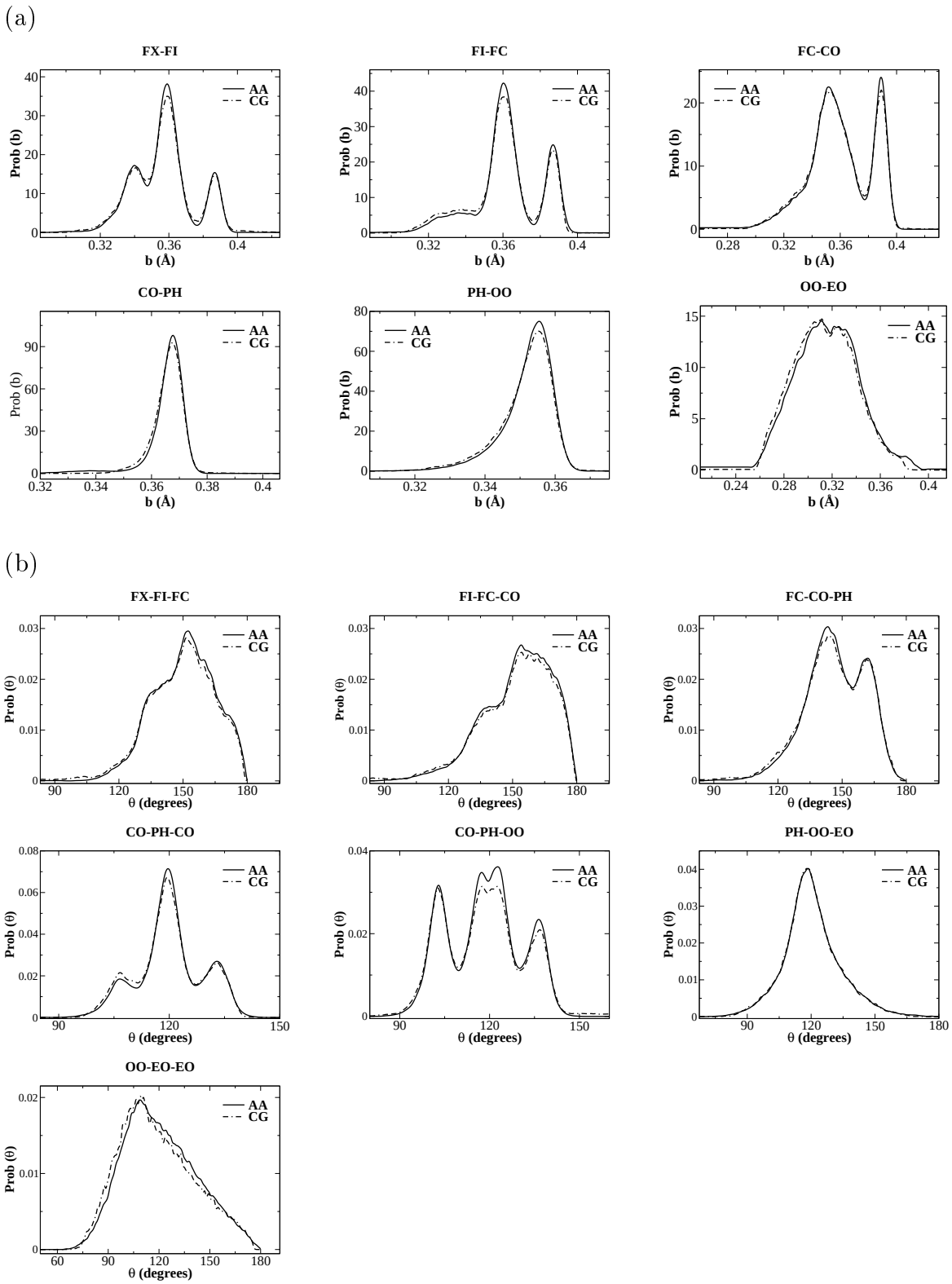

Figure 5.3: Comparison of distribution functions from atomistic and CG simulations of the F2 system: (a) bond distance distributions between two neighboring sites, (b) angle distributions between three ajoining sites.

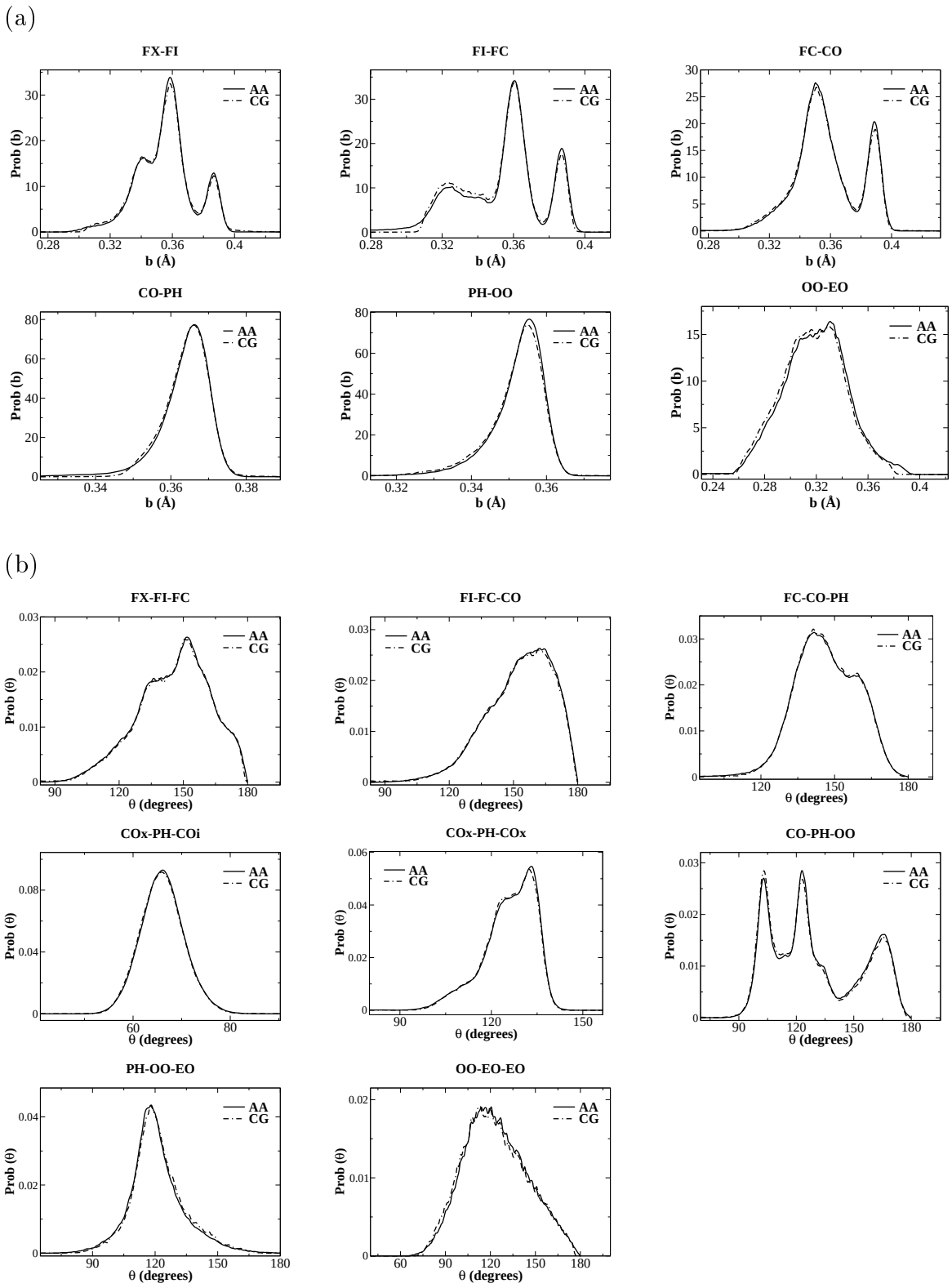

Figure 5.4: Comparison of distribution functions from atomistic and CG simulations of the F3 system: (a) bond distance distributions between two neighboring sites, (b) angle distributions between three ajoining sites.

fluorocarbon branch at the middle of the F3 head group, which readily creates another angle type, labeled as CO_x-PH-CO_i in figure 5.4 (b) (note that CO_x and CO_i refer to CO particle belonging to the left (or right) and the middle fluorocarbon branch, respectively). Steric hindrance caused by this additional branch has also made a wider CO_x-PH-CO_x angle (figure 5.4 (b)) compared to the same type of angle CO-PH-CO (figure 5.3 (b)) in the F2 system. The resulting potentials for bond and angle are not shown here. Their shape is essentially not changed from their initial guess, which are the Boltzmann- inverted potentials of the target bond and angle distributions.

5.3.2 Radial distribution functions and nonbonded potentials

After completing optimisations of bonded interactions, we turn our attention to nonbonded ones. Due to various types of CG particles present in the structure, deriving nonbonded interactions is not a trivial task. In order to obtain a complete set of interactions among these particles, RDFs of the same pair of particles as well as those between different CG types (cross-terms) are needed to be fitted to their targets. Furthermore, the number integral of the RDF between each CG type and water (W site) is also required to match with atomistic simulation to maintain the same amount of water around the hydration shell of the amphiphile units. It would be very difficult to perfectly match all the coarse-grained RDFs to their targets even by using a systematic coarse-graining method like IBI. The problem lies in the fact that the structure between each pair of particles can be sensitive to any change made in the potential of other pairs in the system. To make the optimisation achievable, one has to know the order of potential strength for each pair of particles so that the strongest interacting ones, i.e. the one that has the least change ofin RDF from changing any other pair potential, will be chosen to be fitted first.

It should be noted that in many studies where there are several types of CG particles present in the system, other approaches, such as a semi-empirical or thermodynamic-based coarse-graining, have been applied instead [89, 90, 93, 95, 179]. Apart from bonded interactions, which are normally acquired from a detailed quantum (atomistic) calculations, nonbonded energies for these methods are derived from experi-

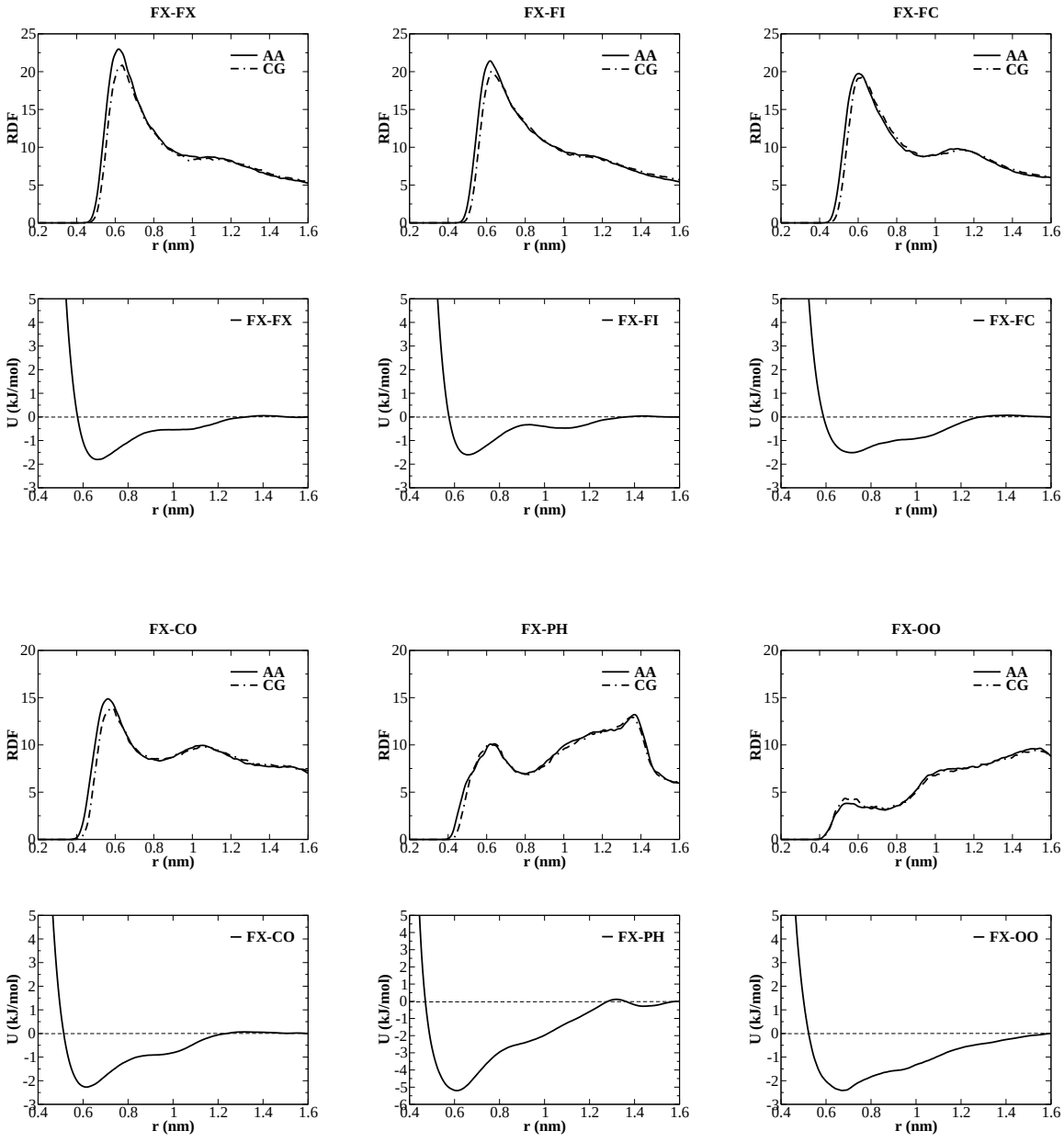

Figure 5.5: Comparison of atomistic and coarse-grained radial distribution functions along with coarse-grained potentials among various amphiphile sites in the F2 system.

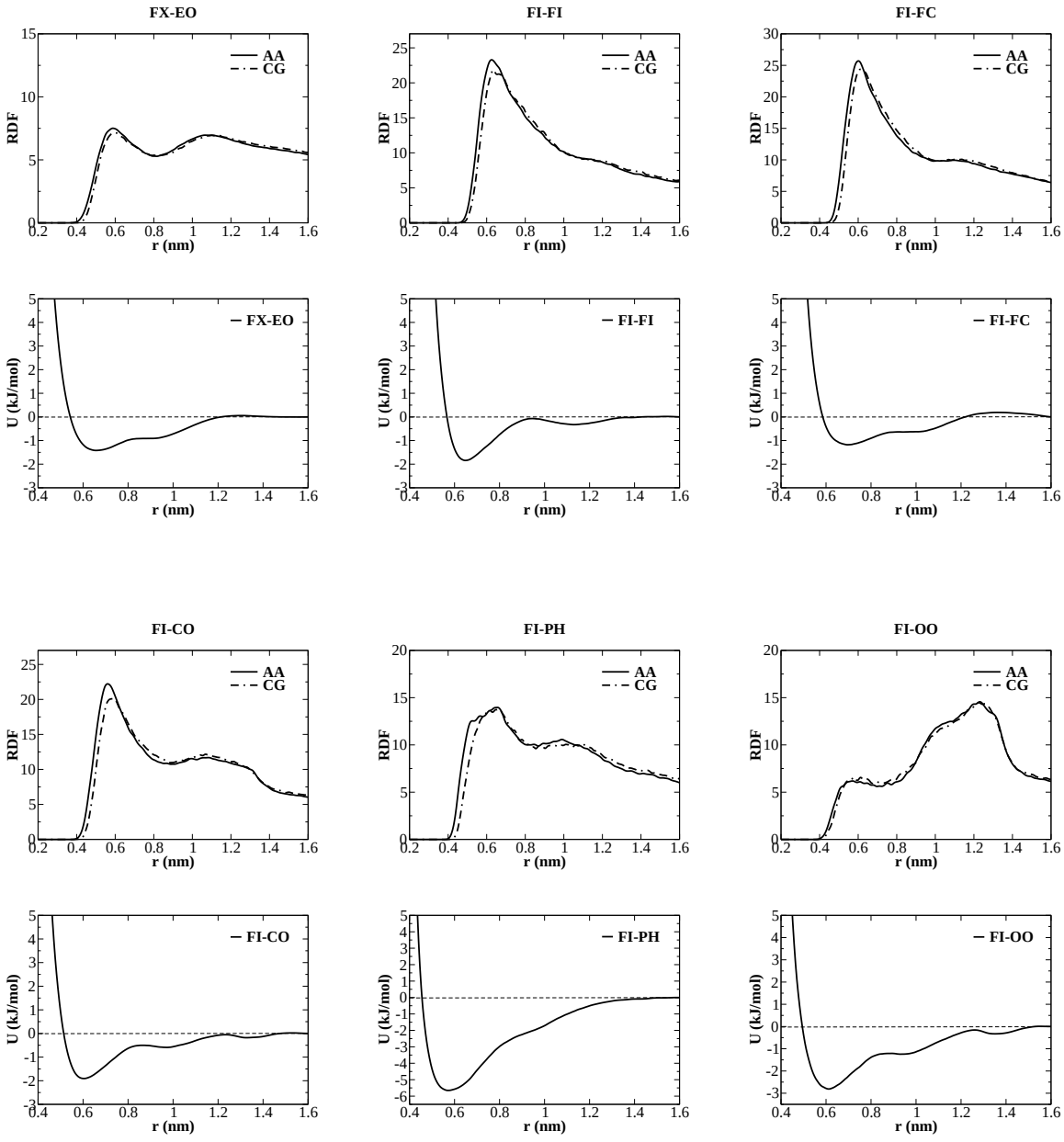

Figure 5.6: Comparison of atomistic and coarse-grained radial distribution functions along with coarse-grained potentials among various amphiphile sites in the F2 system.

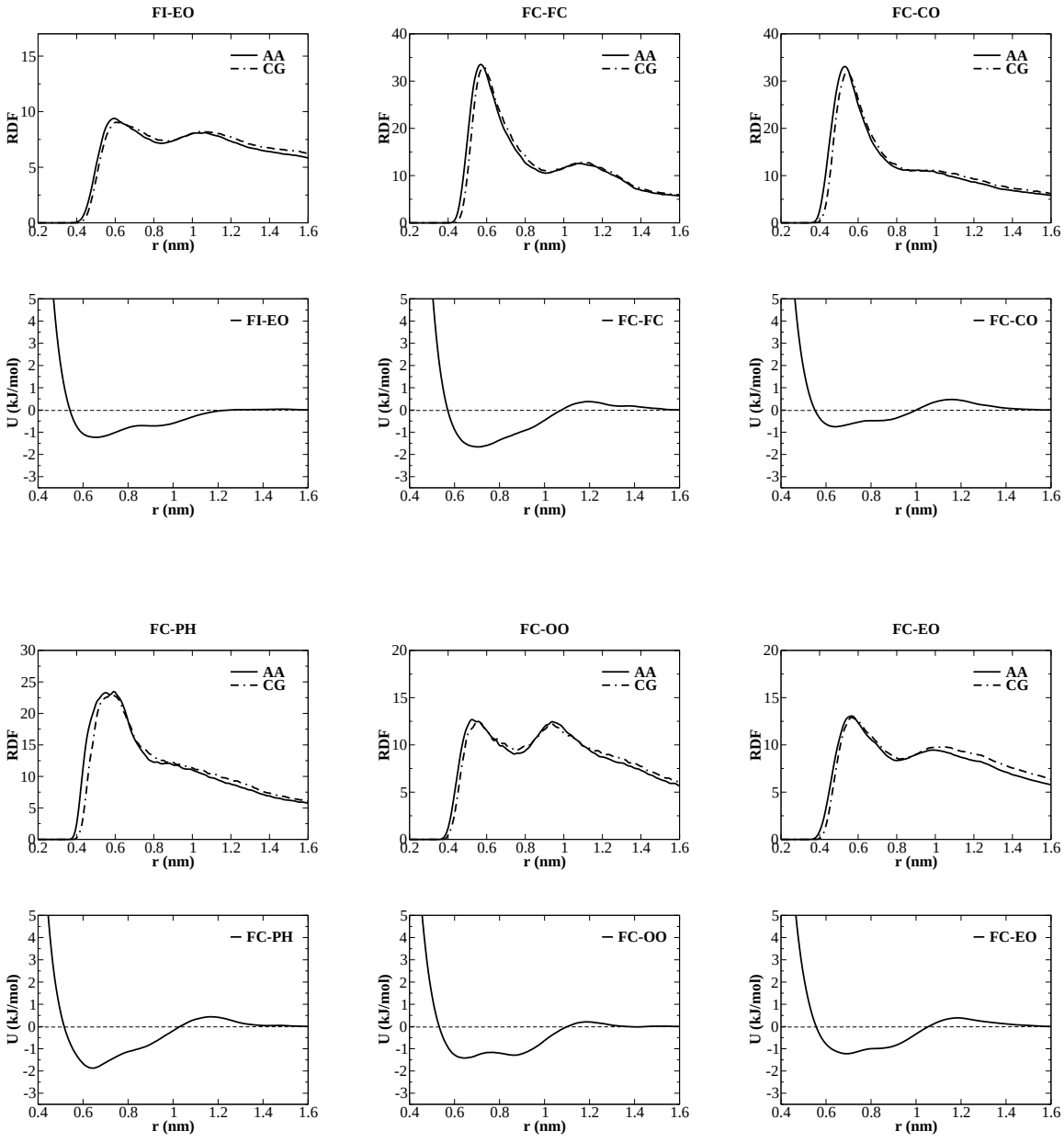

Figure 5.7: Comparison of atomistic and coarse-grained radial distribution functions along with coarse-grained potentials among various amphiphile sites in the F2 system.

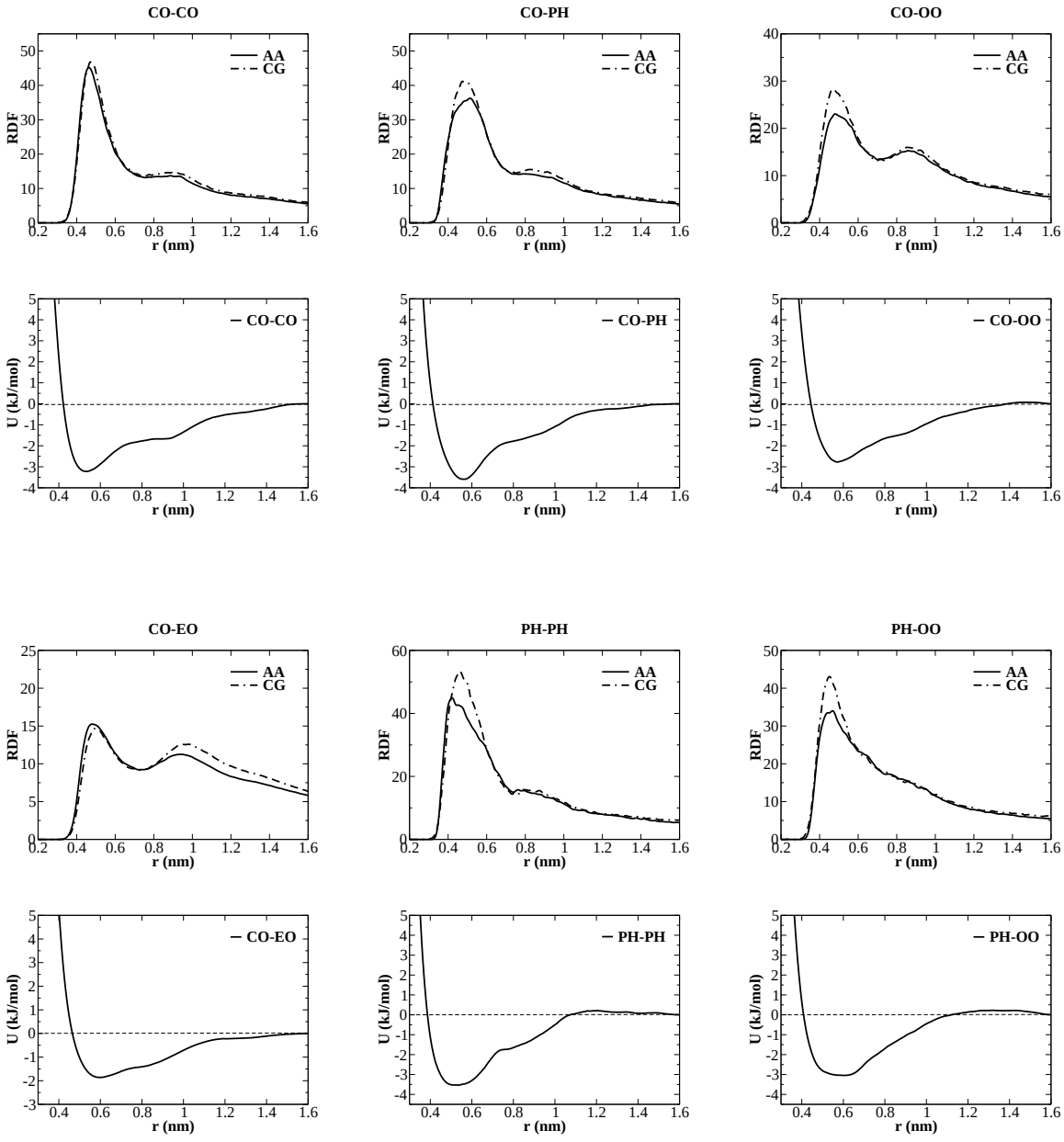

Figure 5.8: Comparison of atomistic and coarse-grained radial distribution functions along with coarse-grained potentials among various amphiphile sites in the F2 system.

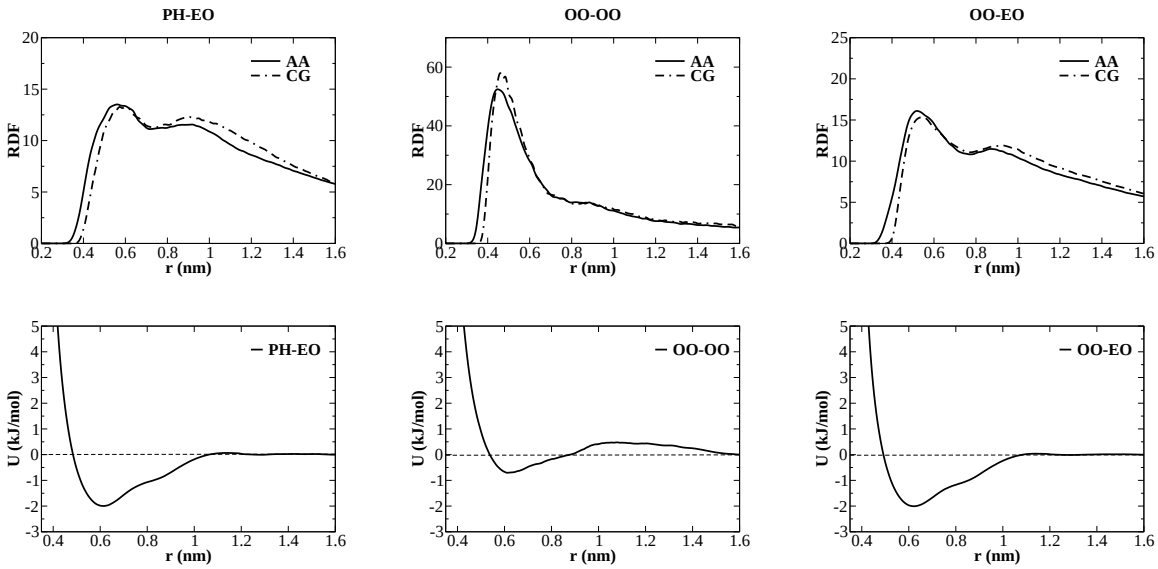

Figure 5.9: Comparison of atomistic and coarse-grained radial distribution functions along with coarse-grained potentials among various amphiphile sites in the F2 system.

mental data. This way of coarse-graining is more convenient than the one we used (structural based coarse-graining) since nonbonded interaction parameters between like and unlike particles can be obtained separately. For example, nonbonded parameters for the same type of particles can be parameterised from properties, e.g. density of a neat liquid [204], and cross interactions between different particle types can be obtained by tuning interaction parameters to reproduce properties of a mixtures such as interfacial tensions [129] or partitioning free energies between polar and apolar phases [90].

Having suggested other choices of coarse-graining, nonetheless, due to a lack of experiment data for the system of interest, together with a lack of systematic way of deriving a model empirically, we therefore decided to carry on with the structural-based coarse-graining approach. The models developed here, thus, are based solely on results from the detailed atomistic simulations.

5.3.2.1 Amphiphile-Amphiphile interactions

Figure 5.5-5.9 and 5.10-5.14 show a comparison series of atomistic and coarse-grained RDFs for different pair sites present in the F2 and F3 systems. These results are considered to be the best fits that can be obtained within the time available for

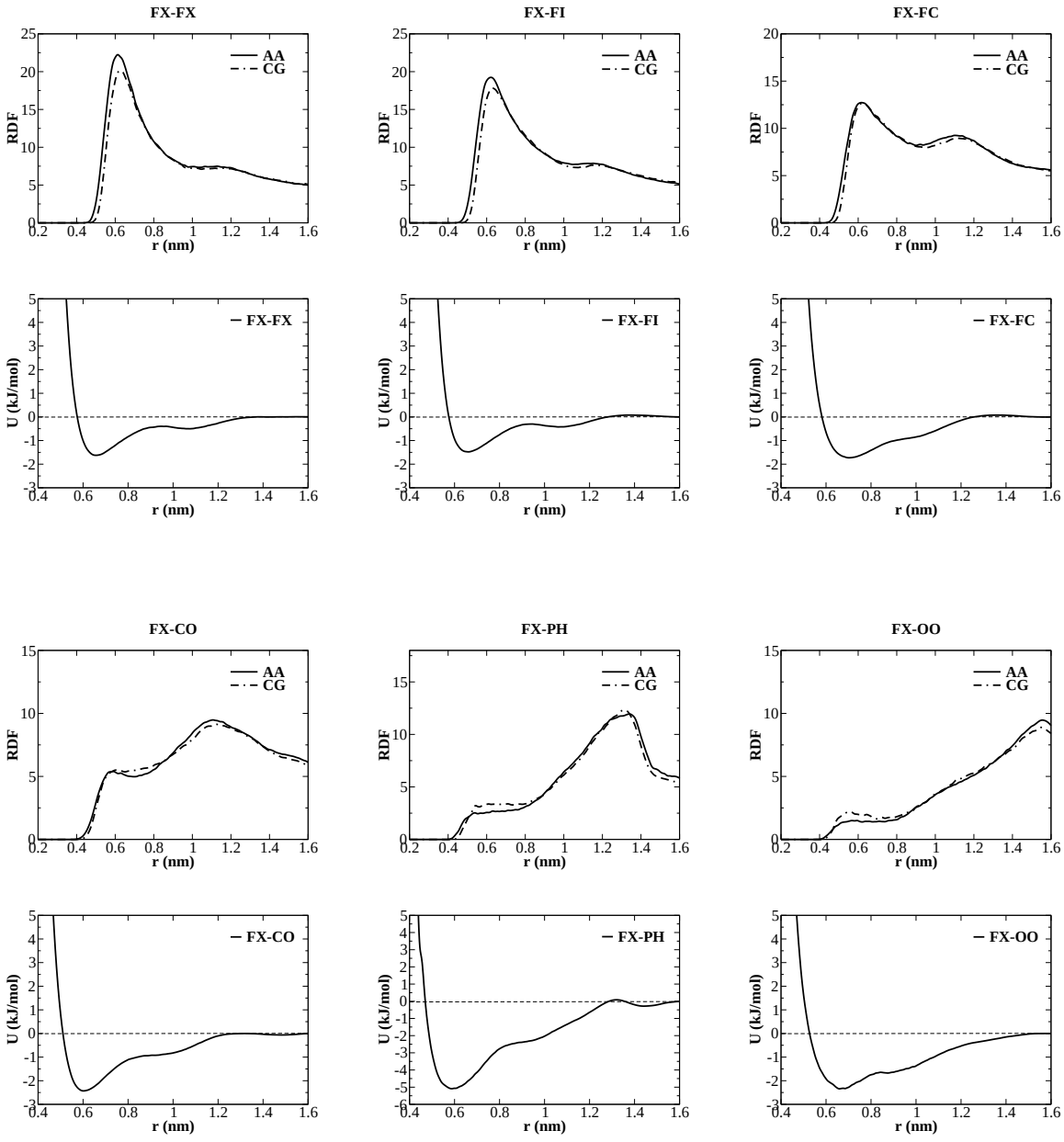

Figure 5.10: Comparison of atomistic and coarse-grained radial distribution functions along with coarse-grained potentials among various amphiphile sites in the F3 system.

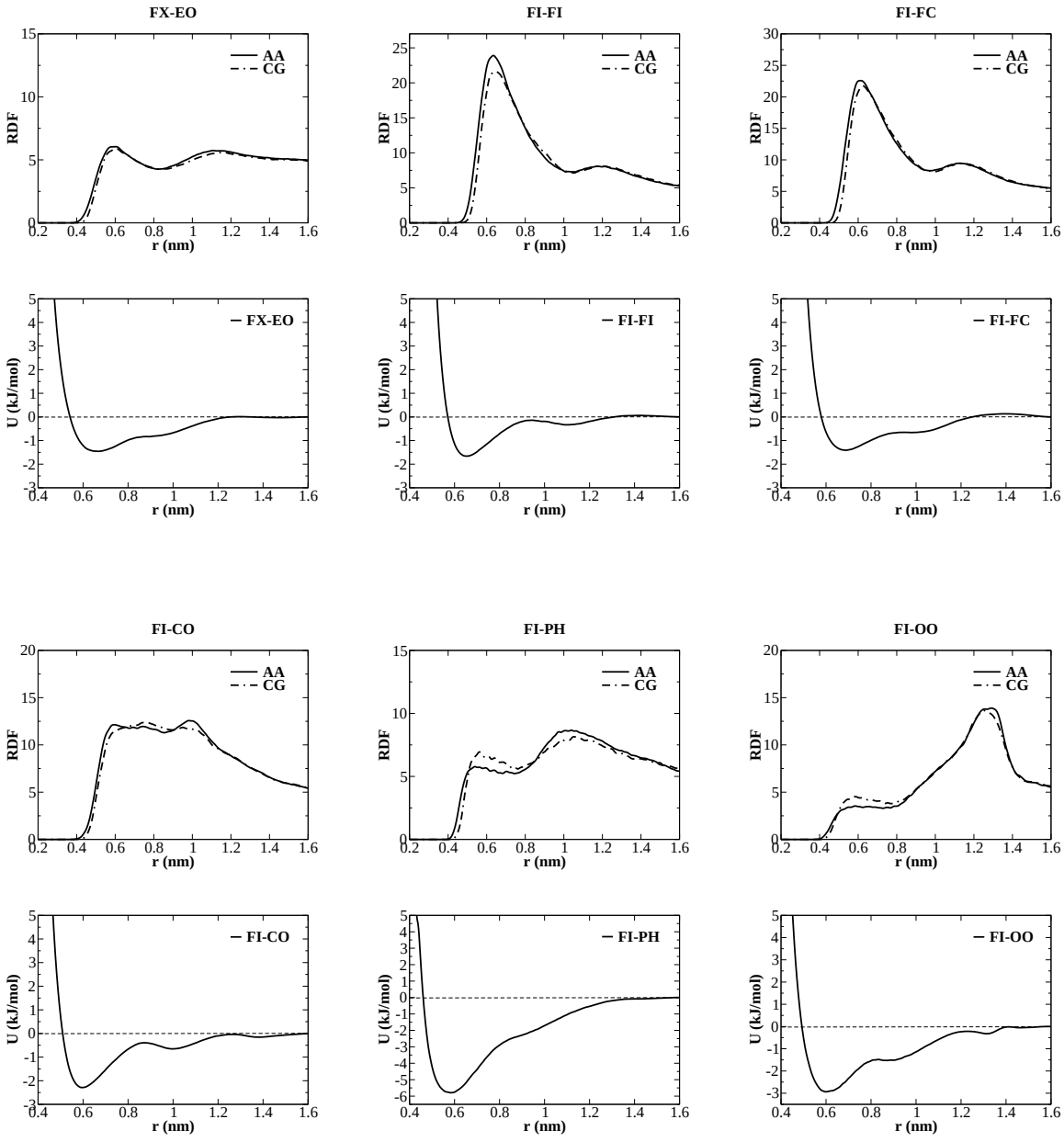

Figure 5.11: Comparison of atomistic and coarse-grained radial distribution functions along with coarse-grained potentials among various amphiphile sites in the F3 system.

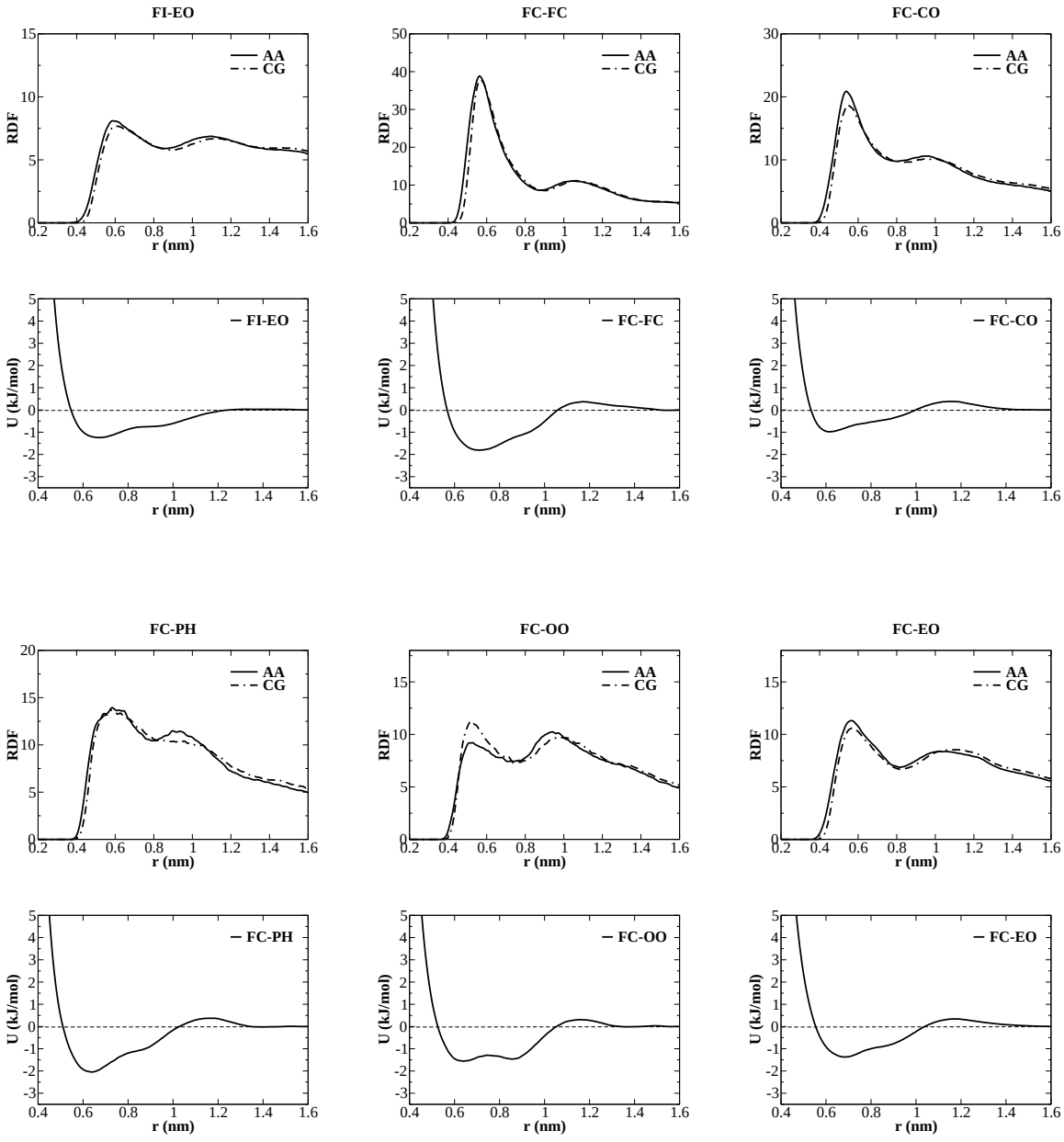

Figure 5.12: Comparison of atomistic and coarse-grained radial distribution functions along with coarse-grained potentials among various amphiphile sites in the F3 system.

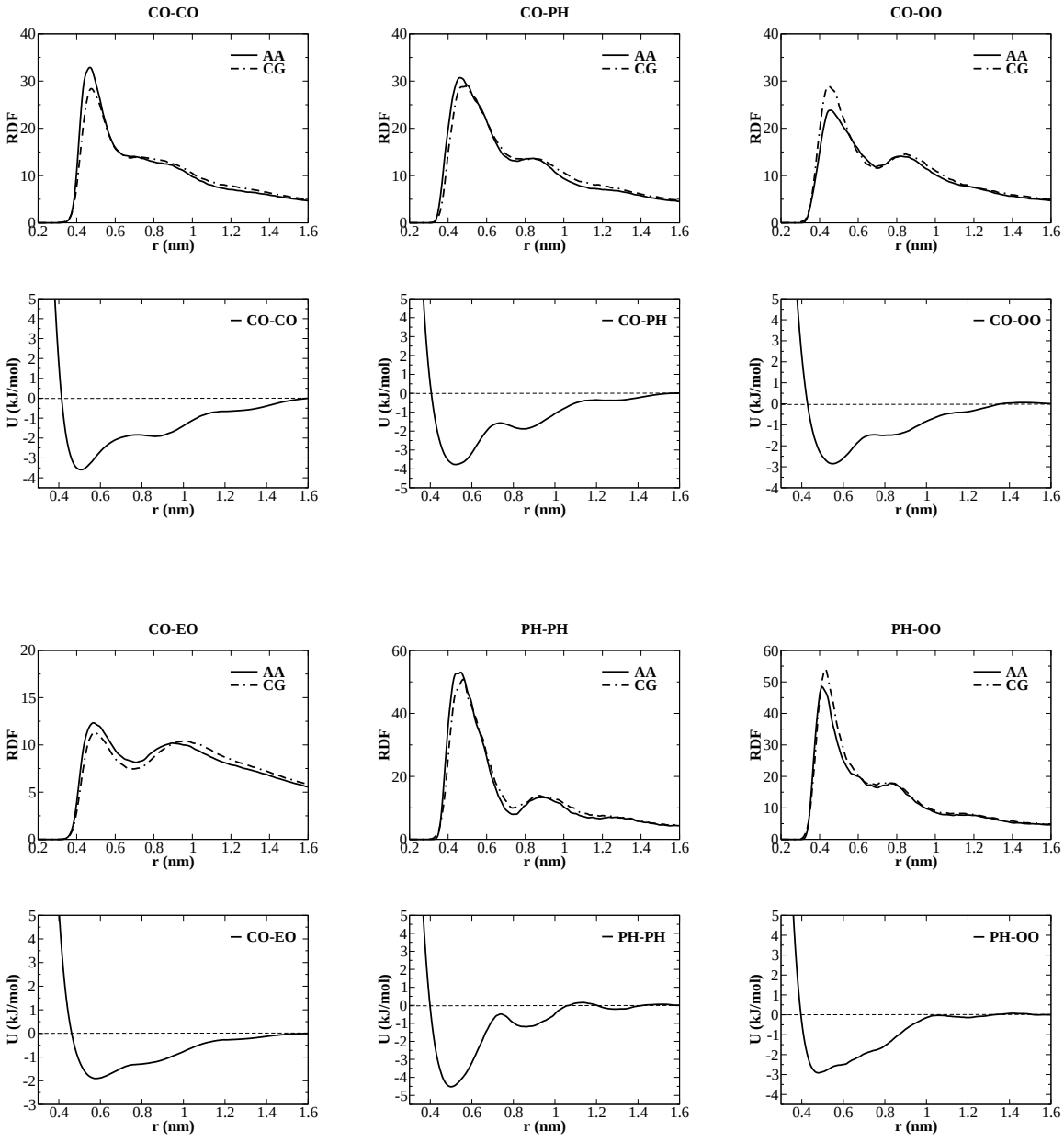

Figure 5.13: Comparison of atomistic and coarse-grained radial distribution functions along with coarse-grained potentials among various amphiphile sites in the F3 system.

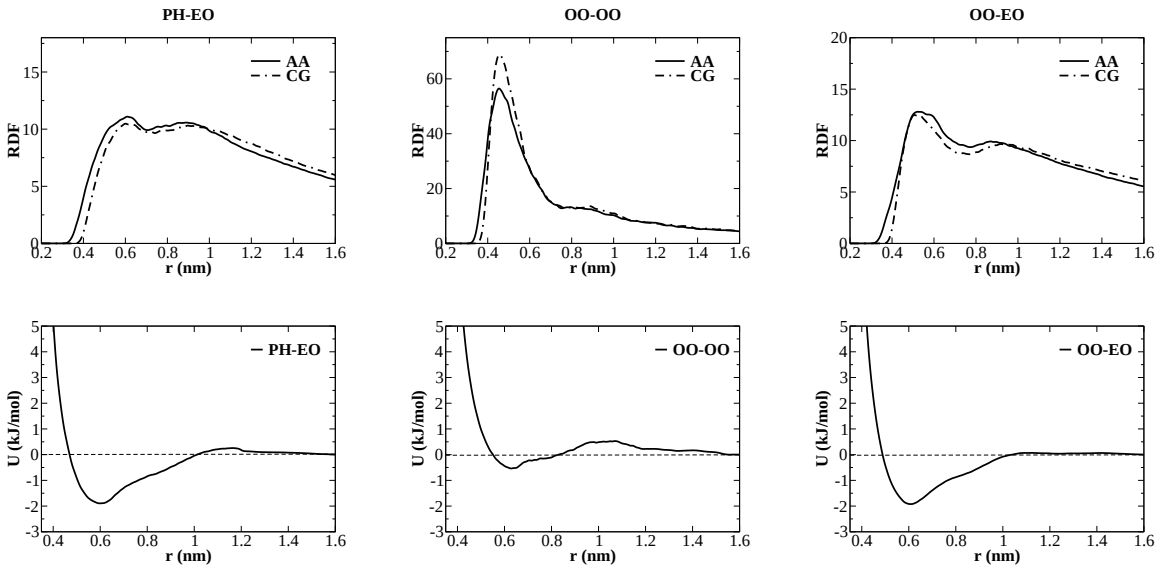

Figure 5.14: Comparison of atomistic and coarse-grained radial distribution functions along with coarse-grained potentials among various amphiphile sites in the F3 system.

doing this work. Since, in each system, there are 27 different RDFs and 6 sets of integration numbers needed to be fitted to their targets, an excellent match of all cases would not be expected from this ultimate task. Although the matches are not perfect, we achieved fits with reasonably good quality. This can be seen from a correspondence between the peak position as well as a comparable amplitude of the coarse-grained and atomistic RDFs.

We should point out here that discrepancies between RDFs obtained from AA and CG come about for two main reasons. The first reason can be attributed to the larger size of CG units relative to atoms, that not allow them to pack together as close as an all-atom model could. This is reflected in a slight shift of the first peak of the coarse-grained RDFs to larger separation distances compared to the atomistic ones, as can especially be seen in the RDFs among FX, FI and FC sites. The second reason is due to a cross-correlation among various RDFs and potential energies applied in the system. The structure of each pair depends not only on its own potential energy but also rely upon other pair potentials in the system. For example, the structure of A-B pair (A and B represent different type of CG particle) is not solely inherited by the pair potential A-B, but may also be imposed by the potential A-C, B-C, etc. In the IBI procedure, some RDFs might be fitted perfectly

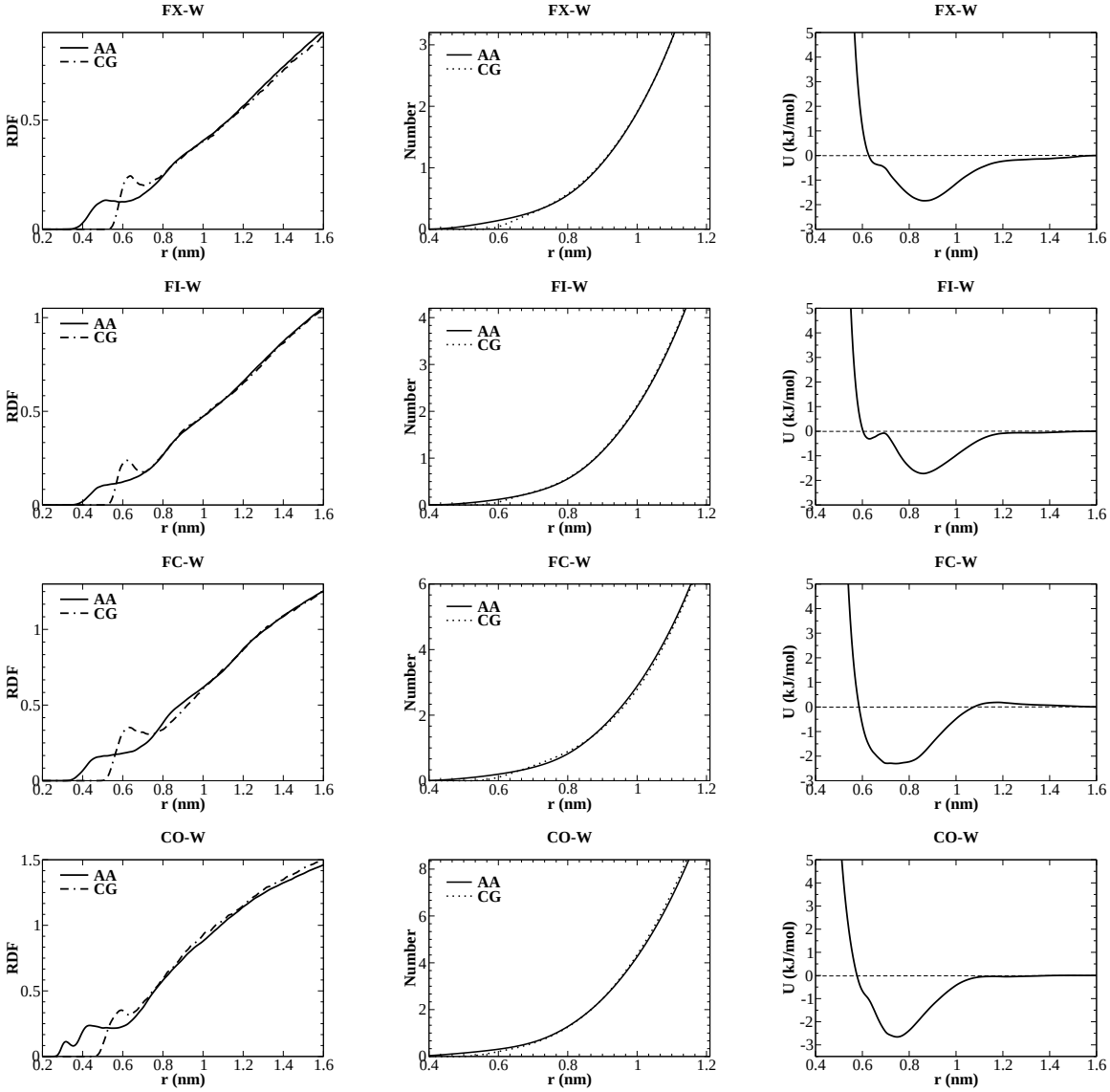

Figure 5.15: Comparison of atomistic and coarse-grained RDFs (left) and their number integral (middle), along with coarse-grained potential (right) between the amphiphile sites and water in the F2 system.

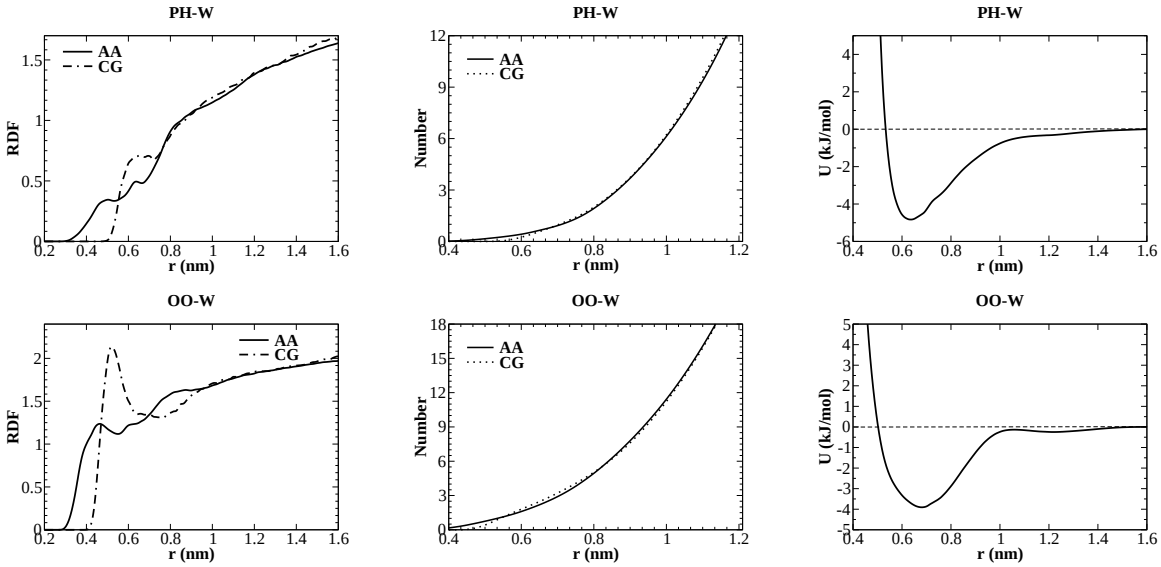

Figure 5.16: Comparison of atomistic and coarse-grained RDFs (left) and their number integral (middle), along with coarse-grained potential (right) between the amphiphile sites and water in the F2 system.

at a very first iteration. One, therefore, might like to fix these good potentials while adjusting others whose structures have not been converged. We, however, found that fitting the rest of the RDFs would never be completed unless we went back and unfixed (reduced or increased) the strength of the previous fixed potentials. Due to this fact, the fitting quality for some pairs was allowed to reduce slightly, to make matching of other structures achievable.

Nonbonded interactions obtained for the F2 and F3 models are shown along with their RDFs in figure 5.5-5.9 and 5.10-5.14. From the figures, for overall pair sites, the maxima and minima of the RDF roughly correspond to minima and maxima in the potential. We started the optimisation process on the F2 model first. The final results from the F2 system were then used as an initial potential for each corresponding pair of particles in F3 system. This saved a considerable amount of time in fitting the latter. Comparison of figures 5.5-5.9 and 5.10-5.14 reveals that there is no significant different between the final potential obtained for corresponding pairs of particles in the F2 and F3 systems.

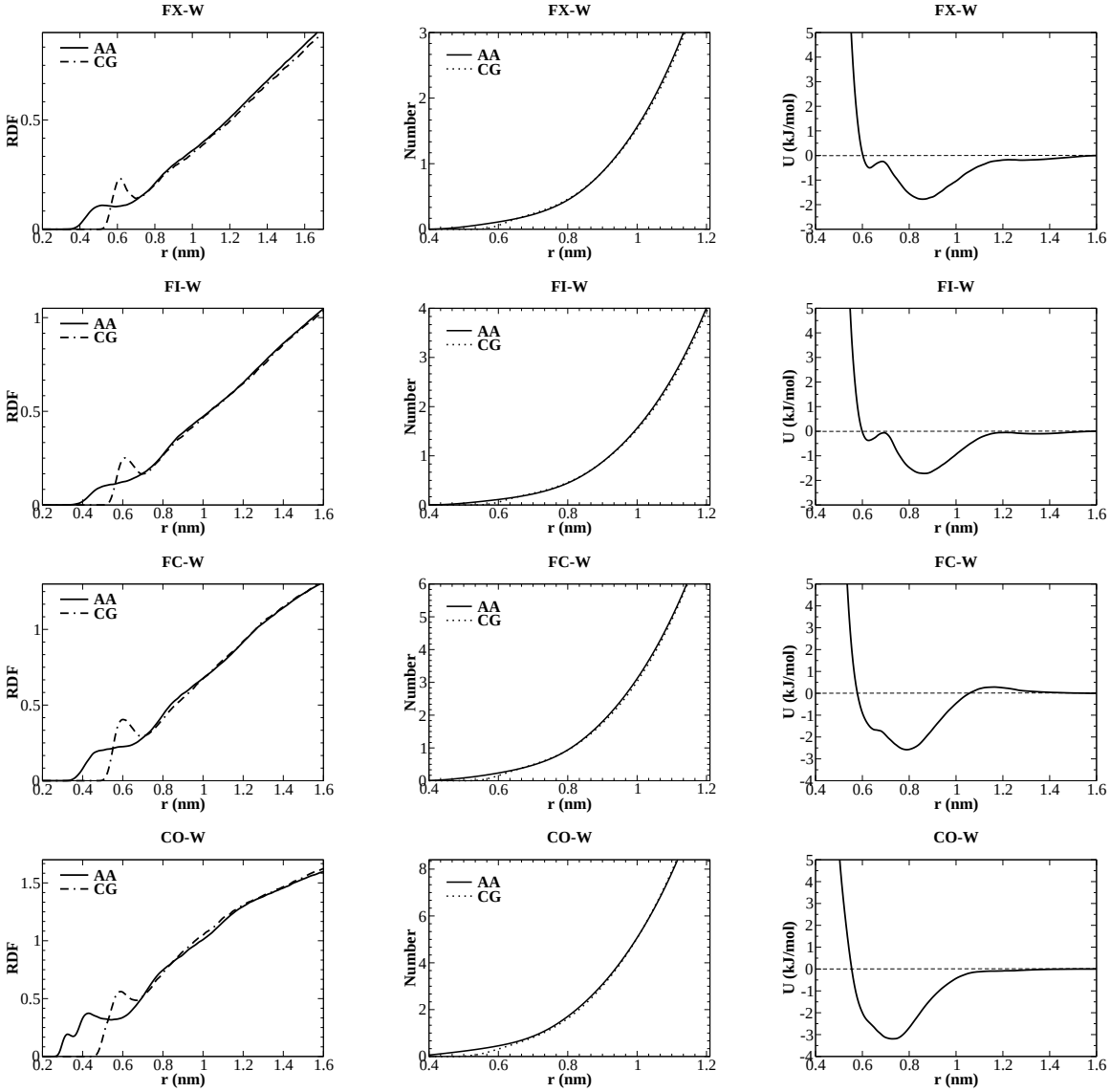

Figure 5.17: Comparison of atomistic and coarse-grained RDFs (left) and their number integral (middle), along with coarse-grained potential (right) between the amphiphile sites and water in the F3 system.

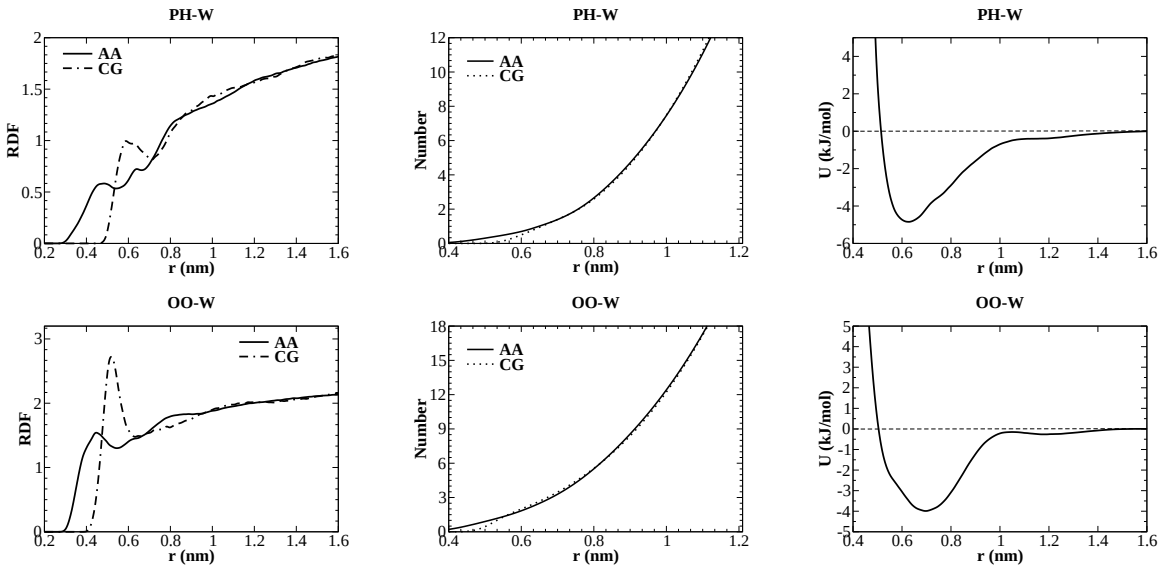

Figure 5.18: Comparison of atomistic and coarse-grained RDFs (left) and their number integral (middle), along with coarse-grained potential (right) between the amphiphile sites and water in the F3 system.

5.3.2.2 Amphiphile-Water interactions

The radial distribution functions together with their number integral between each head group particle and water are shown in figure 5.15-5.16 and 5.17-5.18 for F2 and F3 system, respectively. It is obvious from the figures that correlations (magnitude of RDFs) between polymer units and water are relatively smaller than those among the polymer themselves (see figure 5.5-5.9 and 5.10-5.14). This is simply because of the hydrophobic nature of the head groups that cause molecules to minimise their energy by avoiding interacting with water, while preferentially aggregating with others at the interface. This leads to less correlation between amphiphilic molecules and liquid water, as shown in the RDFs.

It is evident from both the RDF magnitude and the well depth of the potentials (also showed in figure 5.15-5.16 and 5.17-5.18) that interaction strength between head group units and water in both F2 and F3 systems tends to follow the trend: OO-W PH-W $>$ CO-W $>$ FC-W $>$ FI-W $>$ FX-W. This result indicates that, rather than adsorbing along the surface plane, the F2 and F3 head groups prefer aligning themselves perpendicular to the water surface. This organisation behaviour has been reported before by experimental studies of semifluorinated alcohol [82] and

perfluorinated dendrimers [233] systems.

When considering the first peak of RDFs in figure 5.15-5.16 and 5.17-5.18, the closest distance (first hydration shell) between water and each CG particle has been shifted around 1-2 Å from those observed in atomistic systems. This distortion results from the larger size of the W particle (in this case, representing four water molecules), preventing it coming as close to the polymer units as a single water molecule does. Nevertheless, the number integral obtained from the fits matches very well to that of the atomistic simulations, as shown in the middle of figure 5.15-5.16 and 5.17-5.18. It is important to keep the right level of hydration for each CG unit as this implies a reasonable hydrophobic interaction between the head groups and water, which will, indeed, effect adsorption behaviour of the amphiphilic molecules at the water surface.

5.3.3 General observations and density profile

The snapshot images obtained from the target atomistic simulations and their CG counterparts are presented respectively in figure 5.19 and 5.20 for the F2 and F3 systems. In the atomistic simulations, similar behaviour were observed for both the F2 and F3 systems. They both show the formation of a stable layer of amphiphilic polymer at the interface. Observations from MD trajectory movies reveal that amphiphile molecules move laterally from bulk water toward the interface with the fluorinated head group being the first part of the molecule that touch the interface. It was later showed that these head groups move along the surface plane to find other head groups and start clustering together. As evidenced both from the final snapshots and the density profiles in figure 5.19 and 5.20, these fluorinated moieties are likely to form an insoluble layer at the interface with the majority of them residing in the air phase. It can also be noted from the side view of the final snapshots that these fluorinated branches tend to align perpendicular to the water surface, in accordance with results discussed in the previous section. This type of alignment will promote a close-packing among the head groups, which is an efficient way of maximising hydrophobic-hydrophobic interactions.

The calculated surface tension for the atomistic F2 and F3 references is 55.9

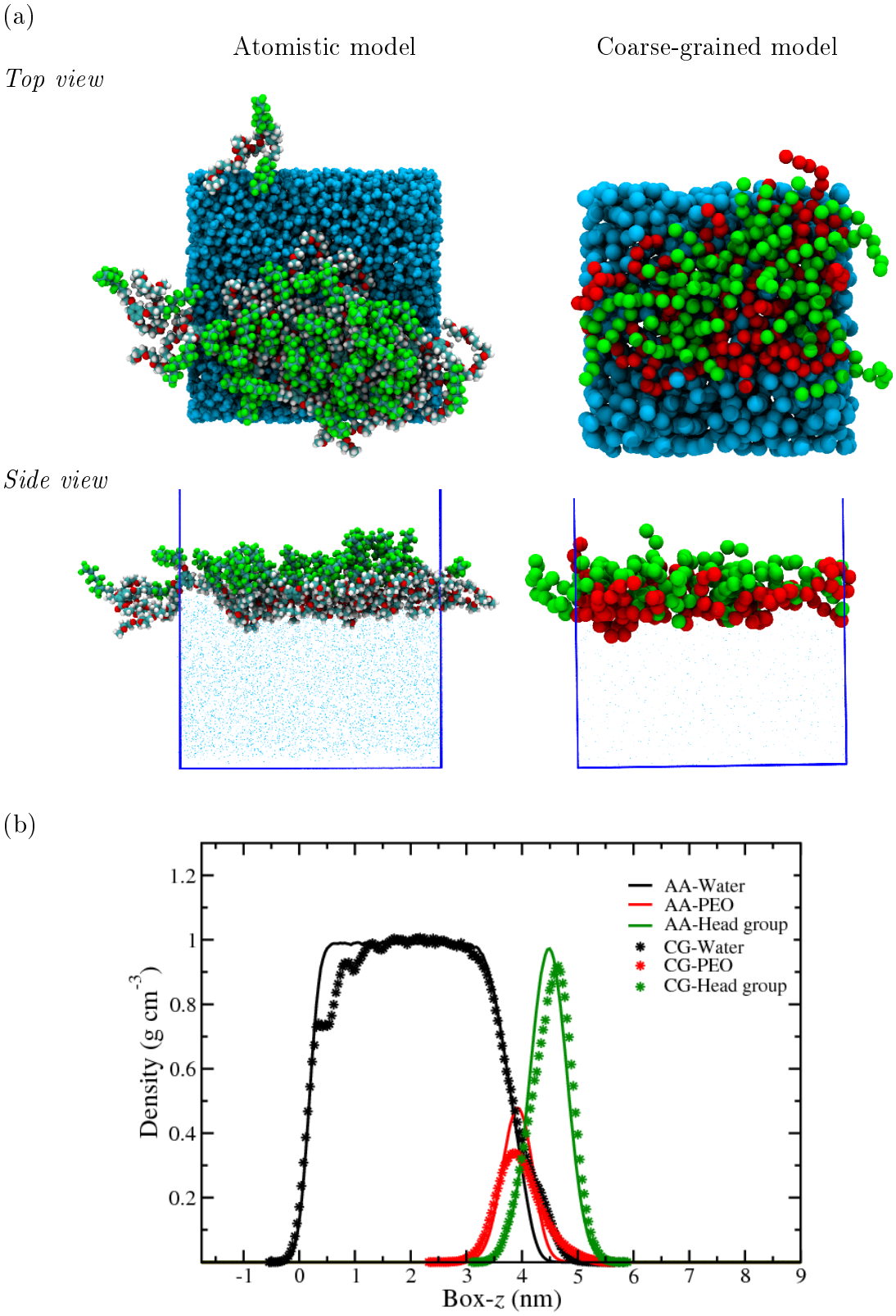

Figure 5.19: (a) Final snapshots from MD simulations of the F2 system: atomistic model (left) and coarse-grained model (right). Color codes are as follows; green: fluorinated head group, red: PEO tail and cyan: water. (b) mass density profiles for the three components of the F2 system: atomistic model (solid line) and coarse-grained model (star symbol).

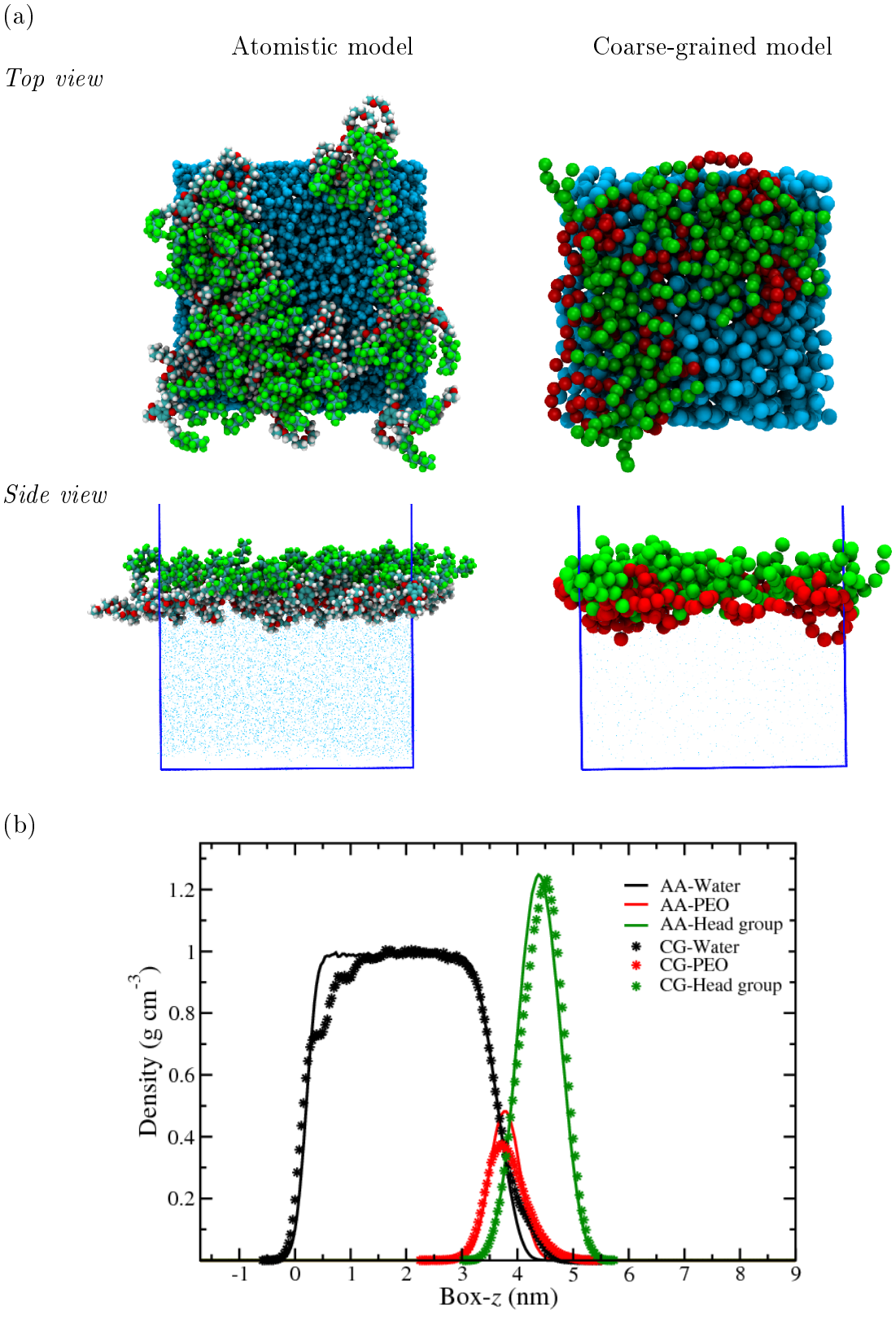

Figure 5.20: (a) Final snapshots from MD simulations of the F3 system: atomistic model (left) and coarse-grained model (right). Color codes are as follows; green: fluorinated head group, red: PEO tail and cyan: water. (b) mass density profiles for the three components of the F3 system: atomistic model (solid line) and coarse-grained model (star symbol).

mN m^{-1} and 57.5 mN m^{-1}, respectively. Theses values are sensible for the water surface in a presence of these amphiphiles (note that the surface tension for pure atomistic TIP4P-Ew water is 65.5 mN m^{-1}). Note that the surface concentration for the F2 and F3 systems is 1.1 mg m^{-2} and 1.5 mg m^{-2}, respectively. As already described in section 4.4.3.3, the fact that all polymer chains are adsorbed at only one water surface is also taken into account in calculations of the surface tensions reported here. The surface tension for the coarse-grained F2 and F3 systems is calculated to be 69.0 mN m^{-1} and 69.2 mN m^{-1}, only about 2 mN m^{-1} lower than that of pure coarse-grained water (71.0 mN m^{-1}). From very strong adsorption of amphiphilic molecules at the water surface shown in figure 5.19 and 5.20, one would expect more reduction of the surface tension in the coarse-grained systems than the values obtained above. This rather high surface tension could be attributed to the coarse-grained potentials that were not specifically optimised for the surface energy of the system.

Due to the lesser hydrophobicity of PEO compared to fluorocarbon head group, PEO segments were found to reside slightly beneath the head group layer at the interface. While some PEO segments appeared to penetrate the water subphase, the majority of them were shown to be adsorbed at the water surface. Since the PEO is included only for the purpose of deriving the potential, the PEO chain length used here is very short compared to those used in experiments. The real PEO molecular weight, comparable to that used in neutron reflectometry will be simulated and discussed later in the next chapter.

Adsorption behaviour from atomistic simulations mentioned above is mimicked similarly well by the coarse-grained models, as shown in the right hand side of figures 5.19 (a) and 5.20 (a). The mass density profiles for the three components (head group, PEO tail and water) of the CG models are compared to their parent atomistic simulation in figure 5.19 (b) for F2 and 5.20 (b) for F3 system. The hydrophobic head group thickness from the CG density profile is in excellent agreement with the atomistic simulation for both F2 and F3 systems. Close inspection of the density profiles reveals that water penetrates the PEO region to a considerably larger extent than it does in atomistic system. Since it was more swollen by water, the

coarse-grained PEO layer became slightly wider than that observed in atomistic simulations. Nonetheless, the overall density profile appears to be consistent between the coarse-grained and the underlying atomistic models. We believe that it will be sufficient to allow us to study adsorption behaviour of the system of interest in the next chapter.

5.4 Conclusions

We have developed coarse-grained models for di- and trifluoro dendritic end-capped poly(ethylene oxide) at an air-water interface. In a similar way to the PEO/water model in chapter 4, coarse-grained interactions are obtained from fitting of structural properties to those of detailed atomistic simulations.

The bond length and angle distributions can be matched excellently to their targets. Matching of the radial distribution functions are not absolutely perfect due to the interdependence between structures and pair potentials among various types of CG particles present in the two systems. Nevertheless, while our coarse graining does leave out considerable atomic level information, the overall structure of the interface, including molecular organisation and density profile, appears to be remarkably consistent between the two models.

In the next chapter, the current CG models will be applied to simulate F2 and F3 polymers in a comparable length-scale to those studied by neutron reflectometry [85]. We expect that they can provide us with useful insights into adsorption behaviour of these amphiphilic polymers at a water-air interface.

Chapter 6

Coarse-grained simulations of amphiphilic polymers at a water/air interface

6.1 Introduction

Polymer brushes have been studied for a number of years due to their ability to modify surface properties to prevent colloid aggregation [8] and to enhance lubrication and adhesion [4–7]. The possibility of using tethering polymers to inhibit protein adsorption [234] and evaluation of their use as self-regulating flow control valves [235, 236] have also been explored. The brush structure can be controlled by appropriately selecting the grafting density, polymer molecular weight, solvent and temperature [237].

A brushlike layer has been observed when functionalizing a low molecular weight PEO ($M_w \approx 3000$ g mol^{-1}) with a single hydrophobic fluorocarbon group [18]. However, when PEO molecular weight is increased further, a single fluorocarbon head group does not appear to tether sufficiently to the water surface to reach high packing brushlike conformation. To increase the surface tethering strength, new amphiphilic polymers, wherein the high molecular weight PEO chain is end-capped by multiple fluorocarbon head groups, have been synthesized and examined [85] to see if these types of head group can be more effective in strongly tethering PEO

chains up to a molecular weight of 10 000 g mol^{-1}. In addition, high molecular weight brushlike self assembling polymers are particularly useful in the situation where it is necessary to enhance the surface properties of a polymer without causing any unfavourable changes to the bulk properties of a material. Typical additives that consist of low molecular weight small molecules tend to cause adverse effects on the bulk polymer into which they are dispersed, such as lowering the glass transition temperature or reducing mechanical strength. Compatible polymers which will self assemble at an interface and impart the desired properties solely upon the surface are therefore highly desirable.

A synergistic combination of experiment and simulation has becoming a powerful means of elucidating the structure of materials at interfaces [67, 238–242]. Whilst experiments are used to explore the physical reality of the system, simulations on the other hand can provide unprecedented access to all positions of all particles at all times, leading to a clearer description of the system of interest. Motivated by the success of earlier works [67, 91], that combine neutron reflectometry and a fully atomistic simulation to provide a molecular-level picture of the organization of amphiphilic polymers at the water/air interface, this work aims at extending the accessible time- and length-scales of the simulation using a coarse-grained molecular model. This class of model has proved to be efficient enough to allow observation of self-assembly at an air-water interface [94–96]. Accordingly, it is encouraging to determine whether this coarser, but faster model, can be use to explain the experimental findings more successfully.

This chapter is concerned with coarse-grained MD simulations of dendritic fluorocarbon end-capped poly(ethylene oxide) polymer at a water-air interface, using the models developed in the previous chapter. In section 6.2.1 a brief introduction is provided to the optical matrix method, which is used to calculate a neutron reflectivity profile for a simulated system. Then we describe how experiments were modelled and how the simulated systems were constructed in section 6.2. Simulation results are presented in section 6.3. Here, neutron reflectometry and general observations are discussed in section 6.3.1-6.3.2, followed by interpretations of results from experiment using the simulation counterparts in section 6.3.3. Comments are

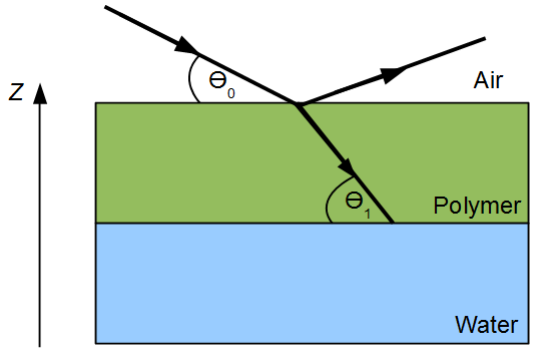

Figure 6.1: Neutron reflection in a simple, three-layer model.

also given for the simulation at high polymer concentrations in section 6.3.4-6.3.5. This chapter is completed with conclusions in section 6.4.

6.2 Methods

6.2.1 The optical matrix method

The optical matrix approach [243,244] involves simulating a reflectivity curve based on a theoretical model where the surface depth profile is described as a series of stratified layers of known thickness and number density.

In a simple three-slab system (i.e. air, polymer layer and water, as shown in figure 6.1), the reflectivity, R, due to the central slab (polymer) can be written as

$$R = \left| \frac{r_{01} + r_{12} \exp(2i\beta_1)}{1 + r_{01} r_{12} \exp(2i\beta_1)} \right|^2, \tag{6.1}$$

where r_{ij} is a Fresnel coefficient, and β_1 is the phase shift of the neutron beam in the polymer layer.

The Fresnel coefficients characterise the optical properties of an interface between two consecutive slabs (i and $j = i + 1$), in terms of their refractive indices as shown in equation 6.2,

$$r_{ij} = \frac{n_i \sin\theta_i - n_j \sin\theta_j}{n_i \sin\theta_i + n_j \sin\theta_j}, \tag{6.2}$$

where n_i is the refractive index of layer i, and θ_i is the angle of incidence of the

neutron beam at the $i/(i+1)$ boundary (air-polymer or polymer-water), after refraction at any previous interface.

The phase shift of the neutron beam can be calculated from equation 6.3

$$\beta_i = \frac{2\pi d}{\lambda} \sin\theta_i, \tag{6.3}$$

where d is the thickness of the polymer layer, and λ is the wavelength of the incident beam.

Theoretically, this approach can be extended to incorporate numerous layers, but in reality the computation becomes exponentially complex. A general solution that overcomes this problem is the characteristic matrix formalism of Born and Wolf [244], where they represent the reflection properties of each stratified layer that models the composition distribution within a characteristic matrix. For example the composition and properties of each layer, i, can be written as a characteristic matrix, M_i, as shown in equation 6.4

$$M_i = \begin{bmatrix} \cos\beta_i & -\frac{i}{\kappa}\sin\beta_i \\ -i\kappa_i \sin\beta_i & \cos\beta_i \end{bmatrix}, \tag{6.4}$$

where $\kappa_i = n_i \sin\theta_i$.

These characteristic matrices are easily multiplied together to give an overall matrix characterising the reflective properties of the entire array of slabs. This resultant matrix is shown in equation 6.5,

$$M_1 M_2 \ldots M_n = M = \begin{bmatrix} M_{11} & M_{12} \\ M_{21} & M_{22} \end{bmatrix}, \tag{6.5}$$

where M_{ij} are the values of the individual elements in the matrix.

The overall reflectivity of the system can then be written in terms of the elements of the matrix, in a fashion analogous to equation 6.1. Equation 6.6 shows the reflectivity in terms of these matrix elements,

$$R = \left| \frac{(M_{11} + M_{12}\kappa_s)\,\kappa_a - (M_{21} + M_{22}\kappa_s)}{(M_{11} + M_{12}\kappa_s)\,\kappa_a + (M_{21} + M_{22}\kappa_s)} \right|, \tag{6.6}$$

where a and s refer to the upper phase (air) and lower phase (bulk water) respectively.

The optical matrix method can be adapted to account for the natural roughness of the various interfaces involved [243] to represent the system more realistically.

Since number density (and therefore scattering length density) is readily calculated from computer simulation, and due to the fact that this simulated data can be simply broken down into slab sequences, the optical matrix method is ideal for generating reflectivity profiles from simulation trajectories to compare to experiment.

6.2.2 Data fitting method

Interpretation of neutron reflectivity data from experiment is generally achieved through comparison (fitting) with simulated reflectivity from a model system. In the fitting procedure, values for the number of layers expected in the system, scattering length densities and the predicted roughness of each layer, as well as information on experimental setup such as incident beam angle, the background noise etc are entered into a computer program in order to achieve the best possible fit for each set of data. Several trial estimates of each individual layer thickness and roughness are usually needed before a satisfactory fit is achieved. Once satisfied that the calculated fits give an acceptable χ^2 value, the output from the program is examined to ensure that the profiles shown are realistic. For example, the surface roughness given by the program should not exceed a value of thickness of the layer itself. The root mean-square roughness of water is typically accepted as 3 Å [245] and even at the reduced surface tensions contributed from polymers this should not exceed a value of 7 Å. In the experimental study by Bartram [85], any fit to the data with an apparent surface roughness exceeding 10 Å was rejected immediately as unrealistic. The output from the fitting program consists of a value for the scattering length density, thickness and roughness of each layer, which can then be converted to a scattering length density vs. sample depth profile.

6.2.3 Modeling experiments

The materials studied by neutron reflectometry [85] contain PEO chains with a molecular weight of around 8100 to 9600 g mol^{-1}. The PEO chain used in simulations therefore designed to contain 200 EO units, corresponding to a molecular weight of 8812 g mol^{-1} (hereafter referred to as 10kPEO).

It is important to note that the F2 and F3 materials analysed in neutron reflectivity measurements are not completely functionalized. The end-capping reactions gave 54% and 51% conversion for F2-10kPEO and F3-10kPEO, respectively. This means that there are around 46% and 49% of unfunctionalized PEO chains (without head group) present in the solutions of F2 and F3 systems. To reproduce the experimental conditions as closely as possible, each simulated system was designed such that it is a mixture of 50% functionalized and 50% unfunctionalized PEO chains (containing equal numbers of modified-and unmodified PEO chains).

It is also important to note that in the experimental study, various polymer concentrations were measured by neutron reflectometry. Each concentration was prepared by diluting down an aqueous stock solution with null reflecting water and concentration was reported in a bulk unit (% w/v). This causes difficulty in simulation setup procedure as it is infeasible to establish such a system in a bulk concentration to match with those from experiment. Even at the lowest concentration, an extremely large simulation box and huge numbers of water are still required. In many neutron reflectometry studies, a polymer film is spread on the water surface, in which the concentration is reported in surface concentration unit (e.g. mg m^{-2}). This allows a direct comparison between experimental and simulation results since such a surface concentration can be modelled easily (considering that a huge volume of water at the bottom of the reservoir (a region far from the surface) can be assumed to not be involved in the phenomena occurring at the surface/interface, and therefore, can be ignored and not be included in the simulation box).

Despite the problem mentioned above, some useful comparisons of neutron reflectivity data can still be made. Considering the behaviour of an amphiphilic polymer at a water-air interface and the hydrophobic nature of fluorocarbon head group as well as an ability of PEO to adsorb at the water surface would drive molecule itself

toward the interface. At a low polymer concentration where there is sufficient surface area available, all molecules should be able to access the surface/interface region and form a single adsorbed layer without leaving any residue in the bulk-phase water (no second layer or micelle formation). If polymer concentration of the simulated and experimental systems is low enough to promote only a single adsorbed layer at their interfaces, different concentration units could be ignored as both systems can be treated similarly as a two-dimensional adsorbed layer. Since we are studying the same neutron scattering species, any match of reflectivity profile found between experiment and simulation at this low concentration range would therefore indicate an identical interfacial organisations between them.

6.2.4 Coarse-grained simulations

Molecular dynamics simulations of the water-air interface were performed using the GROMACS 4.5.5 simulation package (single precision), employing numerical potentials for all types of inter-and intramolecular interactions. We employ three-dimensional periodic boundary conditions for all systems. During MD simulations, we use the the Nose-Hoover algorithm to control the temperature with a temperature coupling constant of 0.5 ps. Equations of motions are integrated applying the Leap-frog algorithm with a time step of 5 fs. A potential cutoff of 1.6 nm was used for nonbonded interactions. Cutoff corrections were obsolete, since all tabulated potentials were designed to shift smoothly to zero at the cutoff distances. No electrostatics were present for the coarse-grained simulations. All calculations were carried out in a canonical ensemble (NVT) at 298 K.

6.2.5 Preparation of a single chain of F2-10kPEO and F3-10kPEO

The initial step of setting up the simulated system is to prepare a single relaxed chain of F2-10kPEO and F3-10kPEO that can be replicated to produce a multiple-chain target system. Note that the terms F2-10kPEO and F3-10kPEO represent the system of di-and trifluoro dendritic end-capped PEO (with M_w PEO = 8812 g

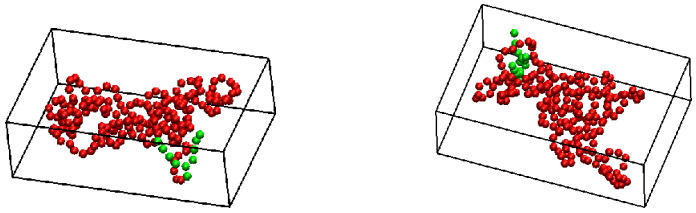

(a) F2-10kPEO (b) F3-10kPEO

Figure 6.2: Snapshots showing the single relaxed chains of di-and trifluoro dendritic end-capped PEO used in this study. The red colour represents the ethylene oxide unit and the green colour represents the fluorocarbon head group.

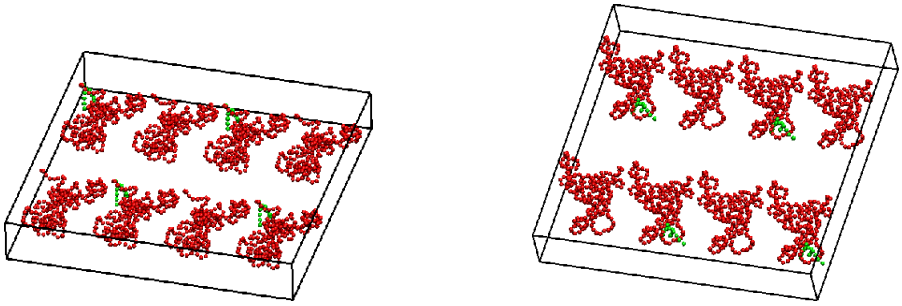

(a) F2mix44 (b) F3mix44

Figure 6.3: Slabs of mixed functionalized- and unfunctionalized PEO polymer used to replicate as starting structures for the target systems.

mol^{-1}), respectively.

To obtain this original single chain, we first built a chain of F2-10kPEO (F3-10kPEO) using bond parameters at their energy minimum. The chain was then subjected to a gas-phase simulation to allow it to adopt a random coil arrangement. The ones chosen as single chain models are showed in figure 6.2 (a) for F2-10kPEO and 6.2 (b) for F3-10kPEO. Note that both polymers have roughly the same size: approximately 100.0 Å, 50.0 Å and 30.0 Å, respectively, in x, y and z dimensions.

6.2.6 Preparation of a slab of mixed F2-10kPEO/10kPEO and mixed F3-10kPEO/10kPEO

Before setting up a water-air interface, slabs containing the desired number of polymer chains were prepared. The single chain from the previous section was first replicated by 2 and 4 times along the x and y dimensions, respectively. This results in 8 polymer chains in a box size of 200.0 Å by 200.0 Å by 30.0 Å (with the z dimension being the smallest). The mixture of F2-10kPEO/10kPEO (F3-10kPEO/10kPEO)

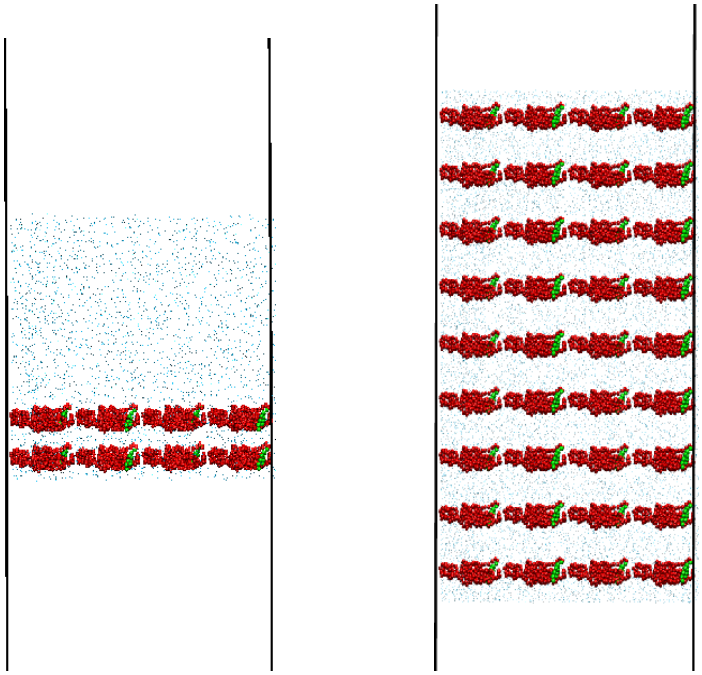

(a) F2mix88 (b) F2mix3636

Figure 6.4: Examples of starting configurations used in simulation of amphiphilic polymers at a water-air interface. (a) low concentration (all chains were shifted to be close to one end of the water slab) and (b) high concentration (chains were placed throughout the water slab).

was then obtained by simply removing the head group of every alternate molecule, leaving only half of them remaining functionalized. Therefore, each system contains 4 functionalized- and 4 unfunctionalized PEO chains, as depicted in figure 6.3 (a) and (b).

To simplify notation, hereafter we refer to each system as "F$x$mixnm", where x represents the number of fluorocarbon branches of the head group, which could be 2 or 3 in this study. n and m are usually equal, representing respectively the number of functionalized- and unfunctionalized PEO chains in the system. For example, the system containing 4 molecules of F2-10kPEO and 4 molecules of 10kPEO, will be referred to as F2mix44.

For preparations of systems that require more polymer chains, the F2mix44 slab can be replicated along the z dimension as needed until the number of polymer chains match the requirement. For example, the F2mix88 system can be obtained from replicating of the F2mix44 system by 2 times along the z direction.

6.2.7 Setting up a water-air interface

Many water-air interface systems with polymer concentration ranging from low to high, have been created in this study. They are all constructed in a similar way, which is described as follows.

For each system, it is necessarily to have a water slab thick enough to represent a bulk water phase as well as to accommodate the polymer chains in their fully extended conformation. Therefore, before solvating with water, the z length of polymer slab prepared from the previous section was increased by about 2.5 times of the current z length. Since there are two interfaces in the simulation box (due to periodic boundaries), all the polymer chains were shifted to be close to one end of the slab (as shown in figure 6.4 (a)) to encourage all chains to diffuse to the same surface when they reach equilibrium. This will be convenient for comparisons of results among simulated systems. However, for high concentration systems where a large slab of many polymer chains was created, all chains can not be located close to only one side of the water surface. They have to be placed throughout the water slab, as shown in figure 6.4 (b).

It should be noted that, apart from the z dimension that can be extended as appropriate, we kept the x and y lengths the same for each system at 200.0 Å (surface area = 200 × 200 $Å^2$). For a PEO chain with M_w = 8812 g mol^{-1}, the radius of gyration and the root mean-squared end-to-end distance are estimated to be 39.2 Å and 96.3 Å, respectively [210], therefore, the box size used here is certainly large enough to accommodate the polymer chains in their fully extension in both x and y directions.

After solvating with water, the z dimension was further increased by a factor of approximately three times of the current length. This created a water/air interface in the simulation box with sufficient distance between the two interfaces to prevent their interaction. Each system was first subjected to energy minimisation, followed by a short equilibration run to allow an equilibrated water/vapour interface to form. Once the water/air interface was set up, a production run was conducted for data analysis.

In this study, a series of air-water interface systems have been constructed and

Table 6.1: Detailed information for simulated systems. The z-length in brackets is the size before solvating with water. Note that one water bead is equivalent to four real water molecules.

System	$n_{\mathrm{F2-10kPEO}}$	$n_{\mathrm{F3-10kPEO}}$	n_{10kPEO}	n_{Water}	z length	simulated time
F2mix22	2	-	2	29,579	300 (100) Å	100 ns
F2mix33	3	-	3	29,495	300 (100) Å	100 ns
F2mix44	4	-	4	51,752	450 (150) Å	100 ns
F2mix55	5	-	5	51,353	450 (150) Å	100 ns
F2mix66	6	-	6	50,950	450 (150) Å	120 ns
F2mix77	7	-	7	54,009	540 (180) Å	120 ns
F2mix88	8	-	8	53,896	540 (180) Å	120 ns
F2mix1212	12	-	12	59,366	600 (200) Å	150 ns
F2mix2424	24	-	24	84,852	900 (300) Å	200 ns
F2mix3636	36	-	36	113,633	1200 (400) Å	300 ns
72F2-10kPEO	72	-	-	112,558	1200 (400) Å	300 ns
F3mix22	-	2	2	29,567	300 (100) Å	100 ns
F3mix33	-	3	3	29,503	300 (100) Å	100 ns
F3mix44	-	4	4	51,826	450 (150) Å	100 ns
F3mix55	-	5	5	51,231	450 (150) Å	100 ns
F3mix66	-	6	6	50,829	450 (150) Å	120 ns
F3mix77	-	7	7	53,993	540 (180) Å	120 ns
F3mix88	-	8	8	53,724	540 (180) Å	120 ns
F3mix1212	-	12	12	58,619	600 (200) Å	150 ns
F3mix2424	-	24	24	84,712	900 (300) Å	200 ns
F3mix3636	-	36	36	113,485	1200 (400) Å	300 ns
72F3-10kPEO	-	72	-	112,121	1200 (400) Å	300 ns

simulated. Detailed information for each simulation, including number of polymer chains and water beads, box size before and after solvating with water, and simulation time, are summarised in table 6.1.

6.3 Results and discussion

6.3.1 Neutron reflectometry and general observations

Using the simulation trajectory dump file, it is possible to produce a number density profile which show the number per unit volume of fluorocarbon head group, EO units and water varying across the simulation box. As examples, the profiles in figure 6.5

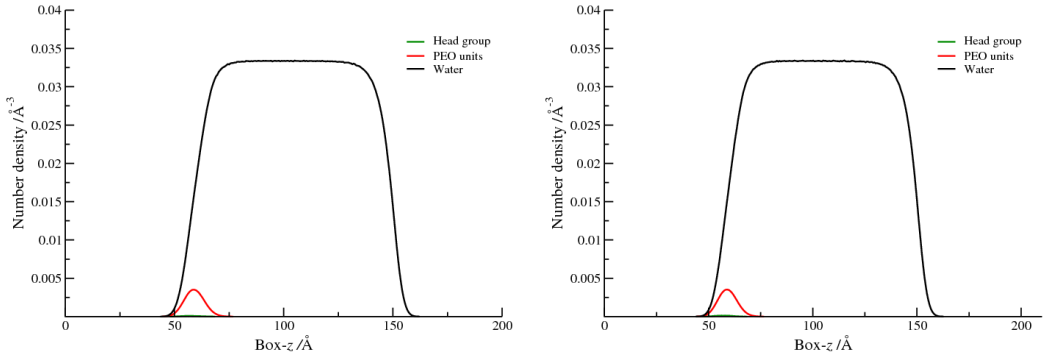

(a) F2mix44 (b) F3mix44

Figure 6.5: Examples of number density profiles from simulations of di-and trifluoro dendritic end-capped PEO at a water-air interface.

(a) and (b) show the change in number density along the z-axis (perpendicular to the water surfaces) for F2mix44 and F3mix44 systems, respectively. The number density profile is in turn converted to a scattering length density (SLD) profile using equation 1.3 and scattering length data in table 1.1 of chapter 1. According to the previous experimental study [85], neutron reflectivity was measured in null reflecting water and all the PEO segments were fully deuterated while the fluorocarbon head group was left fully hydrogenous. These factors were taken into account in calculation of the SLD from simulation data. The SLD profiles were then used to calculate a neutron reflectivity profiles employing the optical matrix method described earlier in section 6.2.1. To generate a neutron reflectivity profile, the SLD for each system was divided into many small layers with a thickness of approximately 5 Å each. A surface roughness of 3 Å was used for each layer. This value is about the same order as a typically accepted roughness of a water surface [245]. The experimental systems have had the background reflectivity subtracted, so in all plots of reflectivity (simulated and experimental), a constant background of about 3.7×10^{-6} was added to the reflectivity values in this study. This will allow more objective comparisons to be made between the various systems.

6.3.1.1 F2 system

The scattering length density as a function of position in a direction perpendicular to the water surface for F2mix22 to F2mix88 systems are plotted together in figure 6.6 (a). It is immediately apparent from the profiles that there is an excess of polymer

(a)

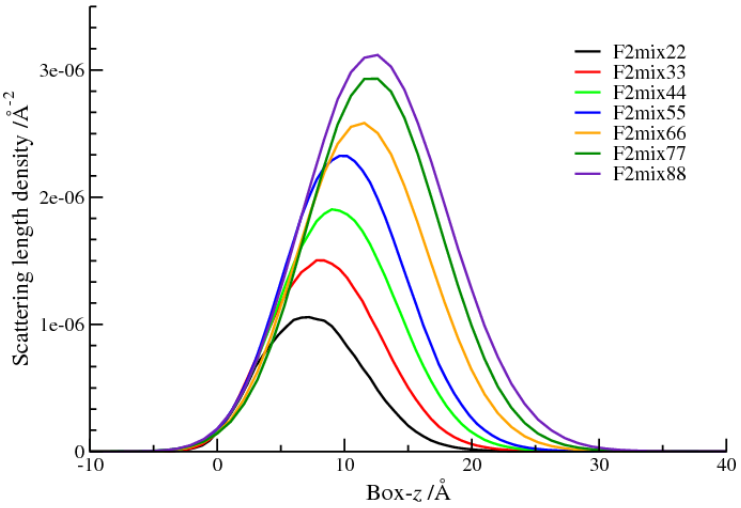

(b)

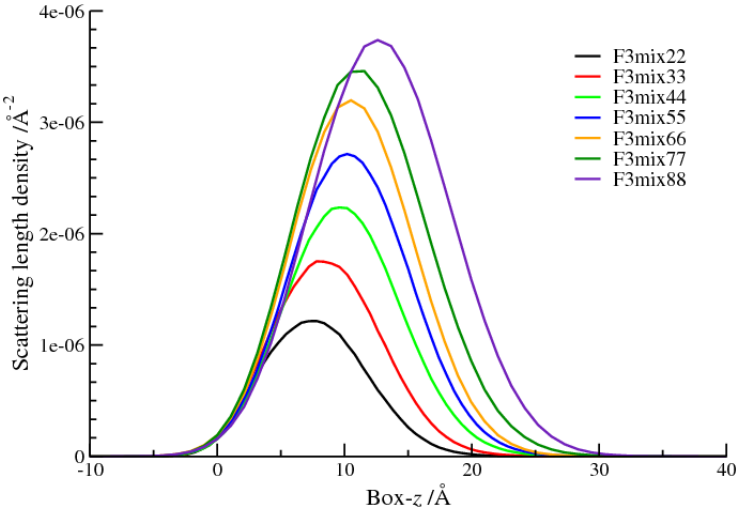

Figure 6.6: Scattering length density profiles calculated from simulations of F2 (a) and F3 (b) systems in null reflecting water. Polymer layer is formed at the interface region and the left-hand side (-z) and right-hand side (+z) represent air- and bulk water phase, respectively.

(a)

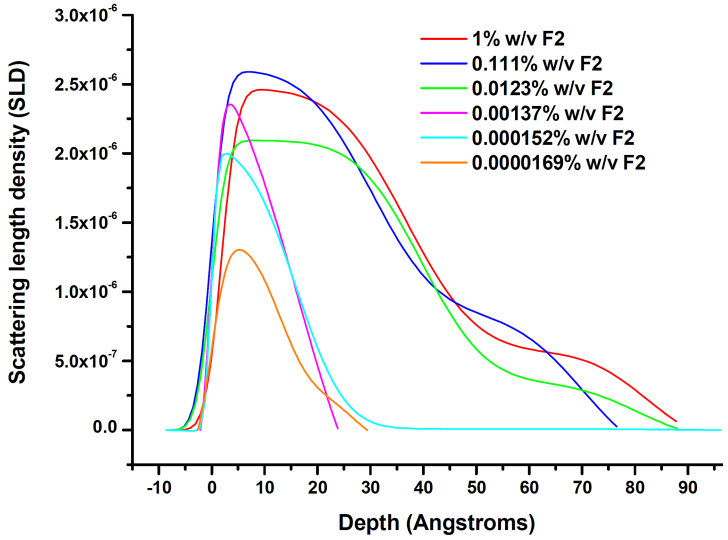

(b)

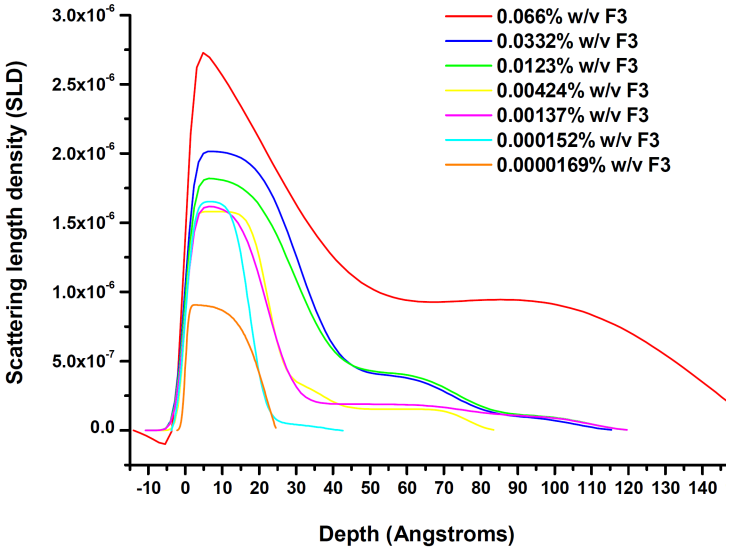

Figure 6.7: Scattering length density profiles for varying weight percentages of F2 (a) and F3 (b) in null reflecting water. Theses data are provided by Bartram [85], which were obtained from fits using a single to triple layer model.

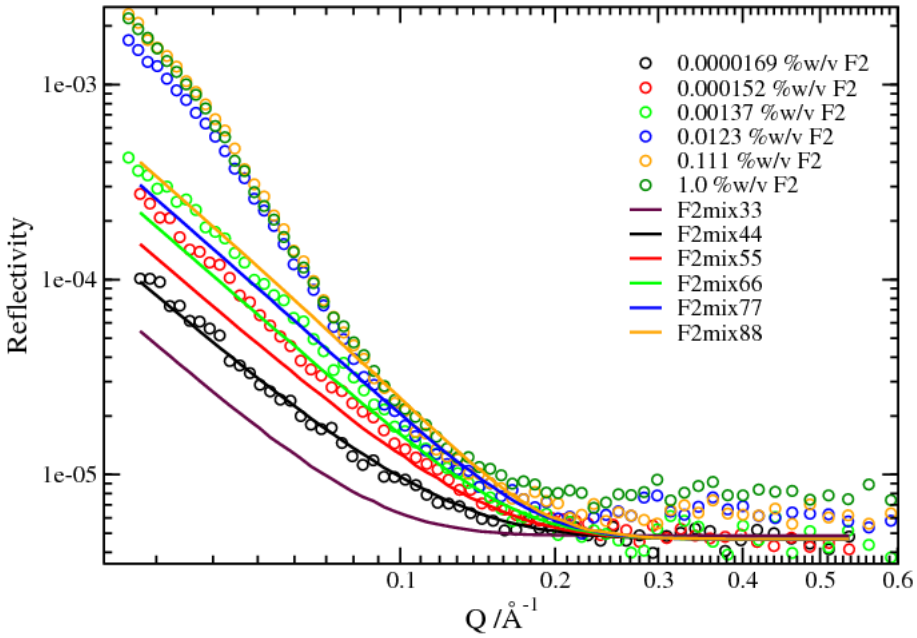

Figure 6.8: Simulated neutron reflectivity profiles (solid line) in comparison to the experimental results (circle) for the F2 system in null reflecting water.

formed at the water-air interface. As can be seen from the density peaks, this excess is increased at the interface as the concentration of polymer is increased.

Observation of changes through the course of the simulation shows that, for the F2mix22-F2mix88 simulations, both functionalized- and unfunctionalized PEO chains have moved readily out of the bulk water toward the interface. There is no evidence indicating that modified chains have reached the interface before the unmodified ones. Chains that are initially placed closer to the interface were likely to reach the interface first. After approaching the interface region, polymers then spread along the surface plane and form a thin adsorbed layer there with just a few PEO chains occasionally extended into the bulk water. In every simulation, it took less than 30 ns for all the polymer segments to diffuse from the bulk water to the interface and form a stable layer there. This behaviour then persisted until the end of the simulation, indicating that the system has reached equilibrium. We point out here that the density profiles and other results reported in this chapter are calculated after each system has reached its equilibrium state.

The neutron reflectivity profiles generated from SLD profiles of F2 simulations are plotted together with the reflectivity data from experiment in figure 6.8. As

pointed out before in section 6.2.3, the profiles generated from simulation and experiment can not be compared directly due to different concentration units. We only show here first the overall trend of the profiles observed within the two studies. From the results showed in figure 6.8, it is encouraging to see that the trends of increasing reflectivity with polymer concentration seen experimentally are reproduced by the simulations. This trend is only to be expected, since the concentration of deuterium atoms (the only significantly reflecting species in the system) increases with surface concentration. The features such as slope and shape of the profiles are fairly similar for both studies, especially at low concentration region.

In the experimental study of the F2 system by Bartram [85], fitting of neutron reflectivity profiles using a two to three layers model yielded scattering length density profiles as showed in figure 6.7 (a). From the surface excess and the SLD shape, the author suggested that a single surface layer can only be supported for concentrations below 0.00137 %w/v. A critical concentration at which the material become saturated at the surface was suggested to occur at around 0.00137 %w/v. Above this concentration, the SLD profiles show the presence of considerable amounts of polymeric material in the bulk subphase, leaving open the possibility that this could be due to stretching of PEO tails, the presence of a second layer beneath the first, micelle formation, or a combination of these. As mentioned earlier in section 6.2.3, a useful comparisons of neutron reflectivity profiles can be made between experimental and simulation studies at low concentration, where both systems show only a single adsorbed polymer layer. Therefore we focus on comparing of simulated reflectivity profiles with those measured experimentally at a concentration below 0.00137 %w/v. If the simulated and experimental profiles are to represent identical interfacial organisations, the profile must follow similar trajectories of comparable magnitude and produce features such as the slope and shape of the profile.

In this study, the reflectivity profile generated from the F2mix44 simulation was found to match very well with experiment data at the lowest concentration (0.0000169 %w/v), as plotted separately in figure 6.9. Moreover, the profile generated from the F2mix66 system also shows good agreement with the experimental 0.000152 %w/v (see figure 6.11). The thickness of polymer layer as obtained from

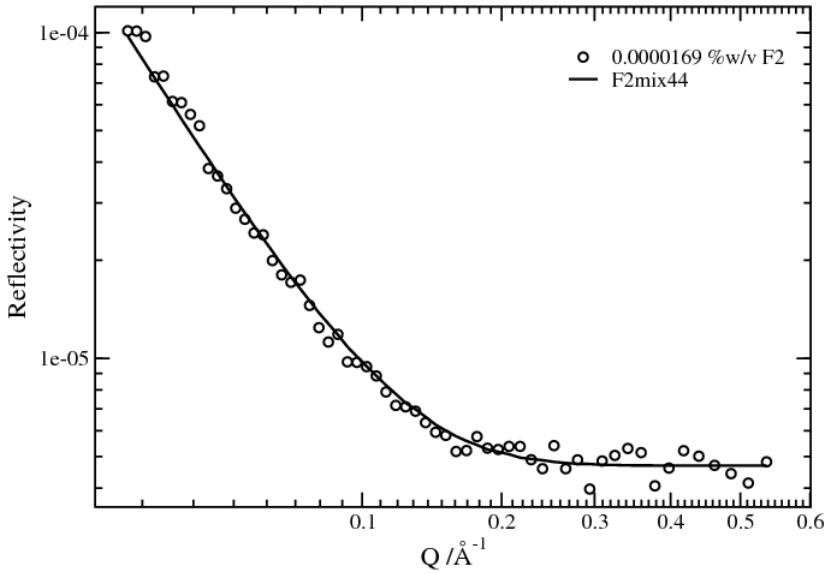

Figure 6.9: The match between reflectivity profiles from the experimental 0.0000169 %w/v and the F2mix44 simulation.

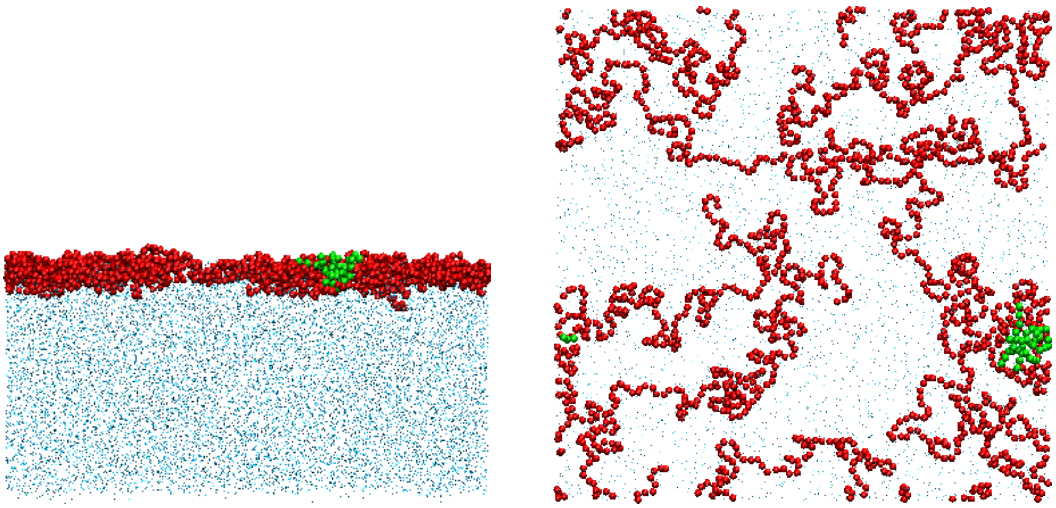

Side view Top view

Figure 6.10: Final snapshots from 100 ns MD simulation of F2mix44 system.

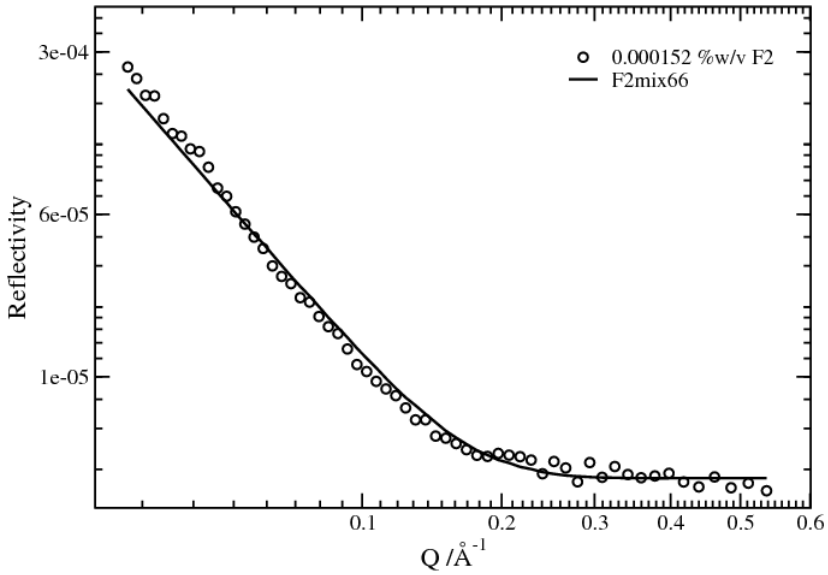

Figure 6.11: The match between reflectivity profiles from the experimental 0.000152 %w/v and the F2mix66 simulation.

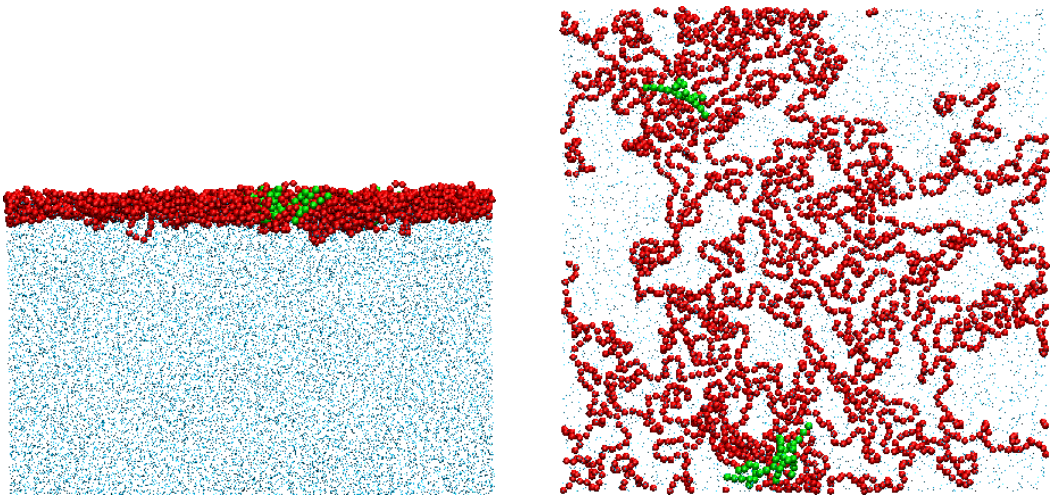

Side view Top view

Figure 6.12: Final snapshots from 100 ns MD simulation of F2mix66 system.

fitting of the experimental reflectivity using a double layer model is around 30 Å for both 0.0000169 %w/v and 0.000152 %w/v systems (see the SLD profiles in figure 6.7 (a)). The corresponding F2mix44 and F2mix66 simulations yield thicknesses of approximately 25 Å and 30 Å (see the SLD profiles in figure 6.6 (a)), in accordance with experimental fitting models.

The final configurations of the F2mix44 and F2mix66 simulations are depicted in figure 6.10 and figure 6.12. It is obvious from these simulations that the fluorocarbon end as well as ethylene oxide segments are able to adsorb at the interface. Both simulations show the formation of a flat layer of polymer at the interface with only small PEO segments looping into the bulk water. The top view of both simulations reveals that there are some assemblies of the head groups at the interface. This is expected behaviour since the head groups would prefer aggregation with each other to maximise their hydrophobic-hydrophobic interactions. As implied by the agreement of neutron reflectivity profile and the polymer layer thickness, molecular organisation in the two experimental studies (0.0000169 %w/v and 0.000152 %w/v) or at least in the lowest concentration one (0.0000169 %w/v), should be expected to be similar to that observed in their corresponding simulation systems.

6.3.1.2 F3 system

The scattering length density profiles for F3mix22-F3mix88 systems are plotted together in figure 6.6 (b). As was seen in the previous results for the F2 polymer, it is again apparent from the profiles that there is an excess of F3 formed at the water-air interface with this excess increasing as the polymer concentration is increased. It can be seen that the profile shape and thickness for each F3 system are very similar to those of F2 simulation at equivalent number of chains. However, due to the greater amount of reflecting species (fluorine atoms) in the F3 head group, each F3 system provides slightly higher SLD magnitude than the corresponding F2 one.

The SLD profiles were converted to neutron reflectivity profiles and are shown together with those measured experimentally in figure 6.13. Again, the simulated profiles, particularly at low concentrations, follow similar slopes and shapes as those from experiment. The reflectivity profile generated from the F3mix33 simula-

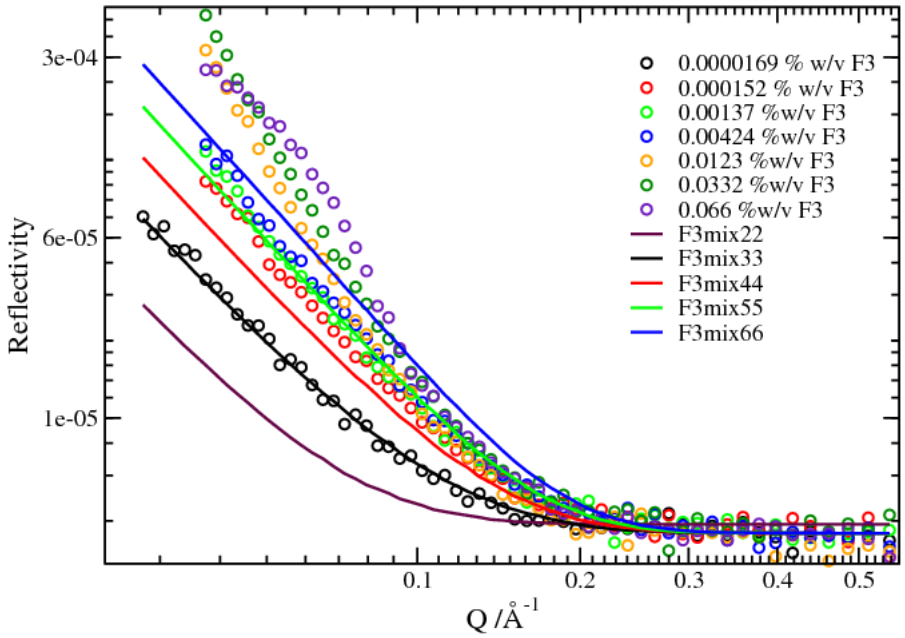

Figure 6.13: Simulated neutron reflectivity profiles (solid line) in comparison to the experimental results (circle) for F3 system in null reflecting water.

tion is almost perfectly matched to that of experiment at the lowest concentration (0.0000169 %w/v), as plotted in figure 6.14. The F3mix33 simulation yields a polymer layer thickness of approximately 23 Å, which is only about 2 Å thinner than the result from experiment. The predicted reflectivity profile from F3mix55 also follows the same line with those of the 0.00137 %w/v and 0.00424 %w/v experiments, as shown in figure 6.16. However, the polymer layer thickness as obtained from fitting of neutron reflectivity data for both experiments is about 40 Å, which considerably greater than that yielded by the F3mix55 simulation (∼25 Å).

The final snapshots from the simulations of the F3mix33 and F3mix55 are shown in figure 6.15 and 6.17. A molecular structure obtained from these two simulations is essentially similar to that described previously for the F2mix44 and F2mix66 systems, showing that polymer adsorb to the interface by a combination of fluorocarbon head group and PEO segments. Spreading of polymer chains along the surface plane with the formation of the head groups assemblies are also observed in the snapshot top views of both F3 systems.

Once again, the excellent agreement of the neutron reflectivity and polymer layer thickness of the F3mix33 simulation and the lowest experimental concentra-

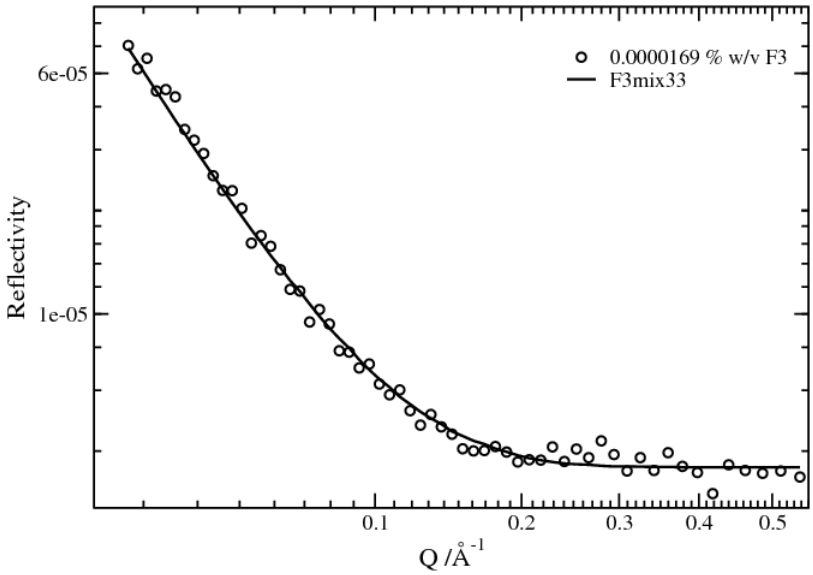

Figure 6.14: The match between reflectivity profiles from the experimental 0.0000169 %w/v and the F3mix33 simulation.

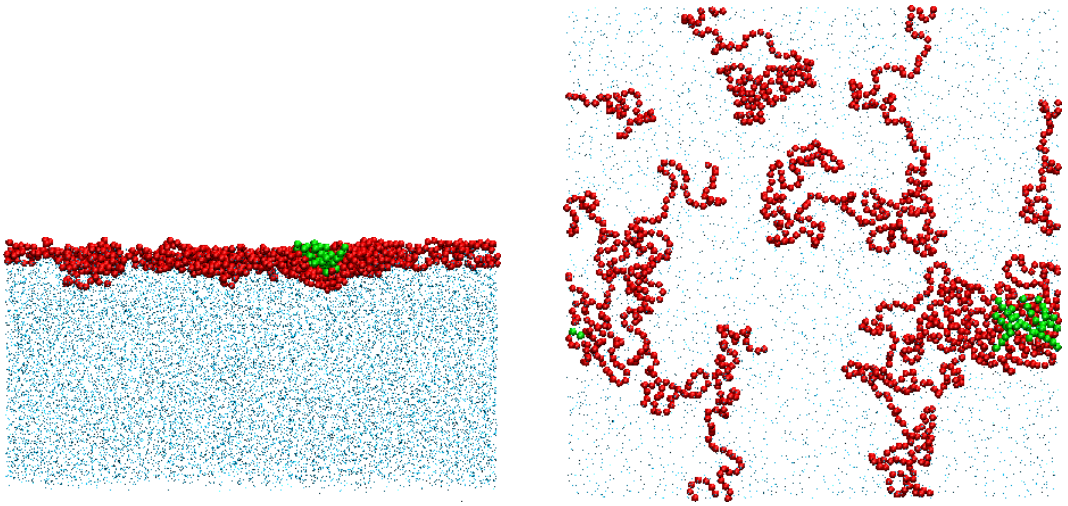

Side view Top view

Figure 6.15: Final snapshots from 100 ns MD simulation of F3mix33 system.

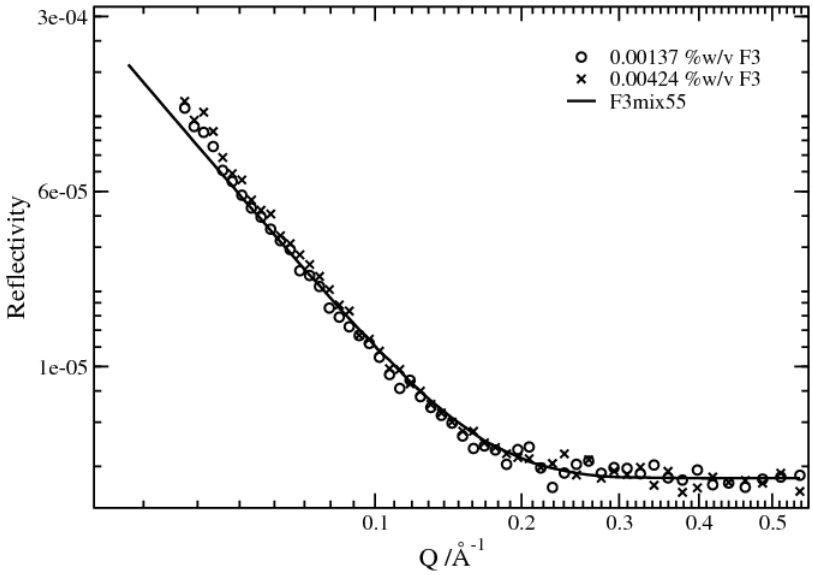

Figure 6.16: The match between reflectivity profiles from the experimental 0.000137-0.00424 %w/v and the F3mix55 simulation.

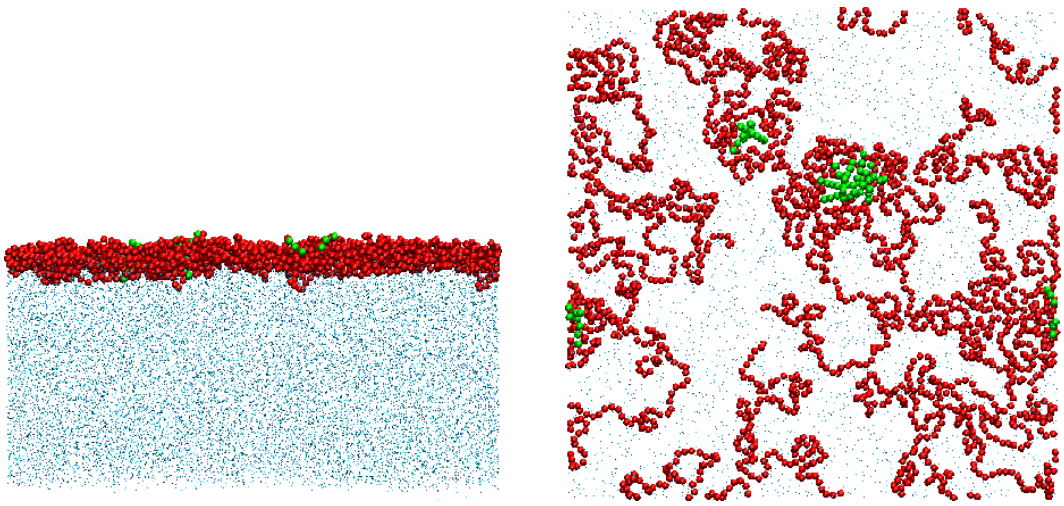

Side view Top view

Figure 6.17: Final snapshots from 100 ns MD simulation of F3mix55 system.

tion (0.0000169 %w/v) indicates a similar interfacial organisation in simulation and experiment. According to the SLD profiles obtained from fitting of experimental data (shown in figure 6.7 (b)), the surface becomes saturated with polymer at concentrations around 0.00137-0.00424 %w/v. These two experimental concentrations should thus be considered as high concentration ones, and polymer adsorption will be more complicated than just a single adsorbed layer. For this reason, although the F3mix55 simulation has provided a good match of reflectivity profile to those of the two experiments, this might not necessarily means that both experiment and simulation have adopted similar interfacial structure.

Having discussed the neutron reflectivity results for both F2 and F3 systems, it appears that the coarse-grained simulations provide a more detailed description of interfacial organisation in comparison to the models typically adopted in neutron reflectometry studies. The former technique is able to resolve the polymer layer profile on the sub-Angstroms scale, and more importantly, a clear picture of the microstructure of the amphiphilic polymer at the interface can be obtained using this simulation technique.

6.3.2 Simulations at high polymer concentration

Since experiment and simulation were studied in different concentration units, a molecular picture at a high concentration region can not be drawn directly by comparison of the neutron reflectivity profile. Nevertheless, as shown in the previous section, the characteristics identified in the simulated profiles at low concentrations can be related to the experimental data reasonably well. Accordingly, it is encouraging to use the current models to simulate at higher polymer concentration to see what would be observed if we increase polymer concentration until the system reach its critical surface concentration and beyond. Information acquired from these simulations will be used to compare and discuss with the experimental results in section 6.3.3.

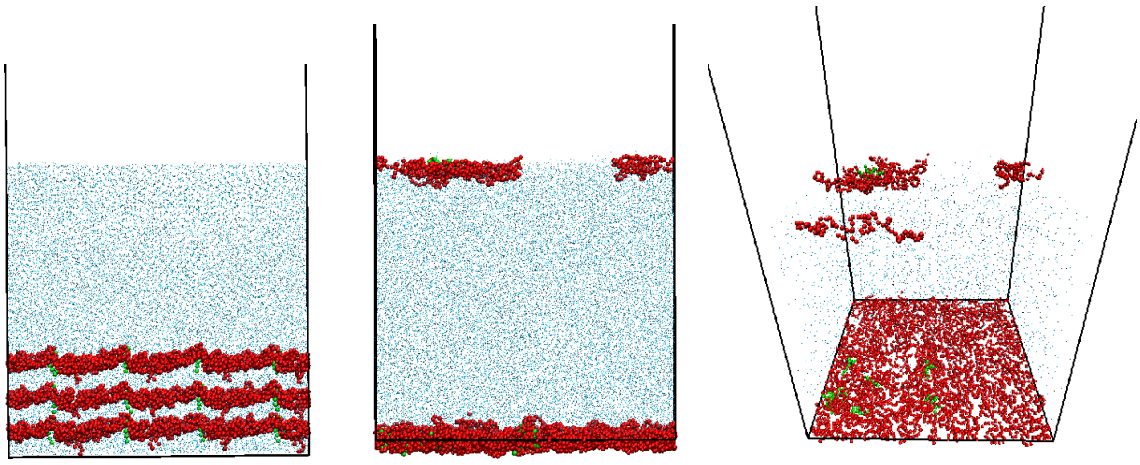

t = 0 ns t = 150 ns (side view) t = 150 ns (top view)

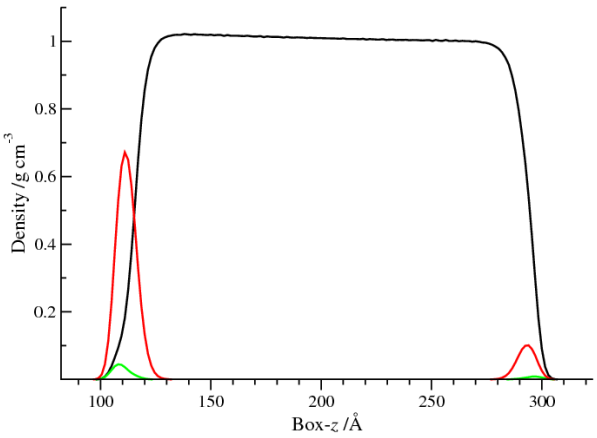

Figure 6.18: Starting (t = 0 ns) and final (t = 150 ns) configurations from the water-air interface simulation of F2mix1212 system. The plot shows mass density profiles for fluorocarbon head group (green line), PEO (red line) and water (black line) along the normal to the air–water interface.

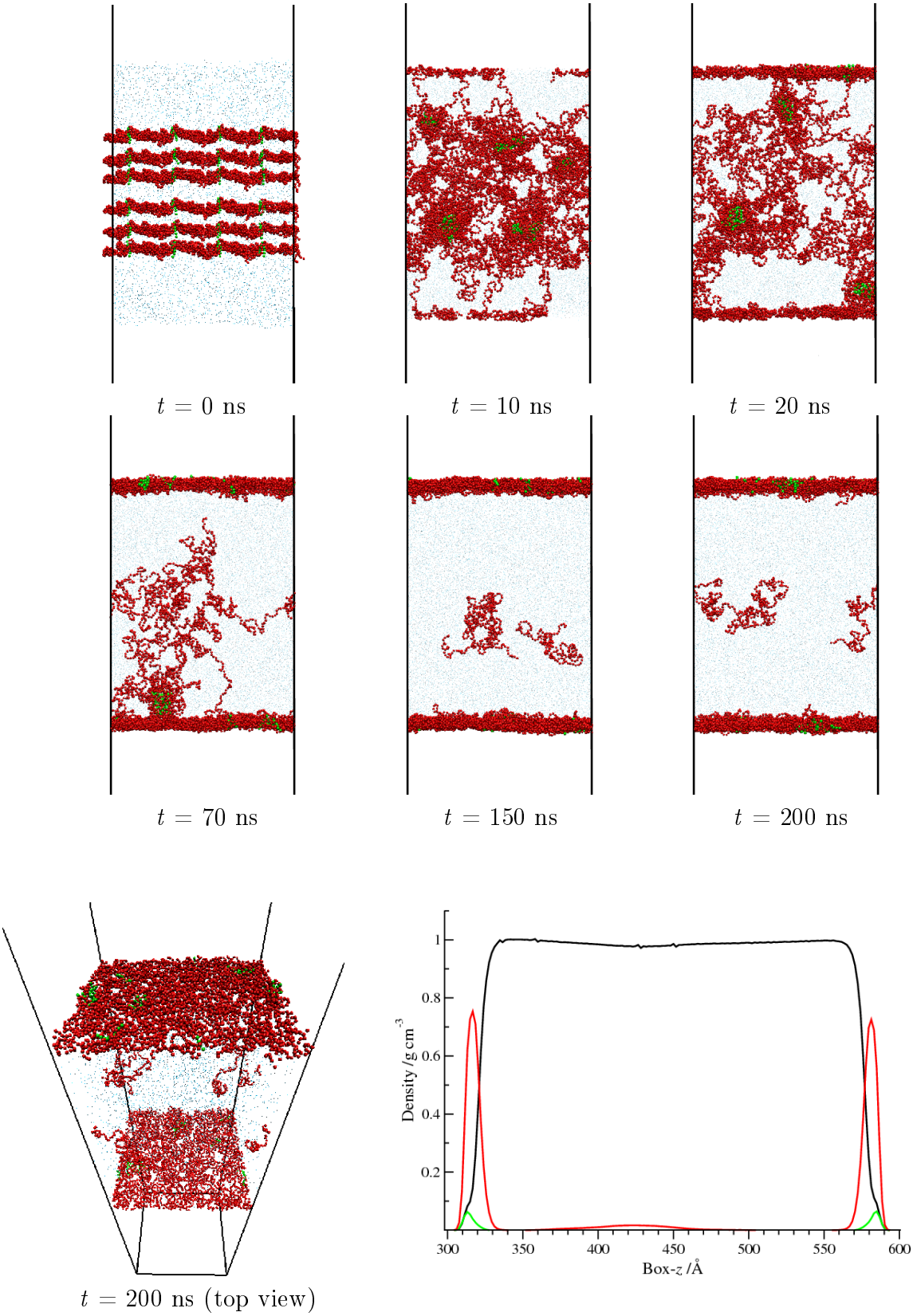

Figure 6.19: Snapshots from the water-air interface simulation of F2mix2424 system. The bottom plot shows mass density profiles for fluorocarbon head group (green line), PEO (red line) and water (black line) along the normal to the air–water interface.

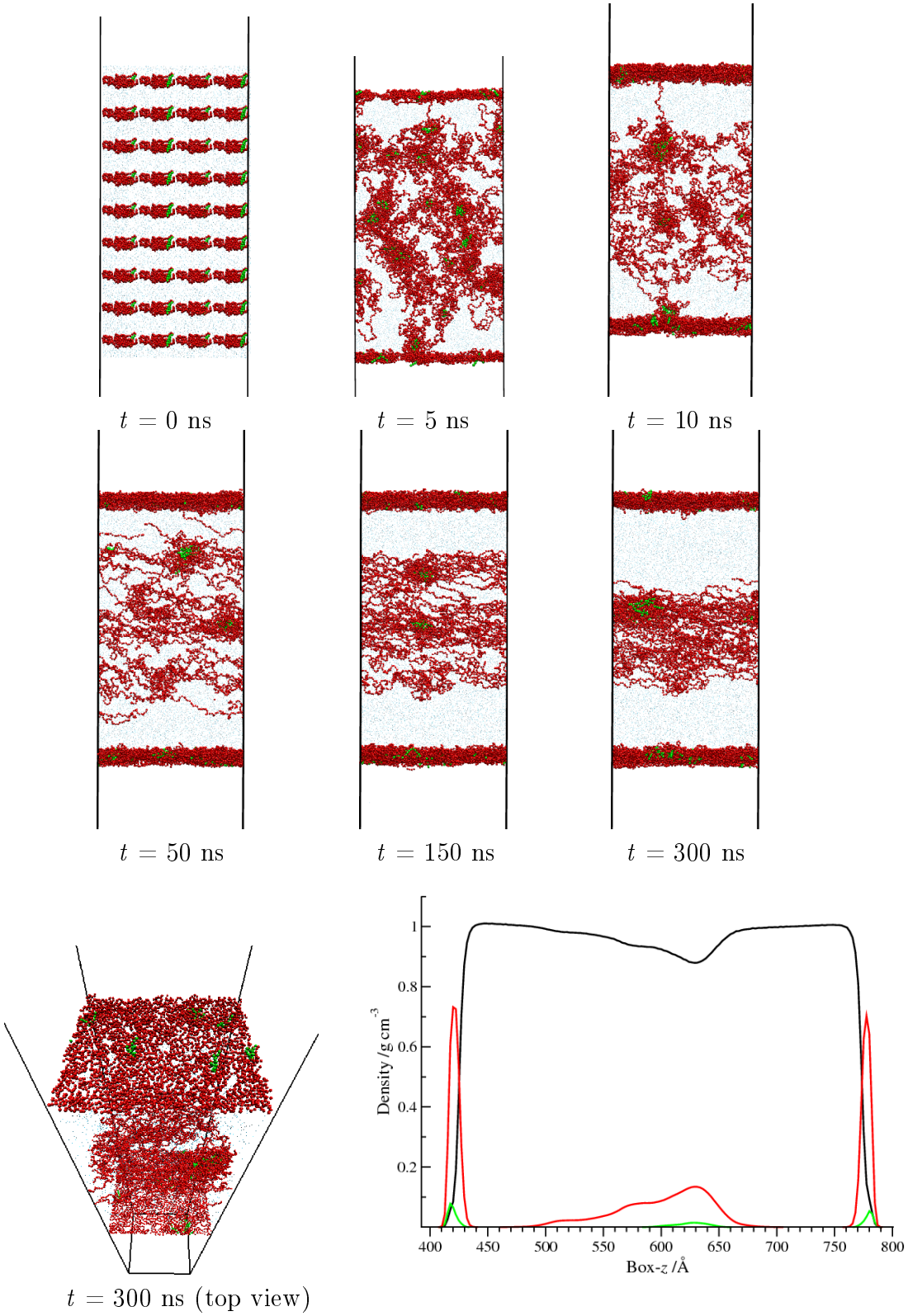

Figure 6.20: Snapshots from the water-air interface simulation of F2mix3636 system. The bottom plot shows mass density profiles for fluorocarbon head group (green line), PEO (red line) and water (black line) along the normal to the air–water interface.

6.3.2.1 F2 system

Upon increasing number of polymer chains in simulation study, we found that surface saturation likely to occur at high surface concentrations for the F2mix1111 or F2mix1212 system. This is evidenced form the simulation of the F2mix1212 that showed 3 chains (2 chains of modified PEO and 1 chain of unmodified PEO) at the other interface of the simulation box, as shown in the final snapshot of this system in figure 6.18. This is possibly because there is no more room for these chains to pack at the nearest surface which is already crowded by other chains. As a result, with long enough simulation, these chains diffused through the water slab to find another interface at the far side. The density profile for the three components (head group, PEO and water) for this system is also plotted alongside the final configuration in figure 6.18.

Having estimated the surface saturation point, it is very interesting to see what would happen if we increase the polymer concentration further than this. In order to do so, the two higher concentrations; F2mix2424 and F2mix3636, have been constructed and simulated. A series of snapshots that capture interesting phenomena occurring during the simulation are showed in figure 6.19 (F2mix2424) and 6.20 (F2mix3636). Exploration of simulation trajectories from both systems shows that, once the simulation was started, end-capped PEO chains readily formed micelle-like structures in the bulk water to lower unfavourable head group-solvent interactions. These micelles then moved laterally out of the bulk water and eventually filled up at available space at the surface. While adsorption of micelles at the surface occurs, at the same time, unmodified PEO chains are also shown to diffuse from the bulk phase and be able to adsorb to the surface as well.

One interesting behaviour that we observed from these simulations is that, after reaching the interface, the head groups of micelles disaggregated from each other and distributed randomly along the surface plane, as shown in the top views of the final configurations in figure 6.19 and 6.20. For a clearer picture of this phenomenon, snapshots showing disaggregation of the head groups of micelles after reaching the surface are given in figure 6.21. The most likely explanation for this phenomenon is that, once micelles are adsorbed at the surface, the local increase in surface cov-

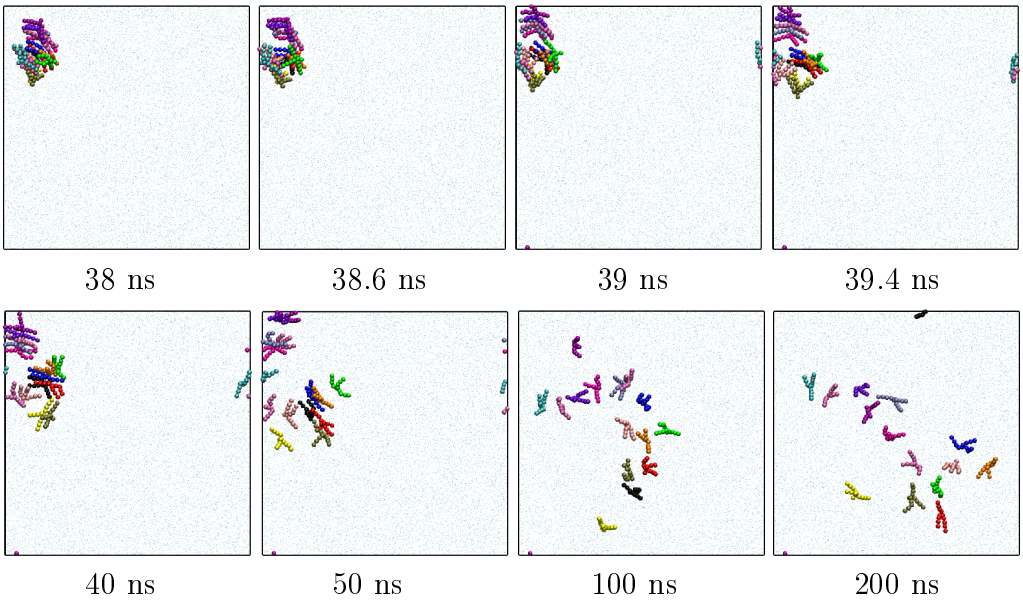

Figure 6.21: Snapshots showing breaking up of the head groups of micelle after approaching the surface. These snapshots are taken from the F3mix2424 simulation (only behaviour at one surface is showed here).

erage will lower the local surface tension, and creating surface tension gradients (Marangoni forces) on the surface. These pulling forces can overcome the micelle's binding force, which eventually, tear the aggregate apart. This explanation was proposed by Colegate and Bain in their study of the adsorption kinetics of surfactants at the air-water interface [246]. They suggested that, in one sense, the surface is acting as an catalyst for micellar disintegration.

Since there are two interfaces (due to periodic boundaries) available for the polymer to occupy, almost all polymer chains in the F2mix2424 system are able to find space at the surface and form a stable layer there. In this system, there were only 3 unmodified PEO chains remaining in the bulk water, which could not join with others as both interfaces had already saturated. For the F2mix3636 system, there is a considerable amount of polymer left in the bulk phase after the two surfaces have already saturated. This includes both unmodified PEO chains and a micelles formed by the modified ones. Examination of the final snapshot in figure 6.20 reveals that there are 11 functionalized- and 19 unfunctionalized PEO chains left in the bulk solution. This result, as well as the 3 unmodified PEO chains found in the bulk water of the F2mix2424 system, implies that the hydrophobic head group of the

PEO chain has enhanced the adsorption ability of the chain.

Observations of a simulation trajectories of the F2mix3636 system shows that, after the surfaces have saturated, there is no further contact between polymers in the adsorbed layer and free materials in the bulk phase water. These excess polymers (unabsorbed polymers and micelles) seem to remain steady in the bulk phase water. In the real experiment one would expect these excess materials to move as close as possible to the interface, i.e. reside right beneath the first adsorbed layer, to favour polymer interactions between the upper and lower layers as well as to avoid interacting with water in the bulk phase. A slow diffusion could be one reason that explains why these excess materials did not approach the surface. As can be seen in the final configuration of the F2mix3636 system, the excess materials tend to form large and dense clusters (including micelles) together in the bulk water. This could lead to a decrease in diffusivity of the cluster due to its higher mass and larger dimension. Figure 6.22 shows the variation of the mean square displacement (MSD) in the z-direction (the direction toward the surface) of one of the end-capped chains that remain in the bulk water. It clearly shows from the plot that the diffusion of this chain is decreased drastically after it has accumulated into the big micelle in the bulk solution at the simulation time of $\sim$170 ns. This supports the assumption that the micelle remaining in the bulk solution diffuse with a very slow rate. Longer simulation times might be required for this cluster to diffuse to the surface (this will be discussed further in section 6.3.4).

One important result that can be extracted out from simulation is the polymer layer thickness. According to the density profiles plotted in figure 6.19 (F2mix2424) and figure 6.20 (F2mix3636), the polymer layer thickness at the interface for both systems is estimated to be 25-30 Å, which is not significantly increased from those observed in the low and medium concentrations. The thickness and magnitude of the density profiles for F2mix1212, F2mix2424 and F3mix3636 systems are roughly in the same order, indicating that no further polymer can be adsorbed at the surface after surface saturation. Close inspection off the final snapshots and the density profiles of the adsorbed layers reveal that as well as fluorocarbon ends being adsorbed, a considerable amount of PEO units are also adsorbed at the air-water interface,

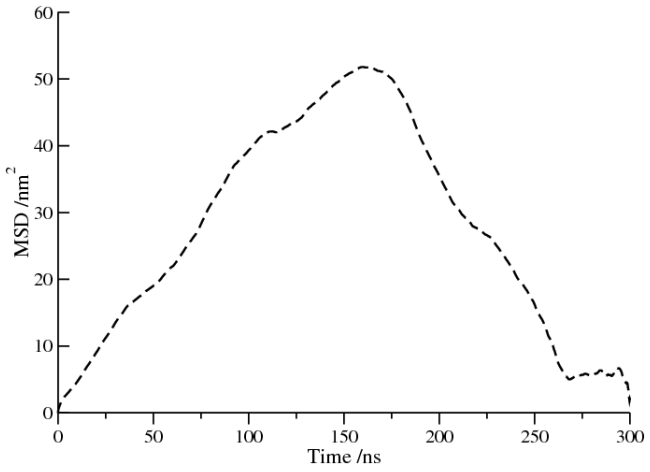

Figure 6.22: Variation of mean square displacement with time for one of the end-capped PEO chains that remain in the bulk solution of the F2mix3636 system.

promoting a rather flat adsorbing structure. No evidence of a stretched PEO conformation is observed for all the F2 simulations.

6.3.2.2 F3 system

The surface saturation for F3 is also found to occur for the 12:12 mixture (F3mix1212), as evidenced from snapshots from this simulation (figure 6.23) that show a fully occupied interface with 20 chains (8 chains of modified PEO + 12 chains of unmodified PEO) and the remaining 4 chains of modified PEO diffused through the water slab to another interface.

Following the previous simulations performed for the F2 system, the F3mix2424 and F3mix3636 were constructed and simulated for comparison. Figure 6.24 and 6.25 show the starting and final configurations for F3mix2424 and F3mix3636 systems, and also show interesting behaviour captured during the the course of equilibration. For both systems, the adsorption behaviour follows a similar trend as those observed in the F2 simulations. This includes initial adsorptions by near-surface polymers (both micelles and unmodified PEO chains). As before, where there is surface space available at the interfaces, unmodified PEO chains (as well as micelles) in the bulk then moved to adsorb there. After reaching the interface, micelles then breakup, merging into the surface.

For the F3mix2424 system, there is only 1 unfunctionalized chain remianing

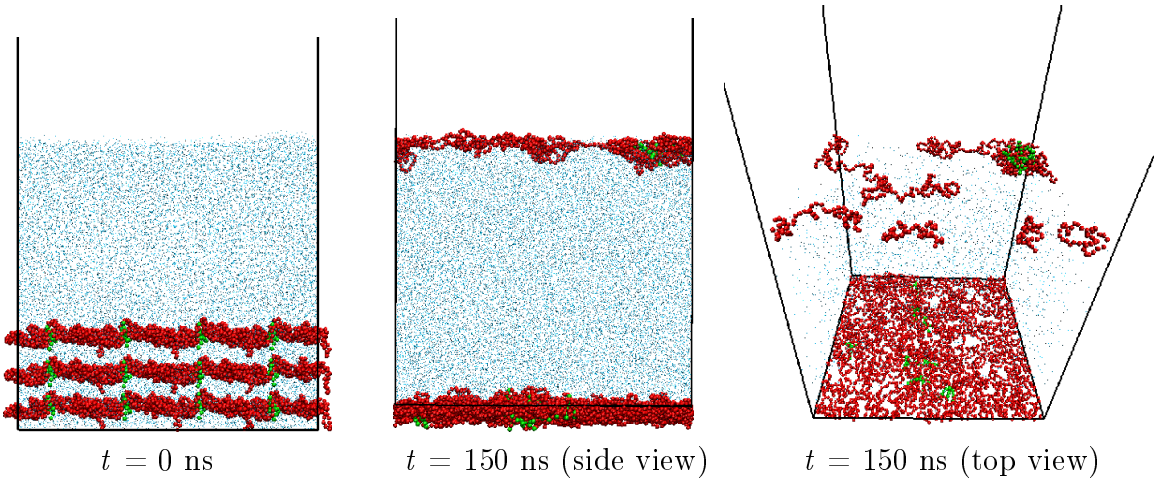

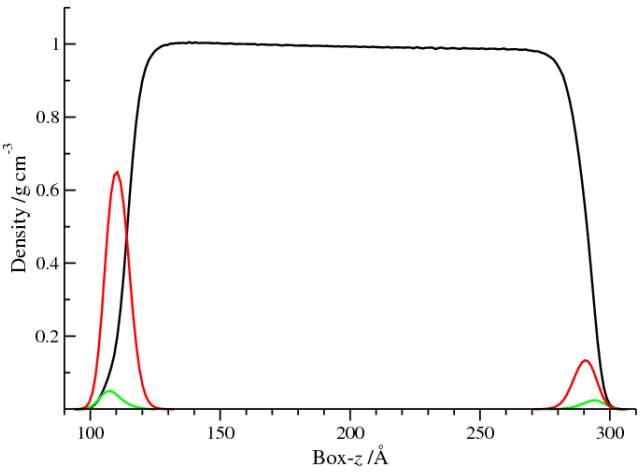

Figure 6.23: Starting (t = 0 ns) and final (t = 150 ns) configurations from the water-air interface simulation of F3mix1212 system. The plot shows mass density profiles for fluorocarbon head group (green line), PEO (red line) and water (black line) along the normal to the air–water interface.

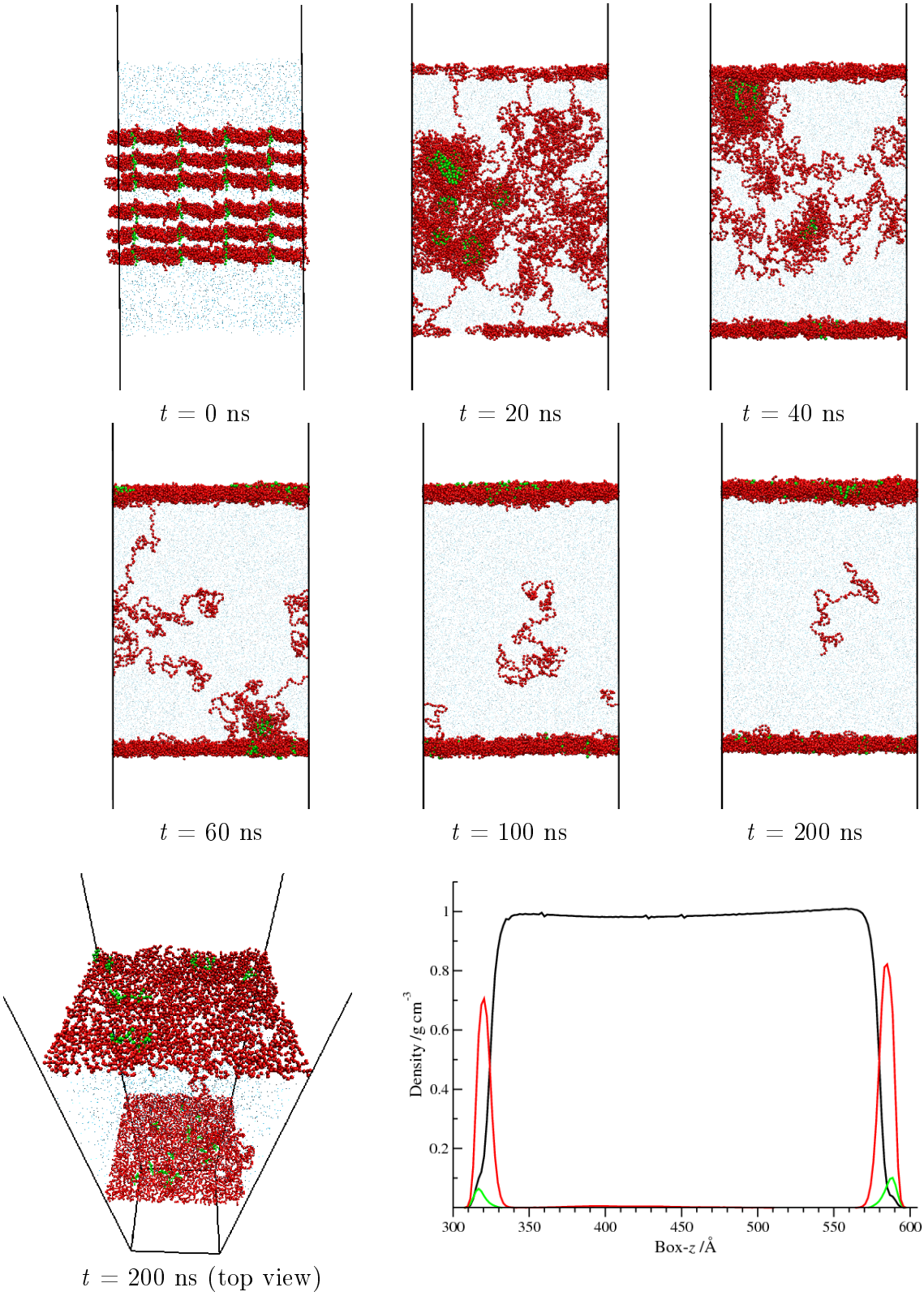

Figure 6.24: Snapshots from the water-air interface simulation of F3mix2424 system. The bottom plot shows mass density profiles for fluorocarbon head group (green line), PEO (red line) and water (black line) along the normal to the air–water interface.

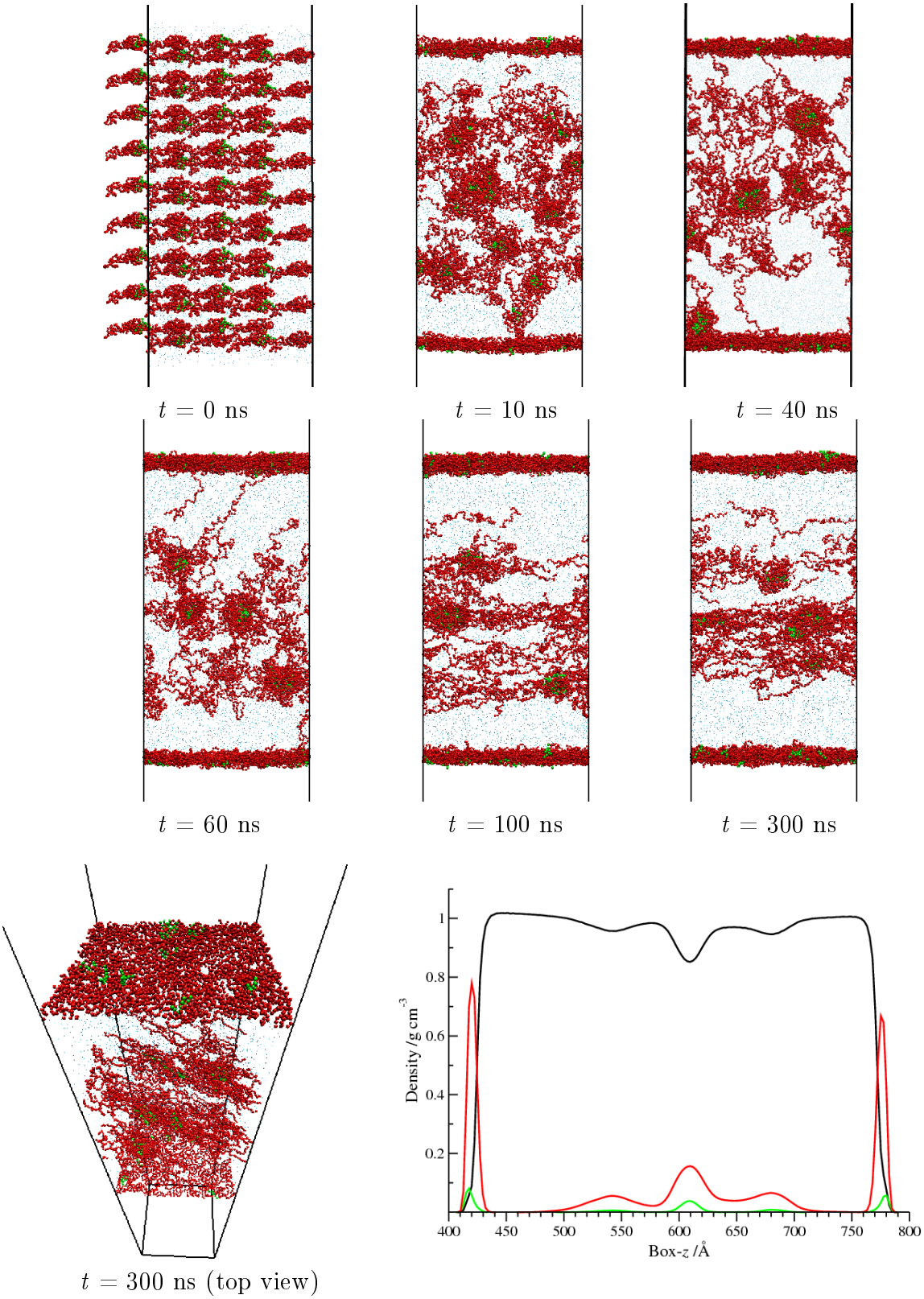

Figure 6.25: Snapshots from the water-air interface simulation of F3mix3636 system. The bottom plot shows mass density profiles for fluorocarbon head group (green line), PEO (red line) and water (black line) along the normal to the air–water interface.

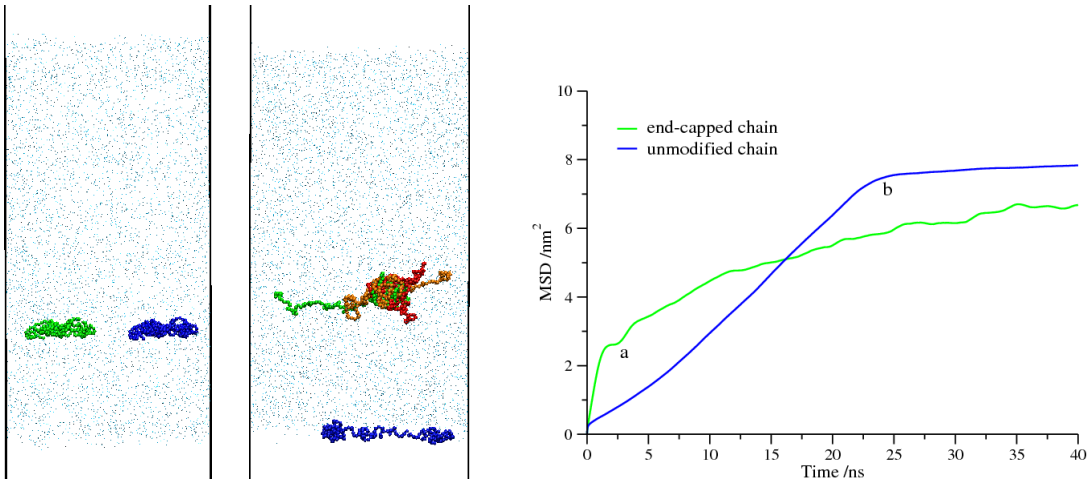

Figure 6.26: Snapshots showing behaviour of the end-capped chain (green chain) and the unmodified chain (blue chain) at the beginning (0 ns) and end (300 ns) of the F2mix3636 simulation. The plot in the right-hand side shows variational of MSD with time of these two chains.

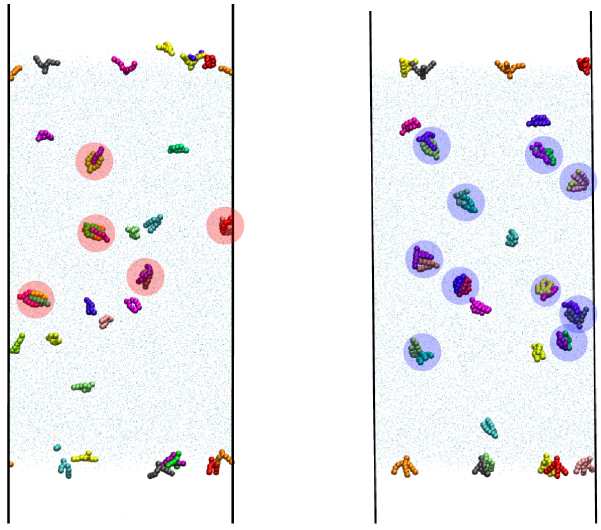

Figure 6.27: Snapshots at the very beginning (5 ns) of simulations of the F2mix3636 and F3mix3636 systems. The highlights show head groups of micelles forming in each system (note that any aggregation by two or more end-capped chains is counted as one micelle).

in the bulk water after both surfaces have reached their saturation point. The F3mix3636 system has both micelles and pure PEO chains left in the bulk phase. Further investigation reveals that among the polymer chains that remained in the bulk water, there are 17 and 14 chains of functionalized-and unfunctionalized PEO polymer respectively. This means that there are more unmodified PEO chains adsorbed at the surface than the end-capped ones, which is not an expected result since the chains with fluorocarbon head group should have a greater propensity for surface adsorption than the unmodified ones (as in the F2mix3636 case where there are 25 modified- and 16 unmodified PEO chains found in the adsorbed layers). The likely explanation for this result is as follows. As mentioned before for simulations at high polymer concentration, end-capped chains tend to form micelles in the bulk water before moving to the surface. A larger dimension and higher mass of these micelles (compared to bare PEO chain) makes it move more slowly to the surface. As a result, when the surface is nearly saturated, bare PEO chains which can diffuse faster, take the available surface space instead. Figure 6.26 compares between the MSD in the z-direction of one of the unmodified PEO chains that can diffuse to adsorb at the surface and an end-capped one that formed a micelle with others in the bulk solution and did not reach the surface. Note that both modified and unmodified chains were started at the same position of the F3mix3636 box, as also depicted in figure 6.26. From the MSD plot, the end-capped chains shown to diffuse quickly toward the surface at the beginning of the simulation. However, after forming a micelle with other end-capped chains (at simulation time of $\sim$3 ns, marked as "a" in the plot), the chain diffusion is retarded, and after a simulation time of about 30 ns the MSD is shown to be increasing at a constant (but slow) rate, indicating that the end-capped chain is trapped in the bulk solution in the form of a micelle. In contrast, the free PEO chain is shown to diffuse continuously to the surface and shows a greater MSD than the end-capped chain after a simulation time of about 17 ns. The MSD of this unmodified chain is then constant after the simulation time of $\sim$25 ns (marked as "b" in the plot), corresponding to the time that the chain reach the surface. The more fluorocarbon branches in the F3 head group (compared to the F2 one) could induce higher affinity between them, which in turn, could lead to

further formation of micelles at the beginning of the simulation as shown in figure 6.27. Since there are more of micelles formed in the bulk phase of F3 system, it is reasonable to have more micelles left in this system due to their slow diffusion toward the surface.

The polymer thickness as averaged from the two surface layers of the F3mix3636 system is about 25-30 Å. This thickness value is in the same order as those of the F3mix1212 and F3mix2424 simulations and does not differ from that produced from the F2 simulation at equivalent concentration. As can be seen in the final structures in figure 6.23-6.25 and the density profiles provided alongside, the air-water interface region is occupied by a combination of F3 head group and ethylene oxide units. Again, PEO segments prefer lying flat along the surface plane rather than stretching down into the water subphase.

6.3.3 Interpretation of experimental results

Information obtained from coarse-grained simulations from the previous two sections are now used to compare and interpret the experimental results from the studies of F2 and F3 materials by Bartram [85] and partially from the study of the F1 material by Richards et al. [18]. Note again that the F2 and F3 materials consist of around 50% unfunctionalized PEO chains while all of the PEO chains in F1 contain the fluorinated functionality. The molecular structure for these materials have already been shown in figure 1.8 of chapter 1.

Let us first consider the adsorption behaviour in the low polymer concentration. Previous experiments carried out on F2-10kPEO and F3-10kPEO materials at low polymer concentration region (less than 0.00137 %w/v) showed a low surface excess of around 20-25 Å, a similar value to that shown for the top layer of F1-10kPEO material studied previously. This thickness is only indicative of a pancake-like layer where the water surface was suggested to be adsorbed by both fluorocarbon ends and ethylene oxide segments of the polymer molecule [18, 85]. Our simulations yielded the same thickness value as those of the experiments, and more importantly, the simulated neutron reflectivity profiles agree well with those acquired experimentally at this concentration regime. Simulation pictures also affirm that the surface is

occupied by both fluorocarbon ends and ethylene oxide segments.

Upon increasing polymer concentration beyond the saturation point, experiments found two-layer organization, consisting of a second layer (micelles) at the underside of an upper layer at the air-water interface. The upper layer dimensions for the F2 and F3 were found to be about 40-60 Å and at certain concentrations the F1 material showed a very similar result. However, because the layer thickness is at most only 1-1.5 times the radius of gyration of the free chain (∼40 Å), a stretched brushlike layer is not supportable as a description of the organization [18]. The results from our simulations coincide quite well with these experimental findings. We have shown in the simulations that after the surface is fully saturated with an adsorbed material, some micelles as well as free PEO chains were left in the bulk phase water. No stretched brush conformation is observed for the upper layer of both F2-10kPEO and F3-10kPEO simulations. As well as fluorocarbon ends being adsorbed, a significant number of ethylene oxide units are also adsorbed at the air-water interface, leading to a flat layer structure. This absorption behaviour is also suggested by experimental studies of F1-10kPEO system at high polymer concentration [18].

In the experimental study of the F3 material, the author suggested that the tethering strength of this polymer is significantly higher than that of the F2 and F1 materials as they can be observed at a much greater depth into the bulk water (compare the SLD profiles of the highest concentration for F2 (1.0 %w/v) and F3 (0.066 %w/v) in figure 6.7 (a) and (b)). The author concluded that the high surface excess found in F3 must be as a direct result of either very large amounts of chain stretching or the formation of multiple PEO layers, both indicate a strongly surface active species, but while chain stretching indicates surface tethering, multilayer adsorption also indicates bulk aggregation (micelle formation). Our simulations, however, showed no significant enhancement for adsorption of PEO chains when changing from the F2 to F3 head group. Both systems yielded almost the same surface excess and no evidence of a stretched PEO conformation is seen. It might be argued that it is because a mixed adsorption by both modified and unmodified PEO chains occurs at the surface that leads to a rather flat structure found in simulations, while in reality the unmodified PEO chains at the surface might be all replaced by

the functionalized ones, and could possibly lead to a different interfacial structure such as a brushlike conformation.

To clarify this point, we have carried out the additional simulation where every PEO chains is end-capped with a F3 head group (100% functionalized). This simulated system contains 72 chains of F3-10kPEO (named as 72F3-10kPEO), and has an equivalent number of PEO chains to the F3mix3636 simulation performed previously. A fully functionalized F2 system (72F2-10kPEO) was also performed for comparison. As clearly shown in the final configurations and the density profiles of these simulations in figure 6.28 and 6.29, no such stretched brush structure is observed even when the surface is fully occupied by the end-capped polymers. The polymer layer thickness for 72F3-10kPEO is about 30 Å, which is not different from the results of the 72F2-10kPEO simulation. Further examination of the final snapshots revealed that there are 23 and 18 polymer chains left in the bulk water of the 72F3-10kPEO and 72F2-10kPEO respectively. These remaining chains formed a micelle together in the bulk as expected. Since there are more chains left in the bulk phase of F3 simulation, the micelle of this system has a larger size than that of the F2 one. The results obtained here suggest that the F3 head group does not lead to a significantly higher surface tethering strength (chain stretching), but induces more bulk aggregation (larger micelle formation) compared to the F2 material. The high polymer density found in a greater depth in the experimental study of F3 is therefore likely to come from larger/more micelles formed underside the adsorbed upper layer.

It should also be noted that the SLD of the 0.066 %w/v F3 system is obtained from the fit that used only a triple layer model with a relative large value for the layer thickness and surface roughness for each polymer slab. It could possibly be an overestimation of these layer thickness (and the surface roughness in the fit) that imitate too high a polymer density at the mixing (overlapping) region between PEO tails from the upper layer and those of the micelles in the bulk phase, which eventually made it look like part of a stretched brush from the upper adsorbed layer. It is also worth considering that the fluorine content is only about 3% and 5% by mass for the F2 and F3 chain respectively, and these values are still very

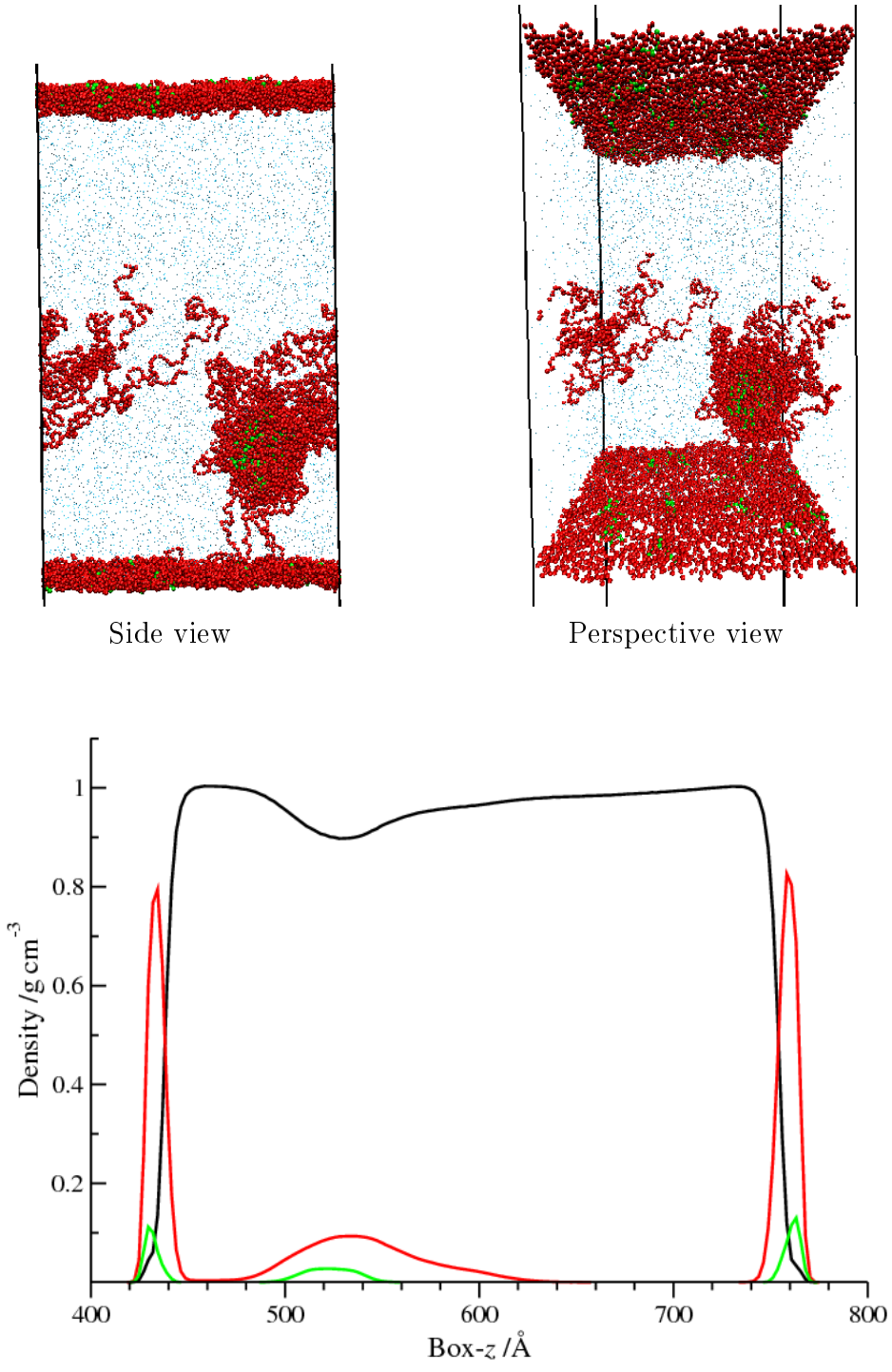

Figure 6.28: Final snapshots from 300 ns simulation of 72F2-10kPEO at the water-air interface. The bottom plot shows mass density profiles for fluorocarbon head group (green line), PEO (red line) and water (black line) along the normal to the air–water interface.

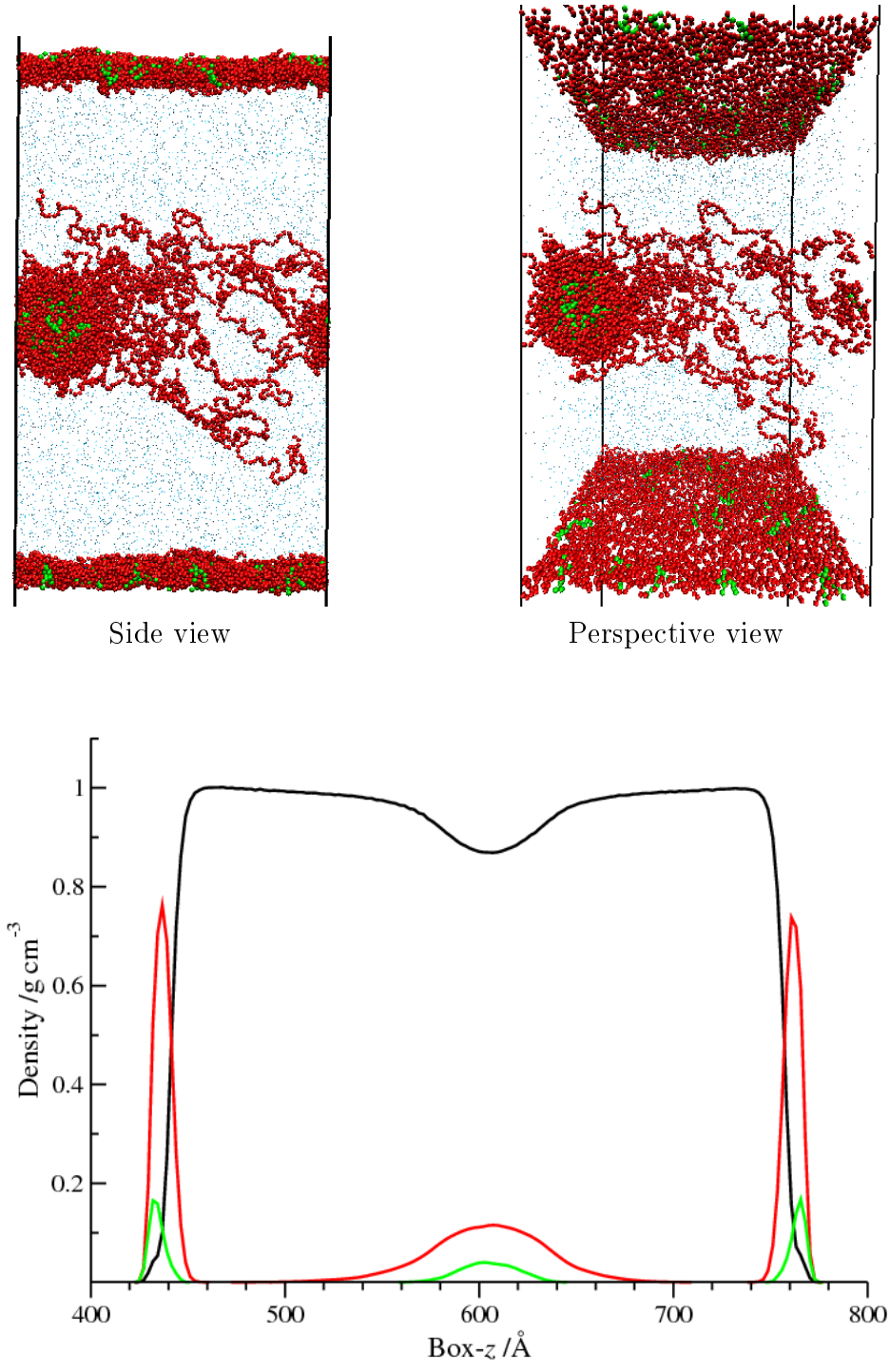

Figure 6.29: Final snapshots from 300 ns simulation of 72F3-10kPEO at the water-air interface. The bottom plot shows mass density profiles for fluorocarbon head group (green line), PEO (red line) and water (black line) along the normal to the air–water interface.

small compared to 95% by mass of ethylene oxide content in each chain. It would therefore not be surprising to see a rather flat adsorbed layer in both F2 and F3 systems as the adsorption behaviour is dominated by ethylene oxide units.

6.3.4 Comments on simulation at high polymer concentrations

Although both experimental and simulation studies show no evidence of a brushlike layer organisation at high polymer concentration, experiments found more extension of ethylene oxide segments into the bulk subphase. The overall thickness of upper layer as obtained from fitting of experimental reflectivity data is around 40-60 Å, which is about 20 Å thicker than the value yielded by simulations. This difference can be subjected to many reasons when dealing with these non ideal systems. Kinetics of competitive adsorption of micelles and unmodified PEO chains could be one important factor.

To mirror experimental conditions as much as possible, end-capped polymers as well as unmodified chains were put throughout the water slab to allow polymers to diffuse from the bulk and form surface layer self-assemble at an interface. Because of this condition, some micelles in the bulk find it hard to reach the surface due to their slow diffusion. This results in a mixed adsorption at the surface by both end-capped and bare PEO chains, which leads to a rather flat interfacial structure found in simulations. While this behaviour is observed in our simulations, different adsorption activities might be occurring in a real experiment. For example, due to a lower surface energy (greater surface affinity) of fluorocarbon head group compared to ethylene oxide unit, some micelles might find a way to diffuse from the bulk water to replace an unmodified chains at the surface, leading to more adsorption of the end-capped chains (or the most likely case is that the surface is saturated first with the end-capped chains). If there are plenty of end-capped chains in the system (which should be true in experiment at high polymer concentration), the system should reach equilibrium where ethylene oxide segments initially adsorbed at the interface are displaced by fluorocarbon head groups and excluded down to the subphase. An increase in adsorption of the head groups at the interface will

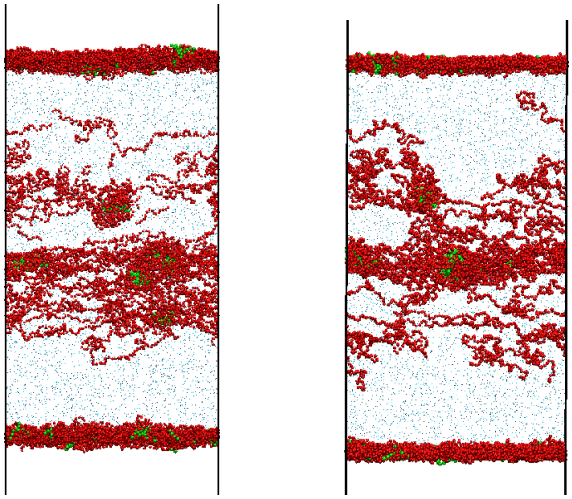

Figure 6.30: Final snapshots from the first 300 ns (left) and the additional 500 ns (right) simulations of the F3mix3636 system.

also leads to more repulsion among their PEO tails underneath, promoting more extension of polymer layer as found in the experiment.

To examine if the behaviour mentioned can be observed by simulation, the final configuration of the F3mix3636 system that has already run for 300 ns was taken and subjected to a further run with simulation time of 500 ns, in order to see if the remaining micelles in the bulk water can diffuse to the surface and to see if we can get any exchange of adsorption between the unmodified PEO chains and the functionalized ones from the micelles (note that it took approximately 6 days to performed this 500 ns simulation with 64 parallel computing nodes). Unfortunately, no such behaviour as mentioned above is observed. The final configuration obtained from this very long time simulation is essentially unchanged from the first 300 ns one. The remaining micelles do not diffuse to the surface and still remaining in the bulk water, as shown in figure 6.30. At this stage, it comes to our attention that the truly equilibrium state for the high polymer concentration systems might not be accessible by the time scales provided by the CG simulation.

Considering the adsorption kinetics from micellar solutions, the established models assume that micelles have to break down to monomers in the subphase region before adsorption can occur [247–249]. However, Colegate and Bain have shown later that micelles of nonionic surfactants can adsorb to an air-water interface without first breaking down into monomers in the bulk solution [246]. This latter behaviour

is found in our simulations where some micelles are shown to diffuse directly from the bulk water to adsorb at the interface. For simulation at high polymer concentrations, in order for the bulk phase micelles (those that have been remained in the bulk water) to adsorb at the surface, the most possible path way is that they must first break down in solution to release monomers so that they can diffuse easier to the surface. We know of no work examining the relaxation time required for the F2 and F3 micelles (or other micelles forming by similar amphiphilic polymers) to break down to monomers. The only information available is from the study of adsorption kinetics of $C_{14}E_8$ surfactant $[CH_3(CH_2)_{13}(OCH_2CH_2)_8OH]$ at a water-air interface by Colegate and Bain [246]. It was reported that exchange of $C_{14}E_8$ monomers between micelles and the solution take $\sim 10^{-5}$ second to occurs [250]. However, a micelle can only shed about 10% of its monomers by this fast process (one $C_{14}E_8$ micelle consists of 72-120 monomers). For the total disintegration of the whole micelle, the relaxation time of $\sim$4 seconds is required [251] and increasing the length of the alkyl chain will increase this relaxation time further. Since the F2 and F3 polymers have much longer chain length than the $C_{14}E_8$ surfactant, it would therefore imply that longer time is needed for these micelles to break down to monomers. Assuming that the F2 and F3 micelles could break down to monomers as fast as $C_{14}E_8$ could ($\sim$10 microsecond), this is however, still not be practical to observe on the timescales we are working with.

Assuming that micelles in the bulk solution can diffuse to the surface or can release monomers to the surface, the adsorption process can still be complicated in our study since there are both end-capped and free PEO chains present in the system. This means that the exchange adsorption between these monomers and the free PEO chains initially adsorbed at the surface is also needed to be taken into account. Let us therefore consider how long it would take for these micelles (or their monomers) to displace unmodified PEO chains that have alredy adsorbed at the surface. There is no previous study examining exchange adsorption of F2 (F3) polymer and free PEO chain at the water-air interface. However, for other related studies, competitive adsorption of chemically different polymers [252–254] as well as that of homopolymers with different chain lengths [255–257] have been investigated

extensively in the literature. Depending on the nature of the competitive polymers, the rate of exchange adsorption can be controlled either by the bulk diffusion of polymers or processes occurring at the surface. The latter can be attributed to factors such as interfacial chain dynamics (interfacial entanglement) or segment-surface contacts (segmental adsorption energy) of the chains being replaced. Granick and co-workers [252, 258] observed that the replacement of adsorbed polystyrene (PS) by poly-(methyl methacrylate) (PMMA) in organic solvents on oxidized silicon could take several hours. They suggested that the rate of exchanging adsorption is controlled by mobility of both PS and PMMA at the surface, which are very slow due to relatively rigid structure of both polymers. In contrast, Dijt *et al.* [255] showed that the displacement of short PEO chains ($M_w \approx 7$ K) on silica by longer ones ($M_w \approx 400$ K) was completed within minutes, and the exchange rate was bulk diffusion controlled. The fast surface kinetics were attributed to PEO's greater flexibility and surface mobility. However, for short PEO chains of higher M_w ($\sim$120K), the displacement by longer chains becomes slow and less complete [257], indicating that the segmental adsorption energy (energy barriers) of the short chain plays an important role in the kinetics. The study of competitive adsorption of fluorescein dianion end-capped PEO (F-PEO) and native PEO of the same molecular weight on negatively charged silica surfaces [259] revealed that exchange between F-PEO and native PEO is controlled by the diffusion rate of the chains to the surface, and take several minutes for the replacement process to complete. From the information provided here, it suggests that even we could run the simulation long enough to see micelles diffuse to the surface or to see micelles release monomers to the surface, much longer time is still required to allow full exchange of the end-capped and bare PEO chains at the interface. For this reason, it seems to be not possible to see equilibrated adsorption of the high concentration systems even by using coarse-grained simulation.

6.3.5 Grafting polymers at the water-air interface

For simulation at high polymer concentrations, it is possible to help the system reach equilibrium state faster. For example, we can help all the head groups of

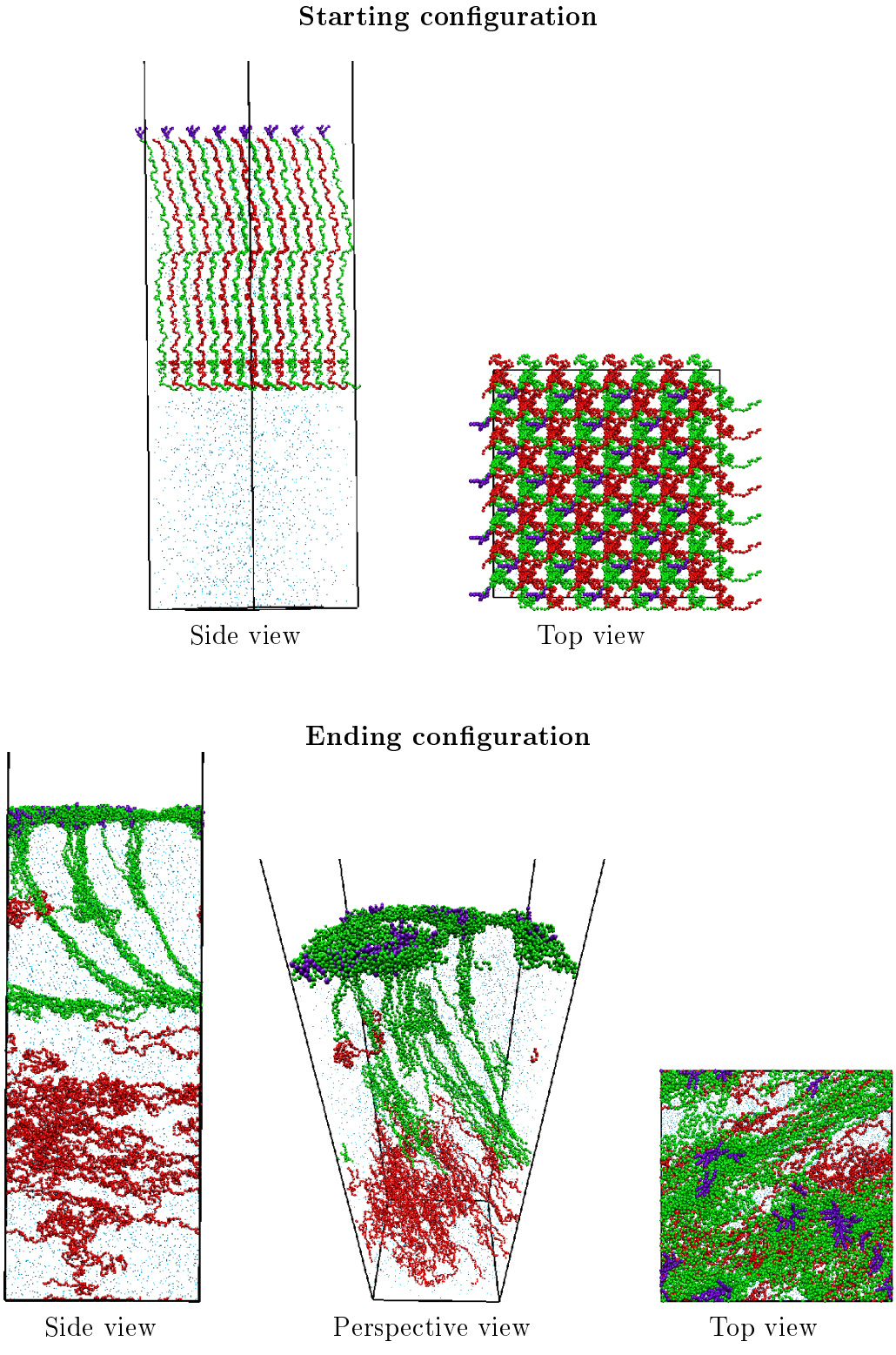

Figure 6.31: Starting (t = 0 ns, top) and final (t = 200 ns, bottom) configurations from simulation of F3mix3636 system with a polymer chains grafting at the water-air interface. The red, green and violet colours represent bare PEO chain, end-capped PEO chain and head group of the end-capped chain, respectively.

amphiphilic polymers to find the surface without first diffusing from the bulk water phase. The efficient way to do this is by grafting the head groups of polymers at the interface and allow PEO tails to stretch down into the subphase as shown in figure 6.31 (starting configuration). The unmodified PEO chains were presented to the system by simply removing the head group of every alternate molecule at the surface, leaving only half of them remaining functionalized as shown in figure 6.31. It should be noted that this set-up is analogous to an experimental study in which polymeric materials are spread onto the water surface, which is different from the method of preparation in the experimental study of F2 and F3 polymers (polymers were dissolved in the liquid subphase) [85]. Since a stretched conformation is used as a starting configuration, an extremely long water slab is needed to accommodate the polymers (note that each chain consists of around 200 ethylene oxide units). The structure showed in figure 6.31 is the F3mix3636 system in the the water slab of 200.0 Å, 200.0 Å and 650.0 Å, respectively in x, y and z dimensions, and contains about 180,000 water beads (720,000 water molecules), much larger than the simulations previously performed.

Figure 6.31 (botom) shows the final configuration from the simulation that lasted 200 ns. It obviously shows that all of the unmodified polymers were excluded down to the bulk subphase. The fluorocarbon head groups are shown to tether strongly at the interface with some of their ethylene oxide tails still remaining as stretched as the starting conformation. However, some of the PEO tails of the end-capped polymers are shown to diffuse from the subphase and adsorb at the surface. Since the simulation time is only 200 ns, the stretched PEO tails seen in the final configuration may not be the indicative of a brush conformation. We suspect that if the simulation is allowed to run further, these stretched tails may also fold up (diffuse) to the surface and adsorb there at available surface space as some have already. The result obtained from this set-up looks promising as it show preferential adsorption of the end-capped polymers as should occur in reality. It is also interesting to see what would be observed if we could increase the grafting density (put more of end-capped chains) in the system. Unfortunately, the simulation performed here is very computational expensive, which is mainly due to huge number of water used. With 64 parallel

computing nodes, it required more than a week to perform 200 ns calculation for this system. Hence, it still does not seem to be practical to explore equilibrium adsorption of F2 and F3 materials at high concentration using the current coarse-grained models.

6.4 Conclusions

Coarse-grained simulation of a large PEO molecule ($M_w \approx 10000$ g mol^{-1}) end-capped with multiple fluorocarbon head groups at a water-air interface has been carried out at a range of concentrations. Polymers were put throughout the water slab to allow them to diffuse from the bulk solution and form surface layer self-assembly at an interface as previously carried out in experiment. Density profiles have been successfully converted to scattering length density profiles, which in turn are used to generate simulated neutron reflectivity plots, using the optical matrix method. The reflectivity profiles from simulation are in good agreement with those of experiment at low polymer concentration, although direct comparison could not be made due to different studied concentration units. The simulated polymer layer thickness is in the same range as that acquired experimentally at this low concentration regime, both studies indicate a flat adsorbed layer where both fluorocarbon ends and ethylene oxide segments are seen to be adsorbed at the air-water interface.

Upon increasing concentration until the surface is saturated with polymers, simulations show formations of micelles (as well as a free PEO chains) at the underside of an adsorbed layer at the air-water interface, in accordance with experimental findings. No evidence of a stretched brush conformation is observed from the F2 and F3 simulations. It is shown from these simulations that polymer is adsorbed to the interface by a combination of fluorocarbon ends and ethylene oxide segments, resulting in a rather flat layer structure. This behaviour is again coincident with that explained in an experimental study of the F1 material carried out previously. In simulation studies, the F3 material was showed to induce greater formations of micelle in the bulk water phase compared to the F2 one. However, both materials do not appear to be organised efficiently at the interface to promote a brushlike

structure.

Although a brush conformation is not suggested from either experimental or simulation studies, experiment found more extension of PEO segments into the bulk subphase, promoting the adsorbed layer thickness of around the same order as the radius of gyration of the free chain. Simulation however yielded about 20 Å thinner for this surface excess layer, and the mixture adsorption by both end-capped and bare PEO chains are responsible for this. Rather than a mixed adsorption by functionalized and free PEO chains, it is expected in reality that the surface should be saturated first with chains functionalizing with hydrophobic head group, which could lead to more extension of PEO tails as seen in experiment. It is therefore suggested that the truly equilibrated adsorption for the high polymer concentration systems may not be yet reached within accessible simulation times. Much longer simulation time is required for micelles remaining in the bulk solution to diffuse and exchange with the free PEO at the surface. This behaviour however does not seem to be observable with the time scales provided by the current coarse-grained models.

Neutron reflectometry enables the physical structure of interface systems to be determined. However a great deal of modeling to interpret the raw data is required. Simulations are clearly model dependent, but are very valuable due to the molecular-level picture that they can produce. By using them together one can obtain the advantages of both, and in the same time, minimise the drawbacks. Study of very large amphiphilic polymers may not be fully succeeded by the coarse-graining level used in this study. However, systems with short to moderate polymer chain length would be more ideal to study using this combined technique [67, 242].

Chapter 7

Summary

Previous atomistic simulations have been shown to provide invaluable insight into adsorption behaviour of amphiphilic polymer sitting at a water-air interface [67,92]. Neutron reflectivity profiles generated from these simulations were in good agreement with the experimental reflectivity curve, particularly at low surface concentrations. However simulations at very high surface concentrations fail to produce adequate results due to the limits of atomistic simulation in terms of time and length scales. To circumvent this problem, a coarse-grained molecular simulation, which has successfully been applied to various polymeric and biological systems, was introduced in this thesis work.

The first stage involved in this study was the development of coarse-grained models for water. The models, with one coarse-grained bead representing one water molecule, satisfactorily reproduced the bulk liquid properties, e.g. the radial distribution function and density. By applying a long-range attraction for the potentials, the models provided comparable interfacial tension to that of atomistic water models. However, the vapor-liquid density profile and the vapour pressure were found to deviate significantly from atomistic simulation results, and could not be reproduced correctly by any kind of applied potential. We concluded from this study that it is not possible to simultaneously reproduce all the underlying atomistic/experiment properties using only simple isotropic coarse-graining potential. Although structural features of water is neglected, the higher level of coarse-graining such as a 4-to-1 mapping (four water molecules per one bead) was found to provide correct physical

properties both in bulk and at interface conditions [183]. For this reason, and with consideration of more computational efficiency that they can provide, compared to the 1-to-1 mapping models, the 4-to-1 mapping water was therefore taken as a solvent model for the remaining work.

A coarse-grained model for polyethylene oxide (PEO)/water, the crucial part of this study, was developed in the next stage of the project. The model was derived using structural probability distributions from detailed atomistic simulation, which in turn, showed successful reproduction of the theoretical and experimental scaling law for radius of gyration in aqueous solution. The transferability of the model to the water-air interface system has also been explored. In accordance with experimental observation, PEO chains were found to form a layer at the water-air interface with increasing of the surface excess as the polymer concentration is increased. The surface saturation concentration and the polymer layer thickness from CG simulations were in good agreement with experimental findings. The model was also seen to provide much more efficiency in speeding up the system to equilibrium compared to the underlying atomistic simulation.

The PEO/water model from the previous stage was then incorporated in the development of CG models of di- and trifluoro dendritic end-capped PEO at an air-water interface which have been studied previously by neutron reflectivity technique. Coarse-grained interactions were derived from fittings of structural properties to those of a detailed atomistic simulations. The interfacial structure of the parent atomistic simulations, including molecular organisation and density profile, were reproduced similarly well by the resulting coarse-grained models.

The final stage was the CG simulations of an amphiphilic polymers at the water-air interface, using a chain length comparable to that studied in the real experiment. Neutron reflectivity profiles generated from simulations at low polymer concentrations were in good agreement with those of experiment, encouraging simulations at higher concentrations using the present models. Simulations at high polymer concentrations showed formations of micelles underneath the adsorbed layer at the air-water interface, consistent with the picture suggested by neutron reflectivity study. For the adsorbed layer, polymer was seen to adsorb at the interface by a

combination of fluorocarbon ends and ethylene oxide segments, leading to a rather flat layer structure. No stretched brush conformation was observed from these high concentration simulations. This behavior was similarly observed from both F2 and F3 simulations and coincided well with that suggested in experimental study of F1 material carried out previously. In simulations, the F3 polymer showed to induce greater formations of micelle in the bulk subphase compared to the F2 material. Both materials, however, did not appear to promote any brushlike organisation at the water-air interface. Although a brush conformation is not suggested from either experimental or simulation studies, experiment found a significantly thicker surface excess layer than that observed in simulations. It is noted from this result that the time scales provided by the current CG models might not be sufficient to allow the system to be fully equilibrated to the state where micelles remaining in the bulk solution can diffuse and exchange with the free PEO at the surface and promote thicker surface excess layer as observed in experiment.

We have shown in this study that coarse-grained simulation is a powerful technique to study behaviour of amphiphilic polymers at the water-air interface. To study very large amphiphilic systems at high polymer concentrations as in this study, however, a higher level of coarse-graining (coarser model) might be required to allow observation of equilibrated adsorption behaviour. It is also noted from our simulation that grafting polymers at the interface can help the system reach equilibrium faster.

The coarse-graining level used in this study is certainly suitable to apply to the study of amphiphilic systems with short to moderate polymer chain lengths in future work. For example, a spread film of polynorbornene/poly(ethylene oxide) [16, 17] or poly(methyl methacrylate)/poly(ethylene oxide) graft copolymers [14] at the air-water interface, that have been determined previously by neutron reflectometry, are good systems to look at. Coarse-grained simulation can also be used to help study of other related systems. The behaviour of amphiphilic bent-core molecules at water surfaces [260] or structure of micelles formed by hydrophobically end-capped PEO [261, 262] are interesting examples.

One interesting new approach, which we have not had chance to apply or trial

involves "thermodynamic-based" coarse-graining. This approach involves inclusions of some thermodynamic properties in the fitting of coarse-grained parameters. In our study, surface/interfacial tension as well as hydration free energy are of key importance in characterizing the self-organized amphiphilic structure at the water air-interface [94, 129, 180]. In cases where these thermodynamic data are available, it would be very useful to test this different approach to the development of coarse-grained models to compare with our current one, which is based solely on structural information from detailed atomistic simulation.

Bibliography

[1] P. C. Painter, M. M. Coleman, *Fundamentals of polymer science : an introductory text*, (Technomic Pub. Co.: Lancaster, Pa, 1997).

[2] N. McCrum, C. P. Buckley, C. B. Bucknall, *Principles of polymer engineering*, (Oxford University Press: New York, 1997).

[3] J. Klein, *J. Phys. Condens. Matter* **12**, A19 (2000).

[4] Z. Z. Zhang, Q. J. Xue, W. M. Liu, W. C. Shen, *J. Appl. Polym. Sci.* **76**, 1240 (2000).

[5] R. Tadmor, J. Janik, J. Klein, L. J. Fetters, *Phys. Rev. Lett.* **91** (2003).

[6] J. B. Kim, H. J. Yun, Y. G. Kwon, B. W. Lee, *Polymer* **41**, 8035 (2000).

[7] G. Allegra, G. Raos, C. Manassero, *J. Chem. Phys.* **119**, 9295 (2003).

[8] D. H. Napper, *Polymeric Stabilisation of Colloid Dispersions*, (Academic Press: New York, 1983).

[9] R. Gref, Y. Minamitake, M. T. Peracchia, V. Trubetskoy, V. Torchilin, R. Langer, *Science* **263**, 1600 (1994).

[10] V. P. Torchilin, *J. Controlled Release* **73**, 137 (2001).

[11] R. Duncan, *Nat. Rev. Drug Discovery* **2**, 347 (2003).

[12] R. K. Thomas, *Neutron Reflection from Polymer Bearing Surfaces*, (Richards, R. W., Eds.; Ellis Horwood: London, 1995).

[13] J. Penfold, R. K. Thomas, *J. Phys.: Condens. Matter* **2**, 1369 (1990).

[14] S. K. Peace, R. W. Richards, M. R. Taylor, J. R. P. Webster, N. Williams, *Macromolecules* **31**, 1261 (1998).

[15] A. F. Miller, R. W. Richards, J. R. P. Webster, *Macromolecules* **33**, 7618 (2000).

[16] A. F. Miller, R. W. Richards, J. R. P. Webster, *Macromolecules* **34**, 8361 (2001).

[17] A. F. Miller, R. W. Richards, J. P. R. Webster, *J. Phys. Chem. B* **107**, 6717 (2003).

[18] R. W. Richards, J. Sarica, J. R. P. Webster, S. A. Holt, *Langmuir* **19**, 7768 (2003).

[19] J. A. Hunt, N. Cowlam, *J. Non-Cryst. Solids* **156**, 812 (1993).

[20] M. M. Neilson, J. Bowers, E. Manzanares-Papayanopoulos, J. R. Howse, M. C. Vergara-Gutierrez, P. J. Clements, A. N. Burgess, I. A. McLure, *Phys. Chem. Chem. Phys.* **1**, 4635 (1999).

[21] Y. Y. Huang, G. P. Felcher, S. S. P. Parkin, *J. Magn. Magn. Mater.* **99**, L31 (1991).

[22] F. Canet, C. Bellouard, S. Mangin, C. Chatelain, C. Senet, R. Siebrecht, V. Leiner, M. Piecuch, *Eur. Phys. J. B* **34**, 381 (2003).

[23] V. F. Sears, *Neutron News* **3**, 26 (1992).

[24] *http://www.ncnr.nist.gov/resources/sldcalc.html.*

[25] A. W. Adamson, *Physical Chemistry of Surface, 4th Edition*, (Wiley: New York, 1982).

[26] L. R. Cox, E. H. Dunlop, A. M. North, *Nature* **249**, 243 (1974).

[27] R. C. R. Figueredo, E. Sabadini, *Colloids Surf., A* **215**, 77 (2003).

[28] J. M. Douillard, S. Pougnet, B. Faucompre, S. Partyka, *J. Colloid Interface Sci.* **154**, 113 (1992).

[29] W. C. K. Poon, A. D. Pirie, M. D. Haw, P. N. Pusey, *Physica A* **235**, 110 (1997).

[30] S. K. Jewrajka, G. Erdodi, J. P. Kennedy, D. Ely, G. Dunphy, S. Boehme, F. Popescu, *J. Biomed. Mater. Res., Part A* **87A**, 69 (2008).

[31] M. Kovac, M. Gaberscek, S. Pejovnik, *Solid State Ionics* **131**, 323 (2000).

[32] M. D. Dimitriou, Z. Zhou, H.-S. Yoo, K. L. Killops, J. A. Finlay, G. Cone, H. S. Sundaram, N. A. Lynd, K. P. Barteau, L. M. Campos, D. A. Fischer, M. E. Callow, J. A. Callow, C. K. Ober, C. J. Hawker, E. J. Kramer, *Langmuir* **27**, 13762 (2011).

[33] W.-S. Young, J. N. L. Albert, A. B. Schantz, I. Epps, Thomas H., *Macromolecules* **44**, 8116 (2011).

[34] W. Zhang, Z. P. Du, C. H. Chang, G. Y. Wang, *J. Colloid Interface Sci.* **337**, 563 (2009).

[35] E. L. Furness, A. Ross, T. P. Davis, G. C. King, *Biomaterials* **19**, 1361 (1998).

[36] L. Kurniawan, G. G. Oiao, X. Q. Zhang, *Macromol. Biosci.* **9**, 93 (2009).

[37] A. Lundquist, P. Wessman, A. R. Rennie, K. Edwards, *Biochim. Biophys. Acta* **1778**, 2210 (2008).

[38] A. K. Gaharwar, C. P. Rivera, C.-J. Wu, G. Schmidt, *Acta Biomater.* **7**, 4139 (2011).

[39] M. Ukawala, K. Chaudhari, T. Rajyaguru, A. S. Manjappa, R. S. R. Murthy, R. Gude, *J. Drug Targeting* **20**, 55 (2012).

[40] Y. C. Bae, J. J. Shim, D. S. Soane, J. M. Prausnitz, *J. Appl. Polym. Sci.* **47**, 1193 (1993).

[41] S. Saeki, N. Kuwahara, M. Nakata, M. Kaneko, *Polymer* **17**, 685 (1976).

[42] J. Bailey, F. E., J. V. Koleske, *Poly(ethyleneoxide)*, (Academic Press: New York, 1976).

[43] R. D. Rogers, M. A. Eitman, Eds., *Aqueous Biphasic Separations*, (Plenum Press: New York, 1995).

[44] R. M. Ottenbrite, S. J. Huang, K. Park, Eds., *Hydrogels and Biodegradable Polymers for Bioapplications*, (American Chemical Society: Washington, DC, 1996).

[45] J. M. Harris, S. Zalipsky, Eds., *Poly(ethylene glycol) Chemistry and Biological Applications*, (American Chemical Society: Washington, DC, 1997).

[46] A. M. Kulkarni, A. P. Chatterjee, K. S. Schweizer, C. F. Zukoski, *J. Chem. Phys.* **113**, 9863 (2000).

[47] R. Kjellander, E. Florin, *J. Chem. Soc., Faraday Trans. 1* **77**, 2053 (1981).

[48] G. Karlstrom, *J. Phys. Chem.* **89**, 4962 (1985).

[49] R. E. Goldstein, *J. Chem. Phys.* **80**, 5340 (1984).

[50] A. Matsuyama, F. Tanaka, *Phys. Rev. Lett.* **65**, 341 (1990).

[51] S. Bekiranov, R. Bruinsma, P. Pincus, *Phys. Rev. E* **55**, 577 (1997).

[52] E. E. Dormidontova, *Macromolecules* **35**, 987 (2002).

[53] G. N. Malcolm, J. S. Rowlinson, *Trans. Faraday Soc.* **53**, 921 (1957).

[54] Y. C. Bae, S. M. Lambert, D. S. Soane, J. M. Prausnitz, *Macromolecules* **24**, 4403 (1991).

[55] K. Devanand, J. C. Selser, *Macromolecules* **24**, 5943 (1991).

[56] S. Masatoki, M. Takamura, H. Matsuura, K. Kamogawa, T. Kitagawa, *Chem. Lett.*, 991 (1995).

[57] H. Matsuura, T. Sagawa, *J. Mol. Liq.* **65-6**, 313 (1995).

[58] R. Begum, H. Matsuura, *J. Chem. Soc., Faraday T rans.* **93**, 3839 (1997).

[59] N. Goutev, K. Ohno, H. Matsuura, *J. Phys. Chem. A* **104**, 9226 (2000).

[60] X. Z. Yang, Z. H. Su, D. C. Wu, S. L. Hsu, H. D. Stidham, *Macromolecules* **30**, 3796 (1997).

[61] N. B. Graham, N. E. Nwachuku, D. J. Walsh, *Polymer* **23**, 1345 (1982).

[62] C. Branca, A. Faraone, G. Maisano, S. Magazu, P. Migliardo, A. Triolo, R. Triolo, V. Villari, *J. Phys.: Condens. Matter* **11**, 6079 (1999).

[63] R. L. Cook, H. E. King, D. G. Peiffer, *Phys. Rev. Lett.* **69**, 3072 (1992).

[64] B. Hammouda, D. Ho, S. Kline, *Macromolecules* **35**, 8578 (2002).

[65] D. Bedrov, O. Borodin, G. D. Smith, *J. Phys. Chem. B* **102**, 5683 (1998).

[66] D. Bedrov, M. Pekny, G. D. Smith, *J. Phys. Chem. B* **102**, 996 (1998).

[67] P. M. Anderson, M. R. Wilson, *J. Chem. Phys.* **121**, 8503 (2004).

[68] G. D. Smith, D. Bedrov, O. Borodin, *Phys. Rev. Lett.* **85**, 5583 (2000).

[69] G. D. Smith, D. Bedrov, *J. Phys. Chem. B* **107**, 3095 (2003).

[70] G. D. Smith, D. Bedrov, *Macromolecules* **35**, 5712 (2002).

[71] S. Wu, *Polymer Interface and Adhesion*, (Marcel Dekker: New York, 1982).

[72] C. L. Yaws, *Chemical Properties Handbook: Physical, Thermodynamic, Environmental, Transport, Safety, and Health Related Properties for Organic and Inorganic Chemicals*, (McGraw-Hill: New York, 1998).

[73] A. R. Rennie, R. J. Crawford, E. M. Lee, R. K. Thomas, T. L. Crowley, S. Roberts, M. S. Qureshi, R. W. Richards, *Macromolecules* **22**, 3466 (1989).

[74] J. A. Henderson, R. W. Richards, J. Penfold, R. K. Thomas, J. R. Lu, *Macromolecules* **26**, 4591 (1993).

[75] J. R. Lu, T. J. Su, R. K. Thomas, J. Penfold, R. W. Richards, *Polymer* **37**, 109 (1996).

[76] M. W. Kim, B. H. Cao, *Europhys. Lett.* **24**, 229 (1993).

[77] B. H. Cao, M. W. Kim, *Faraday Discuss.* **98**, 245 (1994).

[78] M. W. Kim, *Colloids Surf., A* **128**, 145 (1997).

[79] D. J. Kuzmenka, S. Granick, *Polym. Commun.* **29**, 64 (1987).

[80] C. Selve, J. C. Ravey, M. J. Stebe, C. Elmoudjahid, E. M. Moumni, J. J. Delpuech, *Tetrahedron* **47**, 411 (1991).

[81] M. J. Owen, *Siloxane Polymer, Chapter 7*, (Prentice Hall: Englewood Cliffs, New Jersey, 1993).

[82] Y. Ren, M. S. Shoichet, T. J. Mccarthy, H. D. Stidham, S. L. Hsu, *Macromolecules* **28**, 358 (1995).

[83] Z. H. Su, T. J. McCarthy, S. I. Hsu, H. D. Stidham, Z. Y. Fan, D. C. Wu, *Polymer* **39**, 4655 (1998).

[84] J. Bowers, A. Zarbakhsh, J. R. P. Webster, L. R. Hutchings, R. W. Richards, *Langmuir* **17**, 131 (2001).

[85] S. A. Bartram, *Adsorption of Dendritic Fluorocarbon End-Capped Poly(Ethylene Oxide) at an Air-Water Interface A Synthetic, Analytical and Computational Study*, (Ph.D. thesis, Durham University, UK, 2009).

[86] J. C. Shelley, M. Y. Shelley, *Curr. Opin. Colloid Interface Sci.* **5**, 101 (2000).

[87] S. Karaborni, *Langmuir* **9**, 1334 (1993).

[88] R. G. Larson, L. E. Scriven, H. T. Davis, *J. Chem. Phys.* **83**, 2411 (1985).

[89] S. J. Marrink, A. H. de Vries, A. E. Mark, *J. Phys. Chem. B* **108**, 750 (2004).

[90] S. J. Marrink, H. J. Risselada, S. Yefimov, D. P. Tieleman, A. H. de Vries, *J. Phys. Chem. B* **111**, 7812 (2007).

[91] A. F. Miller, M. R. Wilson, M. J. Cook, R. W. Richards, *Mol. Phys.* **101**, 1131 (2003).

[92] P. M. Anderson, *Conformational behaviour of amphiphilic molecules in aqueous solution and at a water/air interface : computational studies at the molecular level*, (Ph.D. thesis, Durham University, UK, 2004).

[93] G. Srinivas, J. C. Shelley, S. O. Nielsen, D. E. Discher, M. L. Klein, *J. Phys. Chem. B* **108**, 8153 (2004).

[94] W. Shinoda, R. DeVane, M. L. Klein, *Soft Matter* **4**, 2454 (2008).

[95] W. Shinoda, R. DeVane, M. L. Klein, *Soft Matter* **7**, 6178 (2011).

[96] S. Baoukina, L. Monticelli, H. J. Risselada, S. J. Marrink, D. P. Tieleman, *Proc. Natl. Acad. Sci. U.S.A.* **105**, 10803 (2008).

[97] R. W. Hockney, S. P. Goel, J. W. Eastwood, *J. Comput. Phys.* **14**, 148 (1974).

[98] W. C. Swope, H. C. Andersen, P. H. Berens, K. R. Wilson, *J. Chem. Phys.* **76**, 637 (1982).

[99] A. D. MacKerell, D. Bashford, M. Bellott, R. L. Dunbrack, J. D. Evanseck, M. J. Field, S. Fischer, J. Gao, H. Guo, S. Ha, D. Joseph-McCarthy, L. Kuchnir, K. Kuczera, F. T. K. Lau, C. Mattos, S. Michnick, T. Ngo, D. T. Nguyen, B. Prodhom, W. E. Reiher, B. Roux, M. Schlenkrich, J. C. Smith, R. Stote, J. Straub, M. Watanabe, J. Wiorkiewicz-Kuczera, D. Yin, M. Karplus, *J. Phys. Chem. B* **102**, 3586 (1998).

[100] D. Van der Spoel, E. Lindahl, B. Hess, G. Groenhof, A. E. Mark, H. J. C. Berendsen, *J. Comput. Chem.* **26**, 1701 (2005).

[101] A. D. Mackerell, M. Feig, C. L. Brooks, *J. Comput. Chem.* **25**, 1400 (2004).

[102] J. N. Israelachvili, *Intermolecular and Surface Forces*, (Academic Press, 1992).

[103] F. Jensen, *Introduction to Computational Chemistry*, (Wiley, 2007).

[104] H. J. C. Berendsen, J. P. M. Postma, W. F. Vangunsteren, A. Dinola, J. R. Haak, *J. Chem. Phys.* **81**, 3684 (1984).

[105] S. Nose, *Mol. Phys.* **52**, 255 (1984).

[106] W. G. Hoover, *Phys. Rev. A* **31**, 1695 (1985).

[107] M. Parrinello, A. Rahman, *J. Appl. Phys.* **52**, 7182 (1981).

[108] S. A. Adelman, J. D. Doll, *J. Chem. Phys.* **64**, 2375 (1976).

[109] B. Hess, C. Kutzner, D. van der Spoel, E. Lindahl, *J. Chem. Theory Comput.* **4**, 435 (2008).

[110] G. E. Moore, *Electronics* **38**, 114 (1965).

[111] *www.ks.uiuc.edu/Research/namd.*

[112] *http://lammps.sandia.gov.*

[113] *www.gromacs.org.*

[114] *www.charmm.org.*

[115] T. C. Germann, K. Kadau, *Int. J. Mod. Phys. C* **19**, 1315 (2008).

[116] M. L. Klein, W. Shinoda, *Science* **321**, 798 (2008).

[117] J. A. Anderson, C. D. Lorenz, A. Travesset, *J. Comput. Phys.* **227**, 5342 (2008).

[118] M. S. Friedrichs, P. Eastman, V. Vaidyanathan, M. Houston, S. Legrand, A. L. Beberg, D. L. Ensign, C. M. Bruns, V. S. Pande, *J. Comput. Chem.* **30**, 864 (2009).

[119] F. Muller-Plathe, *Chemphyschem* **3**, 754 (2002).

[120] C. Peter, K. Kremer, *Soft Matter* **5**, 4357 (2009).

[121] T. Murtola, A. Bunker, I. Vattulainen, M. Deserno, M. Karttunen, *Phys. Chem. Chem. Phys.* **11**, 1869 (2009).

[122] P. G. DeGennes, *Scaling Concepts in Polymer Physics*, (Ithaca, NY: Cornell Univ. Press, 1979).

[123] M. Doi, S. F. Edwards, *The theory of polymer dynamics*, (Clarendon Press: Oxford, 1986).

[124] K. Binder, *Monte Carlo and Molecular Dynamics Simulations in Polymer Science*, (UK: Oxford Univ. Press, 1995).

[125] S. O. Nielsen, R. E. Bulo, P. B. Moore, B. Ensing, *Phys. Chem. Chem. Phys.* **12**, 12401 (2010).

[126] K. Kremer, F. Muller-Plathe, *MRS Bull.* **26**, 205 (2001).

[127] S. Albo, E. A. Muller, *J. Phys. Chem. B* **107**, 1672 (2003).

[128] B. M. Mognetti, L. Yelash, P. Virnau, W. Paul, K. Binder, M. Mueller, L. G. MacDowell, *J. Chem. Phys.* **128**, 104501 (2008).

[129] S. O. Nielsen, C. F. Lopez, G. Srinivas, M. L. Klein, *J. Chem. Phys.* **119**, 7043 (2003).

[130] C. Avendano, T. Lafitte, A. Galindo, C. S. Adjiman, G. Jackson, E. A. Mueller, *J. Phys. Chem. B* **115**, 11154 (2011).

[131] G. Santangelo, A. Di Matteo, F. Muller-Plathe, G. Milano, *J. Phys. Chem. B* **111**, 2765 (2007).

[132] A. Villa, N. F. A. van der Vegt, C. Peter, *Phys. Chem. Chem. Phys.* **11**, 2068 (2009).

[133] B. Hess, S. Leon, N. van der Vegt, K. Kremer, *Soft Matter* **2**, 409 (2006).

[134] D. Stueber, T.-Y. Yu, B. Hess, K. Kremer, R. D. O'Connor, J. Schaefer, *J. Chem. Phys.* **132**, 104901 (2010).

[135] D. Reith, M. Putz, F. Muller-Plathe, *J. Comput. Chem.* **24**, 1624 (2003).

[136] S. Jain, S. Garde, S. K. Kumar, *Ind. Eng. Chem. Res.* **45**, 5614 (2006).

[137] J. Fischer, D. Paschek, A. Geiger, G. Sadowski, *J. Phys. Chem. B* **112**, 13561 (2008).

[138] H. Wang, C. Junghans, K. Kremer, *Eur. Phys. J. E* **28**, 221 (2009).

[139] A. P. Lyubartsev, A. Laaksonen, *Phys. Rev. E* **52**, 3730 (1995).

[140] R. L. Henderson, *Phys. Lett. A* **A 49**, 197 (1974).

[141] V. Ruehle, C. Junghans, A. Lukyanov, K. Kremer, D. Andrienko, *J. Chem. Theory Comput.* **5**, 3211 (2009).

[142] F. Ercolessi, J. B. Adams, *Europhys. Lett.* **26**, 583 (1994).

[143] S. Izvekov, G. A. Voth, *J. Chem. Phys.* **123**, 134105 (2005).

[144] S. Izvekov, G. A. Voth, *J. Chem. Theory Comput.* **2**, 637 (2006).

[145] Q. Shi, S. Izvekov, G. A. Voth, *J. Phys. Chem. B* **110**, 15045 (2006).

[146] J. Zhou, I. F. Thorpe, S. Izvekov, G. A. Voth, *Biophys. J.* **92**, 4289 (2007).

[147] W. G. Noid, J. W. Chu, G. S. Ayton, G. A. Voth, *J. Phys. Chem. B* **111**, 4116 (2007).

[148] L. Larini, L. Lu, G. A. Voth, *J. Chem. Phys.* **132**, 164107 (2010).

[149] K. Kamio, K. Moorthi, D. N. Theodorou, *Macromolecules* **40**, 710 (2007).

[150] P. Carbone, H. A. K. Varzaneh, X. Y. Chen, F. Muller-Plathe, *J. Chem. Phys.* **128** (2008).

[151] C. Peter, L. Delle Site, K. Kremer, *Soft Matter* **4**, 859 (2008).

[152] G. Milano, S. Goudeau, F. Muller-Plathe, *J. Polym. Sci., Part B: Polym. Phys.* **43**, 871 (2005).

[153] J. Ghosh, R. Faller, *Mol. Simul.* **33**, 759 (2007).

[154] J. R. Silbermann, S. H. L. Klapp, M. Schoen, N. Chennamsetty, H. Bock, K. E. Gubbins, *J. Chem. Phys.* **124** (2006).

[155] A. Villa, C. Peter, N. F. A. van der Vegt, *J. Chem. Theory Comput.* **6**, 2434 (2010).

[156] D. Reith, B. Muller, F. Muller-Plathe, S. Wiegand, *J. Chem. Phys.* **116**, 9100 (2002).

[157] A. A. Louis, *J. Phys. Condens. Matter* **14**, PII S0953 (2002).

[158] M. E. Johnson, T. Head-Gordon, A. A. Louis, *J. Chem. Phys.* **126**, 144509 (2007).

[159] H. Fukunaga, J. Takimoto, M. Doi, *J. Chem. Phys.* **116**, 8183 (2002).

[160] K. A. Maerzke, J. I. Siepmann, *J. Phys. Chem. B* **115**, 3452 (2011).

[161] T. Vettorel, H. Meyer, *J. Chem. Theory Comput.* **2**, 616 (2006).

[162] H.-J. Qian, P. Carbone, X. Chen, H. A. Karimi-Varzaneh, C. C. Liew, F. Mueller-Plathet, *Macromolecules* **41**, 9919 (2008).

[163] C. F. Abrams, K. Kremer, *J. Chem. Phys.* **115**, 2776 (2001).

[164] H. S. Ashbaugh, H. A. Patel, S. K. Kumar, S. Garde, *J. Chem. Phys.* **122**, 104908 (2005).

[165] K. R. Hadley, C. McCabe, *J. Phys. Chem. B* **114**, 4590 (2010).

[166] Z. Wu, Q. Cui, A. Yethiraj, *J. Phys. Chem. B* **114**, 10524 (2010).

[167] S. O. Yesylevskyy, L. V. Schafer, D. Sengupta, S. J. Marrink, *PLoS Comput. Biol.* **6**, e1000810 (2010).

[168] R. Kumar, J. R. Schmidt, J. L. Skinner, *J. Chem. Phys.* **126**, 204107 (2007).

[169] M. P. Allen, D. J. Tildesley, *Computer Simulations of Liquids*, (Oxford: Oxford Science Publications, 1987).

[170] J. S. Rowlinson, B. Widom, *Molecular Theory of Capillarity*, (Clarendon, Oxford, 1982).

[171] C. Vega, E. de Miguel, *J. Chem. Phys.* **126**, 154707 (2007).

[172] H. J. C. Berensen, J. P. M. Postma, W. F. van Gunsteren, J. Hermans, *Intermolecular Forces*, (edited by B. Pullman: Reidel, Dordrecht, p.331, 1982).

[173] W. L. Jorgensen, J. Chandrasekhar, J. D. Madura, R. W. Impey, M. L. Klein, *J. Chem. Phys.* **79**, 926 (1983).

[174] H. J. C. Berensen, J. R. Grigera, T. P. Straatsma, *J. Phys. Chem.* **91**, 6269 (1987).

[175] M. W. Mahoney, W. L. Jorgensen, *J. Chem. Phys.* **112**, 8910 (2000).

[176] H. Nada, J. P. J. M. van der Eerden, *J. Chem. Phys.* **118**, 7401 (2003).

[177] H. W. Horn, W. C. Swope, J. W. Pitera, J. D. Madura, T. J. Dick, G. L. Hura, T. Head-Gordon, *J. Chem. Phys.* **120**, 9665 (2004).

[178] J. L. F. Abascal, C. Vega, *J. Chem. Phys.* **123**, 234505 (2005).

[179] J. C. Shelley, M. Y. Shelley, R. C. Reeder, S. Bandyopadhyay, M. L. Klein, *J. Phys. Chem. B* **105**, 4464 (2001).

[180] W. Shinoda, R. Devane, M. L. Klein, *Mol. Simul.* **33**, 27 (2007).

[181] T. Ha-Duong, N. Basdevant, D. Borgis, *Chem. Phys. Lett.* **468**, 79 (2009).

[182] A. Lyubartsev, A. Mirzoev, L. Chen, A. Laaksonen, *Faraday Discuss.* **114**, 1 (2010).

[183] S. W. Chiu, H. L. Scott, E. Jakobsson, *J. Chem. Theory Comput.* **6**, 851 (2010).

[184] S. Riniker, W. F. van Gunsteren, *J. Chem. Phys.* **134**, 084110 (2011).

[185] U. Essmann, L. Perera, M. L. Berkowitz, T. Darden, H. Lee, L. G. Pedersen, *J. Chem. Phys.* **103**, 8577 (1995).

[186] C. Vega, J. L. F. Abascal, I. Nezbeda, *J. Chem. Phys.* **125**, 034503 (2006).

[187] A. Baranyai, A. Bartok, A. A. Chialvo, *J. Chem. Phys.* **124**, 074507 (2006).

[188] F. Franks, *Water: A Matrix of Life*, (Royal Society of Chemistry, 2000).

[189] M. N. Rodnikova, *J. Mol. Liq.* **136**, 211 (2007).

[190] W. Wagner, A. Pruss, *J. Phys. Chem. Ref. Data* **22**, 783 (1993).

[191] D. Eisenberg, W. Kauzmann, *The Structure and Properties of Water*, (Clarendon Press Oxford, 1969).

[192] D. Pablo, Kremer, Espanol, Allen, Ensing, Muller-Plathe, Bolhuis, van der Vegt, M. Muller, Milano, Carbone, Lyubartsev, Voth, Wilson, van der Sman, Holm, Theodorou, Marrink, Frenkel, Graham, Boek, Deserno, Jackson, Lowen, *Faraday Discuss.* **144**, 93 (2010).

[193] B. Hess, H. Bekker, H. J. C. Berendsen, J. G. E. M. Fraaije, *J. Comput. Chem.* **18**, 1463 (1997).

[194] J. Fischer, D. Paschek, A. Geiger, G. Sadowski, *J. Phys. Chem. B* **112**, 2388 (2008).

[195] C. Junghans, M. Praprotnik, K. Kremer, *Soft Matter* **4**, 156 (2008).

[196] R. L. Jaffe, G. D. Smith, D. Y. Yoon, *J. Phys. Chem.* **97**, 12745 (1993).

[197] G. D. Smith, R. L. Jaffe, D. Y. Yoon, *J. Phys. Chem.* **97**, 12752 (1993).

[198] G. D. Smith, R. L. Jaffe, D. Y. Yoon, *J. Am. Chem. Soc.* **117**, 530 (1995).

[199] H. Yoshida, T. Tanaka, H. Matsuura, *Chem. Lett.*, 637 (1996).

[200] P. M. Anderson, M. R. Wilson, *Mol. Phys.* **103**, 89 (2005).

[201] W. L. Jorgensen, D. S. Maxwell, J. Tiradorives, *J. Am. Chem. Soc.* **118**, 11225 (1996).

[202] J. M. Stubbs, J. J. Potoff, J. I. Siepmann, *J. Phys. Chem. B* **108**, 17596 (2004).

[203] D. Bedrov, C. Ayyagari, G. D. Smith, *J. Chem. Theory Comput.* **2**, 598 (2006).

[204] H. Lee, A. H. de Vries, S. J. Marrink, R. W. Pastor, *J. Phys. Chem. B* **113**, 13186 (2009).

[205] S. Rangelov, W. Brown, *Polymer* **41**, 4825 (2000).

[206] S. Kuga, *J. Chromatogr.* **206**, 449 (1981).

[207] H. Lee, R. W. Pastor, *J. Phys. Chem. B* **115**, 7830 (2011).

[208] H. J. White, J. V. Sengers, D. B. Neumann, J. C. Bellows, *Release on the Surface Tension of Ordinary Water Substance*, (IAPWS, 1995).

[209] P. Thiyagarajan, D. J. Chaiko, R. P. Hjelm, *Macromolecules* **28**, 7730 (1995).

[210] S. Kawaguchi, G. Imai, J. Suzuki, A. Miyahara, T. Kitano, *Polymer* **38**, 2885 (1997).

[211] N. L. Abbott, D. Blankschtein, T. A. Hatton, *Macromolecules* **25**, 3932 (1992).

[212] C. Branca, A. Faraone, S. Magazu, G. Maisano, P. Migliardo, V. Villari, *J. Mol. Liq.* **87**, 21 (2000).

[213] T. Gilanyi, I. Varga, M. Gilanyi, R. Meszaros, *J. Colloid Interface Sci.* **301**, 428 (2006).

[214] D. J. Kuzmenka, S. Granick, *Macromolecules* **21**, 779 (1988).

[215] M. Darvas, T. Gilanyi, P. Jedlovszky, *J. Phys. Chem. B* **114**, 10995 (2010).

[216] R. L. Shuler, W. A. Zisman, *J. Phys. Chem.* **74**, 1523 (1970).

[217] D. J. Kuzmenka, S. Granick, *Polym. Commun.* **29**, 64 (1988).

[218] M. Kawaguchi, S. Komatsu, M. Matsuzumi, A. Takahashi, *J. Colloid Interface Sci.* **102**, 356 (1984).

[219] M. W. Kim, *Colloids Surf., A* **128**, 145 (1997).

[220] B. B. Sauer, H. Yu, *Macromolecules* **22**, 786 (1989).

[221] M. Tsige, G. S. Grest, *J. Phys. Chem. C* **112**, 5029 (2008).

[222] C. McCabe, D. Bedrov, O. Borodin, G. D. Smith, P. T. Cummings, *Ind. Eng. Chem. Res.* **42**, 6956 (2003).

[223] W. L. Jorgensen, J. D. Madura, C. J. Swenson, *J. Am. Chem. Soc.* **106**, 6638 (1984).

[224] E. K. Watkins, W. L. Jorgensen, *J. Phys. Chem. A* **105**, 4118 (2001).

[225] O. Borodin, G. D. Smith, D. Bedrov, *J. Phys. Chem. B* **106**, 9912 (2002).

[226] O. Borodin, G. D. Smith, *J. Phys. Chem. B* **110**, 6279 (2006).

[227] A. A. H. Padua, *J. Phys. Chem. A* **106**, 10116 (2002).

[228] W. Song, P. J. Rossky, M. Maroncelli, *J. Chem. Phys.* **119**, 9145 (2003).

[229] F. Pierce, M. Tsige, O. Borodin, D. Perahia, G. S. Grest, *J. Chem. Phys.* **128**, 214903 (2008).

[230] F. Pierce, M. Tsige, D. Perahia, G. S. Grest, *J. Phys. Chem. B* **112**, 16012 (2008).

[231] A. E. Ismail, G. S. Grest, M. J. Stevens, *J. Chem. Phys.* **125**, 014702 (2006).

[232] Q. Du, Z. Yang, N. Yang, X. Yang, *Ind. Eng. Chem. Res.* **49**, 8271 (2010).

[233] S. R. Lee, D. K. Yoon, S. H. Park, E. H. Lee, Y. H. Kim, P. Stenger, J. A. Zasadzinski, H. T. Jung, *Langmuir* **21**, 4989 (2005).

[234] I. Szleifer, M. A. Carignano, *Macromol. Rapid Commun.* **21**, 423 (2000).

[235] E. M. Sevick, D. R. M. Williams, *Macromolecules* **27**, 5285 (1994).

[236] V. Kumaran, *Macromolecules* **26**, 2464 (1993).

[237] P. Auroy, L. Auyray, L. Leger, *Phys. Rev. Lett.* **66**, 719 (1991).

[238] J. R. Lu, R. K. Thomas, *J. Chem. Soc., Faraday Trans.* **94**, 995 (1998).

[239] M. Mulqueen, D. Blankschtein, *Langmuir* **15**, 8832 (1999).

[240] J. R. Lu, R. K. Thomas, J. Penfold, *Adv. Colloid Interface Sci.* **84**, 143 (2000).

[241] H. D. Burrows, M. J. Tapia, C. L. Silva, A. A. C. C. Pais, S. M. Fonseca, J. Pina, J. S. de Melo, Y. Wang, E. F. Marques, M. Knaapila, A. P. Monkman, V. M. Garamus, S. Pradhan, U. Scherf, *J. Phys. Chem. B* **111**, 4401 (2007).

[242] I. G. Elliott, D. E. Mulder, P. T. Traeskelin, J. R. Ell, T. E. Patten, T. L. Kuhl, R. Faller, *Soft Matter* **5**, 4612 (2009).

[243] O. S. Heavens, *Optical Properties of Thin Films*, (Butterworth: London, 1955).

[244] M. Born, E. Wolf, *Principles of Optics*, (Peragamon: Oxford, 1980).

[245] A. Braslau, M. Deutsch, P. S. Pershan, A. H. Weiss, J. Alsnielsen, J. Bohr, *Phys. Rev. Lett.* **54**, 114 (1985).

[246] D. M. Colegate, C. D. Bain, *Phys. Rev. Lett.* **95**, 198302 (2005).

[247] E. Rillaerts, P. Joos, *J. Phys. Chem.* **86**, 3471 (1982).

[248] V. B. Fainerman, *Colloids and Surfaces* **62**, 333 (1992).

[249] V. B. Fainerman, A. V. Makievski, *Colloids and Surfaces* **69**, 249 (1993).

[250] K. J. Laidler, *Chemical Kinetics*, (Harper-Collins: New York, 1987).

[251] A. Patist, J. R. Kanicky, P. K. Shukla, D. O. Shah, *J. Colloid Interface Sci.* **245**, 1 (2002).

[252] H. E. Johnson, S. Granick, *Science* **255**, 966 (1992).

[253] E. P. Enriquez, H. M. Schneider, S. Granick, *J. Polym. Sci., Part B: Polym. Phys.* **33**, 2429 (1995).

[254] J. C. Dijt, M. A. C. Stuart, G. J. Fleer, *Macromolecules* **27**, 3229 (1994).

[255] J. C. Dijt, M. A. C. Stuart, G. J. Fleer, *Macromolecules* **27**, 3219 (1994).

[256] M. Santore, Z. L. Fu, *Macromolecules* **30**, 8516 (1997).

[257] Z. L. Fu, M. M. Santore, *Macromolecules* **31**, 7014 (1998).

[258] P. Frantz, S. Granick, *Macromolecules* **27**, 2553 (1994).

[259] Z. L. Fu, M. M. Santore, *Langmuir* **14**, 4300 (1998).

[260] T. J. Smith, W. Iglesias, S. R. Stefanovic, E. K. Mann, C. Tschierske, A. Jakli, D. J. Lacks, *J. Phys. Chem. B* **115**, 12809 (2011).

[261] F. Renou, T. Nicolai, E. Nicol, L. Benyahia, *Langmuir* **25**, 515 (2009).

[262] C. Rufier, A. Collet, M. Viguier, J. Oberdisse, S. Mora, *Macromolecules* **44**, 7451 (2011).